学位論文

Submarine Mud Volcanism from a Standpoint of Subseafloor Material Cycling

（海底下物質循環からみた海底泥火山に関する研究）

平成 27 年 12 月博士（理学）申請

東京大学大学院 理学系研究科

地球惑星科学専攻

喜岡　新

Submarine Mud Volcanism from a Standpoint of Subseafloor Material Cycling

A dissertation presented
by

Arata Kioka

to

the Department of Earth and Planetary Science
Graduate School of Science

in partial fulfillment of the requirements
for the degree of
Doctor of Science

The University of Tokyo
Tokyo, Japan
December 2015

Dissertation Advisor: Author:

Assoc. Prof. Juichiro Ashi **Arata Kioka**

Submarine Mud Volcanism from a Standpoint of Subseafloor Material Cycling

Abstract

Mud volcanism falls behind other mainstream research areas in the Earth and Planetary Science. Mud volcanism on Earth, however, provides profound insights into subsurface cycling of sediment and fluid, plays an important role in the subsurface carbon cycle, and has thus always been of interest to a broad scientific community. In this thesis, I present results of submarine mud volcanism that span a number of independent topics within the broader disciplines of geology, sedimentology, geophysics, and geochemistry. The issues presented in each chapter are slightly different, but the approach handled throughout aims to understand the roles of submarine mud volcanoes on the subseafloor material cycling. The three primary results of this thesis can be summarized as follows: (1) The shape of the submarine mud volcano depends on its width of feeding conduit and erupted volume, and is associated with sediment influxes in subduction zones. (2) Ascent mechanism of ejecta that include fluid-rich muds and clasts from a submarine mud volcano in the eastern Mediterranean Sea is now understood in the light of sample measurements and modeled thermal structure. (3) Methane amounts inside a deep-water mud volcano are studied using seismics, revealing that the amount of methane in its conduits is higher than previously expected from geochemical evidence. All the results obtained in this thesis represent an increase in our understanding of submarine mud volcanism and its relation to subseafloor material cycling.

Contents

Acknowledgments

I have been fortunate to have the opportunity to pursue my research interests in a stimulating environment with influential and inspirational people. There are many more people who deserve my thanks than those listed here, but I hope I have not been overly forgetful in my omissions.

First and foremost it has been such a great pleasure studying with my supervisor, Juichiro Ashi. I would like to express so many thanks to him for his countless insightful pieces of advice, encouragement of my various research pursuits, and being understanding of these interests. Ashi-san is especially thanked for allowing me so much independence in my research pursuits, though the decision often carries risky or might draw some sacrifices, and for sharing all the excitements that I felt over the years. Ashi-san welcomed me to the exciting world of subseafloor material cycling and fluid migration in subduction zones, inspiring me into this study. Ashi-san also gave me opportunities to participate in valuable international/domestic research cruises that were mostly good times to get various inspirations. I am sure if he had not been my supervisor, I would not have broadened my perspective and completed this thesis. I could not have imagined having a better supervisor than Ashi-san.

To my family Father, Mother, wild Balto, and peaceful Fang who I have not thanked enough throughout my life. I am especially so thankful for the moral support and endless opportunities from parents that made my time during this PhD program so enjoyable and enriching. Hereafter, in this Acknowledgments, the order of named people has no concern.

Thanks to all of the OFGS people for making the past 5-years of my OFGS life interesting and enjoyable. To OFGS groupmates M. Fujii, T. Manaka, R. Sawada, A. Seki, and T. Bell for much help to the whole years. They realize that I tend to favor being a lone wolf, but they gave many times of numerous conversations and discussions with me all of which were definitely enjoyable. Fujii-san and Manaka-san are highly thanked for discussions on various scientific studies and encouragement of motivation to improve the whole study, and of course for untold chats. To all lab student members H. Otsuka (Now at AIST), S. Muraoka (EJEC), A. Misawa (OYO), T. Ojima, Y. Nakamura, K. Tara, R. Sawada (MWJ), K. Yagasaki, R. Fukuchi, A. Ohde, and N. Okutsu for interesting discussions and conversations as well as untold chats, adventures, and favorable coffee breaks. To OFGS faculty A. Yamaguchi, A. Omura, K. Okino, T. Yamazaki, and J.-O. Park for discussions and their useful comments at exciting MGG seminar, T. Kanehara, M. Terada, and S. Nakagawa for their hospitality and supports throughout my OFGS life, and Y. Yokoyama for his giving a great chance to participate in the IODP cruise. H. Tokuyama (Now at Kochi U., Japan) took me kindly into a world of submarine mud volcanism through studies in the Eastern Mediterranean Sea.

All co-authors of the individual chapters and publications are kindly acknowledged: Thank you very much J. Ashi, A. Sakaguchi, T. Sato, S. Muraoka, A. Yamaguchi, H. Hamamoto, K. Wang, H. Tokuyama, T. Tsuji, and H. Otsuka, for their great collaboration. I am also deeply grateful to my thesis committee Y. Ikeda, H. Miyamoto, K. Mochizuki, G. Kimura, and J. Ashi for their critical review of this thesis.

In Chapter 2, I highly appreciate P. Henry for his numerous insightful comments to a first version of the manuscript and for discussions that improved this work. This chapter benefited from constructive reviews and editorial handling by three anonymous reviewers and the Editor of *Geophysical Research Letters*. I would also like to thank H. Miyamoto, M. Fujii, R. Hemmi, and K. Yagasaki for their comments and information. Parameters in the Gutenberg-Richter relationship is helpfully examined using the GRTo package [*Amorèse*, 2007]. This work was partially supported by JSPS KAKENHI Grant to J. Ashi (No. 15H02988).

In Chapter 3, special thanks are dedicated to the effort of shipboard scientists and staffs of PENELOPE Cruise (KH-06-4 Leg 6) to acquire the data used in this work. I also thank A. Omura for her kind supports on measurement of density and other pretreatments of samples as well as her helpful comments, and thank G. Kimura, Y. Ikeda, M. Yamano, H. Otsuka, A. Misawa, T. Ojima, M. Fujii, and K. Yagasaki for helpful information and discussions. This chapter benefited from reviews by two anonymous reviewers and the Editor of *Marine Geology*. F. Harmegnies provided the geothermal data obtained during the MEDRIFF project. This study was supported by Grant-in-Aid for Scientific Research on Innovative Areas to J. Ashi (No. 21107003) from MEXT of Japan. This is Geological Survey of Canada contribution 20140139.

In Chapter 4, many thanks are dedicated to the efforts of shipboard scientists and crews of the KT-06-19 cruise (Chief scientist: S. Morita) and Y. Nakamura to acquire the data used in this work. I also thank very much K. Mochizuki and J.-O. Park for insightful suggestions, K. Tara, A. Ohde, K. Yagasaki, K. Tara, R. Fukuchi, and K. Adachi for useful information. This chapter benefited from constructive reviews from three anonymous reviewers for which I am sincerely grateful. Some of the thermodynamic, kinetic, and physical properties of methane and seawater that we calculated here are computed and tested helpfully with SUGAR Toolbox [*Kossel et al.*, 2013]. This work was partially supported by the JSPS Grant-in-Aid for Science Research Program KAKENHI to J. Ashi (No. 15H02988).

Finally, I thank very much M. Strasser, H. Fink, D. Dinten, K. Ikehara, T. Kanamatsu, T. Fujiwara, and G. Wefer for the enjoyable and stimulating Sonne Expedition in Japan Trench. M. Strasser is especially thanked for thoughtful hosting and discussions of my studies at ETH Zürich, and Paleoseismology Workshop where I could discuss and chat with A. Reusch, M. Stupler, U. Mannu, and T. Schwestermann which are so enjoyable. G. G. Akhmanov, D. Giliazetdinova, A. Iurchenko, Alexii, E. Poludetkina, E. V. Kozlova, and Yu. I. Galushkin for their hosting, organization, hospitality, and interesting discussions during my stay at Lomonosov Moscow State University. M. Asada, S. Morita, T. Toki, and T. Tsuji are also thanked for encouragement of my studies into submarine mud volcanism through recent launching of a scientific community toward understanding of mud volcanism. Many figures presented in this thesis were drafted using the Generic Mapping Tools (GMT) software developed by *Wessel and Smith* [1998] that was very helpful throughout my work.

Citations to Previously Published Work

Chapters 2 (with Appendix A) and 3 (with Appendix B) have been published in their entirety in the following 2 papers [*Kioka and Ashi*, 2015; *Kioka et al.*, 2015].

Kioka, A. and J. Ashi (2015), Episodic massive mud eruptions from submarine mud volcanoes examined through topographical signatures, *Geophys. Res. Lett.*, *42*, 8406–8414, doi:10.1002/2015GL065713.

Kioka, A., J. Ashi, A. Sakaguchi, T. Sato, S. Muraoka, A. Yamaguchi, H. Hamamoto, K. Wang, and H. Tokuyama (2015), Possible mechanism of mud volcanism at the prism-backstop contact in the western Mediterranean Ridge Accretionary Complex, *Mar. Geol.*, *363*, 52–64, doi:10.1016/j.margeo.2015.01.014.

Chapter 4 (with Appendix C) has been submitted for publication as the following:

Kioka, A., T. Tsuji, H. Otsuka, and J. Ashi (2016), Methane amount inside a deep-water mud volcano constrained by seismic velocity, *Geophys. Res. Lett.*, revised (1 Dec 2015).

Published papers have been reproduced by permission of the American Geophysical Union (http://publications.agu.org/author-resource-center/usage-permissions/) and the Elsevier (https://www.elsevier.com/about/company-information/policies/copyright/permissions/).

Chapter 1

Introduction and Summary

1.1 Mud volcanism and subsurface material cycling

Drastic mass fluxes in the shallow areas of subduction zone forearcs on millennial-year scales control the evolution and dynamics of the earth. The volume of subducted sediment that bypasses the overriding plate wedge or accretion and underplating processes would affect the net rate of continental growth and evolutionary processes of the whole earth [e.g., *von Huene and Scholl*, 1991; *Scholl et al.*, 1994] (Figure 1.1). On shorter time scales, these tectonic processes strongly affect not only whole material cycling but amounts and distribution of fluids within the overriding plate wedge. The resultant overpressure has profound effects on deformations, earthquake mechanics and thermal regimes in the wedge through its influence on effective stresses [e.g., *Moore and Vrolijk*, 1992]. Fluids in subduction zones that are derived from the incoming plate may move out of the overriding plate to the seafloor by diffusive flows or along structural conduits, or they may migrate to greater depths where they affect various processes such as mantle serpentinization, magma generation and triggering intermediate and deep earthquakes [e.g., *Moore and Vrolijk*, 1992; *Saffer and Tobin*, 2011]. In association with the giant 2011 Tohoku-oki Earthquake, for example, geological evidences have been shown its relation to long-term deformations in Japan Trench [e.g., *Kodaira et al.*, 2012; *Strasser et al.*, 2013; *Fink et al.*, 2014], changes in pore fluid pressures following the earthquake [*Terakawa et al.*, 2013], and rapid release of mantle-derived fluids [*Sano et al.*, 2014]. These fluids strongly affect

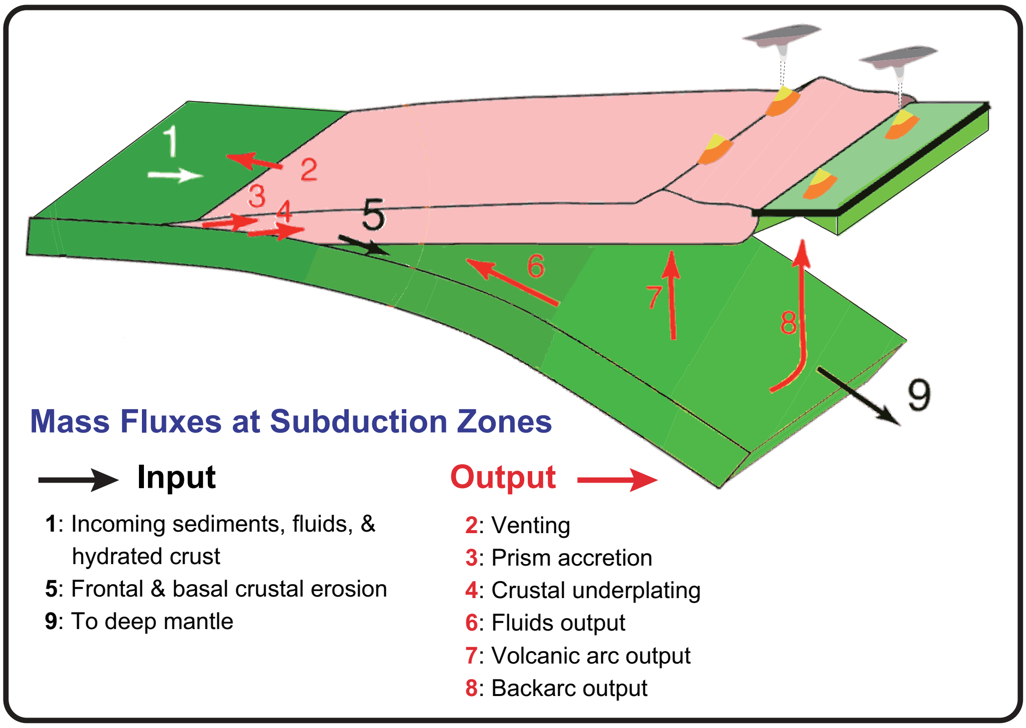

Figure 1.1: The crustal material fluxes at the subduction zones. Arrows indicate various fluxes associated with the partioning, loss, and gain of bulk sediment in the shallow part of the subduction zones, each driven by accretion, underplating, and erosion, chemical and fluid fluxes due to sediment dehydration, venting, volcanic arc, and backarc. Modified from *Scholl et al.* [1994].

the deformation style of the overriding plate wedge. In addition, tectonic loading and mineral dehydration produce fluids within the overriding wedge. These fluids drive excess pore pressure, or overpressure, indicative of disequilibrium that overcomes fluid escape and thus leads to trapping of fluids, which poses profound effects on faulting and earthquake mechanics through its influence on effective stress. Direct observations of overpressure in this setting are rare, as they require deep drilling. Submarine mud volcanoes are possible paths for migration of overpressured fluids from the underthrusting section through the wedge to the seafloor [*Kopf*, 2002]. Thus, studies of mud volcanoes hold promise in picture of subsurface sediment transfer and fluid migration.

Mud volcanoes (Figure 1.2), sedimentary types of volcanoes composed of fine-grained mud [e.g., *Kopf*, 2002; *van Loon et al.*, 2010], are plentiful in various tectonic settings on Earth including on the lakebed [e.g., *Van Rensbergen et al.*, 2002], and candidate mud volcanoes have been reported on Mars [e.g., *Tanaka*, 1997; *Oehler and Allen*, 2010; *Pondrelli et al.*, 2011]. Large number of studies into the mud volcanism on Earth has been conducted especially since the early 1970s [*Higgins and Saunders*, 1974], and about 300 offshore mud volcanoes had been confirmed and the double had been inferred around the early 2000s [e.g., *Dimitrov*, 2002; *Kopf*, 2002]. Despite the uncertainty regarding the number, thousands of submarine mud volcanoes are thought to be present [*Milkov*, 2000; *Kopf*, 2003]. Nevertheless, mud volcanism falls behind other mainstream research areas in the Earth and Planetary Science. Mud volcanism on Earth, however, provides profound insights into subsurface cycling of sediment and fluid, plays an important role in the subsurface carbon cycle (Figure 1.3), and has thus always been of interest to a broad scientific community. They can be viewed as natural tectonic conduits that bring up deep substances and fluids driven by overpressuring at deep depths. Thus, mud volcanoes are useful tools to explore subsurface processes in material cycling such as sediment recycling, fluid migration, and carbon cycling investigated in this thesis. Despite the importance, there has been so far little understanding of mud volcanism itself and its dynamic linkage to subsurface material cycle. In the following Section 1.2, I will first briefly review previous studies into submarine mud volcanism. This aims to marshal our knowledge of submarine mud volcanism and list the problems to further understand the mud volcanism, which leads to an increase in our understanding of the linkage between mud volcanism and subsurface material cycling which is a final goal of this thesis through the results presented in main chapters in this thesis.

1.2 Submarine mud volcanism: A brief review

1.2.1 Geological, sedimentary, and geophysical features

Herein I briefly address several properties of onshore and offshore mud volcanism reviewed from geological, sedimentary, and geophysical evidence. The topics reviewed here include structure, source depths, ascent mechanisms, life span, and discharge rates. Note that a well-known onshore mud volcano, Lusi (named after "Lumpur Sidoarjo") Mud Volcano, East Java, Indonesia, is an unusual mud volcano in several respects [e.g., *Tingay et al.*,

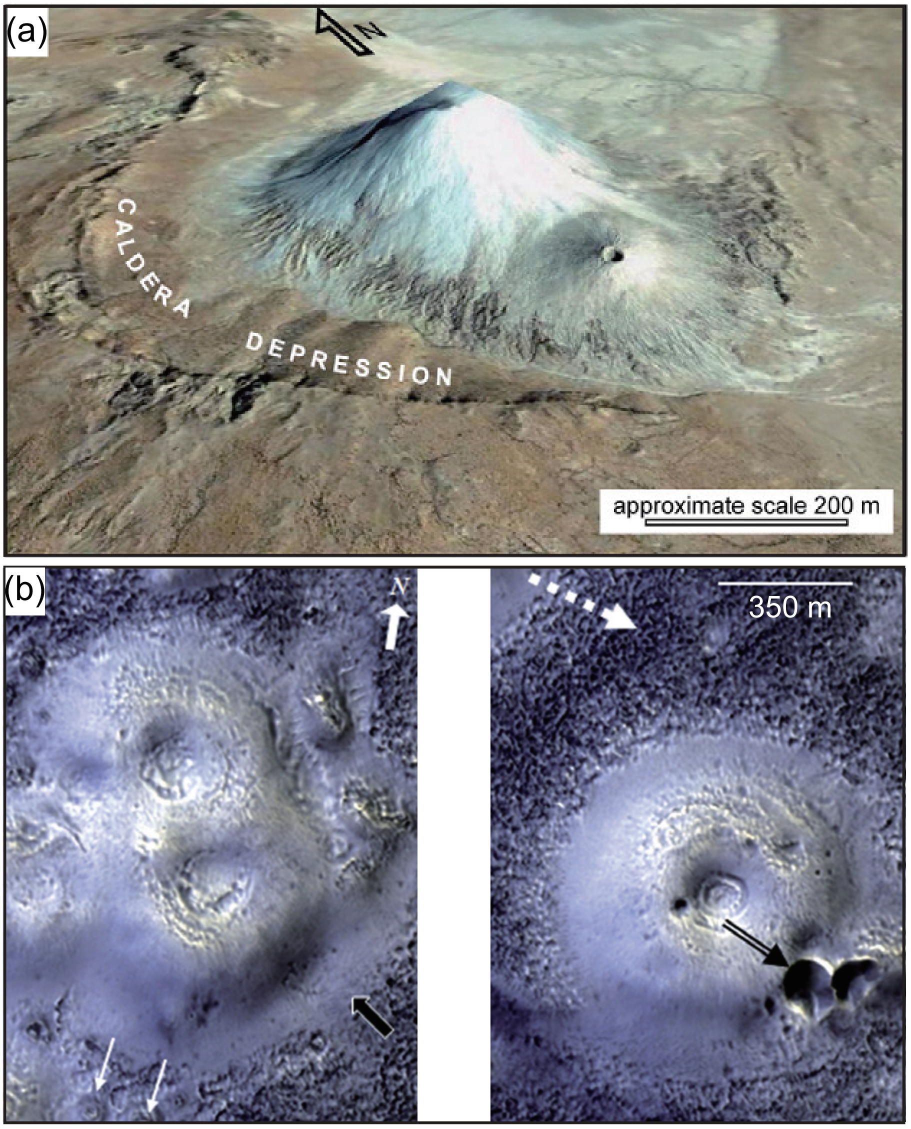

Figure 1.2: Mud volcanoes found on Earth and mud volcano-like structure on Mars. (a) Chandragup mud volcano in eastern Makran, Pakistan [*Bonini*, 2012]. (b) Mud volcano-like mounds in Acidalia Plantia on Mars [*Oehler and Allen*, 2010].

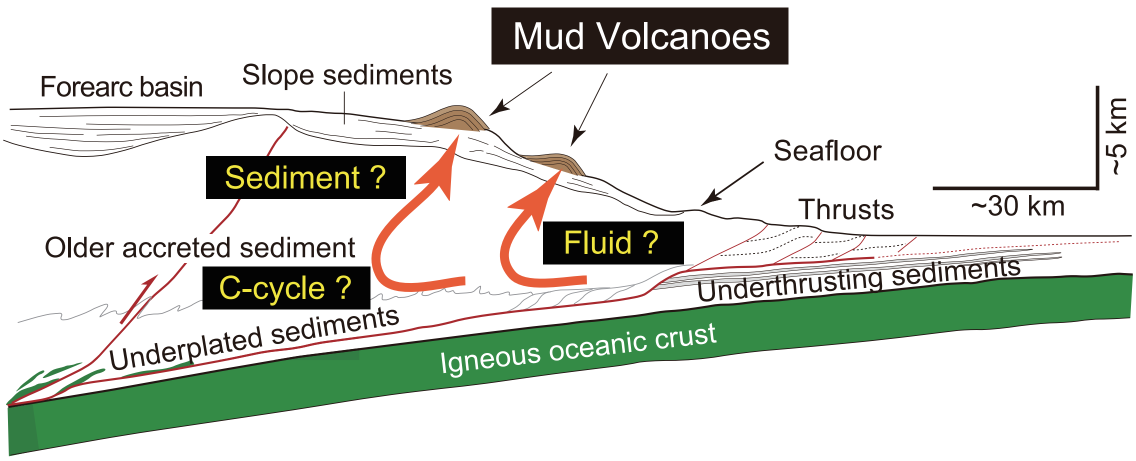

Figure 1.3: A schematic cross section showing tectonic and geological setting of an accretionary margin in the subduction zone. Submarine mud volcanism is strongly related to subseafloor sediment transfer, fluid migration, and carbon cycle. Modified from *Saffer and Tobin* [2011].

2015], while that this onshore mud volcano is often compared with other onshore and offshore mud volcanoes presented here and in previous many studies because it is well-studied.

Structure

Submarine mud volcanism is viewed as the seabed/subseafloor manifestation of mud intrusive processes originated from deep depths (Figure 1.4). Submarine mud volcanism and mud diapirism are well-detected from strong backscattering on the seafloor [e.g., *Chamot-Rooke et al.*, 2005a]. A diapiric ascent, as addressed later, often a primary mechanism to transfer fluid and mud from deep depths to the seafloor to generate the mud volcanoes. However, the term mud diapir is used here for buoyancy-driven upward migration of fluid-rich, fine-grained sediments at a slow speed, as noted in *Kopf* [2002]. Submarine mud volcanoes are generated by diapiric mass and forceful ascended mud from deep depths. The crest is superposed by the conduit of feeder that is the central feature in which fluidized sediment is travelled. Little information regarding width of the conduit has been understood. The size of each conduit or feeder is thought to be less than 10 m or several tens of meters at maximum owing to previous studies [*Kopf*, 2002, and references

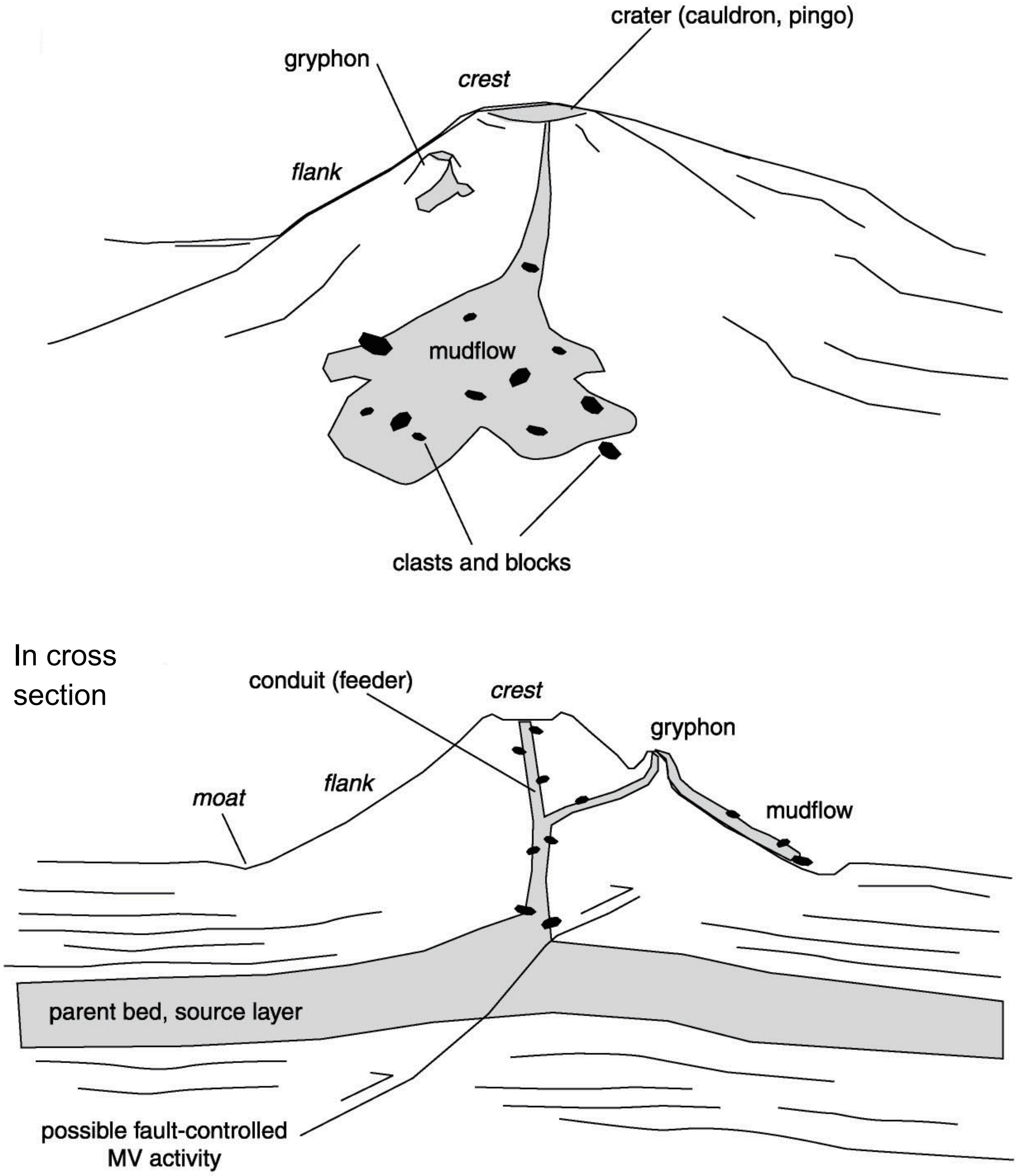

Figure 1.4: A schematic diagram of a mud volcano [*Kopf*, 2002]. Terminology includes: cauldron or pingo (subsided crater area); gryphon (small cones or mud craters at the flank of the mud volcano).

therein], although some studies note the conduit has diameter up to a few kilometer [e.g., *Ivanov et al.*, 1996; *Løseth et al.*, 2003; *Talukder et al.*, 2003]. Theoretical calculations and considerations from physical properties of submarine mud volcanoes assuming Newtonian rheology suggest that the size is likely less than 5 m [*Kopf and Behrmann*, 2000]. In addition, high-resolution 3D seismic data reveal cylindrical zones of amalgamated narrow fluidized mud pipes feeding offshore mud volcanoes [e.g., *Davies and Stewart*, 2005; *Stewart and Davies*, 2006]. The evidence found above indicates major paths of submarine mud volcanoes that are made from multiple mud conduits. While a primary fluidized sediment is escaped from the main conduits from the crest of a submarine mud volcano, the mud volcano often has small cones or mud craters at the flank of mud volcano termed gryphons (Figures 1.4 and 3.3). They serve as secondary ejecta paths possibly resulted from splays of main conduits. Both the main conduits and the gryphons are outlets where mudflows originate. A porosity profile in the mud conduits of submarine mud volcanoes is summarized in Section C.3.

Submarine mud volcanoes are often covered by bacterial mats or carbonates. Some submarine mud volcanoes include clasts of hydrates in their ejecta with fluidized muds [e.g., *Lykousis et al.*, 2009]. Subsidence and the gravitational collapse of the volcanic body are found in some submarine mud volcanoes [e.g., *Henry et al.*, 1990], and most basal angles settle within 0–2°. On seismic reflection images, the "Christmas tree" structure formed by episodic mud eruptions interbedding general marine sediments is often seen in submarine mud volcanoes [e.g., *Somoza et al.*, 2003], suggesting that they are polygenetic. Faults may often play a profound role in mud extrusion as faults are found to be juxtaposed at submarine mud volcanoes from seismic reflection data [e.g., *Kopf et al.*, 2001; *Woodside et al.*, 2002; *Mörz et al.*, 2005; *Viola et al.*, 2005; *Chiu et al.*, 2006; *Praeg et al.*, 2009]. The associated topic is reviewed later.

Source depths

Fluid sources for overpressuring and mud extrusion are arisen from various mechanism [*Kopf*, 2002] driven by compaction, organic matter degradation, lateral fluid flux through stratigraphic horizons, faulting, thermogenic processes, mineral dehydration, hydrother-

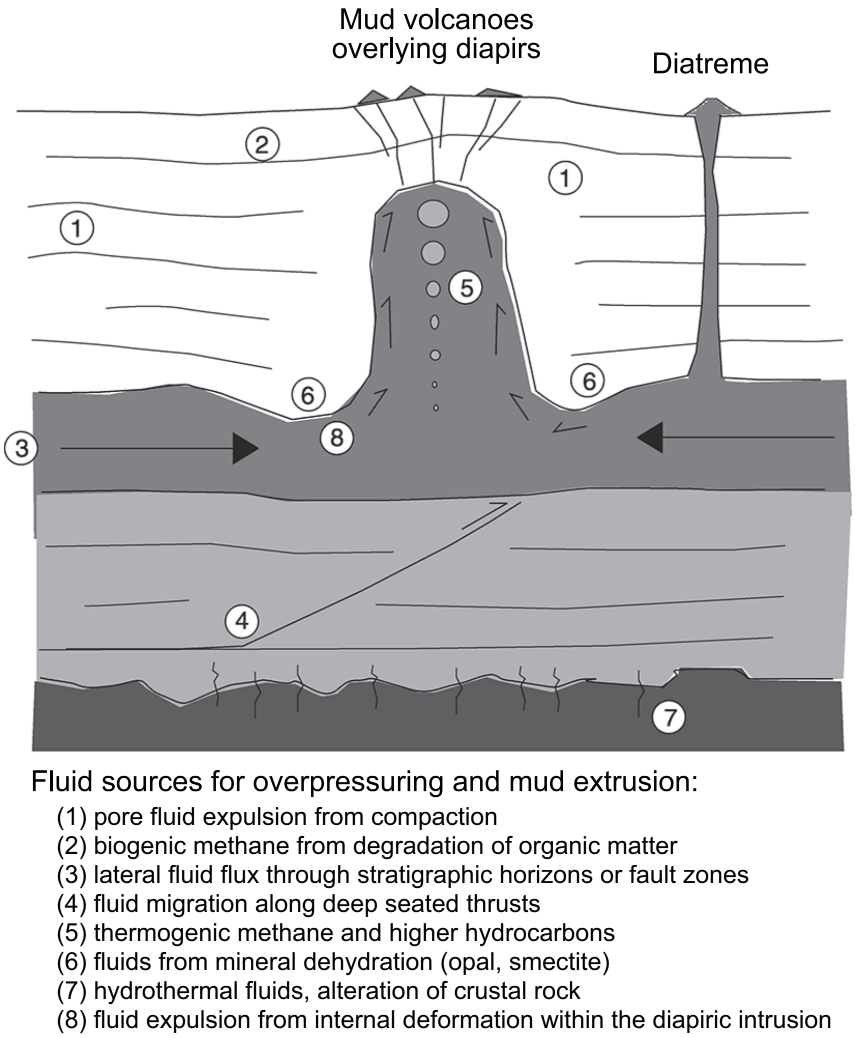

Figure 1.5: A schematic diagram of a mud diapir, mud volcanoes (mud extrusions), and diatreme(-like mud volcano), including possible fluid sources numbered 1–8 [*Kopf*, 2002]. The fluid sources are also discussed from geochemical signatures (see Subsection 1.2.2).

mal fluids, and diapiric intrusion (Figure 1.5). A source depth of the Lusi Mud Volcano is estimated to be $\sim$ 1.5 km from the interferometric synthetic aperture radar (InSAR) observations [*Fukushima et al.*, 2009] and P-wave velocity [*Istadi et al.*, 2009]. *Shirzaei et al.* [2015] find two different shallow (0.3–2.0 km depth) and deep (3.5–4.8 km) sources from the Lusi, by a time-dependent inverse model using multitemporal InSAR data. Håkon Mosby Mud Volcano in Barents Sea roots at a depth of $\sim$ 3 km from a reflection seismic image [*Perez-Garcia et al.*, 2009]. Some submarine mud volcanoes in the Barbados accretionary wedge also have source depths of $\sim$ 2–3 km from reflection seismics [*Brown and Westbrook*, 1988; *Faugéres et al.*, 1997]. Reflection seismic images provide information regarding the source depth while the images face difficulties in its assessment when the source root in deep depths. From burial organic maturity data, mobilized mud from Napoli mud volcano in the central Mediterranean Ridge accretionary wedge is traveled from the depth of 5–8 km below the seafloor [*Schulz et al.*, 1997]. On the other hand, *Kopf et al.* [2000] found the Milano mud volcano located in the central Mediterranean Ridge roots in the depth of $\sim$ 2 km below the seafloor using the same technique. Sublacustrine mud volcanoes in Lake Baikal are thought to be triggered by the gas hydrate dissociation [*Van Rensbergen et al.*, 2002] as found in pockmarks [e.g., *Vogt et al.*, 1994; *Zühlsdorff and Spieß*, 2004], suggesting that they root in the gas hydrate stability zone at depths of hundreds of meters below the lakefloor. These results can conclude that mud volcanoes take on different source depths depending on their background settings, while most of mobilized sediments from submarine mud volcanoes may originate from the depths of 2–10 km below the seafloor. The related topic is also discussed in Chapter 3. The estimate of source depth is also discussed from pore fluids of submarine mud volcanoes. See Section 1.2.2.

Ascent mechanisms

A wide range of mechanisms has been investigated to explain ejecta ascent from mud volcanoes. Overpressures are presumably required to generate massive mud eruptions from mud volcanoes. Mud volcanism is categorized by several types of ejecta ascent, including diapiric ascent, conduit ascent (i.e., through pre-existing paths), and hydrofracture ascent [e.g., *Kopf*, 2002; *Manga et al.*, 2009], but few studies in practice have addressed this topic. While previous studies often undoubtedly assume the diapiric ascent, the ascent mechanism follows different styles when ejecta include clasts. The associated topic is presented in Chapter 3. Liquefaction prior to mud eruptions can lead the eruptions due to increase in pore pressures and fluidizing the mud reducing the resistance to motion. Dilatancy can be also a candidate for extrusion of sediments because mud volcanism is often associated with faulting, suggesting that mud volcanoes have no difficulty in forming regions where dilatancy occurs [*Manga et al.*, 2009]. Bubble formation or growth may also play a role in driving eruptions, as mud volcanoes typically include gases. Gas hydrate dissolution will be also a candidate for triggering mud eruptions [*Van Rensbergen et al.*, 2002]. Direct connection between neighboring earthquakes and mud eruptions is likely weak from compilation of mud eruptions and earthquakes in Azerbaijan during the last 2 centuries [*Mellors et al.*, 2007]. The eruption from Lusi mud volcano did not undergo at a pre-existence edifice. If the ascent occurs through hydrofractures, they will be young or are held open by fluid intrusion. The pressure of drilling fluids in the neighboring well following the earthquake was thus likely sufficient to initiate hydrofractures and trigger the eruption in the Lusi mud volcano [*Davies et al.*, 2008; *Manga et al.*, 2009].

Life expectancy and activity

A life span of each submarine mud volcano is directly related to long-term subseafloor material cycling studied in this thesis. Thanks to the success of the deep-drilling, the activity of Milano Mud Volcano in the central Mediterranean Ridge accretionary complex is known to begin $\sim$ 1.5 Ma [*Robertson and Ocean Drilling Program Leg 160 Scientific Party*, 1996]. Mud eruptions from Bonjardim Mud Volcano in the Gulf of Cádiz also seem to start $\sim$ 1.0–1.5 Ma [*Gutscher et al.*, 2009a]. Submarine mud volcanism in the Barbados accretionry wedge began $\sim$ 200–750 kyr ago based on acoustic stratigraphy [*Langseth et al.*, 1988] and nannofossil dating [*Lance et al.*, 1998]. The Håkon Mosby Mud Volcano in the Barents Sea, one of the most studied submarine mud volcano, is considered to initiate its mud eruption around 330 kyr ago possibly triggered by a submarine landslide [*Perez-Garcia et al.*, 2009]. Most of submarine mud volcanoes in the Western Alborán Sea have been reactivated in the mid-Pleistocene [*Somoza et al.*, 2012], while the latest extrusion activities during the Holocene are found [*Gennari et al.*, 2013]. Submarine mud volcanoes in the El Arraiche mud field of the Gulf of Cádiz is characterized by different types of sediment flows on their flanks [*Van Rensbergen et al.*, 2005]. These findings suggest mud eruptions from submarine mud volcanoes seem to be episodic, short-lived and recurrent over thousands of years. The associated topic is also discussed in Chapter 3. Most mud eruptions from mud volcanoes are short-lived, likely lasting only hours to a few days [*Kopf*, 2002, 2003; *Mazzini et al.*, 2007; *Manga et al.*, 2009]. The eruption from Lusi mud volcano, however, has been ongoing for ~ 10 years since 2006 [*Rudolph et al.*, 2015]. Based on previous assessments of the discharge briefly reviewed later, the eruption from Lusi Mud Volcano will last 20–50 years [*Istadi et al.*, 2009; *Rudolph et al.*, 2011, 2013].

The heat flow often helps assess the recent activity of submarine mud volcanoes, and various heat flow signatures have been found in many submarine mud volcanoes. If the high heat flow is observed on the summit of the mud volcano, this indicates either a continuous seepage of pore water and mud originated from deep depths or the cooling of a recent massive eruption transferring a large volume of high-temperature sediment to the seafloor. If the extremely low heat flow is measured, on the other hand, this may indicate that a local rapid downward of fluid is sometimes arisen from the opening of mud conduits following recent massive eruptions. However, as a submarine mud volcano has concave-downward structure against the surrounding seafloor, an observational heat flow at the mud volcano is subject to cooling by cold bottom water [e.g., *Blackwell et al.*, 1980]. Thus, the heat flow eliminated the topographical effect will be a useful tool to evaluate the mud volcano's activity.

Discharge rate

A discharge rate from each submarine mud volcano is also directly connected to long-term subseafloor material cycling. While Lusi mud volcano is an unusual mud volcano from several aspects, this onshore mud volcano has been well-investigated in this regard. Gravity and ground deformation data observed by the InSAR reveal that discharge rate from Lusi mud volcano was $\sim 10^5$ m^3/day during the early phase of mud eruptions [*Mazzini et al.*, 2007]. The rate is subsequently decreased to $\sim 10^4$ m^3/day [*Rudolph et al.*, 2013], which is equivalent to the order of magnitude of the rate approximated by diapiric ascent. *Rudolph et al.* [2013] expect that the discharge is expected to have the e-folding time of $\sim$ 2 years [*Rudolph et al.*, 2013; *Aoki and Sidiq*, 2014], and will decrease by an order of magnitude of $< 10^3$ m^3/day by 2017 [*Rudolph et al.*, 2013]. Observations in submarine mud volcanoes, on the other hand, are limited as mud eruptions found in general mud volcanoes are episodic and short-lived as presented above. A long-term observation in the Håkon Mosby Mud volcano, however, guided for the first time that sediment movement of $\sim$ 0.5–1 m/day around the active center [*Feseker et al.*, 2014]. The difference of the seafloor relief also helps estimate an average volume flux of $\sim 1.5 \times 10^4$ m^3/yr [*Feseker et al.*, 2014], while this flux value is close to or less than that estimated by a diapiric ascent assuming reasonable conduit width and dynamic viscosity. At the Atalante mud volcano in the seaward of the Barbados accretionry wedge, the fluid flux rate is estimated to be $> 1.5 \times 10^5$ m^3/yr [*Henry et al.*, 1996]. The associated topic is discussed in Chapter 6.

1.2.2 Geochemical and biogeochemical features

Many mud volcanoes have been observed to release gases and fluids during both eruptions and quiescence stages. Their sources are originated at various depths (Figure 1.5). As submarine mud volcanoes are often located within the gas hydrate stability zone (GHSZ) [e.g., *Kvenvolden*, 1988], hydrates might form a spacious reservoir of light hydrocarbons from the ascending fluids in shallow marine sediments [*Ginsburg et al.*, 1999; *Milkov*, 2000; *Bohrmann et al.*, 2003]. The predominant gas released from mud volcanoes is methane, in most of mud volcanoes constituting > 90 vol%, and the reminder includes CO_2, higher hydrocarbons [e.g., *Dimitrov*, 2002; *Etiope and Milkov*, 2004], and H_2S [e.g., *Stamatakis et al.*, 1987] or noble gases [e.g., *Chiodini et al.*, 1996]. In association with CH_4 and H_2S seepages, chemosynthetic communities such as bacterial mats and clams are clustered around submarine mud volcanoes [e.g., *Corselli and Basso*, 1996; *Olu et al.*, 1997; *Olu-Le Roy et al.*, 2004]. Estimates of these gas fluxes are thus also important for understanding of organism bases in submarine mud volcanoes. One of the major geological sources of methane to the atmosphere or the water column is mud volcanoes [*Dimitrov*, 2002; *Kopf*, 2002; *Etiope and Milkov*, 2004]. The two dominant processes that generate methane in nature are known:

the biogenic methane generated by methanogenic archaea and the thermogenic methane generated by breakdown (cracking) of larger organic molecules [*Wuebbles and Hayhoe*, 2002]. Microbial methane formation is thought to occur at shallower sediment depths corresponding to temperatures below 80°C or less [*Wilhelms et al.*, 2001; *Valentine*, 2011; *Stolper et al.*, 2014]. Thermogenic gas is believed to form at temperatures greater than $\sim$ 150°C [*Quigley and Mackenzie*, 1988; *Seewald et al.*, 1998; *Stolper et al.*, 2014], while some studies suggest that it can be formed above $\sim$ 60°C [*Quigley and Mackenzie*, 1988; *Seewald*, 2003]. A predominance of whether the methane origin is biogenic or thermogenic, which is thus used for evaluating source depths guided by the temperature, has been suggested to vary with submarine mud volcanoes from numerous studies. For example, the emitted gas from the Håkon Mosby Mud Volcano in the Barents Sea consists of $> 99\%$ methane with an isotope signature δ^{13}C-CH_4 of -60‰ [*Damm and Budéus*, 2003; *Milkov et al.*, 2004], suggesting a mixed biogenic and thermogenic origins from the Bernard diagram [*Whiticar*, 1990]. Hydrocarbon gases released from submarine mud volcanoes in the Nankai accretionary prism is composed predominantly of methane and is mostly of thermogenic origin (δ^{13}C-$CH_4 > -40$‰) [*Toki et al.*, 2013; *Pape et al.*, 2014].

Majority of the methane dissolving into the sediment porewater, depending on the release rate, could be retained at/near the seafloor by microbial anaerobic oxidation of methane (AOM) [*Treude et al.*, 2003; *Reeburgh*, 2007; *Knittel and Boetius*, 2009], mediated by a consortium of anaerobic methanotrophs (ANME) [*Hinrichs et al.*, 1999; *Orphan et al.*, 2001] and sulphate reducing bacteria (SRB) [*von Rad et al.*, 1996]. AOM regulates a long-term sink for methane-derived carbon, converting methane into biocarbonate and eventually precipitating as an authigenic carbonate [*Peckmann et al.*, 2001]. But, methane ascending through sediments as a free gas could skirt the benthic methane filter [*Knittel and Boetius*, 2009] and immediately reaches the atmosphere [*McGinnis et al.*, 2006], depending on the water depth though. The marine environment stores a vast reservoir of methane of $> 10^{19}$ g carbon [e.g., *Zhang et al.*, 2011]. However, as methane is rapidly dissolved and oxidized near the seabed [*Reeburgh et al.*, 1991; *Valentine et al.*, 2001; *Judd et al.*, 2002], methane released from the seafloor makes little contribution to methane budgets in atmosphere, $\sim$ 1–3% of the total of the annual total sources of atmospheric

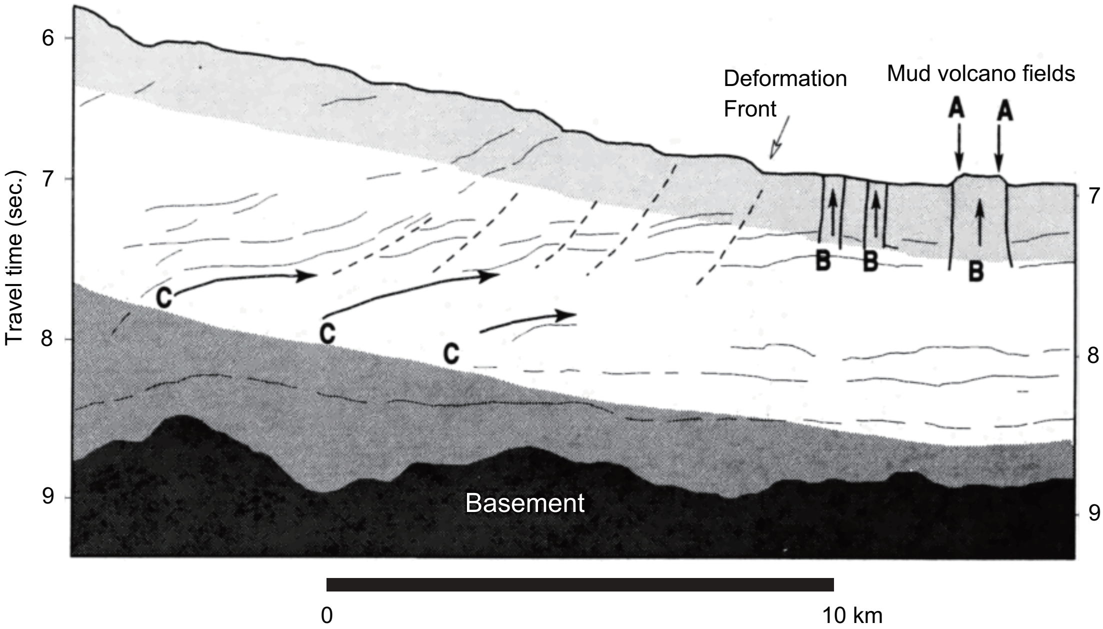

Figure 1.6: Schematic cross section of structure and stratigraphy near the Manon mud volcano field in Barbados. The lightest grey field represents the region of methane hydrate stability, and the darker grey field represents sediments with temperatures $> 100°C$. Location of possible fluid sources are indicated by "A", seawater; "B", gas hydrate dissociation; and "C", upper portion of the zone of mineral dehydration reactions. Modified from *Martin et al.* [1996].

methane [*Lelieveld et al.*, 1998; *Houweling et al.*, 2000; *Wuebbles and Hayhoe*, 2002]. The total methane oxidation in ocean water columns and shallow sediments is estimated to be between 75–304 Tg/yr [*Reeburgh*, 2007]. Worldwide, submarine mud volcanoes are thought to store $\sim 10^{10}$–10^{12} m^3 of methane [*Milkov*, 2000], whereas this is far less than the estimated methane-carbon worldwide in gas hydrates [*Kvenvolden et al.*, 2001]. The total methane released from submarine mud volcanoes into the seawater column is reported to be 27 Tg/yr [*Milkov et al.*, 2003], although this value is highly uncertain because of the unknown total number of mud volcanoes and temporal variability in methane emissions. Therefore, the assessment of total methane flux from submarine mud volcanoes holds promise not only in carbon cycle but also in oceanic pH or climate change, because the AOM converts methane with oxygen into CO_2 whose molecule can impact the pH. The associated topic is presented in Chapter 4.

Previous quantitative estimates on fluid fluxes from submarine mud volcanoes have shown high-rate expulsion, suggesting an important influence on subseafloor geochemical cycle and fluid budgets. Fluids released from submarine mud volcanoes often fall in the range of temperatures, ~ 60–160°C (Table 1.1), where the smectite-illite clay mineral transformation reaction takes place [*Colten-Bradley*, 1987; *Kastner et al.*, 1991; *Brown et al.*, 2001]. One of the useful tracer for fluids mixed with various sources is a chloride ion (Cl^-), because Cl^- is believed to be nonreactive in most diagenetic reactions [e.g., *Gieskes et al.*, 1989]. Fluids from submarine mud volcanoes generally have significantly lower Cl^- concentrations than that of seawater [*Martin et al.*, 1996; *Hensen et al.*, 2007]. The use of Cl^- is often coupled with a oxygen isotope ratio $\delta^{18}O$, because atmospheric water is isotopically lighter than seawater [*Craig*, 1961] and thus the admixture with marine pore fluids makes lower both Cl^- concentrations and $\delta^{18}O$ values. *Martin et al.* [1996] first envisioned using the Cl^- property that fluid sources from submarine mud volcanoes in the Manon mud field in Barbados include: water and methane released during the gas hydrate dissociation, water released during the transformation of smectite to illite, and seawater either diffused or convected into the mud volcanoes (Figure 1.6). In the Barbados accretionary prism, negative chloride isotope ratio $\delta^{37}Cl$ is found in pore fluids from submarine mud volcanoes [*Ransom et al.*, 1995]. The interpretation of this result is still debated, but ion filtering due to sediment compaction is more likely process to explain the observed negative $\delta^{37}Cl$ values (Figure 1.7) [*Godon et al.*, 2004].

Lithium also plays as a useful chemical indicator to draw the origins of fluids and fluid fluxes from submarine mud volcanoes, because lithium is unaffected by seawater owing to its greater content in submarine mud volcanoes than the seawater content [e.g., *Misra and Froelich*, 2012]. The lithium cycle is thought to be important for the carbon cycle including weathering and water-rock interactions [e.g., *Vigier and Goddéris*, 2015]. The lithium isotope ratio ($^7Li/^6Li$) provides geothermal information, because it varies with the reaction temperature [*Wunder et al.*, 2006; *Marschall et al.*, 2007] and is not affected by biologically mediated reactions [*Millot et al.*, 2011]. Pore fluids from mud volcanoes in the Gulf of Cádiz are found to be rooted at temperatures greater than 200°C using the $^7Li/^6Li$ ratios showing light values [*Scholz et al.*, 2009]. The ratio from the Kumano mud volcano No. 5 in the Nankai margin shows among the lightest value of submarine mud

Table 1.1: Characteristics of submarine mud volcano fluids in various areas, and temperatures and depths of the source estimated from the fluid results. E. Med stands for Eastern Mediterranean Sea. Modified from *Ijiri* [2009].

Region	Setting	Source Temp. (°C)	Source Depth (km)	Fluids source	Methane source
Barbados [a]	accretionary margin	75–116	2–4.5	dehydration hydrate dissoc.	biogenic + thermogenic
E. Med [b]	accretionary margin	55–165	3.5–6.8	dehydration	biogenic + thermogenic
Gulf of Cádiz [c]	accretionary margin	60–150 > 150?	~ 5	dehydration + hydrothermal?	biogenic + thermogenic
Costa Rica [d]	erosional margin	85–130	12	dehydration	thermogenic
Black Sea [e]	basin	95–103	3	dehydration	biogenic + thermogenic
Barents Sea [f]	continental margin	90	2.5–3	dehydration	biogenic + thermogenic

[a] *Martin et al.* [1996]; *Godon et al.* [2004].
[b] *Dählmann and de Lange* [2003]; *Haese et al.* [2006].
[c] *Hensen et al.* [2007]. [d] *Hensen et al.* [2004]. [e] *Aloisi et al.* [2004].
[f] *Ginsburg et al.* [1999]; *Lein et al.* [1999]; *Damm and Budéus* [2003].

volcanoes, suggesting the reservoir temperature of < 310°C [*Nishio et al.*, 2015]. Atalante and Cyclops mud volcanoes in Barbados accretionary complex alone provide 1.7×10^4 mol/yr of Li^+ to the oceans [*Martin et al.*, 1996]. Dvurechenskii mud volcano in the Black Sea shows a higher flux around 1.4×10^5 mol/yr [*Aloisi et al.*, 2004]. While these fluxes calculate about 10^{-5}–10^{-6} of the total fluvial Li budget or total inputs to ocean [*Stoffyn-Egli and MacKenzie*, 1984; *Zhang et al.*, 1998; *Misra and Froelich*, 2012], the cumulative flux is likely important if other mud volcanoes have similar efflux.

Boron concentrations also document the temperature of the reaction since the boron in fluids is controlled by sediment-rock-water interactions [*You and Gieskes*, 2001]. Several studies into pore fluids from mud volcanoes have reported high boron concentrations [*Aloisi et al.*, 2004; *Hensen et al.*, 2007; *Toki et al.*, 2014], and the high concentration in fluids is likely originated from desorption of organic matter or smectite-illite alteration at temperatures of 50–160°C [*You et al.*, 1993, 1996]. The total boron fluxes from submarine mud volcanoes may calculate around 0.1–1% [*Aloisi et al.*, 2004] of the total inputs to ocean [*Lemarchand et al.*, 2002]. These results show that mud volcanism plays a profound

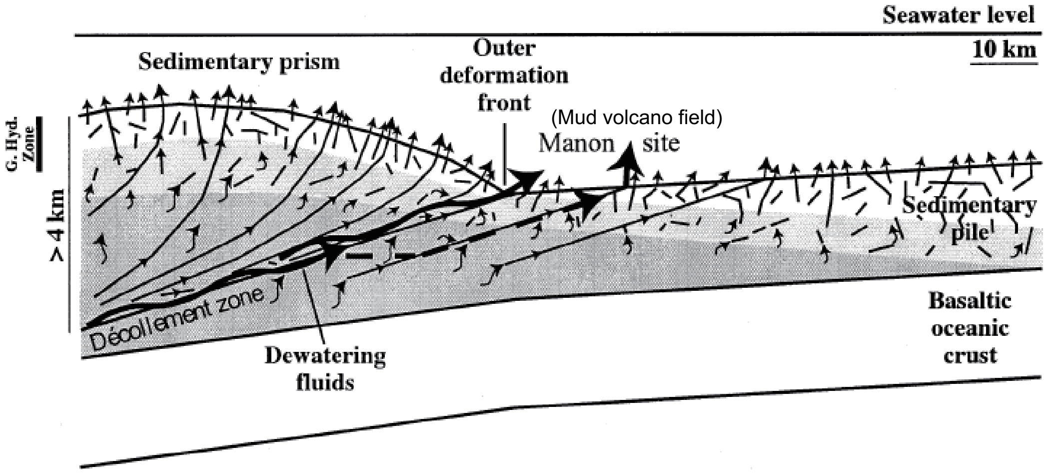

Figure 1.7: A schematic presentation of the model for ion filtration in the prism and sedimentary pile. Ion filtration is believed to be through fractures in the lower porosity light grey area. The low-Cl, high-δ^{37}Cl expelled fluids follow the dense network of fractures. The residual high-Cl, low-δ^{37}Cl fluid remains in the sediment pores. In the deepest part of the sedimentary pile or prism, porosity is reduced to a minimum and expelled fluids have to follow the main fractures (i.e., the décollement zone) to reach the surface. Low-Cl fluids coming from general dewatering of the slab and possibly its dehydration can also flush out these residual pore fluids. Modified from *Godon et al.* [2004].

role in the global boron cycle associated with fluid expulsion [*Kopf and Deyhle*, 2002]. The total iodine fluxes would be also 0.1–1% [*Aloisi et al.*, 2004] of the total inputs to ocean [*Muramatsu et al.*, 2001], although the estimates are limited. A noble gas such as a helium isotope ratio (^{3}He/^{4}He) also provides useful information on the origin of helium regarding primordial or radiogenic [e.g., *Aldrich and Nier*, 1946]. Thus, a higher ^{3}He/^{4}He ratio in a fluid suggests that the fluid is enriched in mantle helium. Application of the ^{3}He/^{4}He ratio to mud volcanism is limited, due to its uncertainty in precise determination of fluid paths, but *Craig et al.* [1978] first envisioned fluids from mud volcanoes have high ratios. In the neighboring mud volcanoes within a given mud field, the two mud volcanoes have different signatures of the ratios (one is typical of radiogenic helium and the other shows mixture of mantle-derived helium) while the values are constant over time [*Kikvadze et al.*, 2010], suggesting that a fluid path in each mud volcano has various styles.

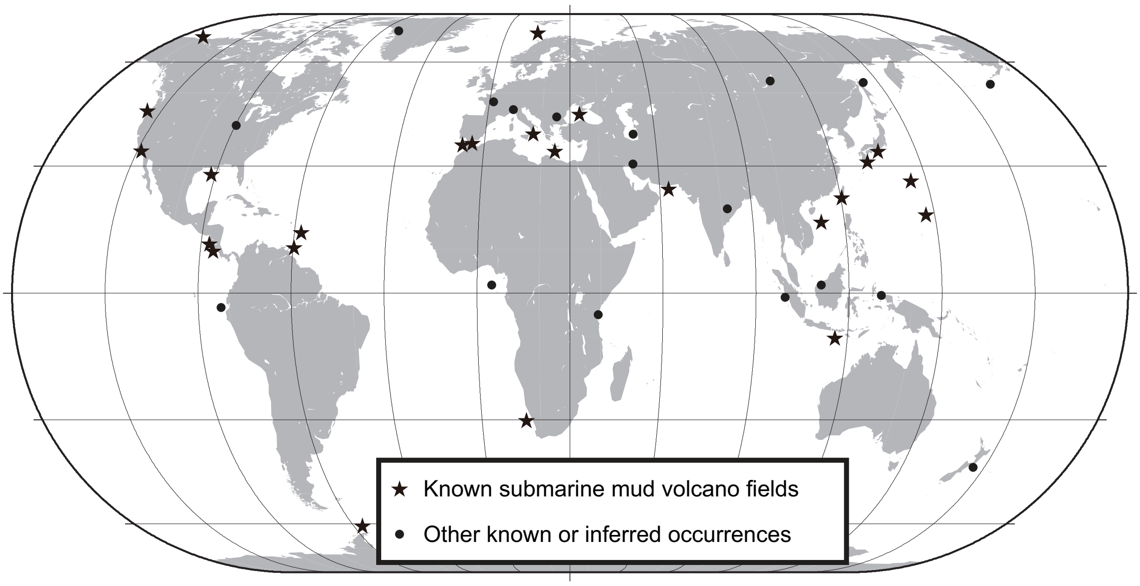

Figure 1.8: Occurrence of submarine mud volcanoes on Earth. Stars show known mud fields of submarine mud volcanoes, while circles represent other inferred occurrence of submarine mud volcanism and known mud fields of onshore mud volcanoes. Modified from *Kioka and Ashi* [2015].

1.2.3 Distribution and morphology

Submarine mud volcanoes have been found in various tectonic settings (Figure 1.8). So far, however, quantitative and statistical studies of mud volcano morphology have been mostly focused on to onshore mud volcanoes on Earth [e.g., *Bonini*, 2008, 2012] or mud volcano-like structures imaged on Mars [e.g., *Tanaka*, 1997; *Oehler and Allen*, 2010; *Pondrelli et al.*, 2011], because more high-quality topographic measurements are easily available for these mud volcanoes than those discovered on Earth's seafloors. Recently, however, studies into morphology of submarine mud volcanoes have been greatly benefiting owing to the satisfactory increase in the number of submarine mud volcanoes that have been surveyed by bathymetric and seismic instruments providing sufficient resolutions. Previous studies, for example, propose that the characteristics of submarine mud volcano's shapes may differ dependent on regions and tectonic backgrounds [e.g., *Kopf*, 2002; *Rabaute and Chamot-Rooke*, 2007] or are related to viscosity or porosity of body depositions and the size of a conduit feeder [e.g., *Lance et al.*, 1998; *Kopf*, 2002]. Some studies remark that mud volcanoes are developed with a conical or a flat top edifice when their water content

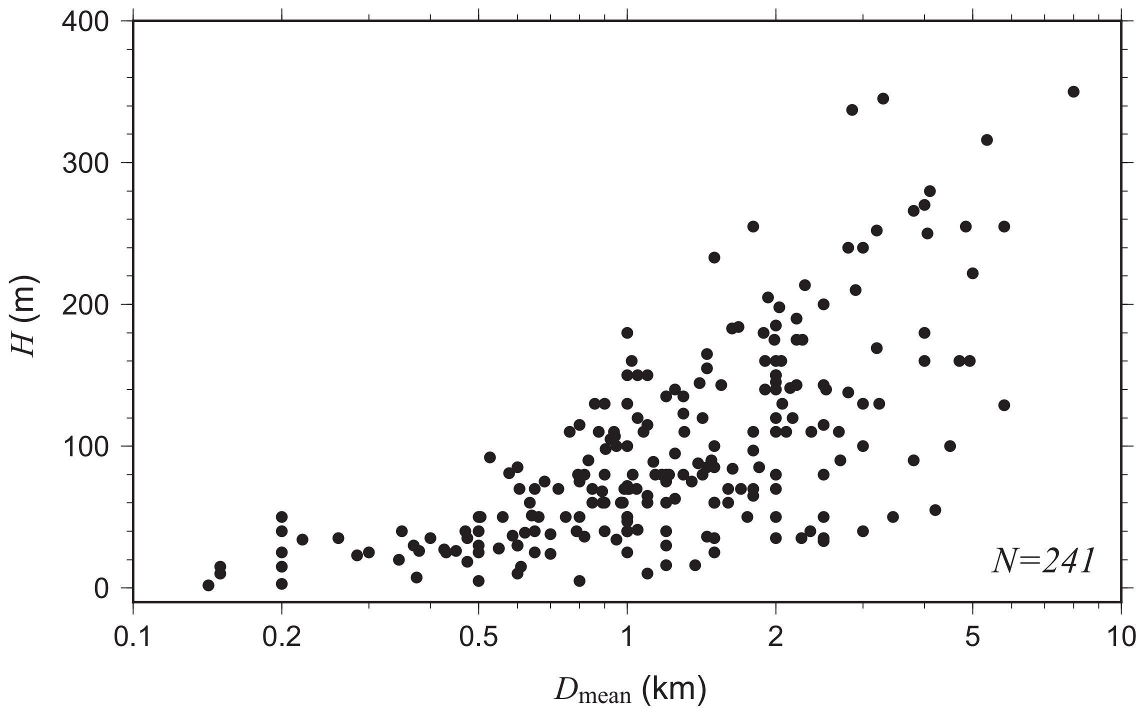

Figure 1.9: A scatter plot of mean diameter D_{mean} (km) versus height H (m) of known submarine mud volcanoes, where the diameter D_{mean} denotes the mean diameter $D_{\mathrm{mean}} = (D_{\mathrm{min}} + D_{\mathrm{max}})/2$, if both the maximum diameter and minimum diameter are available for the given mud volcano, and otherwise denotes a representative diameter of one available in the literature. Large serpentine mud volcanoes in the Izu-Bonin (Ogasawara)-Mariana (IBM) Arc are excluded here. Data from Table A.1 [*Kioka and Ashi*, 2015].

is high [*Barber et al.*, 1986; *Lance et al.*, 1998; *Feseker et al.*, 2009]. Pockmarks, similar expressions of sediment expulsion or mobilization to mud volcanoes, are generally between 50 and 100 m in diameters with depths of 1–3 m, and have higher densities of $\sim 10^1$ km^{-2} than those of submarine mud volcanoes [*Judd and Hovland*, 2007]. Hereafter I present morphological compilation of submarine mud volcanoes, addressing size and geometry of submarine mud volcanoes, and location characteristics of mud fields developing submarine mud volcanoes. See Table A.1 used to produce the following topics.

Size and geometry

In my compilation from Table A.1, the height H of the submarine mud volcano increases when the diameter D_{mean} (Figure 1.9). Note that the diameter D_{mean} here denotes the mean diameter $D_{\mathrm{mean}} = (D_{\mathrm{min}} + D_{\mathrm{max}})/2$, if both the maximum diameter D_{max} and minimum diameter D_{min} are available for the given mud volcano, and otherwise denotes a representative diameter of one available in Table A.1. While the increase trend is found, the height/diameter ratio H/D_{mean} shows a variation as the height H and the mean diameter D_{mean} increase. Interestingly, however, the mean ratio H/D_{mean} is close to that of seamounts detected by gravity data [*Kim and Wessel*, 2011]. Serpentine mud volcanoes developed in the Izu-Bonin (Ogasawara)-Mariana (IBM) Arc are often larger than other submarine mud volcanoes [e.g., *Fryer et al.*, 1999]. All but a few of serpentine mud volcanoes range in the height H up to $\sim$ 350 m and the diameter D_{mean} up to $\sim$ 8 km in my compilation, while a larger submarine mud volcano is likely present in the Eastern Mediterranean [*Kopf et al.*, 2001]. The associated topic is presented in Chapter 2.

Figure 1.10a displays a scatter plot of height H (m) versus plan-view aspect ratio $D_{\mathrm{min}}/D_{\mathrm{max}}$ of submarine mud volcanoes, where D_{max} and D_{min} (km) are maximum and minimum diameter of a given submarine mud volcano. A smaller aspect ratio $D_{\mathrm{min}}/D_{\mathrm{max}}$ indicates an elongated plan view shape of the mud volcano. The aspect ratio $D_{\mathrm{min}}/D_{\mathrm{max}}$ seems to decrease when the height H increases between 0 and 250 m, while the trend is not found for the height above 250 m. Assuming that the topographical effect on the seafloor requires unconcern, this suggests that a mud conduit where ejecta ascent from deep depths to the seafloor shifts as the mud volcano grows, or reflects the stress orientation similar to magmatic volcanoes [e.g., *Nakamura*, 1977]. Figure 1.10b displays a scatter plot of mean diameter D_{mean} (km) versus plan-view aspect ratio $D_{\mathrm{min}}/D_{\mathrm{max}}$ of submarine mud volcanoes, where $D_{\mathrm{mean}} = (D_{\mathrm{min}} + D_{\mathrm{max}})/2$. The mean diameter D_{mean} is sketched to be scatter against the aspect ratio $D_{\mathrm{min}}/D_{\mathrm{max}}$.

Eastern Mediterranean

The Mediterranean Ridge accretionary complex, a large and arcuate sedimentary wedge more than 1500 km long and 300 km wide [e.g., *Emery et al.*, 1966; *Le Pichon et al.*, 1982; *Fusi and Kenyon*, 1996; *Kopf et al.*, 2003], is expanded in the eastern Mediterranean. The development of the accretionary wedge results from $\sim$ 4 cm/yr subduction of the Nubian plate beneath the Aegean Sea along the Hellenic trenches south of mainland Greece and the island of Crete [e.g., *Le Pichon et al.*, 1995; *McClusky et al.*, 2000; *Kreemer and Chamot-*

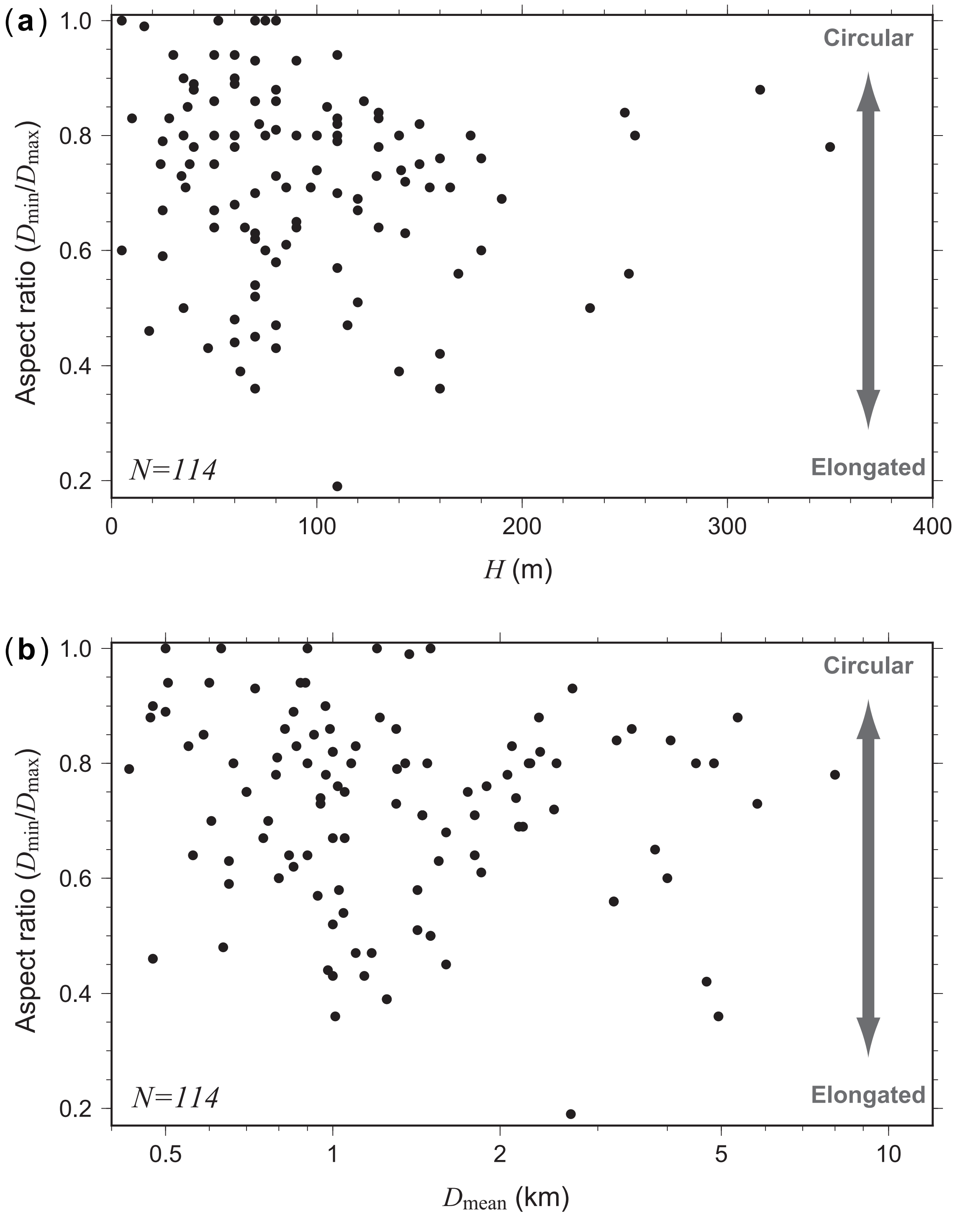

Figure 1.10: (a) A scatter plot of height H (m) versus aspect ratio $D_{\mathrm{min}}/D_{\mathrm{max}}$ of known submarine mud volcanoes, where D_{max} and D_{min} (km) are maximum and minimum diameter of the mud volcano. (b) A scatter plot of mean diameter D_{mean} (km) versus aspect ratio $D_{\mathrm{min}}/D_{\mathrm{max}}$ of known submarine mud volcanoes, where $D_{\mathrm{mean}} = (D_{\mathrm{min}} + D_{\mathrm{max}})/2$. Large serpentine mud volcanoes in the IBM Arc are excluded here. Data from Table A.1 [*Kioka and Ashi*, 2015].

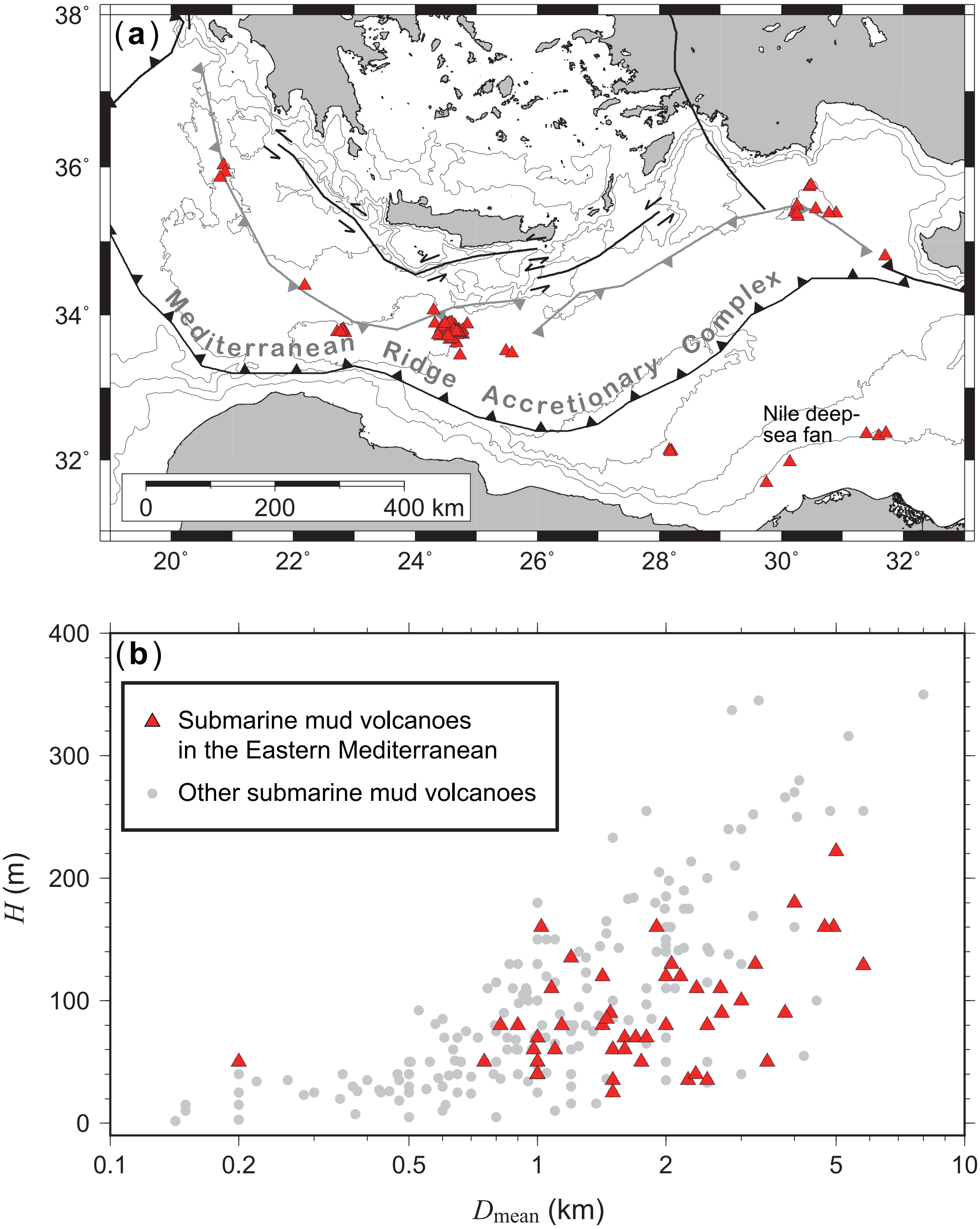

Figure 1.11: (a) Distribution of submarine mud volcanoes in the Eastern Mediterranean. Mud fields are found in Figure 3.1. (b) A scatter plot of mean diameter D_{mean} (km) versus height H (m) of submarine mud volcanoes. Red triangles are submarine mud volcanoes in the Eastern Mediterranean, while gray circles are other known submarine mud volcanoes except for large serpentine mud volcanoes in the IBM system. Data of submarine mud volcanoes from Table A.1 [*Kioka and Ashi*, 2015]. ETOPO1 grid data [*Amante and Eakins*, 2009] are used to illustrate the bathymetry map.

Rooke, 2004]. Submarine mud volcanism in the accretionary wedge is first ascribed by *Ryan et al.* [1982]. This region holds the world's greatest abundance of mud volcanoes [*Kopf*, 2002]. In the Eastern Mediterranean, most of submarine mud volcanoes are found in the inner accretionary wedge forming in the belt-like manner [*Limonov et al.*, 1996], while some submarine mud volcanoes are developed in the Nile deep-sea fan (Figure 1.11a). Submarine mud volcanoes in this region are densely distributed within each mud field (see Figure 3.1 for mud fields). Submarine mud volcanoes in the Mediterranean Ridge Accretionary complex are believed to punctuate where the Messinian evaporite layer is absent or thin [*Camerlenghi et al.*, 1995], because the role of evaporitic sequences prevent extrusion of overpressured sediments at depth to the seafloor. See Chapter 3 for details.

Submarine mud volcanoes with moderate to large diameters D_{mean} are found in the Eastern Mediterranean (1.11b). Despite the range of diameter D_{mean}, submarine mud volcanoes in the Eastern Mediterranean have relatively lower heights H. This suggests that submarine mud volcanoes found here yield lower surface slopes of the mud volcano's body than that in other regions. The associated topic is discussed in Chapter 2.

Gulf of Cádiz

The Gulf of Cádiz is situated west of the Gibraltar Straits offshore SW Iberia and Morocco, accommodating a WNW-ESE convergence between Eurasia and Africa plates at at rate of ~ 5 mm/yr [*Fernandes et al.*, 2003]. A major thrust, the Gulf of Cádiz Accretionary wedge, is bounded in this region, and the wedge has sediment in thickness of > 10 km below the seafloor [e.g., *Gutscher et al.*, 2009b]. About 60 submarine mud volcanoes have been confirmed in the Gulf of Cádiz. Submarine mud volcanoes in this region are widely distributed at water depths ranging ~ 400–4000 m (Figure 1.12a). All known submarine mud volcanoes in the Gulf of Cádiz are punctuated within the accretionary wedge. Mud volcanoes and mud diapirs are clearly seen to be controlled by thrust faults, extensional faults, and strike-slip faults in the Gulf of Cádiz. Most of submarine mud volcanoes show symptomatically aligned trends in NE-SW and NW-SE at depths of 400–2000 m in the eastern accretionary wedge, partly associated with the wrench system [*Pinheiro et al.*, 2003; *Medialdea et al.*, 2009]. Submarine mud volcanoes situated at depths of > 2000 m

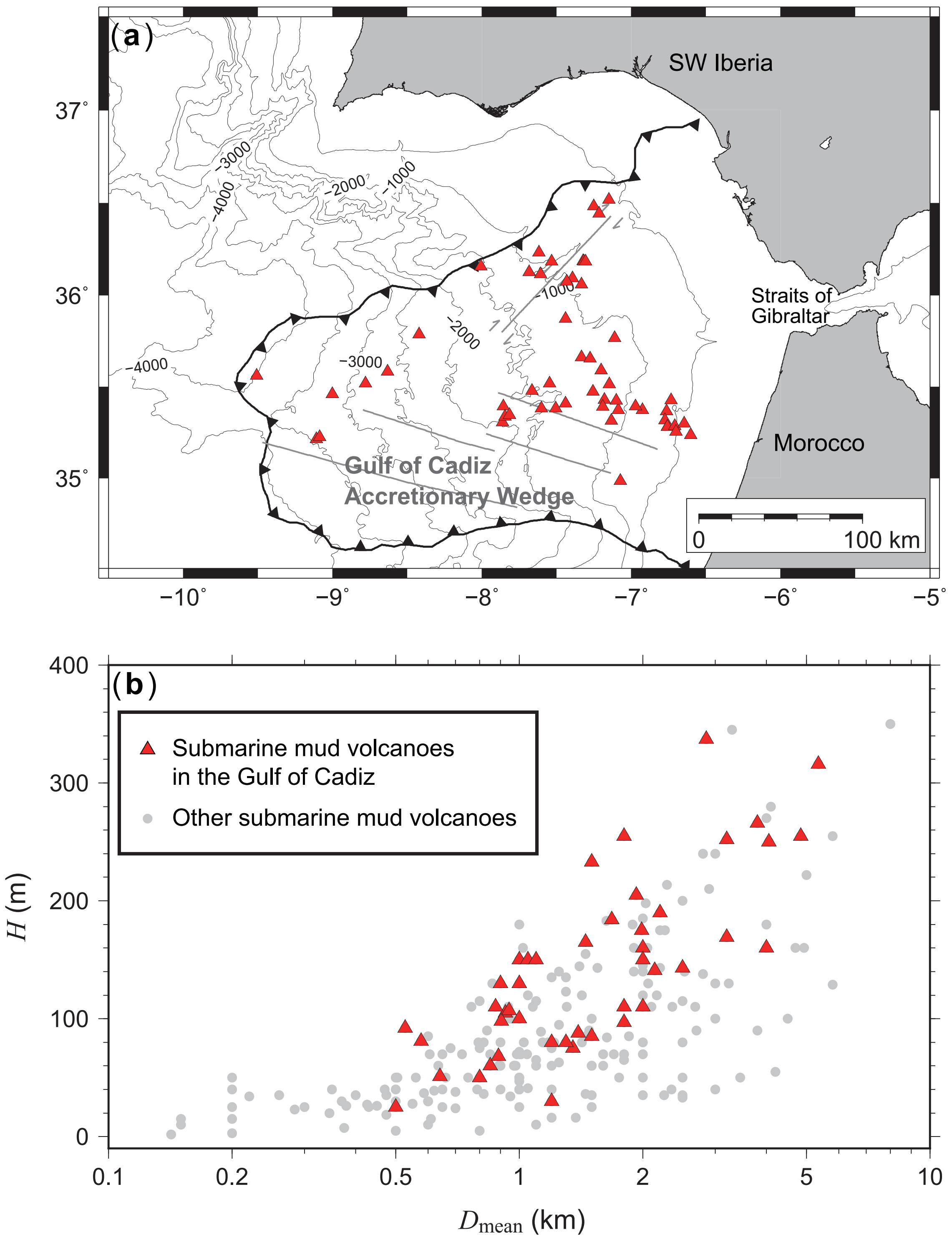

Figure 1.12: (a) Distribution of submarine mud volcanoes in the Gulf of Cádiz. (b) A scatter plot of mean diameter D_{mean} (km) versus height H (m) of submarine mud volcanoes. Red triangles are submarine mud volcanoes in the Gulf of Cádiz, while gray circles are other known submarine mud volcanoes except for large serpentine mud volcanoes in the IBM system. A major thrust and wrench system follow *Zitellini et al.* [2009]. Data of submarine mud volcanoes from Table A.1 [*Kioka and Ashi*, 2015]. Bathymetric data from the SWIM compilation [*Zitellini et al.*, 2009].

are scattered in the western accretionary wedge.

Submarine mud volcanoes with moderate to large diameters D_{mean} are found in the Gulf of Cádiz (Figure 1.12b). Moreover, submarine mud volcanoes in the Gulf of Cádiz have relatively higher heights H, suggesting submarine mud volcanoes found here yield higher surface slopes of the mud volcano's body than that in other regions. The associated topic is discussed in Chapter 2.

Western Mediterranean and Central Mediterranean

Submarine mud volcanoes in the Western Mediterranean are developed in the Western Alborán Basin of Alborán Sea [*Blinova et al.*, 2011; *Somoza et al.*, 2012; *Gennari et al.*, 2013] (Figure 1.13a). The basin has been formed by crustal extension under a NW-SE to WNW-ESE contemporary convergence between the African and Eurasian plates [*Dewey et al.*, 1989] at ~ 5 mm/yr [*Fernández-Ibáñez et al.*, 2007]. Submarine mud volcanoes in this region are densely distributed.

Submarine mud volcanoes in the Central Mediterranean are found in the Ionian Sea and Tyrrhenian Sea (Figure 1.13b). The Ionian Sea is situated in the Africa/Eurasia plate boundary at a very slow convergence rate < 5 mm/yr [*Calais et al.*, 2003] with the Apennine-Maghrebibe connecting system [*Patacca et al.*, 1993], where the Calabrian accretionary prism is well developed. In the Ionian Sea, submarine mud volcanoes are widely found in the inner pre-Messinian clastic accretionary wedge and the inner plateau. No submarine mud volcanoes have been found in the outer Post-Messinian salt bearing accretionary wedge. This suggests that the Messinian evaporitic sequence plays a profound role in preventing extrusion of overpressured sediments at deep depths to the seafloor, as found in the Eastern Mediterranean [*Camerlenghi et al.*, 1995].

Submarine mud volcanoes found in the Western and Central Mediterranean have a wide range of diameters D_{mean} (Figure 1.13c). One of the largest submarine mud volcanoes, Pythagoras Mud Volcano, ~ 8 km in diameter and ~ 350 m in height, is developed in the inner pre-Messinian Calabrian accretionary prism in the Central Mediterranean [*Praeg et al.*, 2009].

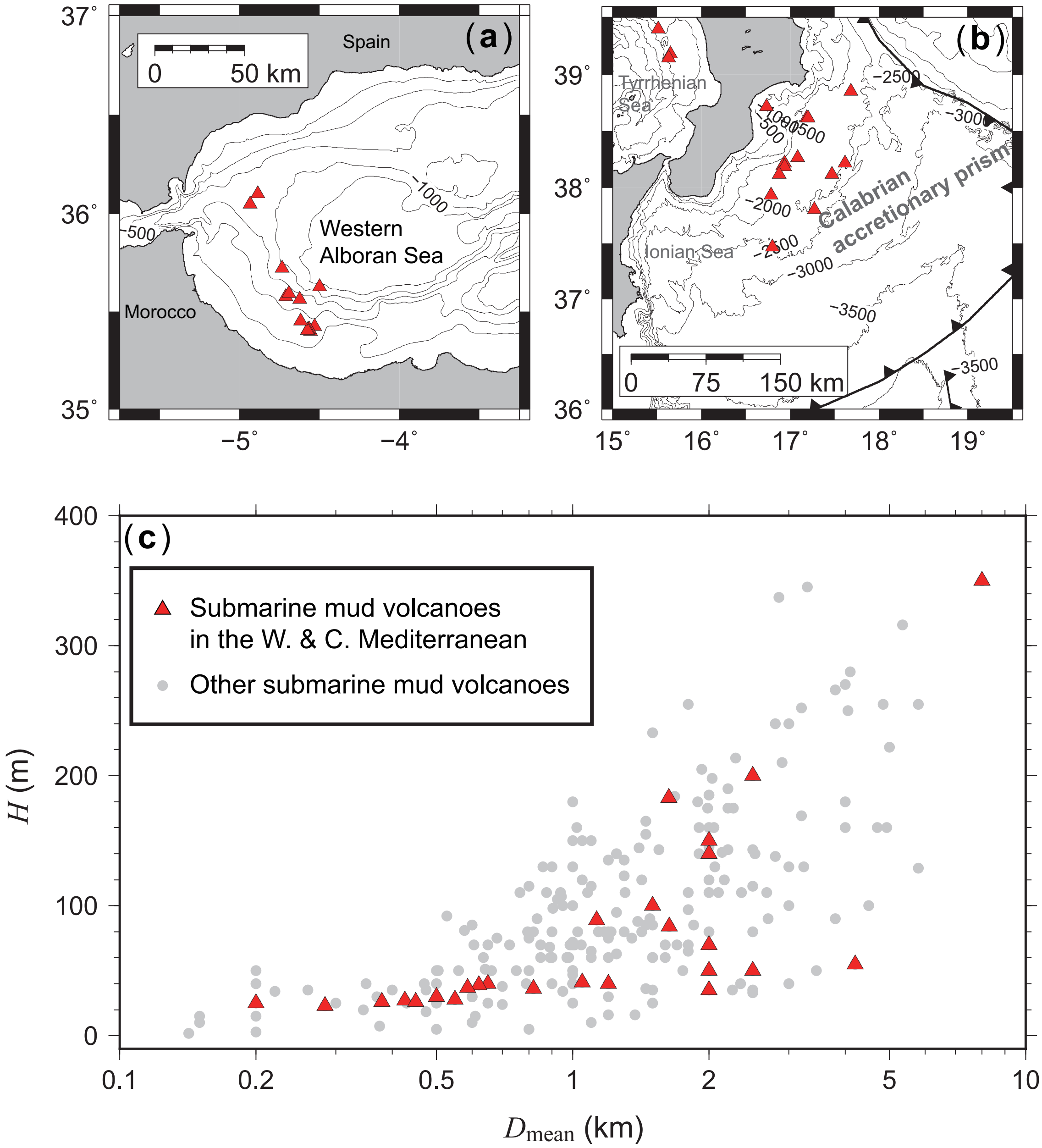

Figure 1.13: (a) Distribution of submarine mud volcanoes in the Western Mediterranean and (b) in the Central Mediterranean. (c) A scatter plot of mean diameter D_{mean} (km) versus height H (m) of submarine mud volcanoes. Red triangles are submarine mud volcanoes in the Western Mediterranean and Central Mediterranean, while gray circles are other known submarine mud volcanoes except for large serpentine mud volcanoes in the IBM system. Data from Table A.1 [*Kioka and Ashi*, 2015]. Bathymetric data from the GEBCO_2014 Grid.

Nankai, SW Japan

Most of submarine mud volcanoes developed in the Nankai accretionary prism are found in the Kumano forearc basin [*Kuramoto et al.*, 2001; *Morita et al.*, 2004; *Pape et al.*, 2014] (Figure 1.14). The Kumano basin is resulted from being offscraped from the incoming trench and the underlying Shikoku Basin [e.g., *Morita et al.*, 2004]. A submarine mud volcano is also locally found on the landward part of the trough floor off Muroto, Shikoku Island [*Ashi and Taira*, 1992]. Twin mud volcanoes (Kumano Knoll #5 and #6 mud volcanoes) are found in the Kumano basin. They presumably share their mud conduits or are resulted from shift of a major conduit reflecting different formation time, although this issue is still debated. Submarine mud volcanoes developed in the Kumano basin have moderate diameters (Figure 1.14b)

SW Taiwan

The area offshore southwestern Taiwan is located at the junction between Chinese continental margin and the southern Taiwan accretionary wedge [*Liu et al.*, 1997]. Most submarine mud volcanoes are found in the upper slope of the accretionary wedge of southern Taiwan (Figure 1.15a). Several submarine mud volcanoes are developed at water depths above 500 m [*Chen et al.*, 2014].

Submarine mud volcanoes in the southwestern Taiwan have a wide range of both diameter D_{mean} and height H (Figure 1.15b). A smallest submarine mud volcano is confirmed in the lower slope of the accretionary wedge [*Chiu et al.*, 2006]. Moreover, submarine mud volcanoes in the Gulf of Cádiz have relatively higher heights H with respect to diameters D_{mean}, suggesting submarine mud volcanoes found here yield higher surface slopes of the mud volcano's body than that in other regions. The associated topic is discussed in Chapter 2.

Costa Rica and Nicaragua

The Pacific erosive margin offshore Costa Rica and Nicaragua undergoes the subduction of the Cocos plate along the Middle America Trench [*Ranero and von Huene*, 2000] with a rapid rate [*DeMets et al.*, 1994]. Mud diapirs offshore Costa Rica have been known

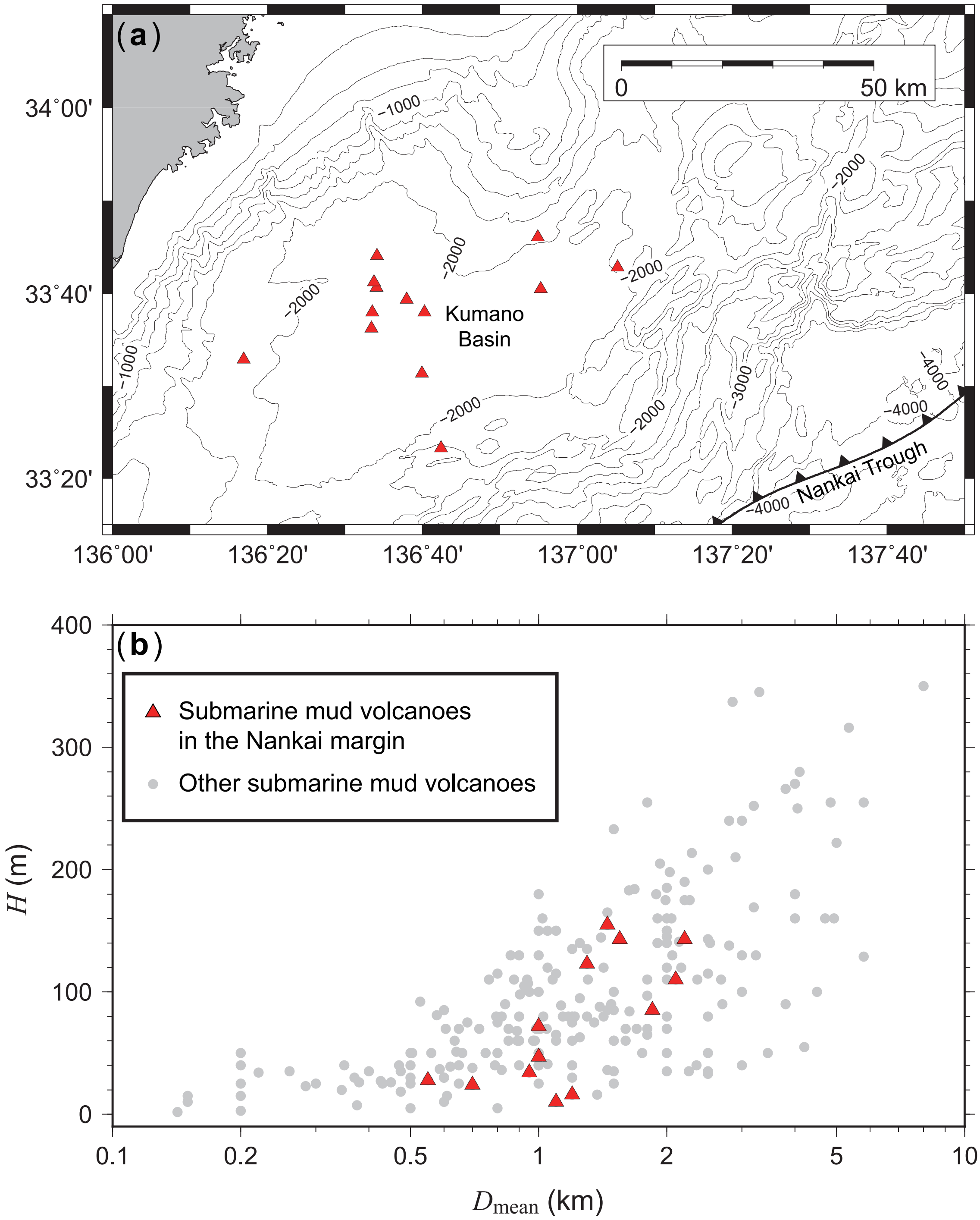

Figure 1.14: (a) Distribution of submarine mud volcanoes in Kumano basin of the Nankai margin. (b) A scatter plot of mean diameter D_{mean} (km) versus height H (m) of submarine mud volcanoes. Red triangles are submarine mud volcanoes in the Kumano basin of the Nankai, while gray circles are other known submarine mud volcanoes except for large serpentine mud volcanoes in the IBM system. Data from Table A.1 [*Kioka and Ashi*, 2015]. A high-resolution bathymetric map in this mud field is found in Figure 4.7a.

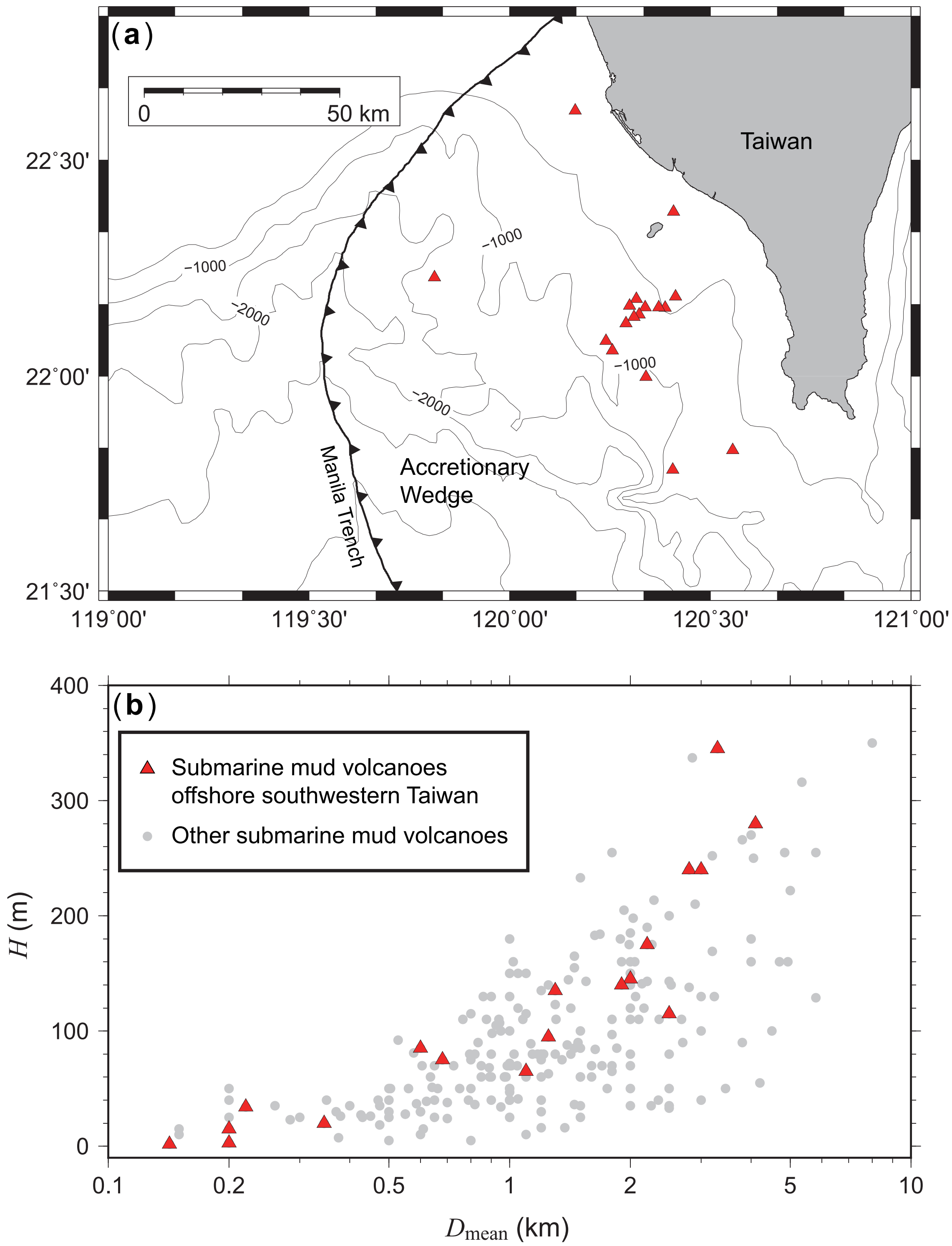

Figure 1.15: (a) Distribution of submarine mud volcanoes in the SW Taiwan. (b) A scatter plot of mean diameter D_{mean} (km) versus height H (m) of submarine mud volcanoes. Red triangles are submarine mud volcanoes in the SW Taiwan, while gray circles are other known submarine mud volcanoes except for large serpentine mud volcanoes in the IBM system. Data from Table A.1 [*Kioka and Ashi*, 2015]. Deformation front of the accretionary wedge is from *Liu et al.* [1997]. ETOPO1 grid data [*Amante and Eakins*, 2009] are used to illustrate the bathymetry map.

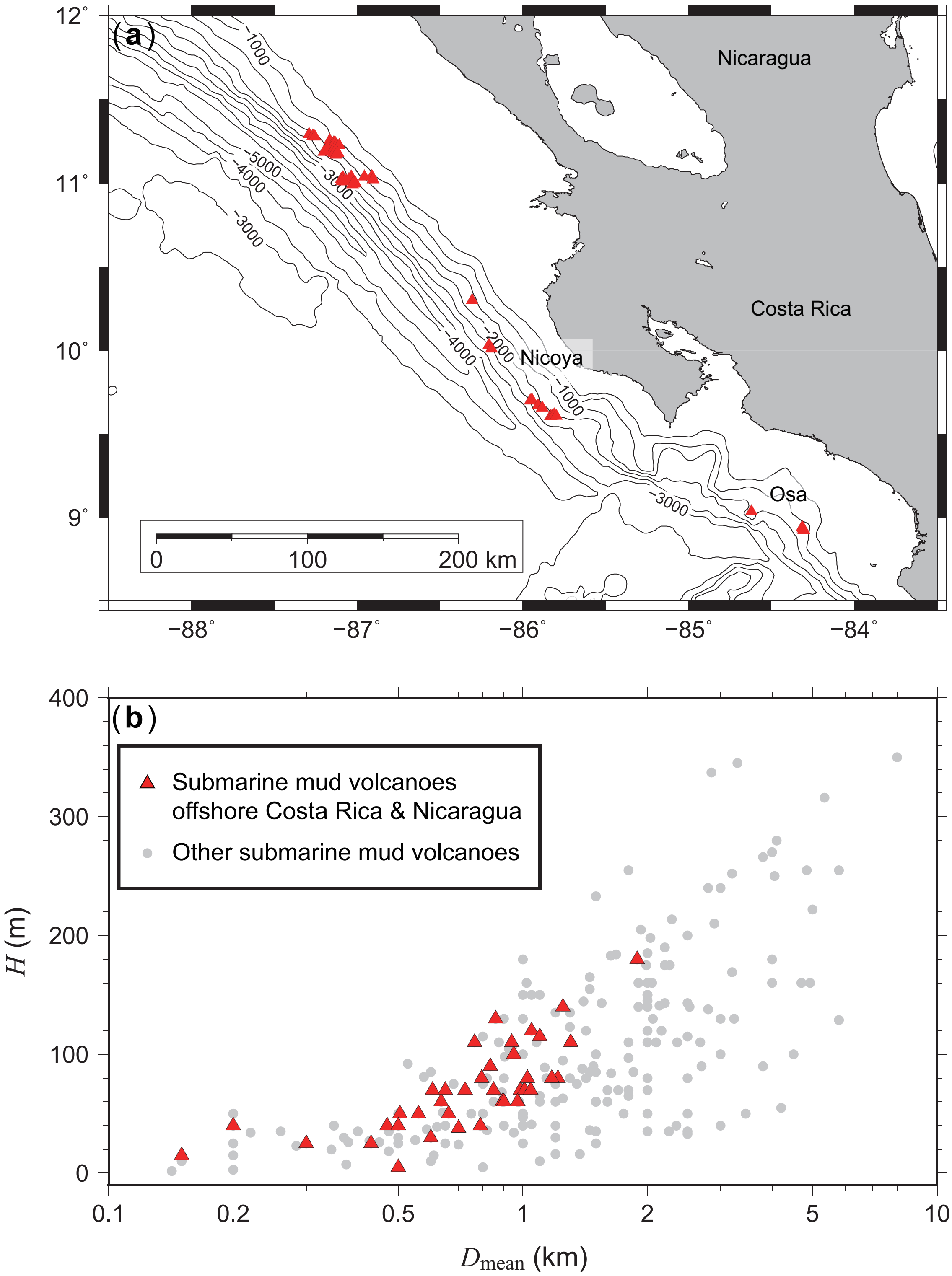

Figure 1.16: (a) Distribution of submarine mud volcanoes in Costa Rica and Nicaragua. (b) A scatter plot of mean diameter D_{mean} (km) versus height H (m) of submarine mud volcanoes. Red triangles are submarine mud volcanoes in Costa Rica and Nicaragua, while gray circles are other known submarine mud volcanoes except for large serpentine mud volcanoes in the IBM system. Data from Table A.1 [*Kioka and Ashi*, 2015]. ETOPO1 grid data [*Amante and Eakins*, 2009] are used to illustrate the bathymetry map.

since the late 1980s using 3D seismic reflection data [*Shipley et al.*, 1990]. Submarine mud volcanoes in this region are underlain on the deformed midslope (Figure 1.16a). Normal faulting across the midslope is likely associated with the mud volcanism here [*Mörz et al.*, 2005]. Some mud volcanoes are covered by continuous, massive and fractured carbonates [e.g., *Mörz et al.*, 2005; *Bürk*, 2007].

Submarine mud volcanoes offshore Costa Rica and Nicaragua have small to moderate diameters D_{mean} (Figure 1.16b). Submarine mud volcanoes here have relatively higher heights H with respect to diameters D_{mean}, suggesting submarine mud volcanoes found here yield higher surface slopes of the mud volcano's body than that in other regions. The associated topic is discussed in Chapter 2.

Other notes

Absence of submarine mud volcanism in the subpolar subduction margins such as southern Alaska and southern Chile margins is recognized (Figure 1.8), while active submarine mud volcanoes are found in Beaufort Sea of the Canadian Arctic [*Paull et al.*, 2015], offshore central British Columbia [*Berkowitz*, 2015], the shallow shelf in the Okhotsk Sea [e.g., *Shakirov et al.*, 2004], and Shetland continental margin off the Antarctic Peninsula [*Tinivella et al.*, 2008]. The absence of submarine mud volcanism in the southern Alaska margin has been long mysterious [*Wallmann et al.*, 1997; *Kopf*, 2002]. I will examine this issue in the future study, though this topic is beyond the scope of this thesis.

1.2.4 Geohazards associated with mud volcanism

One example of a proposed earthquake-triggered eruption is an unprecedented eruption from Lusi (named after "Lumpur Sidoarjo") Mud Volcano, East Java, Indonesia. The large subsidence caused by the eruption damaged transportation and communication infrastructure [*Abidin et al.*, 2009]. The extruded mud covered more than an area of 7 km^2 [*Rudolph et al.*, 2013], displacing more than 60,000 people and causing economic losses more than $4 billion [*Richards*, 2011]. While the eruption was proposed to trigger by the neighboring M_w 6.3 earthquake, 2 days prior to the eruption, by many studies [e.g., *Mazzini et al.*, 2007; *Sawolo et al.*, 2009; *Lupi et al.*, 2013], it has also been proposed to

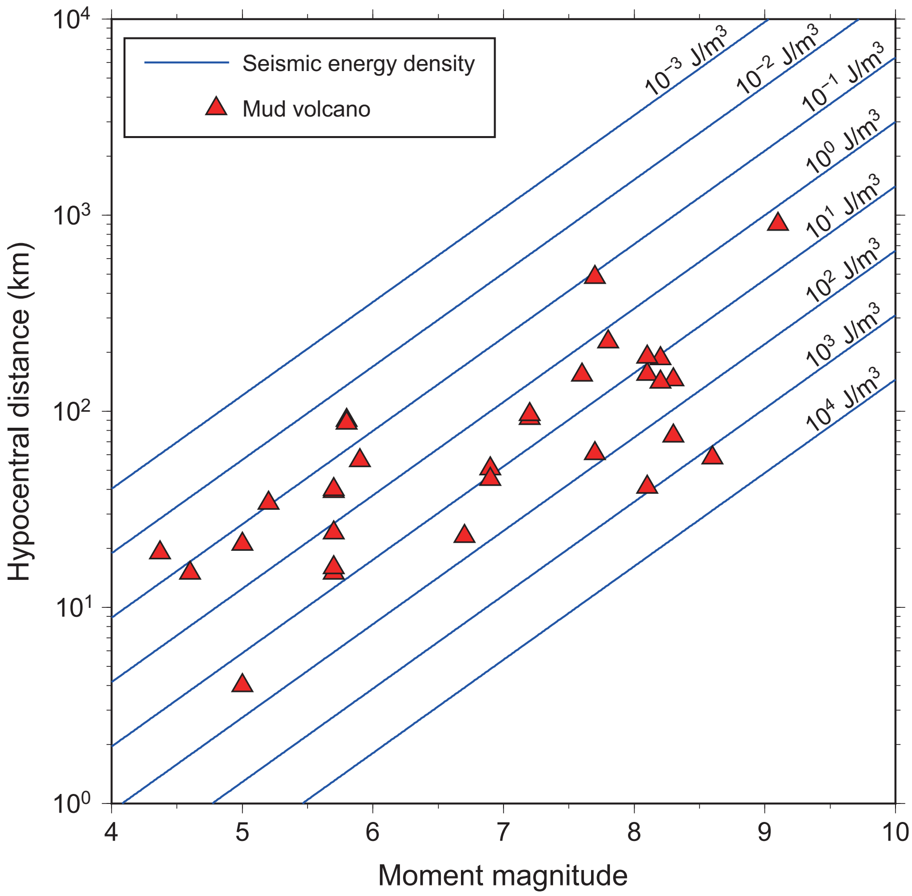

Figure 1.17: Occurrence of earthquake-triggered mud eruptions from onshore mud volcanoes (red triangle) as a function of moment magnitude and hypocentral distance of a given earthquake. The data are compiled from *Wang and Manga* [2010] and *Rudolph and Manga* [2012]. Labeled blue lines show the seismic energy density (e), which is the total kinetic energy per unit volume in a seismic wave train as recorded by a seismograph at a given location [*Wang*, 2007].

be initiated by drilling operations for gas exploration near the eruption site [e.g., *Manga*, 2007; *Davies et al.*, 2008; *Rudolph et al.*, 2015; *Tingay et al.*, 2015]. The issue reviewed here is important from a viewpoint of subsurface material cycling, because the cycling would be responsible for geohazards such as earthquakes and tsunamis associated with mud eruptions from mud volcanoes.

Numerous previous studies have documented a large variety of hydrologic changes following earthquakes, including changes in the eruption behavior of mud volcanoes and geysers, liquefaction of soils, the formation and disappearance of springs, and discharge in streams and groundwater [e.g., *Montgomery and Manga*, 2003; *Manga and Brodsky*, 2006; *Wang and Manga*, 2010; *Manga et al.*, 2012]. Mud eruptions from onshore mud volcanoes in response to earthquakes have been reported from long records of responses to earthquakes in Azerbaijan [*Mellors et al.*, 2007], Italy [*Bonini*, 2009], and Japan [*Chigira and Tanaka*, 1997]. A compilation of mud eruptions shows that the distance over which mud volcanoes respond, within a few days after earthquakes, for a given magnitude of earthquake [*Wang and Manga*, 2010; *Rudolph and Manga*, 2012] (Figure 1.17). The mechanisms by which earthquakes influence the mud eruptions remain controversial, although the primary driver of ejecta ascent requires overpressures. This is arisen from the large distances between a given earthquake and the locations where the responses occur, the response processes occurring at deep depths as reviewed in Subsection 1.2.1, the limited number of observations, and finding that mud volcanoes appear to respond to both static and dynamic stresses [*Manga and Bonini*, 2012; *Rudolph and Manga*, 2012]. The distribution of various hydrologic responses may be scaled by an empirical relation expressed by $\log r = A + BM$, where r is the distance from the earthquake source, beyond which the response is not expected, M the earthquake distance, and A and B the fitting constants [e.g., *Kuribayashi and Tatsuoka*, 1975; *Papadopoulos and Lefkopoulos*, 1993]. Combining this relationship with the classical relation between M and the total seismic energy [*Båth*, 1966], *Wang* [2007] obtains the following empirical relation:

$$\log r = 0.48M - 0.33 \log e - 1.4, \tag{1.1}$$

where r is distance in km, and e is seismic energy density (J/m^3) defined by kinetic energy in ground shaking [*Wang*, 2007]. This relationship is illustrated in a $\log r$ versus M diagram (Figure 1.17). Mud volcanoes are bounded by a constant seismic energy density of $e \sim 10^{-2}$–10^{-1} J/m^3 [*Wang and Manga*, 2010] for triggering the eruptions. The threshold has been used for examining that a drilling-trigger is more likely than an earthquake-trigger for mud eruptions from Lusi Mud Volcano, onshore Indonesia [*Rudolph et al.*, 2015], which is still debated. Moreover, the eastern Mediterranean is known for both submarine mud volcanism [*Kopf*, 2002] and seismically most active in Europe [*McKenzie*, 1972] (Figure 1.18). The area is one of the most suitable fields to examine the linkage

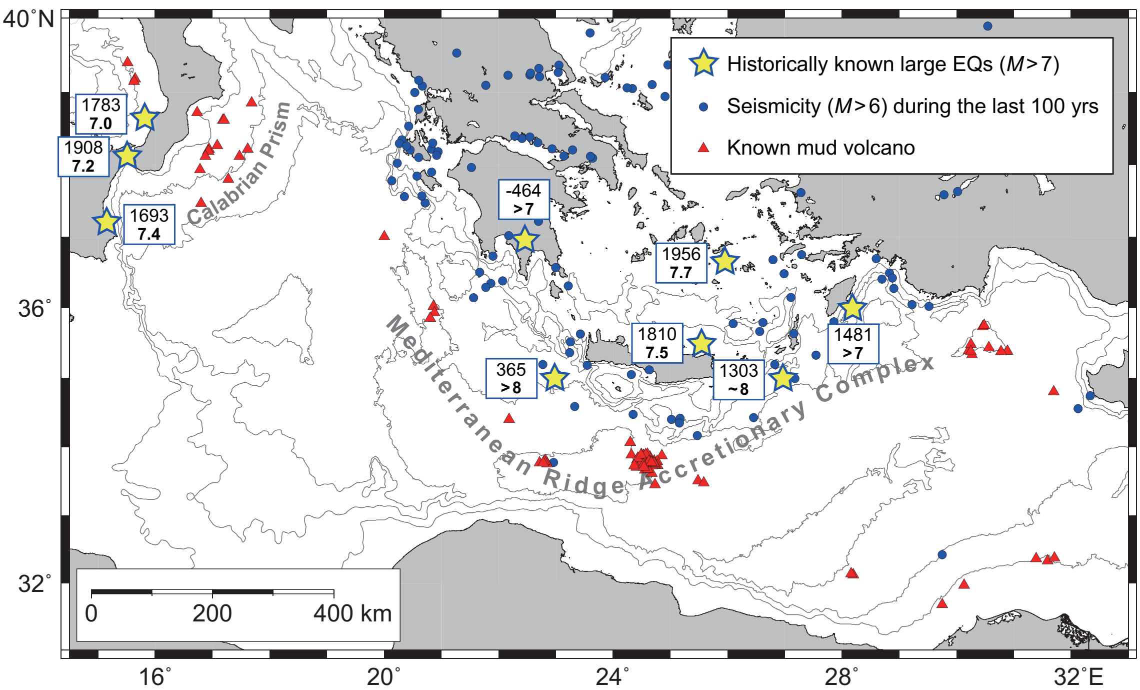

Figure 1.18: Historically known large earthquakes ($M > 7$) [e.g., *Papadopoulos et al.*, 2007], other seismicity ($M > 6$, USGS/NEIC PDE catalog: 1915–2015), and known submarine mud volcanoes in the central and eastern Mediterranean [*Kioka and Ashi*, 2015]. ETOPO1 grid data [*Amante and Eakins*, 2009] are used to illustrate bathymetry map.

between submarine mud volcanism and neighboring large earthquakes. This could also help unveil long-term recurrence of large earthquakes combined marine turbidite records [e.g., *Goldfinger*, 2011] with ejecta records from submarine mud volcanoes and sediment expulsion/mobilization such as pockmarks and associated mass-transport deposits [e.g., *Reusch et al.*, 2016]. The associated topic is made passing reference in Chapters 2 and 3.

Submarine mass failures can often serve as generation of large tsunamis [e.g., *Kawamura et al.*, 2012]. Eruptions from submarine mud volcanoes could also responsible for tsunami generations, although the eruptions themselves are thought not to be primary tsunami generators due to their small scale [e.g., *Li et al.*, 2015]. However, several drastic mud eruptions from onshore mud volcanoes have been observed in New Zealand, California, and Sakhalin, reaching a height of several hundred meters or more [*White*, 1955; *Ridd*, 1970; *Kopf*, 2002]. Thus, the massive mud eruptions from submarine mud volcanoes might serve to generate tsunamis if such eruptions occur, though this validation requires

Table 1.2: Connections between the given chapter and other chapters to understand roles of submarine mud volcanism on subseafloor material cycling studied in this thesis.

	Chapter 2	Chapter 3	Chapter 4
Sediment transfer	✓	✓	△
Fluid migration	✓	✓	△
Carbon cycle	✓	△	✓

further considerable works.

1.3 A note about this thesis

The three main chapters of this thesis fall into three independent topics: (1) Morphology and eruptional dynamics of submarine mud volcanoes (Chapter 2), (2) Ascent mechanism of ejecta from submarine mud volcanoes (Chapter 3), and (3) Amount of methane inside submarine mud volcanoes (Chapter 4). In the following subsections, I separately summarize the motivation behind each chapter and the results obtained, because the parts of this thesis have different goals as presented above. Nevertheless, all the main chapters aim to understand submarine mud volcanism and its roles on subseafloor material cycling from standpoints of sediment transfer, fluid migration, and carbon cycle (Table 1.2). A short discussion of connections between given chapter and other chapters is thus addressed in a section entitled "Connections to other chapter" at the end of each individual chapter. Finally, I will discuss roles of submarine mud volcanism on subseafloor material cycling in Chapter 5 based on results produced in the three main chapters, and will summarize this study in Chapter 6.

Chapter 2

Submarine mud volcanism can be viewed as natural tectonic conduits that bring up deep material and fluid to the seafloor to explore subseafloor geological processes without deep-drilling. In particular, broad interests have been significantly boosted since the review paper published in 2002 [*Kopf*, 2002]. But roles of mud volcanism on subsurface material cycling have been long puzzled, while this issue must be solved in order to understand subseafloor geological processes through submarine mud volcanism. In this chapter, I made a first effort in making a catalog (Table A.1) through compilation of topographical properties of submarine mud volcanoes that includes sufficient information to investigate the issue. The catalog reveals that mud volcanoes are highly variable in size and geometry as found in "magmatic" volcanoes, which makes a question what factors (e.g., tectonic regimes) drive the variation. The compilation is thus forwarded to infer various dynamics of massive mud eruptions from offshore mud volcanoes in the light of previous authoritative studies into granular flows. While this approach is relatively straightforward, I have never seen anything like this in the literature. I found that a surface slope of mud volcano body sheds light on the dynamics of episodic mud eruptions from offshore mud volcanoes. As this study takes a first shot at global census on shapes and eruptional dynamics of offshore mud volcanoes, I believe the results presented in this chapter are important and will be of widespread interest to a broad scientific community. Final goals of this chapter include building of scaling law between mud volcano's shape and mud volume of individual mud eruptions, which is a future study by incorporating thermodynamic and kinetic terms.

Chapter 3

Physics of ejecta ascent from mud volcanoes has often been unsuspectingly thought to be a diapiric flow (i.e., a flow driven by a force of buoyancy manifested by density contrast), while the ascent in practice is much complicated rather than we have expected [*Manga et al.*, 2009]. However, an examination into ascent mechanism and its background physics is important especially for understanding of roles of submarine mud volcanism on subseafloor sediment recycling and fluid migration. In this chapter, I present for the first time detailed ascent dynamics of submarine mud volcanism in the western Mediterranean Ridge Accretionary Complex of the Eastern Mediterranean Sea, in the light of vitrinite reflectance measurements of ejecta samples from a submarine mud volcano and thermal structure modeling. The Mediterranean Ridge studied here is an intriguing area from viewpoints of existence of numerous submarine mud volcanoes as well as thick Messinian evaporitic sequences and other geological aspects. Moreover, understanding of ascent mechanism needed many geological constraints is benefited from previous numerous studies, as the Mediterranean Ridge has been historically studied owing to greatest number of submarine mud volcanoes. The samples were obtained from Médée-Hakuho Mud Volcano in the western Mediterranean Ridge using a remotely operated underwater vehicle during a Japanese-Greek collaborative research cruise in winter 2007. The thermal structure was designed in this study mainly for enhancing results of the vitrinite reflectance, but this result will be also applied to many kinds of geological studies and future deep-drilling such as the IODP (International Ocean Discovery Program) projects in our targeted area, because thermal regime also affects subseafloor material cycling. I found the evidence that the studied mud volcano has two-fold ascent mechanism which is strongly related to geological and tectonic regimes in the Mediterranean Ridge Accretionary Complex. I believe most of the results presented in this chapter are important and will be of widespread interest to our community.

Chapter 4

As reviewed in the previous section, mud volcanoes are among the largest geological sources releasing hydrocarbon gases and CO_2 into the atmosphere or the water column [e.g., *Dimitrov*, 2002; *Etiope and Milkov*, 2004]. An estimate of potential methane concentration inside submarine mud volcanoes is an urgent issue especially into clarification of the "Missing methane" problem. This problem is first appealed by *Milkov et al.* [2003], in which they show that global methane effluxes from deep-water mud volcanoes are now underestimated partly because of lacking of in-situ measurements. Since then, many studies have made efforts in analysis of sampled seawater from offshore mud volcanoes to get to know their methane fluxes. However, these challenges based on sample measurements are unsatisfactory to solve potential methane fluxes from deep-water mud volcanoes, as these geochemical measurements have been confined to above or subsurface of mud volcanoes, though full understanding requires secure deep-drillings. Moreover, a long-term observation on a mud volcano offshore Norway reveals a higher methane emission than expected [*Feseker et al.*, 2014]. Since then, broad interests into methane inside deep-water mud volcanoes have been further boosted. In this chapter, I took a first shot at geophysical estimation of the amount of methane inside a deep-water mud volcano using seismic data available easier than deep-drillings or long-term observations. I developed and tested a novel method for estimation of methane concentration inside a deep-water mud volcano using seismics. I showed first geophysical evidence of unexpectedly large methane concentration inside a deep-water mud volcano. While this approach is relatively straightforward, it is novel and new—I have never seen anything like this in the literature. This new method is general, not specific to the application in the SW Japan that I tested here, and I expect it will be broadly applied to all deep-water mud volcanoes using seismic data. The result presented in this chapter guides to reestimate global methane efflux from deep-water mud volcanoes using our method and long-term observations, and to repicture the role of submarine mud volcanism on subseafloor carbon cycle. The result is important and will be of interest to broad scientific communities including not only mud volcanism but also climate change.

Chapter 2

Morphological fingerprints of submarine mud volcanoes

2.1 Summary

The role of mud volcanism on subsurface fluid migration and material cycling has long been debated. Here, we compile the heights and radii of offshore mud volcanoes, and estimate a mean volume of episodic massive mud eruptions based on previous studies into granular flows. The volume is estimated as a function of the ratio of height to basal radius of the mud volcano's body under reasonable assumptions of the sizes of the mud conduit. Nearly all known offshore mud volcanoes are found to be polygenetic with the mean individual eruption volume of the pie-type mud volcano being several orders of magnitude larger than that of the cone-type. The frequent occurrence of pie-type mud volcanoes in accretionary margins characterized by high sediment influx, is explained by their efficiency in the transport of large amounts of fluidized sediments from deep depths to the seafloor.

2.2 Introduction

Mud volcanoes are commonly found in a variety of tectonic settings [*Kopf*, 2002] and act as natural conduits that bring to the surface substances and fluids driven from the deep by overpressure. Thus, mud volcanoes are useful in exploring the subsurface processes active in material cycling and fluid migration. Many studies into mud volcanism on Earth since the early 1970s have confirmed around 300 offshore mud volcanoes with that figure doubling around a decade ago [*Dimitrov*, 2002; *Kopf*, 2002]. Nevertheless, quantitative and statistical studies of mud volcano morphology have mostly been restricted to onshore mud volcanoes on Earth [*Bonini*, 2008, 2012] or mud volcano-like structures imaged on Mars [*Tanaka*, 1997; *Oehler and Allen*, 2010], due to the greater availability of high-quality topographic measurements for Martian mud volcanoes in contrast to those discovered on Earth's seafloor, although the interpretation that the Martian features are in fact mud volcanoes remains controversial [*Pondrelli et al.*, 2011]. However, the recent increase in the number of submarine mud volcanoes that have been surveyed by bathymetric and seismic instruments with high resolutions has greatly benefited morphological studies of mud volcanoes.

Previous studies have proposed that the shapes of submarine mud volcanoes may differ with region and tectonic background [*Kopf*, 2002; *Rabaute and Chamot-Rooke*, 2007] or that they are related to the viscosity or porosity of body depositions as well as the size of the conduit feeder [*Lance et al.*, 1998; *Kopf*, 2002]. Some studies suggest that mud volcanoes develop a conical or a flat-top edifice depending on their water content [*Barber et al.*, 1986; *Lance et al.*, 1998; *Feseker et al.*, 2009]. However, submerged mud volcanoes (such as the submarine mud volcanoes discussed here) are often unlikely to follow this trend when their ejecta mix with seawater immediately on reaching the surface. The isostatic model used by *Murton and Biggs* [2003] to estimate mud flow rates from offshore mud volcanoes, which would enable to examine the surface morphology, is inapplicable to shallower- or deeper-depths originated mud volcanoes as it is independent of the real source depths of mud volcanoes. For example, some mud volcanoes in the Eastern Mediterranean have moderate heights but relatively deep source depths of around 5–9 km below the seafloor [*Schulz et al.*, 1997; *Kioka et al.*, 2015]. Similarly, serpentine mud volcanoes in the Izu-Bonin (Ogasawara)-Mariana (IBM) Arc system also vary in source depths with roots reaching up to 30 km [*Fryer et al.*, 1999].

Offshore mud volcanoes are less affected by obvious weathering and surficial erosions and thus document the eruptive and depositional regimes during their development more clearly than onshore mud volcanoes, which are more difficulty to study because of these changes. Hence, we compiled bathymetric and seismic reflection data and literature to make a catalog of submarine mud volcanoes (Table A.1). Morphological studies were performed on the catalog of submarine mud volcanoes, to better understand subseafloor material cycling and fluid migration. Our compilation shows that offshore mud volcanoes are highly variable in their sizes and aspect ratios, i.e., the ratio of body height to basal radius (Figure 2.1).

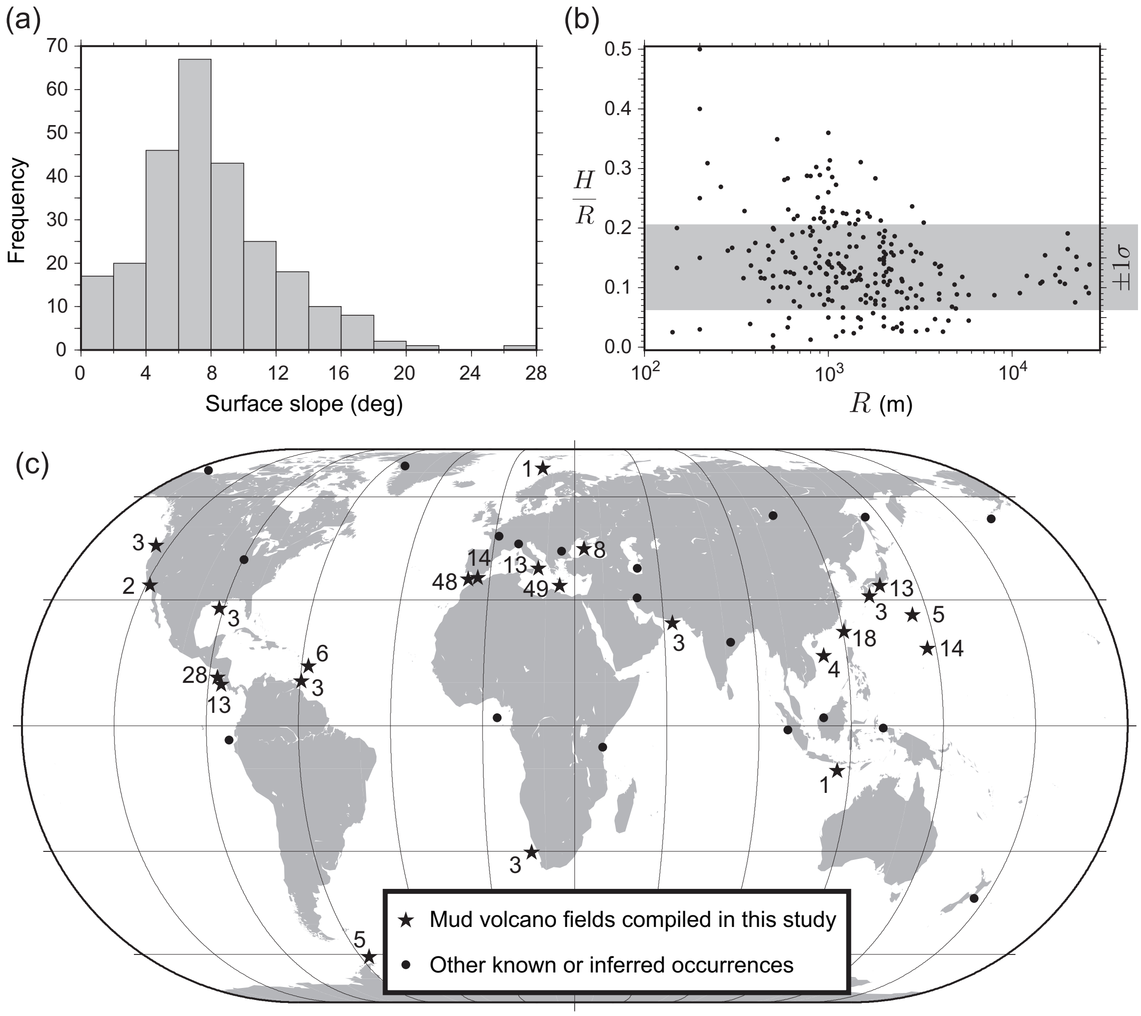

Figure 2.1: Examples of compiled data in the catalog of offshore mud volcanoes (Table A.1) including (a) the mean surface angle (degrees) and (b) radius R (m) versus the aspect ratio of the mud volcano's body, H/R (the ratio of height to radius of the mud volcano's body). (c) Offshore mud volcano fields and the number of mud volcanoes from each mud volcano field used in this study (black stars). Other regions with known or the inferred presence of onshore/offshore mud volcanoes [*Kopf*, 2002] are also plotted (black dots).

To explain these differences, we studied the dynamics of submarine mud volcanoes that underpins their episodic massive mud eruptions, affecting their sizes and aspect ratios. Estimating the potential volume of a mud eruption from a mud volcano is challenging, owing to a number of factors. However, we addressed this issue here by combining the aspect ratios of the mud volcanoes with previous studies of dense granular flows [*Lajeunesse et al.*, 2004, 2005; *Lube et al.*, 2004; *Lagrée et al.*, 2011]. This study would be able to estimate the volumetric flux of episodic massive mud eruptions from each offshore mud volcano to address the roles of mud volcanism on fluid migration and material cycling, and the processes governing them that have long been unclear.

2.3 Data and Methodology

2.3.1 A compilation of mud volcanoes

To date, no catalogs of offshore mud volcanoes with information sufficient for the issue presented here have been reported. We compiled the heights and radii of offshore mud volcanoes distributed around the world from bathymetric data or from the literatures (Table A.1). The data used here ($N = 258$) include submarine mud volcanoes in the regions illustrated in Figure 2.1c (see Table A.1 for details). The radius of each mud volcano R here denotes the mean radius, $R = (R_{\max} + R_{\min})/2$, if both the maximum radius $R_{\max}$ and minimum radius $R_{\min}$ are available for the mud volcano, and otherwise denotes a representative radius of those available in the literature. The shapes of the mud volcanoes are approximated to be elliptic cones or circular cones, and thus the volumes and mean surface slopes of the mud volcanoes are given by $\pi R_{\max} R_{\min} H/3$ or $\pi R^2 H/3$ and $\arctan(H/R)$, respectively, where H is the height of the mud volcano. Since some of offshore mud volcanoes have flat-topped crests (i.e., truncated cones) or contain depressions, we here define H as the maximum height of the mud volcano. We also do not take into account the subsidence of ejecta at the crest or on the whole volcano body, which affects the height and radius of a mud volcano.

The compiled data set shows that offshore mud volcanoes are highly variable in their sizes and geometries (Figure 2.1). The radii of offshore mud volcanoes, including the large serpentine mud volcanoes in the IBM Arc [*Fryer et al.*, 1999] are on the order of 10^2 to 10^4 m. Their mean surface slopes are also highly variable, ranging around $7.8° \pm 4.1°$ ($\pm 1\sigma$) and are generally lower than the angle of repose. Interestingly, the mean surface slope value is close to that of seamounts ($\sim 7.7°$) detected through altimetry-based gravity data [*Kim and Wessel*, 2011], though this topic is beyond the scope of this study.

2.3.2 Applications of previous granular flow studies to mud volcanoes

The rheology of mud is often described with a nonlinear viscoplastic Herschel-Bulkley model [e.g., *Herschel and Bulkley*, 1926; *Huang and García*, 1998]. Although this model is known to fit rheological data of mud over a wide range of shear rates [*Nguyen and Boger*, 1992; *Coussot and Piau*, 1994], the flow index approximating the degree of non-Newtonian behavior has a very large range depending on materials of mud flow [*Coussot and Piau*, 1994; *Tran et al.*, 2015; *Vona et al.*, 2015]. Unlike magmatic volcanoes whose dynamic viscosity of magma has a wide span of values, $\sim 10^{-1}$–10^{14} Pa·s [*Hess and Dingwell*, 1996; *Giordano et al.*, 2008], the range of dynamic viscosities of the ejecta from mud volcanoes is narrow, ranging over 10^3–10^6 Pa·s based on measurements and laboratory experiments even accounting for a moderate variation in water content [*Kopf and Behrmann*, 2000; *Manga et al.*, 2009; *Rudolph and Manga*, 2010], while progressive water dilution makes smaller values [*Vona et al.*, 2015]. However, both magmatic and offshore mud volcanoes show similar variations in surface slope angles up to $\sim 30°$ (Figure 2.1). This suggests that there are other ways to describe the magnitudes of eruptions from offshore mud volcanoes, without referring to variations in dynamic viscosity which are applicable to magmatic volcanoes (e.g., a shield volcano yields a gentle eruption).

Dense granular flows are commonly observed in geophysical phenomena such as rock or snow avalanches, landslides, and debris or pyroclastic flows [*Iverson*, 1997; *Dade and Huppert*, 1998; *Legros*, 2002; *Ekström and Stark*, 2013]. Experimental studies into the collapse and spreading of dry granular columns onto horizontal beds have revealed that the flow duration, the spreading velocity, and the final extent of the deposit can be described independent of basal properties, bed size, density and shape of granular material, and the released mass [*Lajeunesse et al.*, 2004, 2005; *Lube et al.*, 2004]. The phenomenology of this slumping process thus depends only on the initial aspect ratio of the column $a_0 = H_0/R_0$, where H_0 and R_0 are the initial column height and width, respectively (Figure 2.2a), as reported in axisymmetric collapses experiments [*Lajeunesse et al.*, 2004, 2005; *Lube et al.*, 2004], particle mechanics computations [*Staron and Hinch*, 2005], and the implementation of a so-called $\mu(I)$-rheology [*GDR MiDi*, 2004; *da Cruz et al.*, 2005] in an incompressible 2-D Navier-Stokes solver [*Lagrée et al.*, 2011]. The run-out distance R_∞, when normalized by the initial width of the column R_0 (Figure 2.2a), behaves as a power law of the column's initial aspect ratio a_0. The exponent of the power law is dependent only on the geometry of the column, and its value is highly reproducible. The scaling obtained is expressed as:

$$\frac{R_\infty - R_0}{R_0} = \lambda_1 a_0^\alpha, \tag{2.1}$$

$$\frac{H_\infty}{R_0} = \lambda_2 a_0^\beta, \tag{2.2}$$

where λ_1, λ_2, α, and β are positive constants dependent on the ranges of the initial aspect ratio a_0 and the scheme [*Lajeunesse et al.*, 2004; *Lagrée et al.*, 2011]. The relationship between the initial aspect ratio a_0 and the final run-out aspect ratio a_∞ ($= H_\infty/R_\infty$) is then obtained by substituting the equations (Figure 2.2b).

Here, we apply ideas from established studies on dry dense granular flows [*Lajeunesse et al.*, 2004; *Lagrée et al.*, 2011] to the rheology of massive mud eruptions from offshore mud volcanoes (Figure 2.2c), because the power-law behavior of the granular flows is less affected by the flow materials as addressed below. Let an upward dense flow of an initial eruption from an offshore mud volcano yields a cylinder with a height of H_0 and a radius of R_0. The column collapses and spreads onto the seafloor after the initial eruption with a final height H_∞ and a final run-out distance R_∞. The scheme here averages the extents of multiple upward eruptions under the assumption that the final aspect ratio H_∞/R_∞ is preserved. Based on the above, the ratio of the current mud volcano H/R is assumed to be equal to the run-out ratio H_∞/R_∞.

Ejecta of massive eruptions from offshore mud volcanoes are variable in grain size and include some large clasts, but the power-law behavior in the scheme used here is independent of the grain size [*Lajeunesse et al.*, 2004, 2005; *Lube et al.*, 2004]. If an

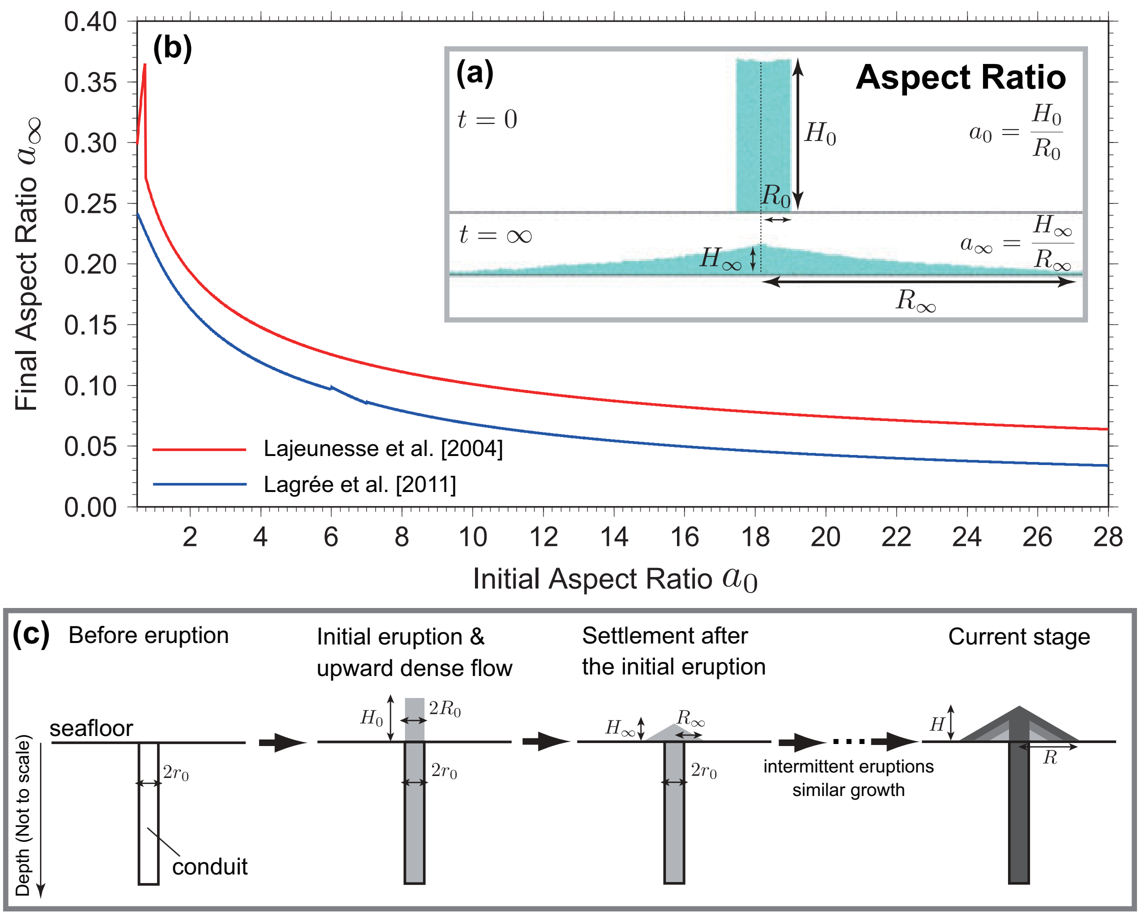

Figure 2.2: (a) Schematic illustration of column collapse experiments (modified from *Lajeunesse et al.* [2004] and *Lagrée et al.* [2011]), with the final maximum thickness H_∞ and the final half-radius (run-out distance) R_∞. (b) The relationship between the initial aspect ratio a_0 and the final aspect ratio a_∞ (red: experiments from *Lajeunesse et al.* [2004]; blue: 2-D $\mu(I)$-rheology continuum model from *Lagrée et al.* [2011]). (c) A schematic model of massive mud eruptions and settlement of offshore mud volcanoes in this study (see text).

eruption has clasts, then the settlement is formed differently with a splatter wall or mound being built first. This wall or mound, however, may then collapse as a result of subsequent eruptions, and, as a result, the scaling can be applied as the effects are averaged over a period of time. When a fluid is present in the granular medium, it has profound effects on contacts between grains and the induction of drag forces on them. However, numerical simulations reveal the equality of the run-out distance R_∞ between grain- and fluid-inertial regimes, because the effects of fluid, including reduction of the kinetic energy during granular collapse and enhancement of the flow by lubrication during granular spread, are presumably canceled out each other [*Topin et al.*, 2012]. Thus, the scheme described above can be applied to massive mud eruptions from submarine mud volcanoes. Bottom water currents, whose effects on surficial erosion are hard to estimate, were not taken into account in this study, although they can flatten the pile. In addition, ejecta from subsequent mud eruptions would likely flow on a certain slope, whereas here we assumed that they flowed on a flat surface.

2.4 Results and Discussion

Conduit radii of mud volcanoes either do not exceed a couple of meters or range around 10 m, according to several measurements and theoretical estimations [*Kopf and Behrmann*, 2000; *Kopf*, 2002; *Rudolph et al.*, 2011], although these estimates remain controversial. High-resolution 3-D seismic images have also revealed cylindrical zones of amalgamated narrow fluidized mud pipes that feed offshore mud volcanoes [e.g., *Davies and Stewart*, 2005; *Stewart and Davies*, 2006]. We estimated the mean volume of episodic mud eruptions of the mud volcano using the scaling law [*Lajeunesse et al.*, 2004; *Lagrée et al.*, 2011], assuming $R_0 = r_0$ for various values of the radius of the mud conduit r_0 (Figure 2.2c). Offshore mud volcanoes with a conduit radius of 1 m have a mean volume of episodic massive eruptions around 10^1–10^2 m^3 while those with a conduit radius of 10 m have mean volumes of 10^3–10^5 m^3. The mean eruptive volume of "pie-type" offshore mud volcanoes (i.e., a mean surface slope of $< 5°$ [*Kopf*, 2002]) is one or two orders of magnitude larger than the mean eruptive volume of the "cone (dome)-type" mud volcanoes (here, a mean surface slope of $> 10°$) (Figure 2.3), while the conduit width and the volume of individual eruptions may increase as the mud volcano grows and thus the calculated volume varies considerably.

More than 95% of offshore mud volcanoes are overwhelmingly larger than the estimated volume of a primary mud eruption (Figure 2.3). This means that nearly all of them are polygenetic, as found as so-called "Christmas tree" structures in their seismic images [e.g., *Somoza et al.*, 2003]. Thus, offshore mud volcanoes reuse their main conduits multiple times, suggesting that they serve effectively to transfer fluids and materials from deep depths to the seafloor. Monogenetic mud volcanoes seem to erupt predominantly in

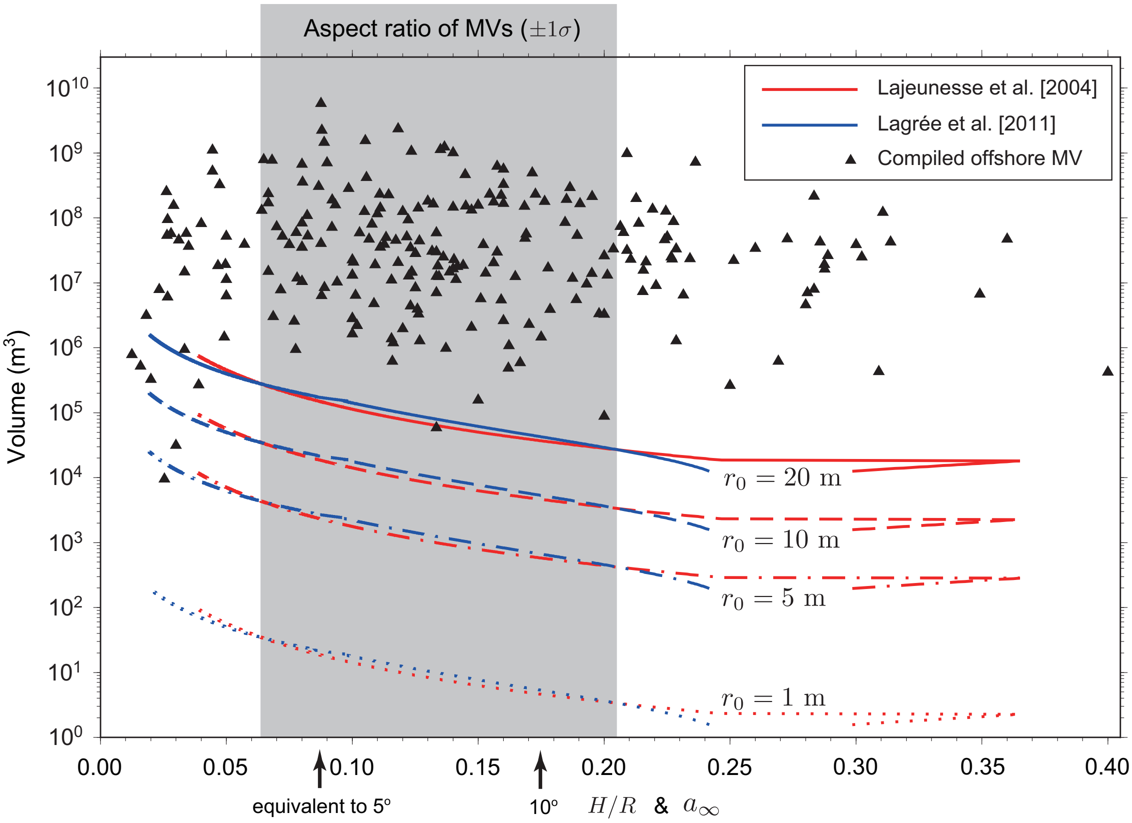

Figure 2.3: Estimated volume of episodic mud eruptions from a single offshore mud volcano under reasonable assumptions of the radius of the mud conduit $r_0 = 1$, 5, 10, and 20 m [*Kopf and Behrmann*, 2000; *Kopf*, 2002], where red and blue lines are derived from the solutions of *Lajeunesse et al.* [2004] and *Lagrée et al.* [2011], respectively. Volumes of compiled offshore mud volcanoes are also plotted (black triangles), but large serpentine mud volcanoes in the IBM Arc are excluded here.

extensional tectonic settings and are not driven by compressional stress similar to magmatic volcanoes [e.g., *Nakamura*, 1977]. This indicates that most of the known submarine mud volcanoes were formed from eruptions caused by background compressional stress. Since some onshore monogenetic mud volcanoes do not necessarily concur with extensional settings, the size of mud chamber or fluid source is also a significant key triggering multiple eruptive phases.

Given that a pie-type mud volcano has a larger-sized conduit [e.g., *Kopf*, 2002], the mean volume of an individual episodic massive eruption from a pie-type offshore mud volcano should be two or three orders of magnitude larger than the one from the cone-type offshore mud volcano (Figure 2.3). Since offshore mud volcanoes are thought to be polygenetic and thus differ in the number of eruptions and time taken to reach the current volume, the current volume of the mud volcano is indeed sketched to be scatter against its aspect ratio (Figure 2.3). For a high initial aspect ratio a_0, the run-out height reaches a limit value [*Lajeunesse et al.*, 2004; *Lube et al.*, 2004; *Lagrée et al.*, 2011] and the slope angle at the toe of the final deposit is saturated at a value of $\sim 5°$ [*Lajeunesse et al.*, 2004]. In the scatter plot (Figure 2.3), the volume seems to decrease when the slope angle increases between 5° and 10°, while the trend is opposite for the angle below 5°. This feature is consistent with the above theoretical relationship. It is thus likely that mud volcanoes with the largest volumes have an average slope angle of 5°, and that the pie-type mud volcanoes have either a lower coefficient of internal friction or a different rheology.

Multiple comparisons performed using the Ryan-Einot-Gabriel-Welsch Q (REGWQ) procedure ($p < 0.05$) [*Ryan*, 1960] showed that pie-type offshore mud volcanoes are uniquely dominant in the western Mediterranean Ridge, Makran, and Barbados accretionary wedges (Table 2.1). These accretionary wedges are characterized by their low taper angles (less than 4°) and high rates of incoming sediments in trenches reaching $\sim 2 \times 10^{-4}$–3×10^{-4} km^2/yr (Table 2.1). These wedges hamper fluid escape and consequently lead to elevated pore pressures [*Saffer and Bekins*, 2006]. Thus, the frequent occurrence of pie-type mud volcanoes in these wedges suggests that they act as efficient conduits to allow the escape of large quantities of fluidized sediments from the wedge to the seafloor as well as for release of the large overpressures. This feature helps estimate a volume balance of extruded muds and incoming sediments [e.g., *Kopf*, 1999] to discuss the roles of mud volcanism on subseafloor material cycling.

The Milano mud volcano in the central Mediterranean Ridge accretionary complex is well investigated, thanks to the successes of deep-drilling projects. Its activity began around 1.5 Ma and it continues to remain active [*Robertson and Ocean Drilling Program Leg 160 Scientific Party*, 1996]. It has a volume of $\sim 1.6 \times 10^8$ m^3 with an aspect ratio of $H/R \simeq 0.09$ in our calculation (Table A.1). Given the radius of the conduit of the mud volcano is ~ 5 m [*Kopf and Behrmann*, 2000], around 40–50 massive mud eruptions per 1000 years on average would be required to obtain the present volume (Figure 2.3), although the drilling on the flank of the mud volcano does not record these frequent events [*Robertson and Ocean Drilling Program Leg 160 Scientific Party*, 1996] partly because of the entrainment by extruded mud flow and slow background sedimentation rates. We extracted from the Advanced National Seismic System (ANSS) catalog a list of earthquakes that occurred between 1961 and 2015 in all depth ranges using a 1° sampling, centered around its location, in order to estimate the Gutenberg-Richter relation [*Gutenberg and Richter*, 1944]. The cumulative number of earthquakes was extrapolated to estimate the number of earthquakes of $M > 6$ per 1000 years, yielding interestingly around 40 events per 1000 years, though this estimate does not take into account the error due to the uncertainty of the b-values. This suggests large earthquakes around the mud volcano ($M > 6$) could be the primary drivers of episodic massive eruptions, if earthquakes can indeed trigger massive mud eruptions as suggested [*Mellors et al.*, 2007; *Manga et al.*, 2009].

Given a mud volcano of a mean slope of 5° with a mud conduit radius of $r_0 = 5$ m, our scheme requires an individual eruptive height of $H_0 \simeq 30$–60 m (Figure 2.2b) to satisfy the volume of episodic mud eruptions derived from the solutions of *Lajeunesse et al.* [2004] or *Lagrée et al.* [2011] (Figure 2.3). The idea that the upward dense flow driven by a massive mud eruption from a submarine mud volcano can reach such heights without suspension or buckling might seem controversial. But, several drastic eruptions from onshore mud volcanoes in New Zealand, northeastern California, and Sakhalin have been observed to reach a height of several hundred meters or more [*White*, 1955; *Ridd*, 1970; *Kopf*, 2002]. In contrast, a direct observation of massive mud eruptions from offshore mud volcanoes by submersible surveys remains difficult, as eruptions are episodic. However, the simultaneous release of gases promotes a further upward flow without effective suspension as ejecta from the mud volcano captures large amounts of these gases. Thus, a massive mud eruption from a submarine mud volcano can reach a height of tens or hundreds of meters, behaving as a dense upward flow.

In nature, however, in most cases the cylinder would start collapsing before it reaches the estimated height. Let us consider the initial gravitational potential energy of a mud head of radius R_0 and height H_0:

$$E_i = \frac{\pi}{2}(\rho_b - \rho_{sw})gR_0^2H_0^2 = \frac{\pi}{2}(\rho_b - \rho_{sw})ga_0^2R_0^4, \tag{2.3}$$

where ρ_b is the bulk density of the mud head, ρ_{sw} is the seawater density, and g is the gravitational acceleration. The initial potential energy is alternatively expressed using equation (2.1):

$$E_i \simeq \frac{(\rho_b - \rho_{sw})ga_0^2}{2\pi(R_\infty/R_0)^4}A_\infty^2 = \frac{(\rho_b - \rho_{sw})ga_0^2}{2\pi(\lambda_1 a_0^\alpha + 1)^4}A_\infty^2, \tag{2.4}$$

which shows a power law scaling among the run-out surface area $A_\infty \simeq \pi R_\infty^2$, the initial potential energy, and the initial aspect ratio a_0. Since the radius of the mud head R_0 is fixed to be the radius of the mud conduit r_0, this relation means that the more energy the massive eruption inputs into the system, the more the run-out avalanche will spread, given that the run-out aspect ratio a_∞ falls exponentially with increasing initial aspect ratio a_0 values (Figure 2.2b). This also suggests that the background theory for qualitative discussions here in practice does not require the building of a dense granular cylinder. Thus, it is possible to use a different parametrization incorporating energy expressed in different forms to estimate massive mud eruptions, which will form the basis of a future study.

The catalog created in this study also needs to be further updated, since it is estimated that there are thousands of offshore mud volcanoes [*Milkov*, 2000; *Dimitrov*, 2002]. Moreover, our scheme tends to underestimate the aspect ratio of offshore mud volcanoes, because we ignore subsidence and the gravitational collapse of the volcanic body that often occurs in pie-type mud volcanoes [e.g., *Henry et al.*, 1990]. Despite such uncertainties due to limited parametric considerations, our study delineates the dynamics of episodic massive mud eruptions from submarine mud volcanoes. The Coulomb's wedge theory (which describes a taper angle; most basal angles of offshore mud volcanoes seem to settle around 0–2°) coupled with the scheme in this study and the scheme of *Murton and Biggs* [2003] might further expand our understanding of the dynamics of mud volcano eruptions. In addition, long-term stationary observations, subbottom profiling, and more information about the physical properties of the ejecta will help us better understand the dynamics of

Table 2.1: Occurrence of pie-type offshore mud volcanoes in each subduction margin. Numbers of pie-type offshore mud volcanoes and all offshore mud volcanoes were extracted from our catalog (Table A.1). Properties of the subduction margins investigated here that include taper angle, convergence velocity, and sediment thickness at trenches are from the literature [*Le Pichon et al.*, 1995; *Clift and Vannucchi*, 2004; *Saffer and Bekins*, 2006; *Fernandes et al.*, 2007; *Gutscher et al.*, 2009a, b; *Heuret et al.*, 2012].

Region	Type [a]	# of pie-shape mud volcanoes	# of all mud volcanoes	Taper angle	Orthogonal convergence velocity (cm/yr)	Sediment thickness at trench (km)	Input rate [b] ($\times 10^{-5}$ km^2/yr)
GOC [c]	A	2	48	$\sim 2°$	0.5	~ 10 [d]	~ 5
WMR [e]	A	7	9	$\sim 2°$	4.0	7.0	28
Makran	A	3	3	2.9°	4.0	7.5	30
Barbados	A	3	6	3.6°	2.8	6.3	18
Nankai	A	3	12	4.0°	4.0	1.5	6
SW Taiwan	A	2	18	4.7°	3.0	2.8	8
Nicaragua	E	0	28	15.0°	7.8	0.5	4
Costa Rica	E	0	12	7.6°	8.0	0.6	5

[a] A: Accretionary type subduction margin; E: Erosional type subduction margin.

[b] The rate is computed as a product of orthogonal convergence velocity and sediment thickness at trench.

[c] GOC: Gulf of Cadíz

[d] Sediment thickness in the eastern gulf.

[e] WMR: Western Mediterranean Ridge.

mud volcanoes.

2.5 Conclusion

Nearly all offshore mud volcanoes that have been discovered appear to be polygenetic, suggesting that they are efficient conduits for subseafloor material cycling. The mean individual volume of episodic massive mud eruptions from pie-type mud volcanoes (a mean surface slope of $< 5°$) is several orders of magnitude larger than the one from cone-type mud volcanoes (a mean surface slope of $> 10°$). The frequency of pie-type mud volcanoes in accretionary margins characterized by high fluxes of incoming sediment is likely due to their role as an efficient escape mechanism for large quantities of fluidized and gas-saturated sediments from deep depths to the seafloor. This study has shed new light on the long-debated issue of the roles of submarine mud volcanism on subseafloor material cycling and fluid migration.

2.6 Connection to other chapters

This chapter will be summarized as: (1) compiled data of submarine mud volcanoes shed new light on their dynamics, (2) the shape of the mud volcano depends on feeding conduit width and erupted volume, and (3) the frequency of pie-type mud volcanoes is associated with subduction inputs. The linkage between mud eruptions from mud volcanoes and neighboring seismicity is reviewed in Chapter 1 and discussed in Chapter 3. Background of ascent mechanism driving massive mud eruptions studied in this chapter is addressed in Chapter 3. Our knowledge presented in this chapter will be applicable to paleoseismology with coupling with other event-records including seismogenic turbidites [e.g., *Goldfinger*, 2011] and sediment expulsion/mobilization such as pockmarks and associated mass-transport deposits [e.g., *Reusch et al.*, 2016], which will help improve our understanding of relation between mud volcanism and earthquakes addressed in Chapter 1. The estimation of eruptional volume, though the first-order estimate is examined here, also helps assess global methane flux investigated in Chapter 4.

Chapter 3

Ascent mechanism of ejecta from a submarine mud volcano at the prism-backstop contact

3.1 Summary

The Eastern Mediterranean seafloor has numerous mud volcanoes, most of which form a well-defined belt within the Mediterranean Ridge (MedRidge) accretionary complex. However, mud volcano fields in the western MedRidge are less well known as those in the central and eastern MedRidge. This study investigates material cycling and fluid migration within the western MedRidge. We propose a possible ascent style of the ejecta forming the Médée-Hakuho Mud Volcano (MHMV) in the western MedRidge by applying the vitrinite reflectance technique to ejecta samples. First, we model the 2-D thermal structure in the western MedRidge, taking into account frictional heating on the plate interface, to help estimate the source depth of the MHMV ejecta. The result suggests an effective coefficient of friction of around 0.01, and a temperature of about $160 \pm 15°C$ along the plate interface at a distance of $\sim$180 km from the deformation front, the location of the seaward toe of the Aegean backstop. Second, we evaluate the source depth of the MHMV ejecta using vitrinite reflectance in conjunction with the modeled thermal structure. The results suggest that the ejecta matrix showing vitrinite reflectance values of $\sim$0.6% was

subjected to a temperature of around 85°C, corresponding to a depth of approximately 5 km below the seafloor (kmbsf), whereas older clasts of Aptian or earlier age, with vitrinite reflectance values of ∼0.6–1.0%, are derived from much deeper depths. Most of the clasts are considered to have been lifted to the depth of 5 kmbsf as a result of underplating at the toe of a rigid backstop that had developed below MHMV after underthrusting related to plate subduction. At that depth, fluid pressures that are dramatically increased because of underplating promote the ascent of fluid-rich sediments and entrain clasts along an existing fault in the accretionary wedge.

3.2 Introduction

Fluids in subduction zones that are derived from the incoming plate may move out of the overriding plate to the seafloor by diffusive flows or along structural conduits, or they may migrate to greater depths where they affect tectonic processes [e.g., *Moore and Vrolijk*, 1992; *Saffer and Tobin*, 2011]. These fluids strongly affect the deformation style of the overriding plate wedge. In addition, tectonic loading and mineral dehydration produce fluids within the overriding wedge. The resultant overpressure may have profound effects on faulting and earthquake mechanics through its influence on effective stress. Direct observations of overpressure in this setting are rare, as they require deep drilling. Submarine mud volcanoes are possible paths for migration of overpressured fluids from the underthrusting section through the wedge to the seafloor. Thus, studies of mud volcanoes hold promise in tracing the spatial distribution of overpressure within accretionary wedges.

Submarine mud volcanoes are plentiful at almost all subduction margins, but the relationship between mud volcanism and underlying tectonics is obscure [*Kopf*, 2002]. They have various geometries, with diameters of up to tens of kilometers and heights of up to several hundreds of meters. The eastern Mediterranean Sea is noted for its extensive field of mud volcanoes, which display many examples of various morphologies [e.g., *Camerlenghi et al.*, 1995; *Hieke et al.*, 1996; *Huguen et al.*, 2004; *Lykousis et al.*, 2009] and form a well-defined belt on the seafloor [*Limonov et al.*, 1996]. Mud volcanoes can be viewed as natural tectonic conduits that bring up deep materials to the seafloor and may be useful setting for exploring fluid migration processes.

This study investigates the formation of Médée-Hakuho Mud Volcano (MHMV), particularly how the ejecta composing it ascended from depth, in order to gain information that cannot be derived from seismic images such as the processes of material derivation at depths and their upward migration. Samples were obtained during a Japanese and European collaborative research cruise in 2007. MHMV lies above the contact between an accretionary prism and a tectonic backstop in the western Mediterranean Ridge (MedRidge) accretionary complex. This area has received relatively little attention, whereas the central and eastern MedRidge have been heavily investigated by Ocean Drilling Project (ODP) surveys and other European projects. We first calculate a model of thermal structure across the western MedRidge, and then use vitrinite reflectance data from the MHMV samples to infer the source and path of its ejecta in light of the thermal model.

3.3 Geological setting

3.3.1 Western Mediterranean Ridge

The eastern Mediterranean is one of the most rapidly deforming regions on Earth [e.g., *McKenzie*, 1972, 1978; *Reilinger et al.*, 2006]. Plate kinematics in this region includes Arabian-Eurasian oblique motion, the Hellenic subduction processes, and Nubian-Eurasian convergence. The MedRidge is a large, arcuate sedimentary wedge more than 1500 km long and 300 km wide [e.g., *Emery et al.*, 1966; *Le Pichon et al.*, 1982; *Fusi and Kenyon*, 1996; *Kopf et al.*, 2003] in the eastern Mediterranean from southwest of the Peloponnesus to south of Rhodes. The development of the MedRidge results from 3 to 4 cm/yr subduction of the Nubian plate beneath the Aegean Sea along the Hellenic trenches south of mainland Greece and the island of Crete [e.g., *Le Pichon et al.*, 1995; *McClusky et al.*, 2000; *Kreemer and Chamot-Rooke*, 2004]. The crust of the incoming Nubian plate in the western MedRidge is believed to be oceanic as suggested by high-resolution seismic images in the western Hellenic subduction zone [*Pearce et al.*, 2012] and forward magnetic modeling in the Ionian Basin [*Speranza et al.*, 2012]. Seismic reflection and refraction surveys and seafloor sampling show that the MedRidge consists of offscraped and stacked sediment units of late Mesozoic and Cenozoic age with a net thickness of up to 12 km [e.g., *de Voogd et al.*, 1992; *Chaumillon and Mascle*, 1997]. The MedRidge is bounded on the north by a seaward (southwest) dipping continental backstop acting as a strong buttress of complex shape, which probably consists of highly indurated sediment of the Hellenic nappes with high seismic velocity [e.g., *Truffert et al.*, 1993; *Lallement et al.*, 1994; *Le Pichon et al.*, 2002]. The ridge includes Messinian evaporitic sequences, locally 2 km thick, a few hundred meters beneath the seabed [e.g., *Chaumillon et al.*, 1996; *Polonia et al.*, 2002].

The presence of Messinian evaporite sequences has a profound influence on deformation mechanisms, style of folding, and fluid overpressuring in the accretionary wedge [e.g., *Davis and Engelder*, 1985]. The MedRidge is unusual in having a very small taper angle, indicative of very low shear stress on its basal décollement that is likely related to the presence of highly ductile evaporite minerals such as halite [e.g., *Chaumillon and Mascle*, 1997; *Polonia et al.*, 2002]. This setting favors the outward growth of the wedge over uplift, and the MedRidge is considered the fastest growing wedge with a rate of >10 km/Myr [*Kastens*, 1991; *Kopf et al.*, 2003]. Numerical simulations show that the great thickness and low permeability of the incoming sediment produces high pore pressures consistent with the taper wedge geometry [e.g., *Saffer and Bekins*, 2006]. The MedRidge has received up to ∼7 km of incoming sediment [*Chamot-Rooke et al.*, 2005b] and is similar in this respect to the Makran margin [*Kopp et al.*, 2000]. The thick and low-permeability sediment combined with the even less permeable Messinian evaporites retards fluid escape, enhances fluid overpressure on the décollement, and elevates pore pressures in the whole wedge. These factors make the MedRidge an atypical accretionary prism, even compared to other accretionary types with similar taper angles or thickness of incoming sediment [e.g., *Clift and Vannucchi*, 2004]. These conditions also help give the region the world's greatest abundance of mud volcanoes (Figure 3.1). *Ryan et al.* [1982] were first to ascribe the mud volcanism in the eastern Mediterranean to mud extrusion from an accretionary prism, triggered by a combination of high pore pressure and deformation caused by tectonic compressional stress. Mud volcanism in the eastern Mediterranean is localized on the MedRidge, forming the Mediterranean Ridge mud diapiric belt [*Limonov et al.*, 1996].

In the western MedRidge, high seismic reflectivity and subcircular patches of mud

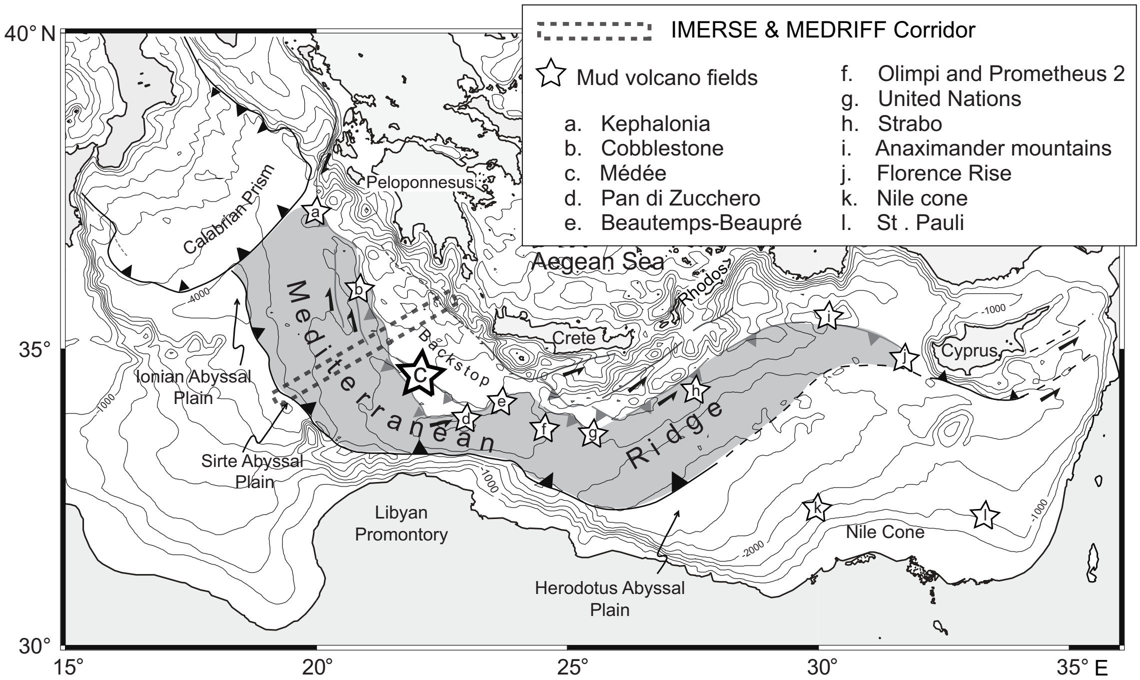

Figure 3.1: Mud fields in the eastern Mediterranean Sea [*Rabaute and Chamot-Rooke*, 2007]. Morpho-structural interpretations follow *Chamot-Rooke et al.* [2005b]. The larger star indicates the Médée mud volcano field, investigated in this study.

volcanoes demarcate a discontinuous belt extending 550 km from the Pan di Zucchero to Kephalonia mud volcano fields [*Chamot-Rooke et al.*, 2005a]. These features are located above the wedge-backstop contact and hence are considered to be associated with active strike-slip faults. Mud volcanoes of all sizes occur here, more than 95% of them located near the wedge-backstop contact and the rest scattered over the prism [*Chamot-Rooke et al.*, 2005a; *Rabaute and Chamot-Rooke*, 2007]. Because of the role of Messinian evaporitic sequences in preventing extrusion of overpressured sediments at depth to the seafloor, mud volcanoes are thought to concentrate where the evaporite layer is absent or thin [*Camerlenghi et al.*, 1995], such as where major strike-slip faults provide pathways for upward migration of fluid and material.

3.3.2 Médée-Hakuho Mud Volcano (MHMV)

During the PENELOPE Cruise above the western MedRidge of January–February 2007 (KH-06-4 Leg 6 survey of R/V *Hakuho-Maru*), detailed seafloor mapping and pinpoint

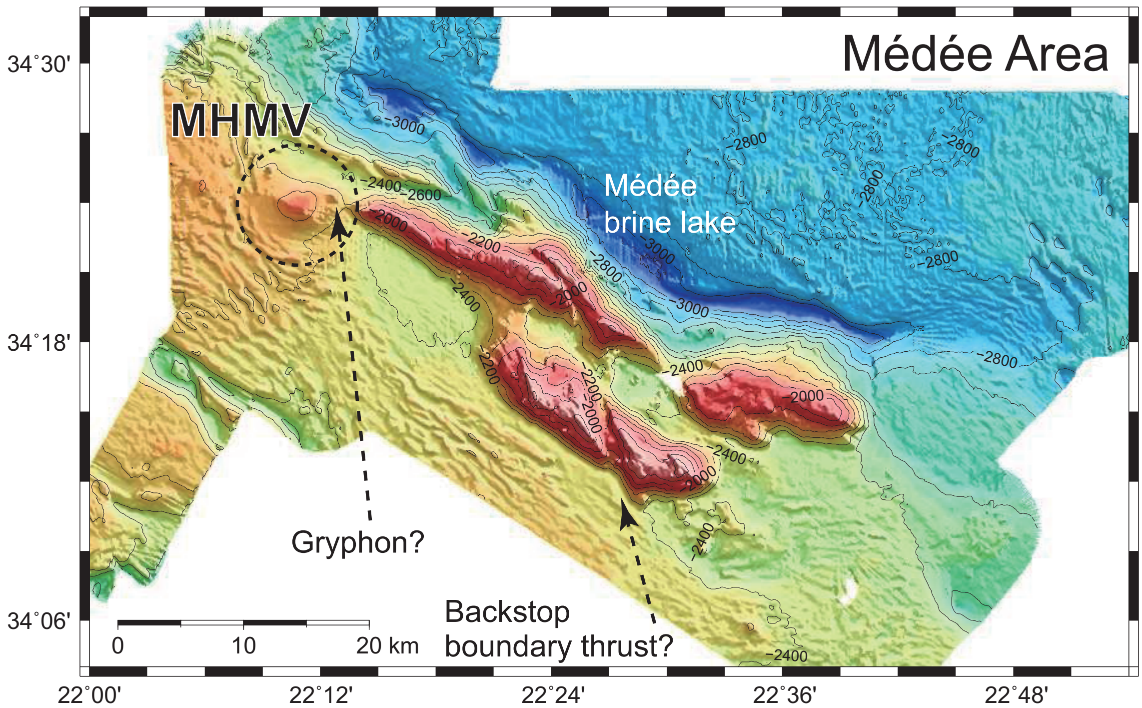

Figure 3.2: Bathymetry of the Médée region, acquired during the PENELOPE Cruise at a survey speed of 10–12 knots using a SeaBeam2120 multibeam echosounder operated at 20 kHz on R/V *Hakuho-Maru*. The transducers had a normal opening of 1° along track and 1° across track. Swath width was 120° for almost all survey lines. MHMV stands for Médée-Hakuho Mud Volcano.

piston coring were done at the newly discovered Médée brine lake and MHMV to its west (Figure 3.2). Coring was done with the Navigable Sampling System (NSS), a remotely operated vehicle (ROV) developed at the Atmosphere and Ocean Research Institute, University of Tokyo [e.g., *Ashi et al.*, 2012, 2014], along with simultaneous seafloor observations. This mud volcano was first recognized during the Médée Cruise in 1995 on the basis of its distinct backscatter intensity [e.g., *Rabaute et al.*, 2003]. *Rabaute and Chamot-Rooke* [2007] reported that an area as large as 76 km^2 of extruded mud, as determined from seabed reflectivity, surrounds MHMV. The mud volcano stands near the backstop boundary at a water depth of 2260 m, has an oval shape in plan view measuring 4.9×6.7 km and reaches 130 m in height with very gentle slopes (Figure 3.2). A small cone or gryphon protrudes from its flank, probably resulting from a splay of the main conduit. Living tubeworms and bacterial mats were seen in video observations using the ROV NSS.

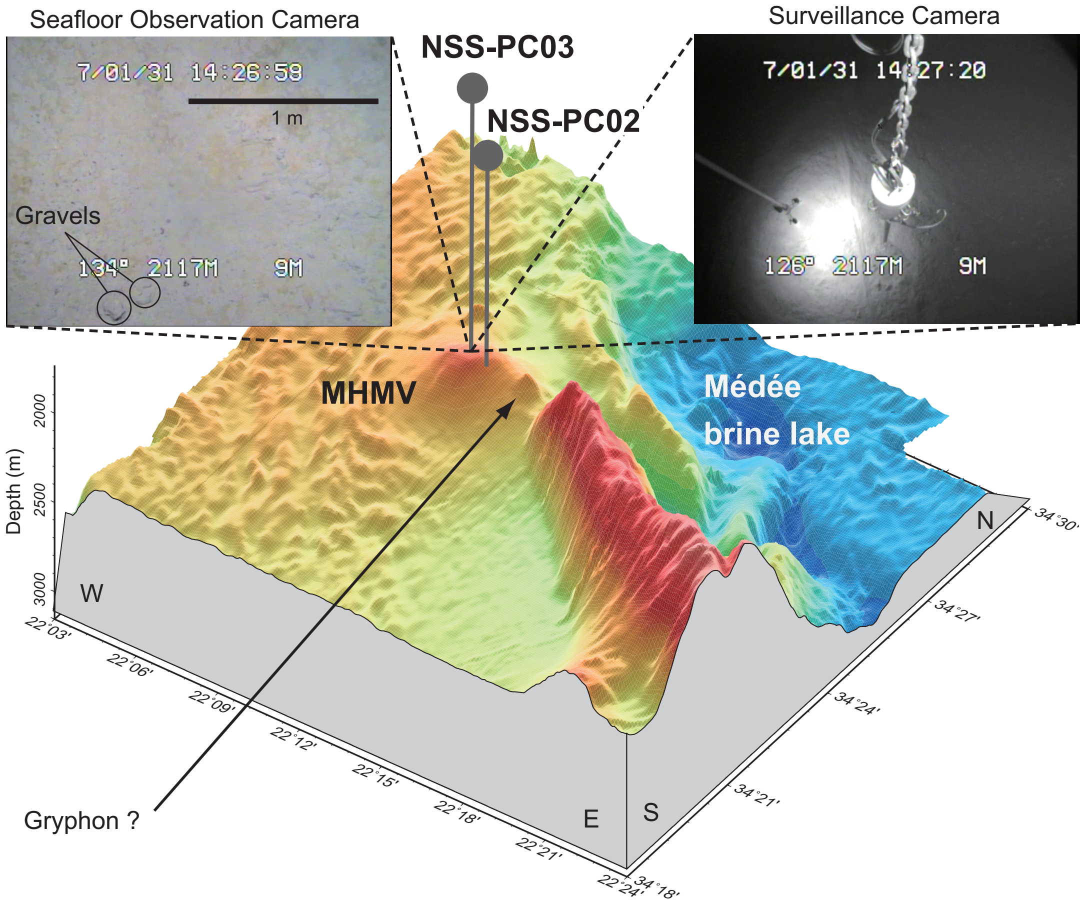

Figure 3.3: Locations of piston cores NSS-PC02 and NSS-PC03, and screenshots of payload and seafloor observation from ROV NSS. Sampling positions of the cores are summarized in Table 3.1.

MHMV is interpreted as recently active from the presence of gravel in the cores and its strong backscatter. ROV NSS observations of gravel near its summit (Figure 3.3) support this conclusion. The reflectivity data obtained during the Médée Cruise in 1995 suggest that MHMV has been active at least once during the past ~30 kyr [*Chamot-Rooke et al.*, 2005a].

In the MedRidge, brine lakes ponded in depressions are thought to have been generated by backthrust fractures serving as conduits for salt or brines to reach the seafloor [*Woodside and Vogin*, 1996]. Their relation to mud volcanoes is not yet certain. The Médée brine lakes, lying on the hinterland side of the backstop boundary thrust near MHMV (Figure 3.2), reach temperatures of 15°C and salinities >300 PSU [*Akoumianaki et al.*,

Table 3.1: Sampling positions of NSS-PC02 and NSS-PC03 cores.

Cores	Longitude	Latitude	Water depth
NSS-PC02	22°11.0' E	34°23.8' N	2134 m
NSS-PC03	22°11.0' E	34°23.9' N	2126 m

2012; *Yakimov et al.*, 2013] similar to those of the nearby Bannock Basin brine lake in the western MedRidge [*Corselli and Aghib*, 1987; *Camerlenghi and McCoy*, 1990]. The Médée brine lakes are thought to have formed where hypersaline water from the dissolution of Messinian evaporites ascended accompanied by slip on the backstop boundary thrust [*Tokuyama et al.*, 2007; *Izumitani et al.*, 2009]. It is likely that the ejecta forming MHMV and this hypersaline water share common flow paths and histories.

3.4 Materials and methods

3.4.1 Samples of MHMV

Ejecta samples from MHMV were obtained by pinpoint piston coring at the summit (NSS-PC03) and on its flank (NSS-PC02) (Figure 3.3, Table 3.1). The mud breccia from MHMV is composed of pebble-sized consolidated and semiconsolidated silty mud clasts in a grayish olive stiff sandy silt matrix (Massive A1 in the classification of *Camerlenghi and Pini* [2009]). The ejecta thus may represent the coarser and more poorly sorted portion of a debris flow. The matrix commonly includes grains a few millimeters in diameter. Clast lithologies are dominated by shale and mudstone, with minor limestone, conglomerate, sandstone and calcarenite, and alkali basalt (Figure B.3). Many shale and mudstone clasts are calcareous or contain veins of coarse sparry calcite. Several mudstone clasts contain microfaults or veins. Most clasts are well consolidated. We focused on clasts larger than 1 cm in diameter because they yielded useful petrographic data, especially for measurement of vitrinite reflectance.

We found no obvious variations in clast abundance in cores NSS-PC02 and NSS-PC03. The maximum diameters of the clasts have a scattered distribution between 11 and 62 mm, which is obviously limited to 80 mm owing to the diameter of the core liner. Volumetric abundances of consolidated or semiconsolidated clasts are ∼11% and ∼13% in cores NSS-PC02 and NSS-PC03, respectively. Although some of the smallest clasts must have gone uncounted by visual inspection, these would not materially affect our estimation of the volumetric abundance. The density of clasts was measured primarily by volumetric means using a gas displacement density analyzer (Accupyc 1330, Micromeritics Co., Ltd.). The values of shale and mudstone clasts have considerable scatter around 2.7×10^3 kg/m^3 and show no trend with depth but tend to have higher densities than ordinary sedimentary rocks, suggesting that these clasts underwent high pressures and hence were indurated or probably fully dewatered. The lack of sorting in the depth profiles of clast size and density is consistent with the debris-flow deposition style of MHMV.

Nannofossils in most of the clasts indicate an age range from Late Jurassic to Early Cretaceous, and no Cenozoic species were found (Table B.1). For example, Sample #C032 (siltstone) contains assemblages of Aptian age as suggested by the occurrence of *Micrantholithus hoschulzii* and *Rucinolithus irregularis*. This occurrence is also observed in a clast from Aros mud volcano in the Cobblestone mud field [e.g., *Premoli Silva et al.*, 1996]. Samples #C045, #C093, and #C098 (siltstones) contain the assemblages of *Nannoconus spp.* (narrow canal), *Nannoconus colomii*, and *Nannoconus steinmannii* that are indicative of Berriasian-Barremian ages. Preservation of the nannofloras in the clasts was poor to moderate. Nannofossils in the matrix are of Late Jurassic to Cretaceous as well as middle Miocene age (Table B.2). The MHMV ejecta thus include older nannofossils than those found in the Cobblestone and Pan di Zucchero mud volcano fields in the western MedRidge or in the Olimpi mud volcano field in the central MedRidge [e.g., *Premoli Silva et al.*, 1996; *Robertson and Ocean Drilling Program Leg 160 Scientific Party*, 1996].

3.4.2 Vitrinite reflectance

Vitrinite, a type of coal maceral, increases systematically in reflectance through the decomposition of organic material and has found widespread use in oil and gas exploration. Because vitrinite reflectance is highly sensitive to peak temperature and duration of heating and is unaffected by retrograde reactions, it has been used as a geothermometer to constrain the signature of frictional heating within natural fault zones [e.g., *Bustin*, 1983; *O'Hara*, 2004; *Sakaguchi et al.*, 2007, 2011] and in laboratory shear experiments [e.g., *O'Hara et al.*, 2006; *Kitamura et al.*, 2012] as well as to estimate received maximum temperatures in accretionary prisms [e.g., *Ohmori et al.*, 1997]. Vitrinite reflectance has also been used to investigate maximum temperatures of mud volcano ejecta [e.g., *Schulz et al.*, 1997; *Kopf et al.*, 2000; *Muraoka et al.*, 2011]. Most of these studies, however, have notable uncertainties in the derived thermal histories of ejecta, partly because the thermal structure below the seafloor for an inverse calculation of maximum temperature from vitrinite reflectance is not well determined. In order to obtain consistent temperature information for estimating time-temperature paths, we calculated a model of the current thermal structure in the target domain as described in the next Section.

Vitrinite reflectance Ro is calculated by an empirical relationship that is calibrated using the H/C and O/C atomic ratios of coals:

$$\mathrm{Ro} = \mathrm{Ro}^0 \exp(3.7F), \tag{3.1}$$

where Ro^0 is the vitrinite reflectance at the surface (assumed to be 0.20%) and F is the overall extent of parallel chemical reactions driving off of H, C and O in the form of H_2O, CO_2 and CH_n [*Sweeney and Burnham*, 1990]. Values of Ro from vitrinite macerals within a clast represent the degree of thermal maturation resulting from its time-temperature history. Using this kinetic model, vitrinite reflectances in the range of 0.3–4.5% and for heating rates in the range of 10^{-15} to 10^{-5} K/s can be precisely calibrated, which covers most geologic situations except for the case of rapid slip generating large frictional heating. In the case of our matrix samples from MHMV, we used the empirical relationship of *Barker and Pawlewicz* [1986] based on more than 600 data pairs of Ro and maximum temperature $T_{\max}$, because the wide age range of the matrix shown by nannofossil analysis precludes using the kinetic model of *Sweeney and Burnham* [1990]. The relationship between Ro and $T_{\max}$ is expressed as

$$\ln(\mathrm{Ro}) = 0.0078 \times T_{\max} - 1.2. \tag{3.2}$$

Barker and Goldstein [1990] suggested that maximum temperature experienced, rather than the time at that temperature, is the major control on thermal maturation within general problems based on the relationship similar to *Barker and Pawlewicz* [1986]. Thus, the maximum temperature of the matrix can be closely constrained even though its thermal history is indeterminate.

In this study, vitrinite reflectance was measured using a Vitrinite Reflectance Microscope Analyzer [*Sakaguchi et al.*, 2011; *Sakaguchi and Mukoyoshi*, 2012]. To avoid excessive heating in the laboratory, care was taken during all drying and polishing procedures not to exceed 40°C. Most clast samples measured in this study have small numbers of vitrinite particles, so the random mean vitrinite reflectance (Ro) was obtained by measurement of as many vitrinite particles as possible in the selected slab. The measured vitrinite particles were well characterized under the optical microscope, and inertinite and vitrinite group macerals were readily distinguished under surface scanning [e.g., *Sakaguchi et al.*, 2007] (Figure B.4). Some reworked coal fragments were observed in matrix and clasts; they have round or trapezoidal shapes as well as high reflectance. These were used to determine vitrinite reflectance. The coexistence of partly bituminized coal and low-grade brown coal indicates that the material had not experienced diagenetic gelification.

Vitrinite reflectance is subject to error for individual particles, because vitrinite is an anisotropic and bireflectant material, and the system used in this study cannot be used to investigate polarization anisotropy. Our reflectance data therefore may have errors within $\pm 0.01\%$ if Ro $< 2.0\%$ as the magnitude of the anisotropy is generally influenced by sediment compaction and increases at higher Ro.

3.4.3 Thermal model

We use 2-D finite element code developed by *Wang et al.* [1995] to develop a steady-state thermal model for the western MedRidge along the MEDRIFF corridor (Figure 3.1) constrained by some heat flow measurements [*Erickson*, 1970; *Della Vedova et al.*, 2003]. The steady-state approximation is reasonable because the thermal state of the very old subducting plate is not expected to change with time significantly and because the overriding plate is less than 15 km thick and accordingly has a thermal time constant of less than two million years. Even at the Nankai subduction zone where the age of the young incoming plate changes with time, the difference between temperature regimes predicted by time-dependent and steady state models is very small [*Wang et al.*, 1995]. The model is based on the following heat transfer equation:

$$\nabla \cdot (k\nabla T) - \rho c\mathbf{v} \cdot \nabla T + Q = 0, \tag{3.3}$$

where T is temperature, k is the thermal conductivity, ρc is volumetric thermal capacity, $\mathbf{v}$ is velocity, and Q is the heat production which includes heat generated by radiogenic elements and in the rock volume and by frictional heating along the plate interface. The velocity $\mathbf{v}$ is nonzero only in the part of the model that represents the subducting plate.

The structure and mesh of our model are illustrated in Figure 3.4. One of the main controls on the thermal regime is provided by the thermal state of the incoming Nubia plate, prescribed as temperatures along the seaward vertical boundary of the model. As is well known from modern heat flow observations that for plates older than about 80 Ma, heat flow no longer decreases with increasing plate age, and the geotherms of very old plates can be modeled using a model of steady-state one-dimensional (1D) heat conduction in a 95 km thick lithosphere with a basal temperature of 1450°C [*Stein and Stein*, 1992]. Because the age of the incoming Nubia plate is as old as 200–250 Ma, as inferred from the synthetic isochron model of [*Müller et al.*, 2008] and forward magnetic modeling [*Speranza et al.*, 2012], it is appropriate to use this 1D model to obtain the temperature profile of our seaward model boundary. However, to account for the presence of thick evaporitic layers overlying the incoming plate, we include a lower thermal conductivity (2 W/m/K) layer on top of the higher-conductivity (3 W/m/K) plate. The blanketing effect of this low-conductivity sedimentary layer makes the plate slightly warmer. Because the recent sedimentation rate is relatively low, the transient cooling effect of sediment deposition [e.g., *Wang and Davis*, 1992] can be ignored. The horizontal heat flow across the landward boundary is assumed to be zero. The upper boundary is assigned the seafloor temperature at its recent value of 14 ± 2°C on the basis of temperature observations [e.g., *Emeis et al.*, 1996; *Della Vedova et al.*, 2003]. Because the geotherms of the seaward boundary is efficiently advected through the horizontal length of the model domain by the slab, model

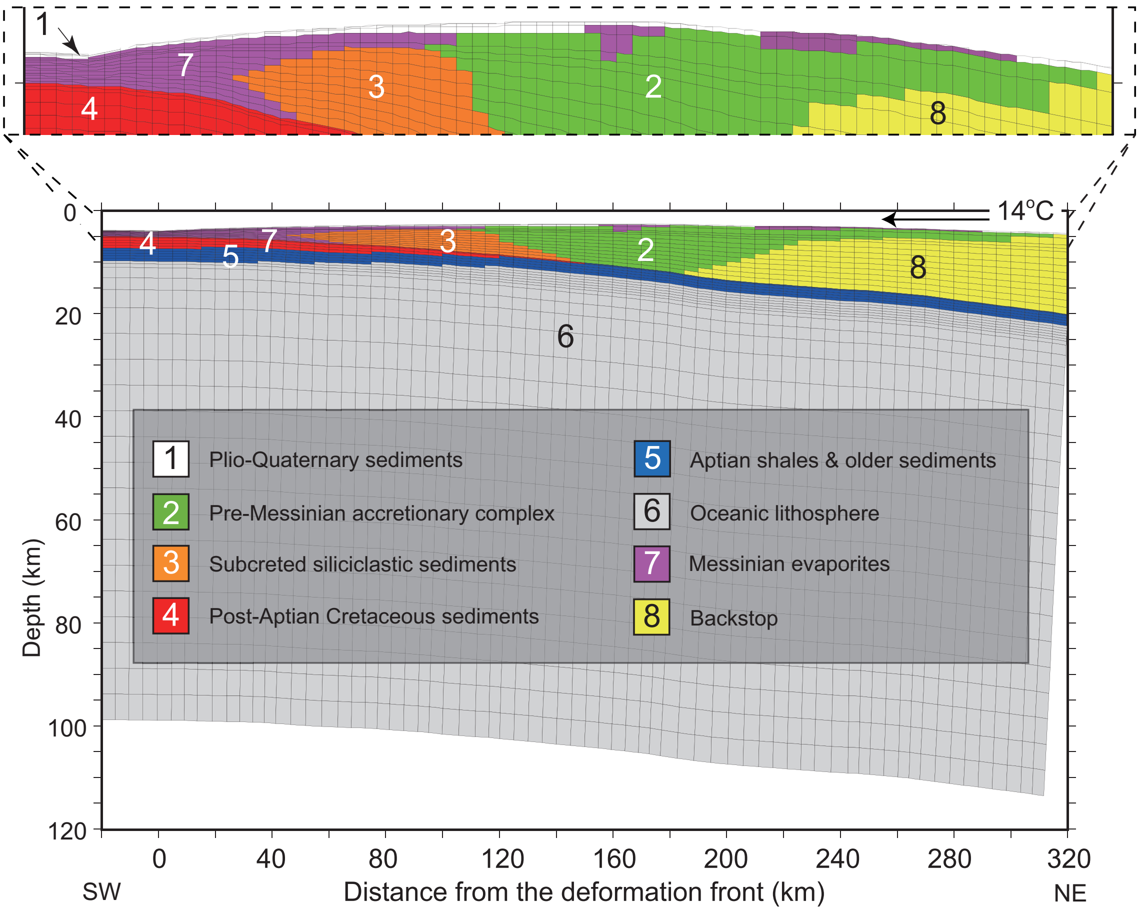

Figure 3.4: Finite element mesh and geological structure of the thermal structure model. Each roughly rectangular element shown has either nodes, with one on each corner and one in the middle of each side of the element. Thermal parameters for each shown lithological units are given in Table 3.2.

results are not sensitive to the boundary condition (temperature 1450°C) assigned to the bottom of the 95 km thick slab.

The finite element mesh of our model extends from 20 km seaward to 320 km landward of the deformation front (Figure 3.4). The mesh geometry was constrained by multichannel seismic reflection and refraction surveys as well as cross-section interpretation along the MEDRIFF and IMERSE (International Mediterranean Ridge Seismic Experiment) corridor [*Fruehn et al.*, 2002; *Reston et al.*, 2002a, b; *Westbrook and Reston*, 2002]. The mesh contains 3196 eight-node elements (9819 nodes) in 48 rows and 69 columns. The overriding plate part contained 15 rows of elements, and the subducting sediment and oceanic lithosphere part contained 33 rows of elements. The margin mesh consists of eight layers

Table 3.2: Thermal parameters used in this study.

Layer	Lithology	Thermal Conductivity k (W/m/K)	RHP Q (μW/m^3)	Thermal Capacity ρc (MJ/m^3/K)
1	Upper sediments	1.0 [a]	1.5 [f]	2.5 [c]
2	Accretionary wedge	1.9 [b]	1.5 [f]	2.5 [c]
3	Subcreted sediments	2.2 [b]	1.5 [f]	2.5 [c]
4	Lower compacted sediments	2.5 [b]	1.5 [f]	2.5 [c]
5	Aptian shales/Older Mesozoic	3.0 [b]	2.0 [g]	2.5 [c]
6	Oceanic lithosphere	2.9 [c]	0.02 [c]	3.3 [c]
7	Messinian evaporates	5.0 [d]	0.01	2.5
8	Backstop	2.8 [e]	1.8 [h]	2.5 [c]

[a] *Della Vedova et al.* [2003].
[b] *Beardsmore and Cull* [2001]; *Clauser and Huenges* [1995]; *Turcotte et al.* [1978].
[c] *Heasler and Surdam* [1985]; *Hyndman et al.* [1995]; *Van den Beukel and Wortel* [1988].
[d] *Wheildon et al.* [1974].
[e] *Barker* [1996]; *Drury* [1986]; *Roy et al.* [1981].
[f] *Hyndman et al.* [1995]; *Yamaguchi et al.* [2001].
[g] *Hyndman et al.* [1995]; *Pasquale et al.* [2001]; *Taira et al.* [1991].
[h] *Miyake et al.* [1975].

following the cross-section interpretation along the MEDRIFF/IMERSE corridor: (1) uppermost sediment layer; (2) pre-Messinian accretionary wedge; (3) underplated sediment; (4) pre-Messinian Tertiary sediment, post-Aptian Cretaceous sediment and lower compacted sediment; (5) subducting Aptian shale and older Mesozoic sediment; (6) oceanic lithosphere; (7) Messinian evaporite layer; and (8) backstop segments. Each model element was assigned a uniform thermal conductivity, heat capacity, and radioactive heat production (RHP) rate (Table 3.2). Parameter values listed in Table 3.2 are based on several previous studies (see Section B.1).

3.5 Results

3.5.1 Vitrinite reflectance and estimate peak temperatures

We measured vitrinite reflectances in 49 clast samples and 12 matrix samples. These results are plotted in Figure 3.5 and summarized in Tables B.3 and B.4. The mean Ro of random matrix samples ranged from 0.5% to 0.7%, and the Ro values of clast samples are scattered from 0.35% to 1.29%. Whereas shale samples have Ro values of $0.59 \pm 0.15\%$, which are close to those of matrix samples, other mudstone samples have relatively high Ro values of $1.04 \pm 0.15\%$.

The distribution of vitrinite reflectance within matrix samples shows a unimodal pattern with a mean of 0.5–0.7% and a few higher values (Figure 3.5c). Clast samples with Ro $>$ 1.0% imply that vitrinite from high-Ro matrix (Ro $>$ 0.8%) in the histograms was mostly not reworked. The mixture of lower-value peaks with high-reflectance outliers suggests that the matrix ascended with fluid-rich mud incorporating deeper materials or terrigenous sediment with high reflectance. Because the matrix samples from MHMV have a wide age range, from Berriasian to Miocene, it is infeasible to obtain a reasonable thermal history with the kinetic model of *Sweeney and Burnham* [1990]. Hence, we prefer the empirical relationship of *Barker and Pawlewicz* [1986] for matrix samples (equation 3.2). Given that Ro values of the matrix were 0.5–0.7%, the peak temperature $T_{\max}$ value of matrix was calculated to be 65–108°C.

Clasts have a wide range of vitrinite reflectance, suggesting a variety of thermal histories. Thus we simulated $T_{\max}$ values from time-temperature paths based on the kinetic formulation of *Sweeney and Burnham* [1990] to quantify the effects of different scenarios of temperature increase. Here, our time simulations were based on the assumption of subduction under steady sate plate motion of 40 mm/yr, because the Nubian-Aegean convergence rate is estimated to have been 30–40 mm/yr since 13 Ma [e.g., *Le Pichon et al.*, 1995]. Other detailed scheme and descriptions are found in Section B.2. These assumptions result in almost the same values of $T_{\max}$ for a given Ro value in our model. The Ro values of shale yielding 0.44%, 0.59%, and 0.74% resulted in the $T_{\max}$ values of 82 ± 4°C, 108 ± 3°C, and 134 ± 3°C, respectively. The Ro values of other mudstone including 0.89%, 1.04%, and 1.19% resulted in the $T_{\max}$ values of 153 ± 3°C, 164 ± 3°C, and 173 ± 3°C, respectively.

3.5.2 2-D Thermal structure

The largest sources of uncertainties in the thermal model are from the plate convergence rate, effective coefficient of friction (μ'), and RHP rate. We tested model sensitivity to

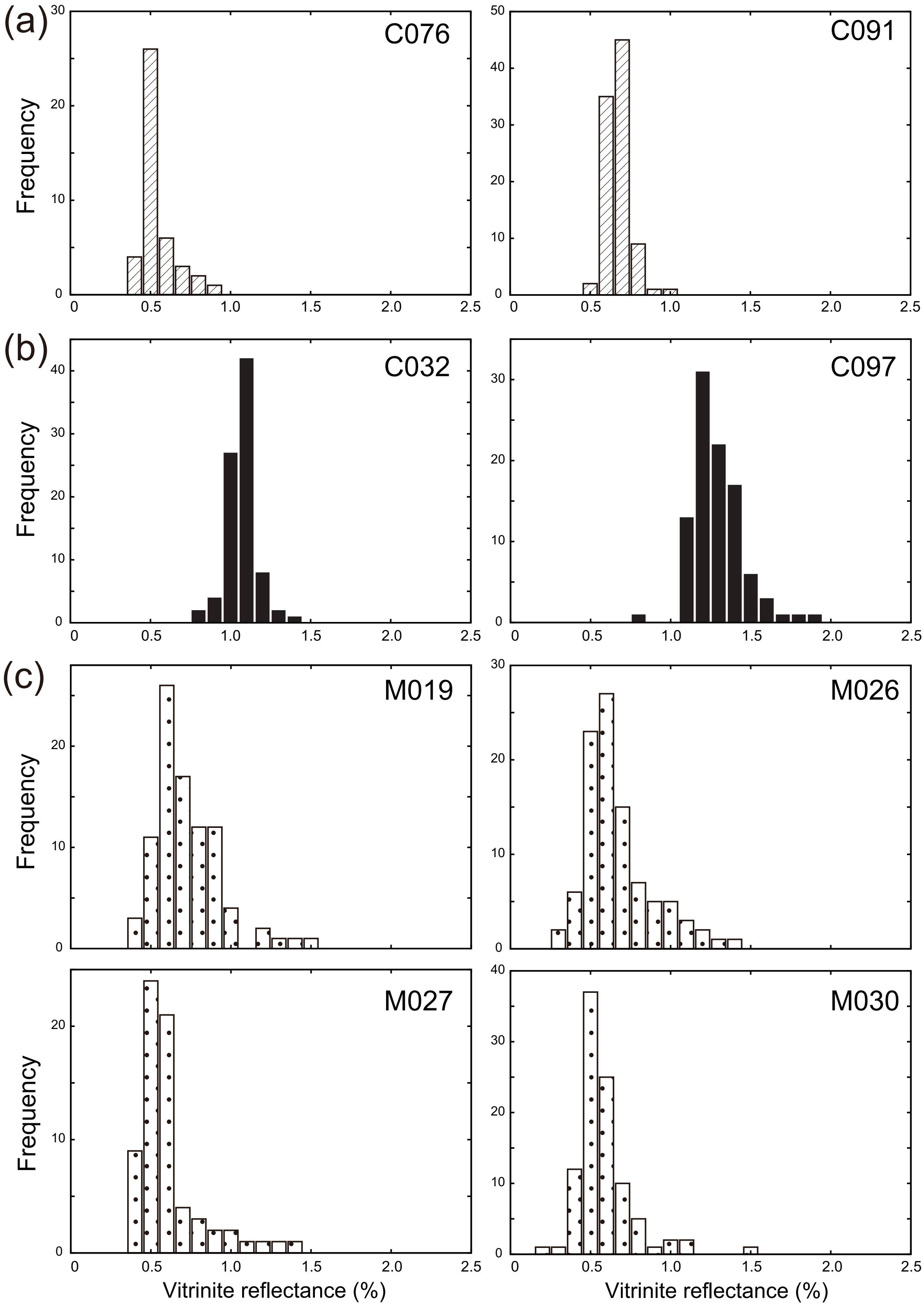

Figure 3.5: Examples of vitrinite reflectance measurements of (a) shale, (b) siltstone/claystone and (c) matrix samples.

Table 3.3: Sensitivity tests and their results in terms of maximum difference in calculated surface heat flow and temperature along the plate interface.

Parameter	Heat Flow	Plate Temp.*
μ' (0.00–0.05)	10 mW/m^2	32 K
RHP rate (1.0–3.0 μW/m^3)	11 mW/m^2	13 K
Plate velocity (10–50 mm/yr)	7 mW/m^2	34 K

* At 200 km landward of deformation front.

these parameters by imposing reasonable variations as listed in Table 3.3. When one of the parameters was varied for testing purpose, all other parameters remained unchanged (Figure 3.6). In our sensitivity check for μ', the calculated surface heat flow fluctuated by up to 10 mW/m^2 between $\mu' = 0.00$ and $\mu' = 0.05$. In the case of the RHP rate, maximum uncertainties in calculated surface heat flow and temperature along the plate interface about 200 km from the deformation front were less than 11 mW/m^2 and 13 K, respectively. The sensitivity test yielded only minor differences with varying plate velocity, such that the lack of a very reliably determined subduction rate of the MedRidge is not of major concern for the purpose of this work (Table 3.3). The minor differences in thermal structures at different plate convergence velocities would be derived from small vertical convection due to the low taper angle of the wedge.

Based on the estimated heat flow and heat-flow observations from MEDRIFF and other projects [*Erickson*, 1970; *Della Vedova et al.*, 2003], the effective coefficient of friction μ' is no more than 0.01 or 0.02. The relation between μ' and the intrinsic friction coefficient of the fault μ is $\mu' = \mu(1 - \lambda)$, where λ is the ratio of pore fluid pressure along the fault and normal stress, approximately the lithostatic pressure for the shallowly dipping subduction fault. Thus, based on commonly used intrinsic rock friction values [e.g., *Byerlee*, 1978], fluid pressure on the plate interface appears to be more than 95% of lithostatic. If the intrinsic friction coefficient is lower because of weak fault gouge, the fluid pressure should be correspondingly lower.

The modeled thermal regime cannot be constrained by heat flows derived from bottom-simulating reflectors (BSRs). Unlike the Nankai Trough [e.g., *Yamano et al.*, 1982; *Ashi et al.*, 2002], BSRs are mostly absent in the MedRidge partly because of the presence of

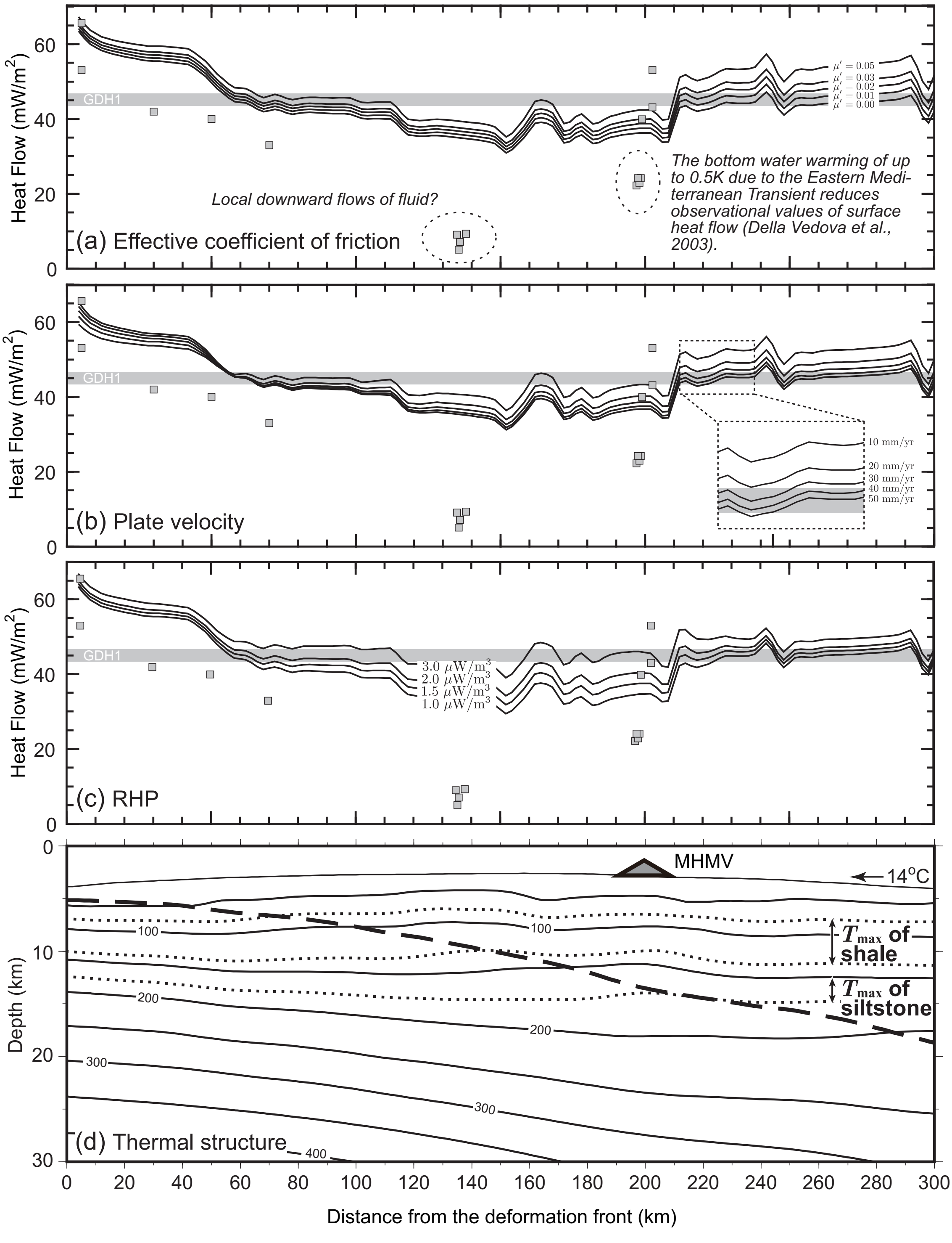

Figure 3.6: (*Continued on the following page.*)

Figure 3.6: (*Preceding page.*) (a) Calculated surface heat flow profiles along the MEDRIFF/IMERSE corridor in the western MedRidge (location in Figure 3.1) for different values of the effective friction coefficient ($\mu' = 0.00$ to 0.05) but fixed RHP rate of 1.5 μW/m^3 at layers 1–4 and subduction rate $v = 40$ mm/yr. Rectangular symbols show observed heat flow data along the corridor [*Erickson*, 1970; *Della Vedova et al.*, 2003], which contain very large uncertainties as discussed in the text. (b) Calculated surface heat flow profiles for different values of subduction rate ($v = 10$ to 50 mm/yr) but fixed effective coefficient of friction $\mu' = 0.01$ and RHP rate of 1.5 μW/m^3 at layers 1–4. (c) Calculated surface heat flow profiles for different values of the RHP rate at layers 1–4 (1.0 to 3.0 μW/m^3) but with other parameters fixed at the values in Table 3.2. (d) Two-dimensional thermal structure along the MEDRIFF/IMERSE corridor based on the parameter settings summarized in Table 3.2 and using an effective coefficient of friction $\mu' = 0.01$ and a plate convergence $v = 40$ mm/yr. The broken line represents the plate interface. The ranges of estimated peak temperatures of shale and other mudstone samples are also presented.

rather impermeable Messinian evaporites [e.g., *Camerlenghi and Pini*, 2009]. Assessing the reliability of the modeled thermal structure is hampered by the large uncertainty of the observed heat-flow data and the absence of BSRs. We assigned an uncertainty of < 15°C to the temperature along the plate interface within 200 km of the deformation front. We then used the thermal structure shown in Figure 3.6 to explore the possible ascent mechanisms of MHMV based on the results of vitrinite reflectance.

3.6 Discussion

3.6.1 Does the extrusion of MHMV demonstrate underplating at the wedge-backstop contact?

In the central MedRidge, several studies have used vitrinite reflectance of mud volcano ejecta to investigate the source depths of the ejecta. *Schulz et al.* [1997] used vitrinite reflectance data from Napoli dome in the Olimpi mud field to suggest derivation from the depth of the décollement zone and its surroundings at 4.9–7.5 km below the seafloor (kmbsf). *Kopf et al.* [2000] assigned a depth of ~2 km to the source of Milano mud volcano in the Olimpi field on the basis of low vitrinite reflectance values indicating that both clasts and matrix were not subjected to elevated temperature. These ejecta ranged in age from late Pliocene to late Pleistocene and were mixed with Miocene sediments that probably originated from upper sedimentary sequences or pre-Messinian parts of the accretionary wedge. In the western MedRidge, *Ryan et al.* [1982] assigned the origin of mud volcanism in the Cobblestone field (Figure 3.1) to the expulsion of mud from the downgoing slab through an accretionary complex.

Early Cretaceous mudstone clasts in MHMV ejecta had higher Ro values ($1.04 \pm 0.15\%$) than matrix samples, whereas shale clasts of Aptian age had Ro values ($0.59 \pm 0.15\%$) similar to the matrix. Several proposed thermal histories of shale and other pre-Aptian mudstones, based on simple estimation by kinetic simulations tested in Section 3.5.1, suggest that these clasts experienced higher temperatures than the matrix and hence were buried deeper before their ascent to the seafloor. On the other hand, the Ro values from matrix samples had a wide range and unimodal distributions with a lower average, consistent with generation in a fluid-rich environment within the accretionary wedge. Given that the matrix from MHMV ejecta experienced peak temperatures of 65–108°C based on the empirical relationship, the source of fluid-rich mud ejecta is probably from the corresponding depth of about 5 kmbsf (the error range is 3.3–5.9 kmbsf) at the distance of 150–180 km from the deformation front, based on the thermal structure (Figure 3.6d). These considerations are relevant to the question of where the fluids originated in sufficient volume to mobilize the ejecta of MHMV.

The presence of Aptian shale underlain by post-Aptian sediment in an accretionary complex has been explained as the result of underthrusting above oceanic crust in the western MedRidge [*Reston et al.*, 2002a]. Peak temperatures $T_{\max}$ experienced by the Aptian shale (108 ± 30°C) approximately correspond to temperatures around the depth of the present dcollement or ~1–2 km above the décollement at the distance of 150–180 km from the deformation front in our thermal structure (Figure 3.6d). Sediments there should be undergoing dehydration and yielding fluids, as in other subduction zones [e.g., *Bethke*, 1986; *Moore and Vrolijk*, 1992; *Bekins et al.*, 1994], and likely causing a fluid-rich condition. Considering the relatively high basal friction at the interface beneath MHMV, this subducting shale was presumably offscraped by the backstop buttress accompanying duplex formation and consequently uplifted by massive underplating beneath the accretionary wedge. Previous experiments [*Gutscher et al.*, 1996, 1998; *Kukowski et al.*, 2002] have suggested that the formation of basal duplexes beneath the buttress followed by a step up from a décollement can be observed, and these conditions are satisfied near the crest of the MedRidge. Our study suggests that the pre-Aptian mudstone and limestone were underplated from underthrusting sediments or were detached from the indurated crystalline backstop, which is likely composed of indurated limestone and a flysch series [e.g., *Le Pichon et al.*, 2002]. The high densities of the clasts from MHMV are consistent with this scenario, as accretion of material to the underside of the wedge by underplating gives rise to higher pressure conditions. Moreover, underplating of the prism may contribute to structural thickening and uplift of the accretionary complex on the MedRidge crest and consequently contribute to slope steepening toward a critical taper angle [e.g., *Davis et al.*, 1983].

3.6.2 Was the ascent of MHMV ejecta diapiric?

Mud volcanism is typified by several types of mud ascent, including diapiric ascent, conduit ascent (i.e. through existing openings), and hydrofracture ascent [e.g., *Kopf*, 2002], but few studies have addressed this topic. If ascent took place through hydrofractures, for example, these features will be young or are held open by fluid replenishment from depth. In this section we evaluate the possibility that MHMV ejecta ascended as diapirs from the depth of ∼5 kmbsf. We assume that the fluids of interest are homogeneous in each of two fluid domains: a mud chamber and the surrounding accretionary wedge (Figure 3.7). Assuming Stokes flow, the velocity of flow (upward or downward) is proportional to the density difference between different fluid domains, the square of radius and the reciprocal of viscosity. The condition for a diapir to rise faster than the clasts in it can settle, assuming Stokes law behavior, can be described as

$$V_d/V_{xl} = (r_d/r_{xl})^2(\Delta\rho_d/\Delta\rho_{xl})(\eta_{mc}/\eta_{ap}) > 1, \tag{3.4}$$

where V_d is the absolute ascent velocity of the diapir, r_d is the radius of the diapir, V_{xl} is the absolute settling velocity of a clast, r_{xl} is the radius of a clast, $\Delta\rho_d$ is the density difference between the diapir and the accretionary prism, $\Delta\rho_{xl}$ is the density difference between a clast and the mud chamber, and the ratio η_{mc}/η_{ap} is the viscosity of the mud

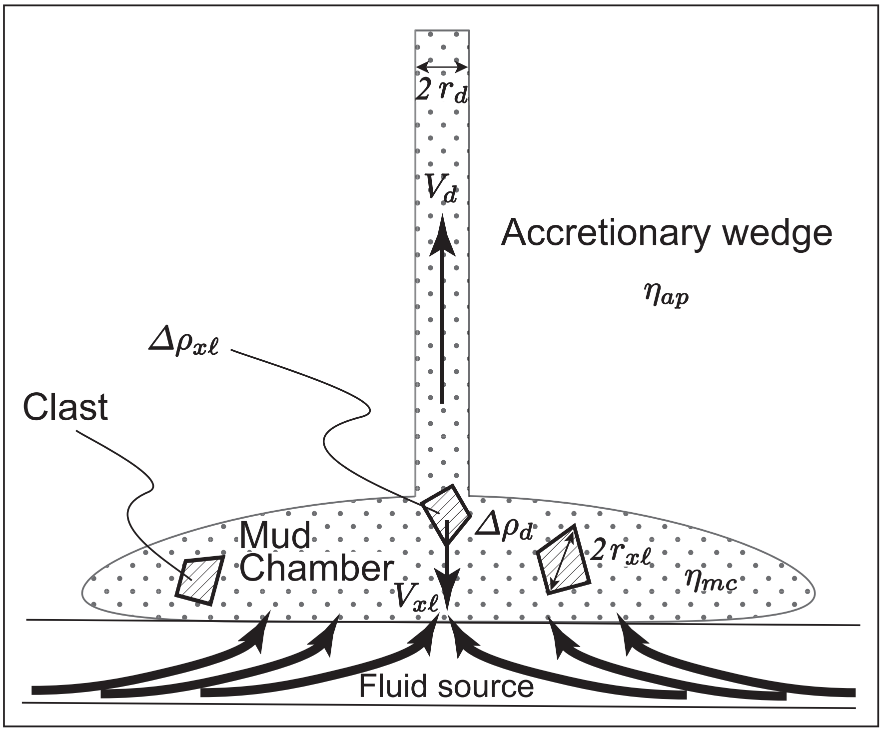

Figure 3.7: Schematic illustration of mud diapir (see text).

chamber relative to that of the accretionary prism (Figure 3.7). This formulation is a modified version of treatment of diapiric ascent occurring in the mantle [*Anderson*, 1981]. Here Corey's shape factor (CSF) [*Corey*, 1949] is not considered because the CSFs of all MHMV ejecta cannot be determined, although settling or ascent velocity is influenced by the shape and roundness of the particles as well as the density and viscosity of the fluid [e.g., *Dietrich*, 1982; *Jiménez and Madsen*, 2003].

Kopf and Behrmann [2000] estimated representative feeder diameters for mud diapirs in the central MedRidge of 2–3 m using Stokes law into Milano mud volcano (body slope ∼5°) and Napoli mud dome (∼6°) (slope values from *Camerlenghi et al.* [1995]). However, *Kopf* [2002] considered that the feeder of a mud volcano with a gentler slope, such as MHMV (∼3°), would be slightly wider. The density differences involved are comparable, whether they are between the diapir and the accretionary prism or between clasts and the diapir. The ejecta from MHMV suspended clasts up to 62 mm in diameter (see Section 3.4.1). Thus, taking a diapir radius $r_d = 10$ m, $r_{xl} = 3$ cm, and $\Delta\rho_d/\Delta\rho_{xl} \sim 1$, we have

$\eta_{ap}/\eta_{mc} < 1.2 \times 10^5$. The viscosity of the accretionary prism η_{ap} has been reported to be 10^{19}–10^{21} Pa·s based on its geometry and heat flow [e.g., *Emerman and Turcotte*, 1983; *Platt*, 2000], or 10^{16}–10^{19} Pa·s at 200–300°C [*Shimizu*, 1995]. Assuming $\eta_{ap} \sim 10^{16}$ Pa·s, a mud viscosity of $\eta_{mc} > 8.3 \times 10^{10}$ Pa·s is required to suspend rocks and avoid fractionation of the diapir while it ascends. Viscosity of the mud chamber or diapir η_{mc} is known to be less than 10^5–10^6 Pa·s [*Kopf and Behrmann*, 2000; *Manga et al.*, 2009] even though the water content of a mud diapir is relatively small [*Manga et al.*, 2009; *Rudolph and Manga*, 2010]. Therefore, the possibility that clasts can ascend in a diapir from a depth of ∼5 kmbsf can be confidently rejected because reasonable physical properties cannot satisfy equation (3.4), whereas an ascent style controlled by diapiric flows or the presence of gases in the uppermost several hundred meters below the seafloor, where the surrounding viscosity is sufficiently low, cannot be rejected.

3.6.3 Was the ascent of MHMV ejecta motivated by faulting after underplating?

Having ruled out the ascent of clasts from ∼5 kmbsf in diapirs, we can evaluate the possibility of ascent in major conduits along faults. The dome-shaped Lich mud volcano, 150 km landward of the deformation front in the central MedRidge, has been found to overlie an active backthrust at about 500 mbsf in seismic reflection data [e.g., *Kopf et al.*, 2001]. Core samples from MHMV show that the ejecta flowed in the style of a debris flow, and thus its flow dynamics probably followed Herschel-Bulkley behavior [e.g., *Manga and Bonini*, 2012] or (yield-)dilatant rheology [e.g., *Nguyen and Boger*, 1992; *Manga et al.*, 2009]. Although we have no evidence of active faulting beneath MHMV, it can be inferred from bathymetric data that a relatively active backstop thrust coupled with right-lateral strike-slip lies between MHMV and Médée brine lake (Figure 3.2). We cannot confirm that MHMV ejecta actually ascended through the backthrust, but the highest vitrinite reflectance values from matrix samples (> 1.3%; Figure 3.5c) are consistent with frictional heating during faulting slip [e.g., *O'Hara*, 2004; *Sakaguchi et al.*, 2007] without contradicting the deep origin of the vitrinite. Thus, we assumed that clasts ascended in fluid-rich mud accompanied by reactivation of the existing backthrust. The stress ratio at angle θ

for frictional reactivation under pore fluid pressure p_f is given by

$$\sigma_1'/\sigma_3' = \left[\sin 2\theta + \mu(\cos 2\theta + 1)\right] / \left[\sin 2\theta + \mu(\cos 2\theta - 1)\right], \tag{3.5}$$

where σ_1' and σ_3' are the effective maximum and minimum stresses, respectively, and μ is the coefficient of friction [e.g., *Sibson*, 1985]. In the accreted sequence, the vertical effective stress σ_v' is interpreted as the effective minimum stress σ_3'. Given that the backthrust in the Médée region has a dip of ~10° and that the coefficient of friction μ is around 0.4–0.5, the pore pressure is estimated from

$$p_f = \sigma_v - \sigma_v' > \sigma_v - \sigma_3' , \tag{3.6}$$

where σ_v indicates vertical confining stress. Note that we assume the differential stress $(\sigma_1' - \sigma_3')$ to be less than 120 MPa. The corresponding pore pressure would be no less than 80 MPa at depths of ~5 kmbsf within the area where the backthrust developed. When the backthrust is not moving, its fine-grain fault gouge retards fluid escape and causes overpressure. Thus, when the fault slips, overpressured mud would bring clasts from depths as rapidly as >1 m/s to transport the largest clasts to the seafloor [e.g., *Manga and Bonini*, 2012]. The fluid responsible for this high pore pressure would originate from underplating of fluid-rich sediments and the dewatering of backstop rocks as described above (Figure 3.8). During episodes of fault slip, ejecta migrated through the fault to the seafloor, possibly behaving as a dilatant fluid. As a result of the rapid deformation at the depth of the fluid source (~5 kmbsf) intrinsic to compacted granular materials, the dilatant fluid (i.e. ejecta) became more viscous and thus its mobility increased.

Various studies point to the recent activities of mud eruptions. These studies were guided by observations of clast-poor, mousy, and very soft mud such as in Napoli mud volcano of the central MedRidge. In Milano mud volcano in the central MedRidge, early stages of mud volcano activity produced clast-rich ejecta whereas later stages produced fine-grained materials [e.g., *Robertson and Ocean Drilling Program Leg 160 Scientific Party*, 1996]. These observations are well-explained by a process of cleaning up a fault conduit by the extrusion of mud breccia in the early stages of the activity. *Chamot-Rooke*

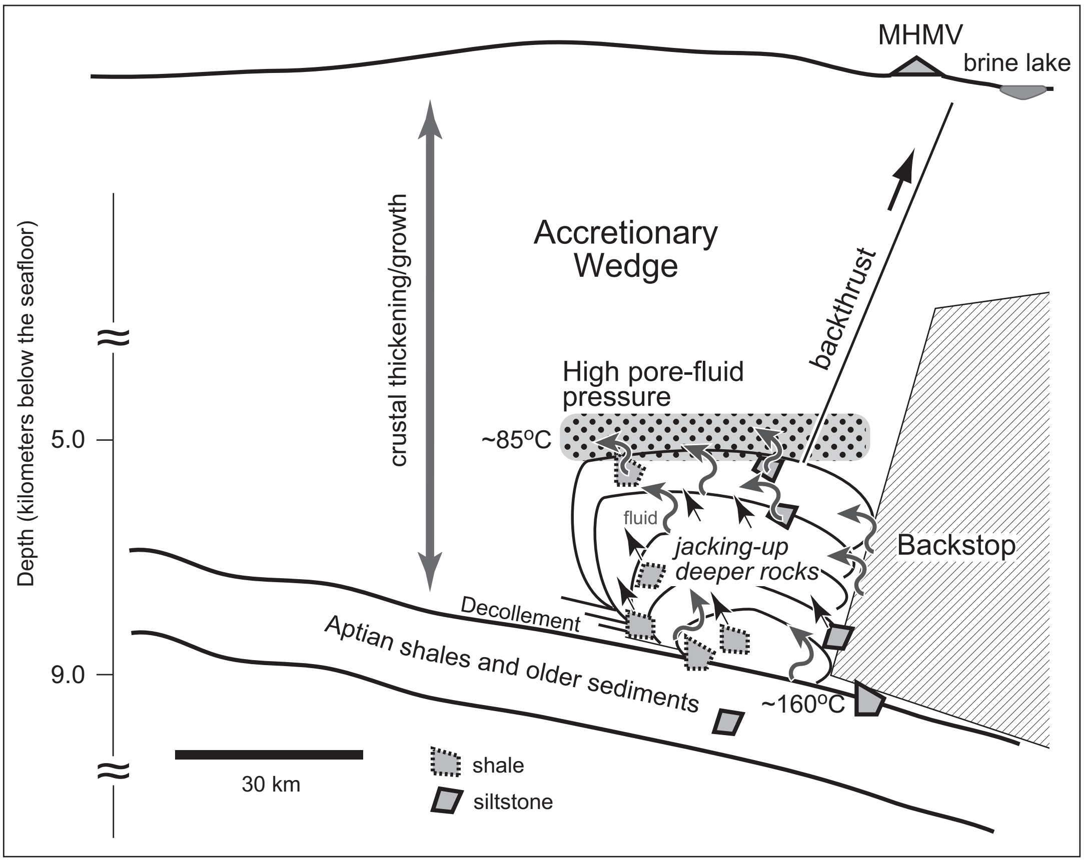

Figure 3.8: Schematic illustration of the mechanism of ejecta ascent to MHMV.

et al. [2005a] attributed the strong backscattering seen at MHMV during the 1995 Médée Cruise to a recent eruption of mud breccia without hemipelagic cover sediment. But, video observations around the summit of MHMV by ROV NSS showed clasts scattered on the seafloor (Figure 3.3). In addition, cores NSS-PC02 and NSS-PC03 from the summit of MHMV contain large clasts in their uppermost 8 cm (Figure B.3). These observations suggest that the latest massive eruption occurred as late as within the last couple of thousand years, because otherwise the clasts would have time to sink back into the conduit, given their known settling speed. Moreover, MHMV is now likely to be in the early stage of its mud volcanism based on the observed features in the central MedRidge. All in all, the scenario of fault slip and subsequent mud eruption of MHMV must have occurred relatively recently. The neighboring Médée brine lake may have formed at the same time.

The Hellenic subduction zone is seismically most active in Europe [e.g., *McKenzie*, 1972]. Considering the age of the latest massive mud eruption at MHMV, some well-known historical M $>$ 8 Crete earthquakes could be the possible triggering events for the mud eruptions. The MHMV is located in a distance of <200 km from the inferred hypocenter of the AD 365 earthquake [e.g., *Shaw et al.*, 2008] and <500 km from that of the AD 1303 earthquake [e.g., *Papadopoulos et al.*, 2007]. Empirical scaling between the magnitude and hypocentral distance of the earthquakes that possibly trigger eruptions of mud volcanoes [*Mellors et al.*, 2007; *Manga et al.*, 2009] allows these earthquakes to be candidates potentially responsible for triggering the massive eruption of MHMV.

3.7 Conclusion

In this study, we investigated the source depth and ascent style of the sediment making up MHMV, which lies at the wedge-backstop contact in the western MedRidge, using vitrinite reflectance data, lithology, and biostratigraphy of clasts combined with a thermal structure model for the western MedRidge.

We propose that MHMV documents underplating around the wedge-backstop contact above the décollement, because its ejecta contain shale of Aptian age and other older mudstone clasts with high vitrinite reflectance and strong induration, although some samples may have been reworked. The vitrinite reflectance data and thermal structure model suggest that the ejecta came from a source deep enough to have been buried near the décollement. In our proposed model for MHMV, the underplated sediment was uplifted after being offscraped against the backstop, and it consequently produced overpressures at a depth of about 5 kmbsf and temperatures around 85°C, as suggested by the vitrinite reflectance values of the ejecta matrix ($\sim$0.6%). High pore pressure, arising from fluid generation by the underplating and compression between the wedge and backstop as well as mineral dehydration, appears to have subsequently promoted slip on a nearby fault. Fluid-rich mud and clasts derived from the region of underplating acquire sufficient shear stress to promote its ascent through the fault conduit during fault slip events. A brine lake ponded near MHMV may have accumulated from the ascent of hypersaline water derived from Messinian evaporites in conjunction with slip episodes on the backstop thrust, consistent with the faulting-motivated ascent of MHMV ejecta along the backstop thrust or parallel thrusts.

We derived a 2-D thermal structure across the western MedRidge. Despite uncertainties due to limited observational constraints, the model serves to compensate for the paucity of deep drilling data and the poorly known convergence velocity. Although our thermal structure model can be further improved by future drilling data, the preliminary results help constrain the thermal regime and advance understanding of the western MedRidge.

3.8 Connection to other chapters

This chapter will be summarized as: (1) ejecta from a submarine mud volcano in the Mediterranean Ridge accretionary complex shed new light on ascent mechanism, (2) thermal history of the ejecta is estimated using vitrinite reflectance technique and new 2-D thermal model, and (3) results suggest two-fold ascent mechanism: underplating and subsequent faulting. This chapter documents fundamental geological constraints on ejecta ascent of submarine mud volcanoes through massive mud eruptions, and thus is strongly connected to Chapter 2. Specifically, the results presented in this chapter provides depths and thermal information of source of large amounts of sediment and fluid, which delineates dynamic material cycling between the seafloor and deep depths. The ascent mechanism can be thus utilized as primary constraints on subsurface sediment transfer and fluid migration through submarine mud volcanism. As will be discussed more in Chapter 4, this work will served as a tie between ascent mechanism and gas amounts of submarine mud volcanoes, because the high-speed ascent reprerented here is perhaps linked to the gas amount in the ejecta path as discussed in this chapter. Major fluid discharge is likely transfered by ejecta ascent, while the ascent has a variety of its mechanism as presented in this chapter. This variation may produce a different style of subseafloor fluid transfer through various ways of mud eruptions from submarine mud volcanoes, which is discussed in Chapter 5.

Chapter 4

Methane amount inside a deep-water mud volcano

4.1 Summary

Mud volcanoes are among the largest geological sources releasing hydrocarbon gases. Numerous studies have revealed their origins and compositions within submarine mud volcanoes. However, estimates of the amount of gas inside deep-water mud volcanoes have been challenging, owing to the difficulty of *in situ* measurements. Here, we provide a basic model bridging methane concentrations and elastic-wave velocities in fluidized mud conduits of submarine mud volcanoes. This model is universally applicable and enables estimates of methane concentration in the mud conduits using seismic data. This approach could produce first-order estimates of stationary methane effluxes from deep-water mud volcanoes. Application of our model to an active deep-water mud volcano reveals that the amount of methane in its conduits is higher than previously expected from geochemical evidence. Our scheme provides an opportunity to re-estimate the total methane flux from submarine mud volcanoes.

4.2 Introduction

The sources of hydrocarbon gases and CO_2 in the atmosphere have yet to be fully explored [*Kvenvolden et al.*, 2001; *Judd et al.*, 2002]. One of the major geological sources of these gases is mud volcanoes [*Dimitrov*, 2002; *Kopf*, 2002; *Etiope and Milkov*, 2004], surficial expressions of overpressured deep-underground sediments [*Higgins and Saunders*, 1974; *Kopf*, 2002] that are efficient pathways to release hydrocarbon gases. They are plentiful in various tectonic settings, and can have diameters up to tens of kilometers and heights of up to several hundreds of meters [*Kopf*, 2002; *Kioka and Ashi*, 2015]. The gas released by mud volcanoes is composed predominantly of methane (generally 90–99 vol%) and is mostly of mixed thermogenic and biogenic origins [*Dimitrov*, 2002; *Kopf*, 2002; *Milkov et al.*, 2003]. Hydrocarbons released from submarine mud volcanoes in the Nankai accretionary margin are mostly thermogenic, originating from an old accretionary prism deeper than 2000 mbsf (meters below the seafloor) [*Toki et al.*, 2013; *Pape et al.*, 2014]. However, the amount of hydrocarbon gas inside submarine mud volcanoes has yet to be accurately estimated, because only seawater from above the crest of the mud volcano and/or sediment samples from a shallow subsurface of the crest have been used to estimate it. Furthermore, numerous observations at both onshore and offshore mud volcanoes have illustrated the high temporal variability of the intensity of methane emissions from each mud volcano [*Higgins and Saunders*, 1974; *Feseker et al.*, 2014], hampering attempts to estimate their gas volume as found at cold seeps [*Tryon et al.*, 1999; *Boetius and Wenzhöfer*, 2013]. A recent long-term observation at the Håkon Mosby Mud Volcano in the southwestern Barents Sea revealed a considerably higher methane concentration than previously reported [*Feseker et al.*, 2014]. Larger volume of methane gas than expected is thus thought to have escaped from deep-water mud volcanoes, suggesting that the global methane flux from the seafloor is probably underestimated, as suggested by previous studies [*Milkov et al.*, 2003; *Etiope and Milkov*, 2004]. Therefore, the assessment of potential methane concentrations inside submarine mud volcanoes is an urgent issue, especially to clarify the total methane flux from the seafloor, to further our understanding of climate change. Since submarine mud volcanoes are the most prominent players in the escape of material from deep underground to the seafloor [*Kopf*, 2002], evaluating the methane percentage also holds promise in unraveling the role of submarine mud volcanism on subseafloor carbon cycling. This issue also drives key biogeochemical processes near the seabed that regulate methane sinking within sediments via the microbial anaerobic oxidation of methane, coupled with sulfate reduction [*Reeburgh*, 2007; *Knittel and Boetius*, 2009].

To address the aforementioned issues, this study aims to estimate methane content in the mud conduits of a deep-water mud volcano using seismic velocity profiles. We develop a basic one-dimensional model demonstrating the stationary gas-charged fluidized mud conduits of a submarine mud volcano in order to determine the pressure, gas volume fraction, and gas density of the mud volcano as a function of depth. These values are used to determine seismic velocities over the fluidized mud conduits of a submarine mud volcano (Figure 4.1). In this study, we first compare our modeled results with the deep-drilling data obtained at mud volcanoes in the Olimpi mud field of the Eastern Mediterranean Sea, in order to evaluate the difference between *in situ* methane values and those calculated from our model. Methane concentration within mud conduits can be also derived based on the seismic velocities acquired by reflection seismics using the multi-channel seismic (MCS) system or the vertical cable seismic system [e.g., *Krail*, 1994], or refraction seismics using ocean-bottom seismometers. The use of these seismic data is benefited from a feasible gain of information at deep depths easier than deep-drilling or long-term observations. Thus, we also apply the above scheme to the seismic velocity profile derived from MCS reflection data to estimate the methane concentration inside the mud conduits of an active submarine mud volcano in the Nankai subduction zone.

4.3 Methane fraction and elastic-wave velocity

4.3.1 Constraints on the scheme in this study

An increase in pore pressure leads to a decrease in effective pressure and elastic-wave velocity [*Todd and Simmons*, 1972; *Winkler and Nur*, 1982]. Seismic velocity displays a significant decrease when the saturated fluid water is replaced by gas [*Wyllie et al.*, 1956, 1958; *Domenico*, 1977]. Thus, in order to obtain the elastic-wave velocity in the conduits of a mud volcano as a function of depth, the relationship between pressure, gas fraction and density of the mud conduits has to be determined. However, natural systems are highly complicated, far exceeding our current knowledge and a complete understanding of the interactions between the aforementioned properties cannot be acquired. Therefore, our scheme hereafter assigns the following five constraints to obtain the relationships between the properties robustly:

1. Our model aims to understand the static profile of elastic-wave velocity with changing methane fractions. In this study, therefore, the total mass fraction of both exsolved and dissolved methane is fixed to be constant in the mud conduits. No flow properties at the lateral boundaries between mud conduits and the surrounding sedimentary sequences are taken into account, because these rates are very low for the duration of our investigated time period, owing to low diffusion rates [*Iversen and Jørgensen*, 1993]. Under these constraints, a steady-state condition can be assumed.

2. Only the methane-seawater-mud mixture in the mud conduits is considered here, and other higher hydrocarbon gases (ethane through pentane), CO_2, and N_2 are not taken into account, as they are known to only be minor components inside offshore mud volcanoes [*Dimitrov*, 2002; *Kopf*, 2002; *Milkov et al.*, 2003].

3. Mud conduits are assumed to be an amalgamated cylindrical zone of fluidized mud pipes feeding the submarine mud volcano, as revealed by high-resolution three-dimensional seismic images [*Davies and Stewart*, 2005; *Stewart and Davies*, 2006]. This assumption is readily validated by a simple estimation using Stokes flow, which suggests the ascent speed in the mud conduits of the mud diapir will be lower than the order of 10^0 m/s, based on its known dynamic viscosity and the diameter of the single mud feeder reaching up to a couple of tens of meters [*Kopf and Behrmann*, 2000; *Kopf*, 2002; *Manga et al.*, 2009].

4. The hydrate-bearing sediment shows a high elastic-wave velocity [e.g., *Helgerud et al.*, 2009]. However, a setting in which the hydrate is absent from within the mud conduits is studied here, even satisfying the conditions of the gas hydrate stability zone. This item is easily justified, because the active mud volcano investigated in this study ejected hydrates mostly during its earlier massive mud eruptions and thus is free of hydrates in the mud conduits.

5. Rise velocities of small bubbles that are lower than 1 m/s even in the seawater column [*Jamialahmadi et al.*, 1994; *McGinnis et al.*, 2006; *Sauter et al.*, 2006] and

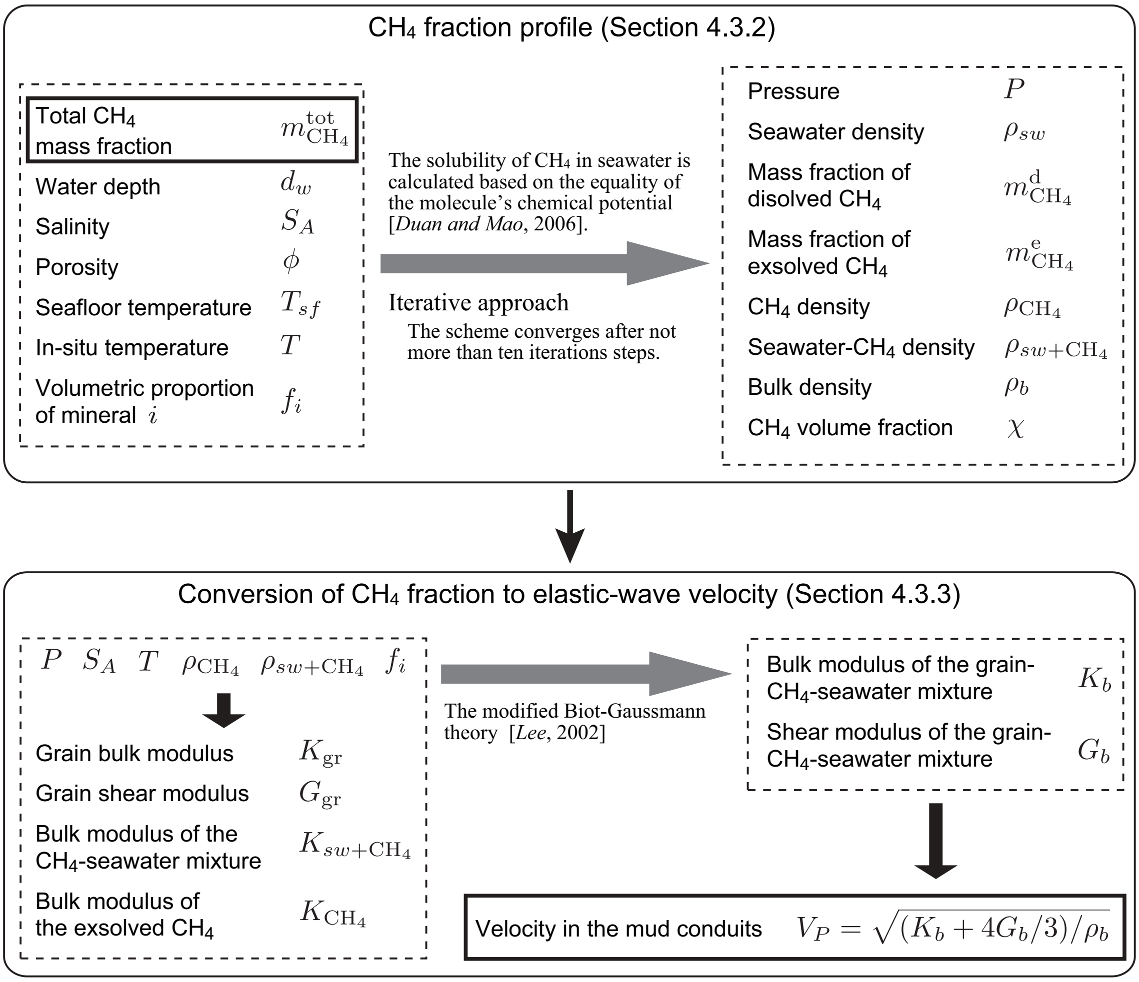

Figure 4.1: Flowchart showing the model presented in this study.

the growth rates of bubbles [*Boudreau et al.*, 2001] are not taken into account, as the "no-growth" condition can be assumed in the stationary problem investigated here [*Gardiner et al.*, 2003; *Algar and Boudreau*, 2010].

The model presented here has two calculations: derivation of dissolved and exsolved methane fraction profiles, and computation of elastic-wave velocity while incorporating the resultant methane profile (Figure 4.1). We will summarize the basic derivation of the methane profile and the resultant changes in the elastic-wave velocity in Sections 4.3.2 and 4.3.3 respectively, and will demonstrate an example of the model result in Section 4.3.4.

4.3.2 Methane gas fraction

The overburden pressure (lithostatic pressure or confining pressure) in the mud conduits of a submarine mud volcano, P (Pa), which is dependent on the function of depth z (mbsf), is given by

$$P(z) = \rho_{sw} g d_w + \int_0^z \rho_b(z') g \, dz', \tag{4.1}$$

where ρ_{sw} (kg/m^3) is seawater density, g (m/s^2) is the gravitational acceleration, d_w (m) is water depth at the top of the mud volcano, and ρ_b (kg/m^3) is the bulk density of the mud volcano body. The bulk density ρ_b is given by:

$$\rho_b(z) = (1 - \phi(z))\rho_{\mathrm{gr}} + \phi(z)\, \rho_{f+g}(z), \tag{4.2}$$

where ϕ is porosity, ρ_{gr} (kg/m^3) is grain density, and ρ_{f+g} (kg/m^3) is the density of the fluid-gas mixture. The grain density ρ_{gr} is defined by equation (4.10), below, by using a constant volumetric proportion of mineral constituents (see Section 4.3.3). The seawater density ρ_{sw} is derived by the reciprocal of the pressure derivative of the Gibbs function at salinity S_A and temperature T (°C) [*Wagner and Pruß*, 2002; *Feistel*, 2008]. The *in situ* temperature T can be approximated from an observational linear thermal gradient ΔT (°C/m) and the observed seafloor temperature T_{sf} (°C).

The derivation of methane solubility in seawater depends on the equality of the chemical potentials of methane in vapor and liquid phases [*Duan and Mao*, 2006]. Methane solubility is not significantly affected by natural minerals [e.g., *Stoessell and Byrne*, 1982; *Crosdale et al.*, 1998], while micropores inherent to clays would affect the solubility slightly [e.g., *Aringhieri*, 2004; *Cheng and Huang*, 2004]. Thus, the mass fraction of dissolved methane $m^{\mathrm{d}}_{\mathrm{CH_4}}$ is calculated by the methane-seawater solution of *Duan and Mao* [2006]. The mass fraction of exsolved methane $m^{\mathrm{e}}_{\mathrm{CH_4}}$ affecting the elastic parameters of the grain-fluid-gas mixture is given by:

$$m^{\mathrm{e}}_{\mathrm{CH_4}}(z) = \frac{m^{\mathrm{tot}}_{\mathrm{CH_4}} - m^{\mathrm{d}}_{\mathrm{CH_4}}(z)}{1 - m^{\mathrm{d}}_{\mathrm{CH_4}}(z)}, \tag{4.3}$$

where $m^{\mathrm{tot}}_{\mathrm{CH_4}}$ is the total mass fraction of exsolved and dissolved methane. Thus, the whole density of the fluid-gas mixture, ρ_{f+g}, at depth z is obtained as:

$$\rho_{f+g}(z) = \left(\frac{1 - m^{\mathrm{e}}_{\mathrm{CH_4}}(z)}{\rho_{sw+\mathrm{CH_4}}(z)} + \frac{m^{\mathrm{e}}_{\mathrm{CH_4}}(z)}{\rho_{\mathrm{CH_4}}(z)} \right)^{-1}, \tag{4.4}$$

where $\rho_{sw+\mathrm{CH_4}}$ ($\mathrm{kg/m^3}$) is the density of the methane-seawater mixture, and $\rho_{\mathrm{CH_4}}$ ($\mathrm{kg/m^3}$) is the density of exsolved methane. The seawater-methane density $\rho_{sw+\mathrm{CH_4}}$ is obtained using the solution of methane in seawater integrated with the dissolved methane. The density of exsolved methane $\rho_{\mathrm{CH_4}}$ is calculated using formulations of its thermodynamic properties [*Setzmann and Wagner*, 1991]. The gas volume fraction (χ) can be derived from the mass fraction ($m^{\mathrm{e}}_{\mathrm{CH_4}}$) weighted by the ratio of bulk and gas density:

$$\chi(z) = \frac{\rho_b(z)}{\rho_{\mathrm{CH_4}}(z)} m^{\mathrm{e}}_{\mathrm{CH_4}}(z). \tag{4.5}$$

The pressure, density, and mass fraction of exsolved gas in mud conduits depend on each other. We hence use an iterative approach and start at the lithostatic pressure profile of the second term of the right hand side of equation (4.1) and work out densities and gas fractions, which are then used in further iterations to determine the depth-dependent pressure in equation (4.1). Within the ranges of depth z and the total gas mass fraction $m^{\mathrm{tot}}_{\mathrm{CH_4}}$ of interest in this study, the scheme converges after no more than ten iterations and produces robust values.

4.3.3 Elastic-wave velocity

The elastic-wave velocity in a gas-charged fluidized mud conduit of a mud volcano, assuming a homogeneous isotropic medium, is given by $V_P(z) = \sqrt{\big(K_b(z) + 4G_b(z)/3\big)/\rho_b(z)}$ (m/s), where K_b (Pa) and G_b (Pa) are the bulk modulus and the shear modulus, respectively, of the grain-methane-seawater mixture in the conduits. As we assume that gaseous methane and the methane-seawater mixture are homogeneously distributed within the pore space, the effective bulk modulus of the composite pore is obtained using the isostress average [*Reuss*, 1929]. Here the bulk and shear moduli are computed using the modified

Biot-Gaussmann theory [*Lee*, 2002]:

$$K_b(z) = K_{\mathrm{gr}}(1-\beta) + \beta^2\left[\frac{\beta-\phi(z)}{K_{\mathrm{gr}}} + \phi(z)\left(\frac{1-\chi(z)}{K_{sw+\mathrm{CH_4}}(z)} + \frac{\chi(z)}{K_{\mathrm{CH_4}}(z)}\right)\right]^{-1}, \tag{4.6}$$

$$G_b(z) = \frac{G_{\mathrm{gr}}K_{\mathrm{gr}}(1-\beta)\big(1-\phi(z)\big)^2 + G_{\mathrm{gr}}\beta^2\big(1-\phi(z)\big)^2\left[\frac{1-\chi(z)}{K_{sw+\mathrm{CH_4}}(z)} + \frac{\chi(z)}{K_{\mathrm{CH_4}}(z)}\right]^{-1}}{K_{\mathrm{gr}} + 4G_{\mathrm{gr}}\left[1-\big(1-\phi(z)\big)^2\right]/3}, \tag{4.7}$$

where K_{gr} (Pa), $K_{sw+\mathrm{CH_4}}$ (Pa), and $K_{\mathrm{CH_4}}$ (Pa) are the bulk moduli of grain, the methane-seawater mixture, and exsolved methane, respectively, G_{gr} (Pa) is the shear modulus of the grains, and β is the Biot coefficient [*Biot*, 1941]. We use the Biot coefficient β calculated using the functional relationship with porosity ϕ for the unconsolidated sediments investigated here [*Lee*, 2002]. The moduli of the solid phase, K_{gr} and G_{gr}, are computed from those of its individual constituents (Table 4.1) using the following Voigt-Reuss-Hill averaging scheme:

$$K_{\mathrm{gr}} = \frac{1}{2}\left[\sum_{i=1}^{n} f_i K_i + \left(\sum_{i=1}^{n}\frac{f_i}{K_i}\right)^{-1}\right], \tag{4.8}$$

$$G_{\mathrm{gr}} = \frac{1}{2}\left[\sum_{i=1}^{n} f_i G_i + \left(\sum_{i=1}^{n}\frac{f_i}{G_i}\right)^{-1}\right], \tag{4.9}$$

where n is the number of mineral components, f_i is the volumetric proportion of mineral i satisfying $\sum_{i=1}^{n} f_i = 1$, and K_i (Pa) and G_i (Pa) are the bulk and shear moduli of the component i [*Hill*, 1952]. The grain density required to calculate the bulk density in equation (4.2) can also be expressed as:

$$\rho_{\mathrm{gr}} = \sum_{i=1}^{n} f_i \rho_i, \tag{4.10}$$

where ρ_i (kg/m^3) is the density of mineral i (Table 4.1). The bulk modulus of the methane-seawater mixture $K_{sw+\mathrm{CH_4}}$ (Pa) is approximated to that of the seawater solution [*Feistel*, 2008] to accommodate changes in pressure P and temperature T within the mud conduits. The bulk modulus of methane $K_{\mathrm{CH_4}}$, dependent on temperature T, pressure P and density $\rho_{\mathrm{CH_4}}$, is calculated using the van der Waals equation [*Morse and Ingard*, 1986; *Batzle and*

Table 4.1: Constant elastic moduli and grain densities in the model employed [*Mavko et al.*, 2009].

i	Constituent	Grain Density (ρ_i)	Bulk modulus (K_i)	Shear modulus (G_i)
1	Clays	2600 kg/m^3	21×10^9 Pa	6.9×10^9 Pa
2	Quartz	2650 kg/m^3	37×10^9 Pa	44×10^9 Pa
3	Plagioclase	2630 kg/m^3	76×10^9 Pa	26×10^9 Pa
4	Calcite	2710 kg/m^3	77×10^9 Pa	32×10^9 Pa
5	Dolomite	2870 kg/m^3	95×10^9 Pa	45×10^9 Pa
6	Halite	2160 kg/m^3	25×10^9 Pa	15×10^9 Pa

Wang, 1992].

4.3.4 Model experiment

An experimental example of the constructed model is illustrated in Figure 4.2. The experiment demonstrates the exsolution level (gas is fully dissolved below the level) incorporating methane solubility in the mud conduits, with an associated downward change in the elastic-wave velocity. Variations in the seismic velocity are sensitive to porosity changes [*Wyllie et al.*, 1956, 1958; *Watkins et al.*, 1972; *Erickson and Jarrard*, 1998]. Porosity changes produce the largest variations in the ranges of interest in our calculations, with for example up to $\sim 7\%$ variation in the resulant elastic-wave velocity V_P against a 10% variation in porosity ϕ (e.g., Figure 4.2d). The theoretical uncertainty in the elastic-velocity produced by our model is around 5%, taking all background theoretical formulations into consideration.

4.4 Application to mud volcanoes in the Eastern Mediterranean Sea using downhole logging data

The Eastern Mediterranean Sea holds the world's greatest abundance of submarine mud volcanoes. Intense emission of methane is known to occur at submarine mud volcanoes in this area. Two mud volcanoes named "Milano" and "Napoli" in the Olimpi mud field of the central Mediterranean Ridge Accretionary complex (Figure 4.3a) had been drilled by

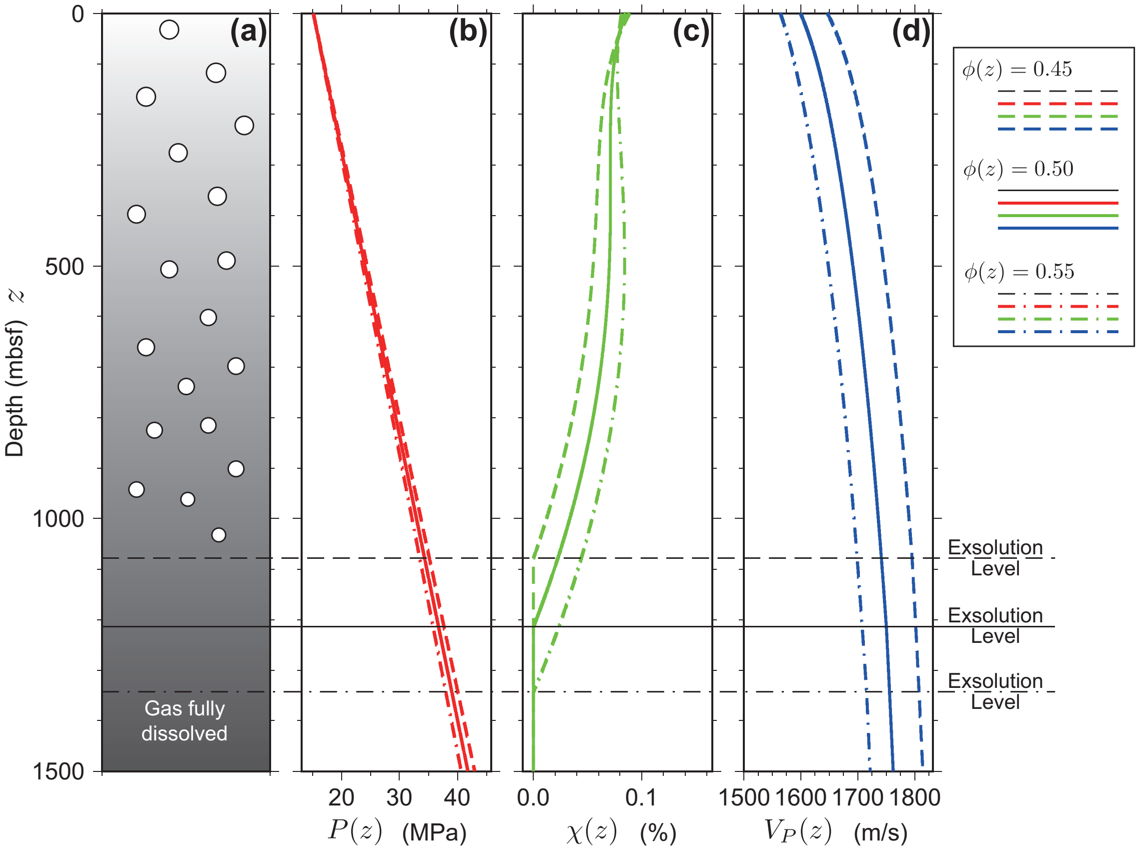

Figure 4.2: Experimental validation of the developed model: (a) schematic diagram, (b) pressure $P(z)$ profile, (c) gas volume fraction $\chi(z)$ profile, and (d) seismic velocity $V_P(z)$ profile. The parameters used in this experiment are $m_{\mathrm{CH_4}}^{\mathrm{tot}} = 0.25\%$, $d_w = 1500$ m, $S_A = 34.0$, $T_{sf} = 5.0°\mathrm{C}$, and $\Delta T = 0.030$ K/m, with changing constant porosities of $\phi(z) = 0.45$, 0.50, and 0.55. The three grain constituents considered here are clay ($i = 1$), quartz ($i = 2$), and plagioclase ($i = 3$) with volume fractions $(f_1, f_2, f_3) = (0.5, 0.3, 0.2)$ (Table 4.1), in order to determine the elastic moduli of the solid phase computed in equations (4.8) and (4.9), and the grain density from equation (4.10).

the Ocean Drilling Program (ODP) Leg 160 [*Emeis et al.*, 1996]. Thus, the available data set including both elastic-wave velocities and methane concentrations allows to compare these data with our modeled results.

To evaluate the difference between methane concentrations from *in situ* measurements and those estimated from our modeled results, we used the data of core sample measurements and downhole logging tools obtained by the ODP Leg 160. P-wave velocities from downhole logging and split cores were acquired at the moat of the Milano mud volcano (Hole 970A) and the flank-moat of the Napoli mud volcano (Hole 971B), respectively

[*Emeis et al.*, 1996]. The crest of the Milano mud volcano is known for having low-salinity pore waters indicative of large amounts of gas hydrates [*De Lange and Brumsack*, 1998]. The moat of the Milano mud volcano at Hole 970A shows higher salinities of $S_A = 37$–99. In contrast, the Napoli mud volcano extensively represents higher salinities (e.g., $S_A = 40$–240 at the Hole 971B), which is likely associated with brine emissions generating brine pools. The seawater density at the Napoli mud volcano is thus calculated using the correlation formula [*Driesner and Heinrich*, 2007] applicable to the high salinity. The bulk modulus of the methane-seawater mixture $K_{sw+\mathrm{CH_4}}$ is forcibly calculated by the general formulation [*Feistel*, 2008]. Volumetric fractions of mineral constituents including clays, quartz, feldspar, calcite, dolomite, and halite are constrained with averaging results of XRD data [*Jurado-Rodríguez and Martínez-Ruiz*, 1998]. Porosity measurements from split cores are used for the porosity profile at each hole, with interpolating the data from fitting curves to produce porosity at a given depth where the data are absent. Temperature at a given depth at the Milano mud volcano is obtained from the downhole logging-tool at the Hole 970A. On the other hand, as geothermal information at the Napoli mud volcano is limited, we used thermal gradient of $\mathit{\Delta} = 30$–40°C/km based on a single temperature measurement at the Hole 971B [*Emeis et al.*, 1996] and heat flow measurements [*Camerlenghi et al.*, 1995]. These values are employed to produce downward profiles of the elastic-wave velocity in relation to changes in the total mass fraction $m^{\mathrm{tot}}_{\mathrm{CH_4}}$, in order to evaluate the likely range of modeled methane amounts at deep depths on each hole of the mud volcano (Figure 4.3).

Methane concentrations released from and inside mud volcanoes in the Eastern Mediterranean Sea have been investigated from numerous measurements. Geochemical measurements in the water column above the Milano mud volcano show up to 20 μmol/L [e.g., *MEDINAUT/MEDINETH Shipboard Scientific Parties*, 2000; *Charlou et al.*, 2003]. Measurements of pore water in the sediment at the Hole 970A record only minor concentrations of methane ranging from 2 to 15 ppm [*Emeis et al.*, 1996], while sufficient pore water samples could not be obtained due to poor recovery of cores at this hole. On the other hand, methane at the Hole 970C on the flank, ~ 1 km crestward from the Hole 970A, is abundant ranging 2000–14000 ppm [*Emeis et al.*, 1996]. Our velocity-based results indicate that the

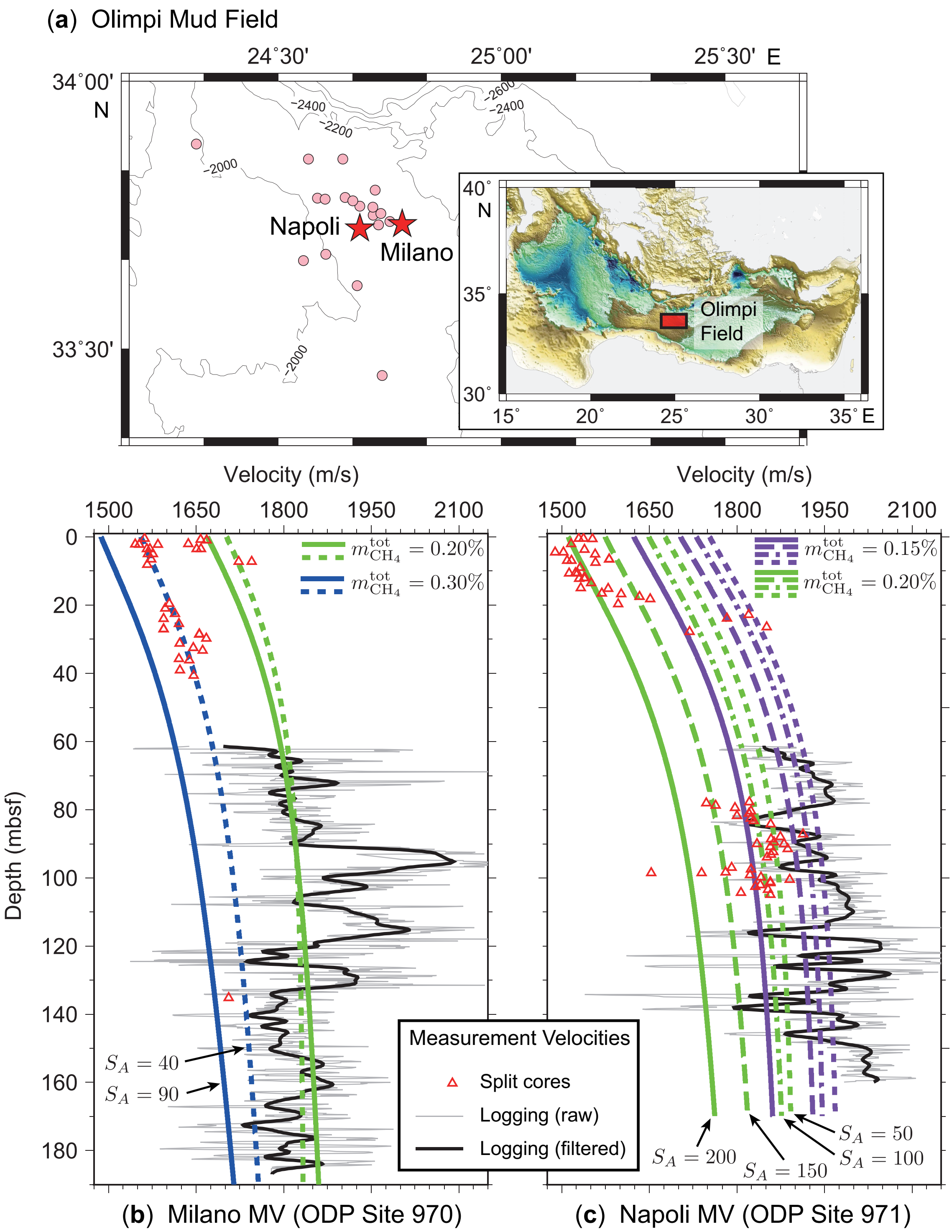

Figure 4.3: (*Continued on the following page.*)

Figure 4.3: (*Preceding page.*) (a) The Olimpi mud field in the eastern Mediterranean Sea. Red stars indicate the Milano and Napoli mud volcanoes investigated in this study, while pink circles show other known mud volcanoes within the Olimpi mud field. Locations of the mud volcanoes are from *Kioka and Ashi* [2015]. Bathymetric data from the GEBCO_2014 Grid. (b) Drilling velocity data and modeled velocities at Milano mud volcano. The downhole logging velocity data in ODP Hole 970A (gray line), the velocity smoothed with a 5 m Gaussian filter (thick black line), and velocity measurements of sediment cores in Hole 970A (red triangles) are plotted. Modeled velocities are demonstrated with varying total methane mass fractions $m_{\mathrm{CH_4}}^{\mathrm{tot}} = 0.20$ and 0.30% (green and blue lines, respectively), and salinity $S_A = 40$, 90 (dot and solid lines, respectively). Volumetric proportions of mineral are $f_1 = 0.31$, $f_2 = 0.16$, $f_3 = 0.03$, $f_4 = 0.41$, and $f_5 = 0.09$ (see Table 4.1 for the numeral i labeled in f_i). Bottom water temperature is $T_{sf} = 14°$C. (c) Drilling velocity data and modeled velocities at Napoli mud volcano. The downhole logging velocity data in ODP Hole 971B (gray line), the velocity smoothed with a 5 m Gaussian filter (thick black line), and velocity measurements of sediment cores in Hole 971B (red triangles) are plotted. Modeled velocities are demonstrated with varying total methane mass fractions $m_{\mathrm{CH_4}}^{\mathrm{tot}} = 0.15$ and 0.20% (purple and green lines, respectively), and salinity $S_A = 50$, 100, 150, 200 (dot, dash-dot, dash and solid lines, respectively). Volumetric proportions of mineral are $f_1 = 0.42$, $f_2 = 0.18$, $f_3 = 0.03$, $f_4 = 0.23$, $f_5 = 0.04$, and $f_6 = 0.10$ (see Table 4.1 for the numeral i labeled in f_i). The thermal gradient is $\Delta T = 30$–40°/km, while the resulted velocity is almost unchanged within this range. Bottom water temperature is $T_{sf} = 14°$C.

methane concentration at Hole 970A is around 2000 ppm on average at the depths of 0–180 mbsf while changing within the likely range of salnities (Figure 4.3b), which is similar to the value obtained geochemically at the Hole 970C. Note that the downhole logging data records relatively higher velocities at the depth shallower than 130 mbsf because the depths of 30–130 mbsf are enriched in clasts with the clast-to-matrix ratio ranging 0.25–0.50 [*Emeis et al.*, 1996]. While measurements in the seawater above the Napoli mud volcano and at a few centimeter of depth in the sediment show a similar value found at Milano mud volcano [e.g., *MEDINAUT/MEDINETH Shipboard Scientific Parties*, 2000; *Charlou et al.*, 2003; *Caprais et al.*, 2010], a higher concentration of $<$ 500 ppm is recorded at the depth shallower than 10 mbsf by pore water measurements [*Emeis et al.*, 1996; *Lazar et al.*, 2011]. At the Hole 971B, methane concentration shows 2000–5000 ppm in general, with occasionally increased by 20000 ppm from headspace analysis [*Emeis et al.*, 1996]. Our modeled results show that 1500–2000 ppm of methane is extensively present at the flank-moat of the Napoli mud volcano, which is close to *in situ* values at the Hole 971B

(Figure 4.3c).

4.5 Application to a mud volcano in the Nankai margin using reflection seismics

4.5.1 Seismic reflectors inside the mud conduit of the mud volcano

More than a dozen mud volcanoes in the Kumano forearc basin of the Nankai accretionary margin have been inspected previously [*Kuramoto et al.*, 2001; *Morita et al.*, 2004; *Pape et al.*, 2014]. The Kumano Knoll No. 3 (KK#3) mud volcano in the Kumano basin (Figure 4.7a) is thought to be currently active based on both sedimentary and geochemical evidence (see Section C.1). Subsurface imaging in the mud conduit of the active mud volcano is generally poor due to associated gas and complex structure. Thanks to high-resolution seismic imaging, however, the mud conduit is thought to behave as an amalgamated cylindrical zone of feeding fluidized mud pipes [e.g., *Davies and Stewart*, 2005; *Stewart and Davies*, 2006]. Chaotic reflection patterns punctuated by seismic continuity that may be associated with disruption of feeder pipes are also recognizable within the mud conduit from other mud volcanoes [e.g., *Stewart and Davies*, 2006; *Cartwright et al.*, 2007; *Somoza et al.*, 2012]. This assures to produce velocity profiles from reflection seismics (Figure 4.4).

We here use the MCS reflection data of the KK#3 mud volcano acquired by *R/V Tansei-maru* (JAMSTEC, Japan) during the KT-06-19 cruise in August 2006 (Figure 4.7b), in order to produce velocity profiles beneath the mud volcano. The seismic source in this survey is generated by the GI gun comprising a total volume of 355 cubic inch. The receiver array is a 48-channel 1200-m-long seismic streamer cable. The MCS data are processed conventionally with trace editing, common mid-point (CMP) sorting (CMP interval is $\sim$ 12.5 m), zero-phase sine-squared tapered band-pass filter (10-15-110-120 Hz), power gain of t^2, deconvolution using the Wiener predictive error filtering, Hyperbolic Radon transform demultiple [*Foster and Mosher*, 1992], Muting, velocity analysis, normal moveout (NMO) correction, common mid-point (CMP) stacking, and time migration [e.g., *Yilmaz*, 2001]. The velocity analysis here follows the method of weighting semblance

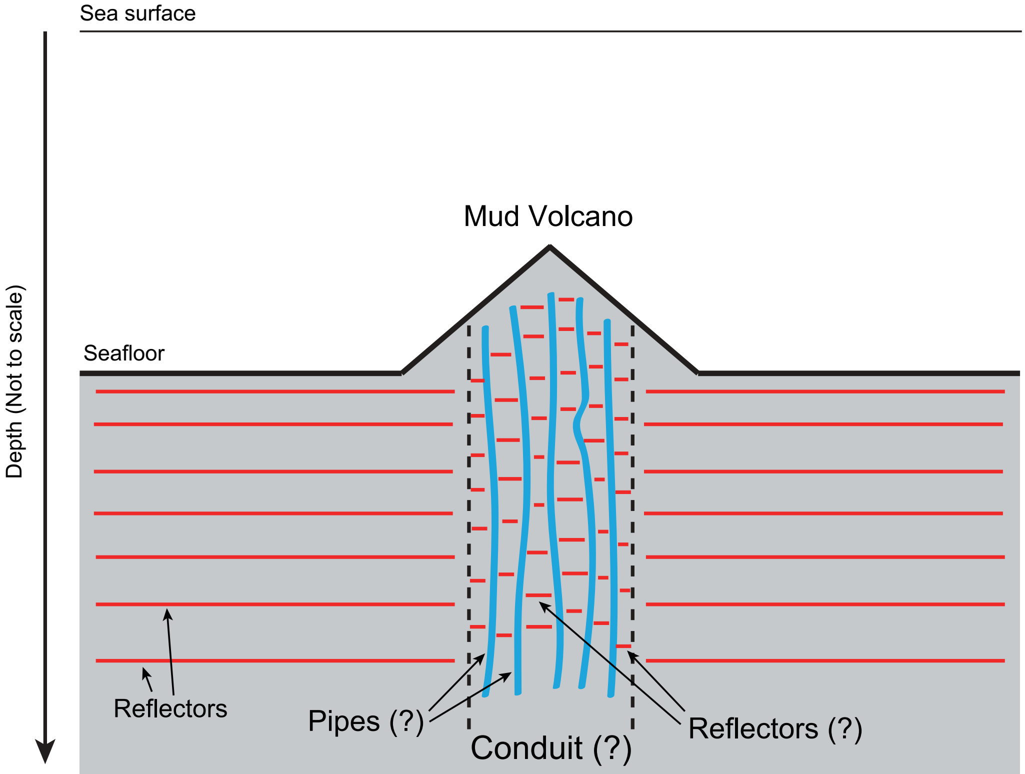

Figure 4.4: Schematic illustration of mud conduits and associated reflectors imaged in reflection seismics. Chaotic reflection patterns surrounded by feeder pipes within mud conduit are recognizable [e.g., *Stewart and Davies*, 2006; *Cartwright et al.*, 2007; *Somoza et al.*, 2012].

spectra [*Luo and Hale*, 2012] using the algorithm that automatically picks optimum velocities (see Section 4.5.2). The vertical resolution (Rayleigh's criterion) lateral resolution (Fresnel zone) within dominant frequencies and studied domain are 3–15 m and 120–250 m, respectively.

As our seismic image itself can provide rather weak reflectors within the mud conduit but not any feeder pipes (Figure 4.7b), pre-processed super-CMP gathers among neighboring 5 CMPs in the mud conduit represent common high-amplitude waveforms within the range of time of interest (Figures 4.5, C.1–C.5). These common high-amplitudes among the CMPs should generate seismic reflectors found in the seismic reflection image. Our seismic data also show the similarity among CMP gathers recorded between the given CMP and neighboring 2 CMPs within the mud conduit of the studied mud volcano (Figures 4.6 and C.10, and also found from neighboring 5 CMPs in Figure C.11). The common

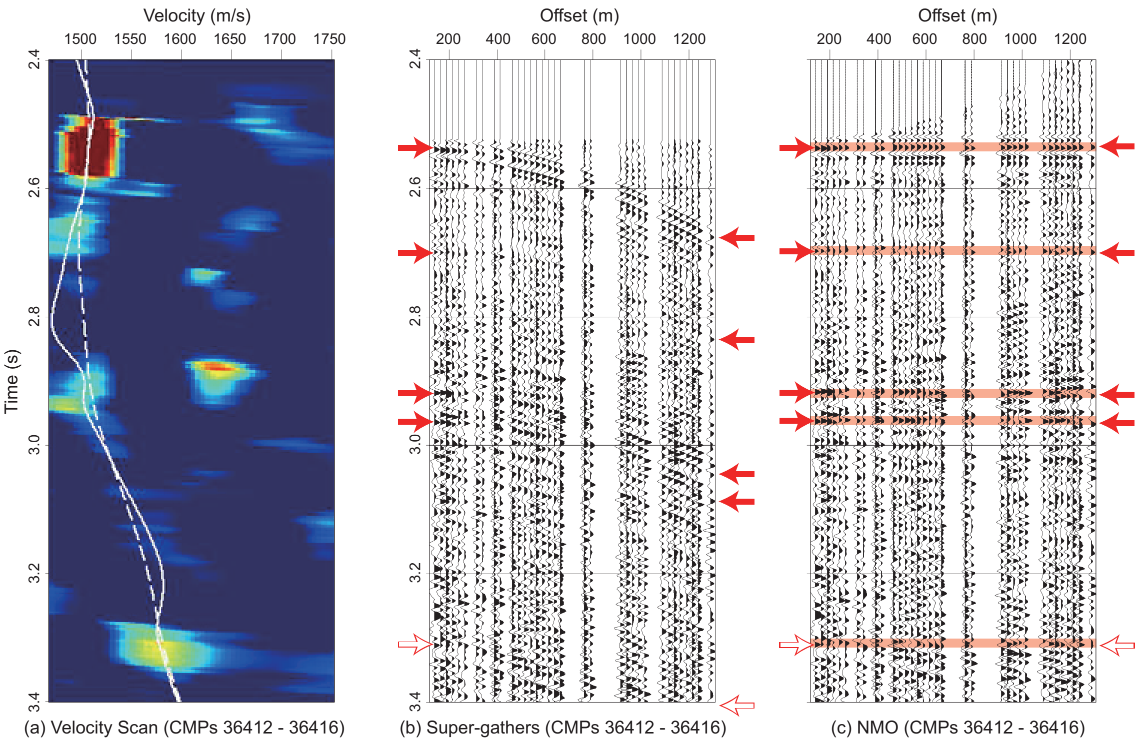

Figure 4.5: A super-gather of the neighboring 5 CMPs in the central part of the mud conduit within the KK#3 mud volcano. (a) Velocity spectra of the super-gather. The white solid line draws automatic picking velocities, while the white dash line shows optimum velocities. (b) A super-gather in the central part of the mud conduit. (c) Moveout-operated super-gathers applying the optimum velocities. Other examples are demonstrated in Figures C.1–C.5.

high-amplitude waveforms found 5 CMPs super-gathers and the similarity among the 3 CMPs suggest that continuous unique seismic reflectors can be found within the mud conduit, allowing to draw the velocity.

4.5.2 Profiles of elastic-wave velocities in the mud conduit

The reflection seismic data can provides elastic-wave velocities in the mud conduit in order to estimate methane amount inside the studied mud volcano, because continuous seismic reflectors are undoubtedly found inside the mud conduit as presented in the previous Section 4.5.1.

The velocity analysis here follows the weighting semblance method employing an offset-dependent weighting function [*Luo and Hale*, 2012]. This weighted semblance-based analysis produces greater sensitivity to velocity changes, giving a higher resolution resulting velocity scanning map than the conventional semblance calculation [*Hale*, 2009; *Luo and Hale*, 2012; *Chen et al.*, 2015]. Semblance maps are produced by the velocity step in 10 m/s and averaging window of the time length in 16 ms. We also use an algorithm that automatically picks optimum velocities [*Fomel*, 2009] to avoid the artificial errors caused by commonly used manual picking. While the picking algorithm controls picked flexibility between two neighboring time samples, we use a rather small search radius in order to assure to pick reasonable values because large changes in the velocity within small time interval are not presumable. Some examples of the velocity analysis in the mud conduit are found in Figures C.6–C.9. The picked velocity trajectory is additionally smoothed using the shaping regularization method [*Fomel*, 2007a] for stabilizing RMS velocities to produce optimum interval velocities [*Claerbout and Black*, 2005].

If a velocity profile from the given CMP produces a large deviation among neighboring several CMPs, the profile is removed because its record can be thought to include a "noisy" waveform. Deviation in the velocity calculated from profiles of neighboring 5 CMPs (except for noisy CMPs), width of 60–70 m falling within the Fresnel zone, represents that our produced velocities in the mud conduit have uncertainties of up to 90 m/s at deep depths within the time domain of interest (Figure C.12). This suggests that the uncertainty in the produced velocity within the mud conduit is ensured to have less than $\pm 5\%$. The

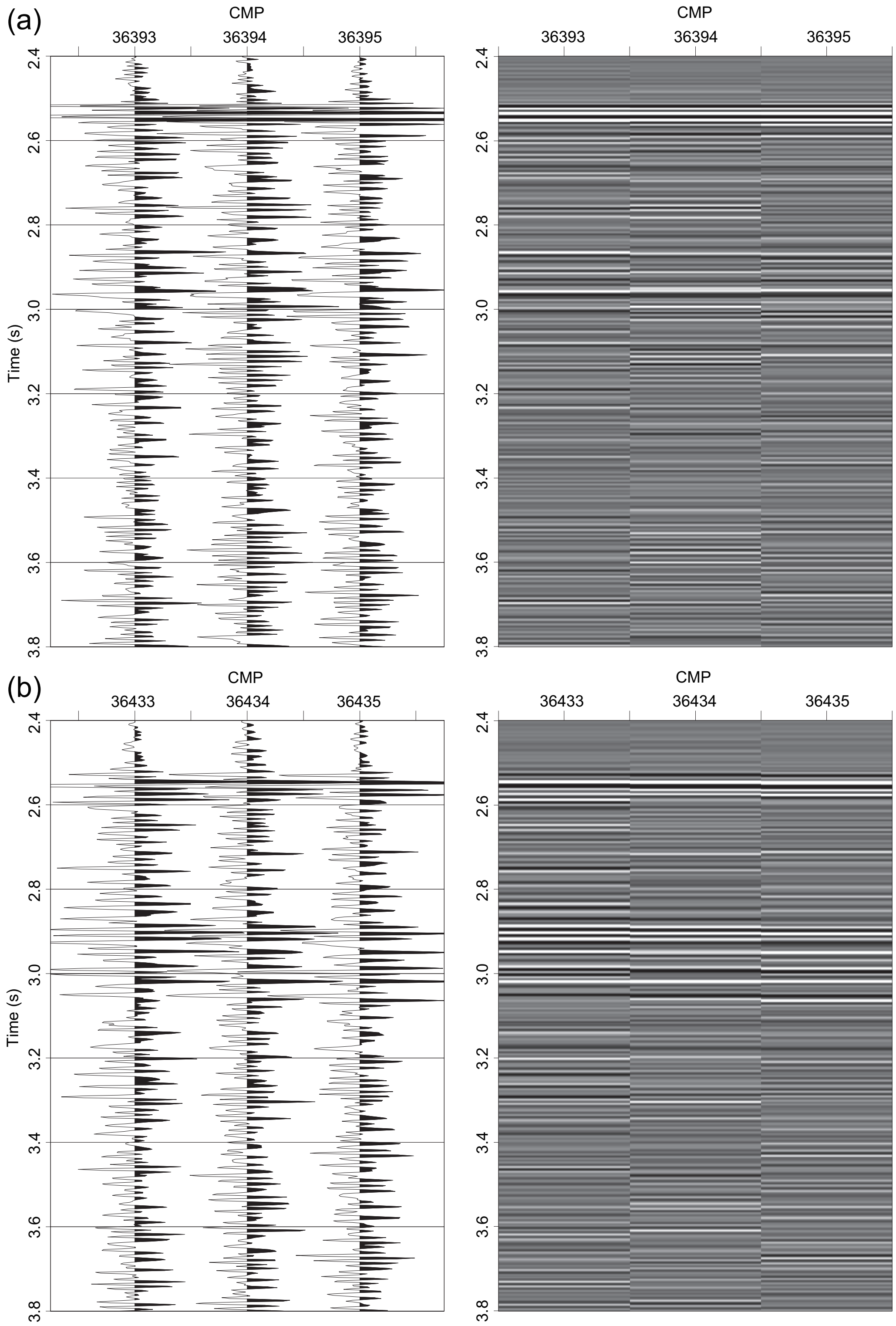

Figure 4.6: Wiggle and raster plots of waveforms recorded in neighboring three CMPs located in mud conduits of the studied submarine mud volcano, in order to see similarity in traces between the given CMP and neighboring 2 CMPs: (a) Central part of the mud conduits and (b) Eastern part of the mud conduits. Other examples are demonstrated in Figure C.10.

final velocity profile of the given CMP found in Figure 4.7c are produced by smoothing of profiles from the neighboring 5 CMPs.

To constrain parameters addressed in Sections 4.3.2 and 4.3.3, we assume that the mineral constituents in the mud conduits of the KK#3 mud volcano follow the same distribution as those from the IODP Site C0002 [*Expedition 315 Scientists*, 2009], including clay, quartz, plagioclase, and calcite (Table 4.1). Salinity in the mud conduits is set to be $S_A = 35.0$ from the results of a push-core sampling study [*Toki et al.*, 2013]. Porosity is almost unchanged in the upper several tens of meters inside the KK#5 and KK#6 mud volcanoes, but in practice decreases downward over deeper depths of our interest due to gravitational compaction. We thus employ porosity functions given by a commonly used relationship to estimate compressibility inside the submarine mud volcano (see Section C.3). While the heat flow associated with the activity of the mud volcano changes the temperature profile [*Feseker et al.*, 2014; *Pape et al.*, 2014], a stationary profile is assumed here using a linear thermal gradient of $\Delta T = 0.042$ °C/m and a uniform seafloor temperature of $T_{sf} = 2$°C (see Section C.4 for the geothermal condition [e.g., *Hamamoto et al.*, 2011]). These values are employed to produce downward profiles of the elastic-wave velocity in relation to changes in the total mass fraction $m^{\mathrm{tot}}_{\mathrm{CH_4}}$, in order to evaluate the likely range of methane amounts in the mud conduits of the active KK#3 mud volcano (Figure 4.7c).

4.6 First geophysical evidence of large methane content inside mud volcanoes

The examination of our model using *in situ* values obtained from deep-drlling measurements in the Eastern Mediterranean Sea reveals that modeled methane concentrations using elastic-wave velocities are compatible with or at least within the same order of magnitude of those estimated from pore water measurements. The testing ensures that our scheme enables to produce averaged methane concentrations at the depths of interest based on elastic-wave velocities. This allows to estimate methane concentrations at other mud volcanoes where their gas amounts inside the mud volcanoes are unknown.

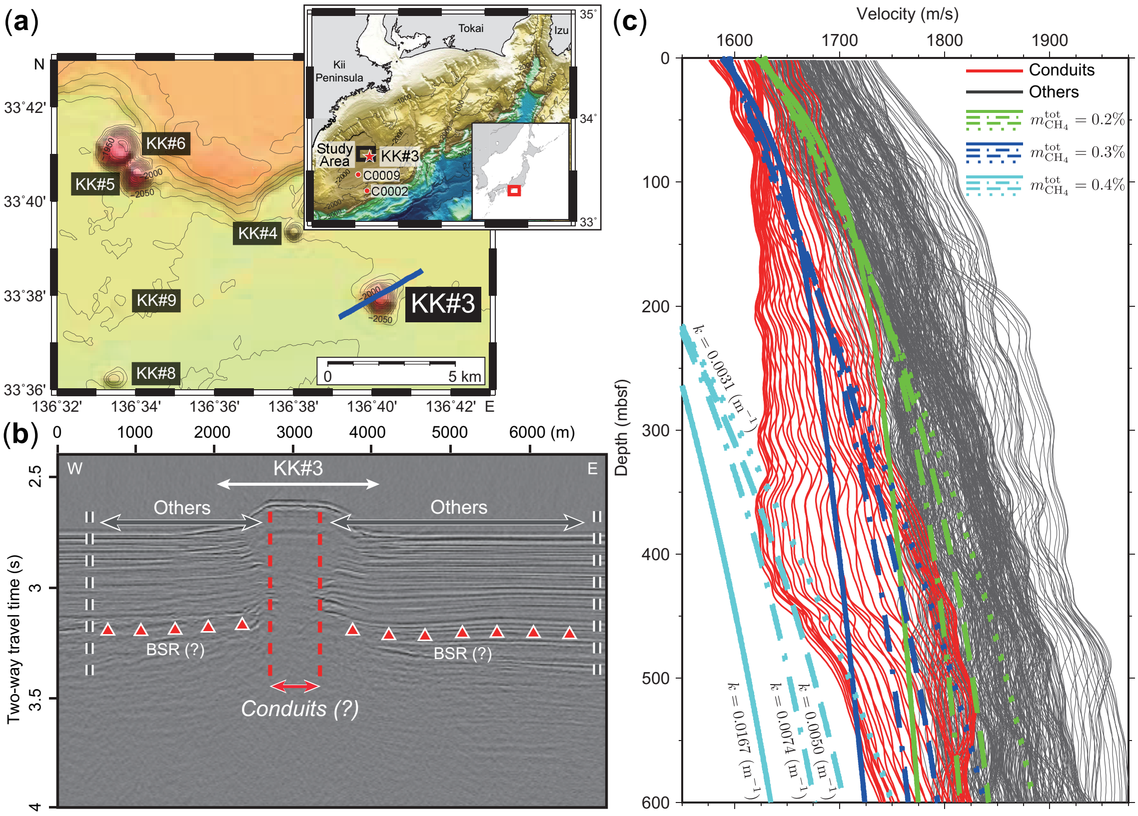

Figure 4.7: (a) Location of the KK#3 mud volcano examined in this study. A blue line over the KK#3 mud volcano presents the MCS survey line tested here. Other neighboring mud volcanoes and IODP sites are also shown. (b) A seismic image of the KK#3 mud volcano. Velocity profiles inside the mud conduits and in the surrounding regions, whose domains are illustrated in red and grey dashed lines, are plotted in Figure 4.7c. Note that the bottom simulation reflector (BSR) that manifests the base of the gas hydrate stability zone may be found here (shown in red triangles) as widely observed in the Nankai margin [*Ashi et al.*, 2002; *Baba and Yamada*, 2004; *Otsuka et al.*, 2015] and more specifically at the IODP Site C0002 [*Daigle and Dugan*, 2014], but that the BSR does not connect across the fluidized mud conduits of the active mud volcano. This suggests that the mud volcano investigated here had mostly ejected gas hydrates during its earlier massive mud eruptions. (c) Velocity profiles from the mud conduits of the KK#3 mud volcano (red lines), sedimentary sequences outside the mud conduits (dark gray lines), and modeled velocities below the top of the mud volcano with varying total methane mass fractions $m_{\mathrm{CH_4}}^{\mathrm{tot}}$ = 0.2, 0.3, and 0.4% (green, blue, and cyan lines, respectively), and k = 0.0167, 0.0074, 0.0050, and 0.0031 m^{-1} (solid, dash-dot, dash, and dot lines, respectively), where k is the compaction coefficient operated in porosity functions (see Section C.3 and Figure C.13). Profiles of the modeled velocity when the porosity is assumed to be unchanged downward are illustrated in Figure C.14. As the BSRs appear to be weak in the studied areas outside the mud conduits, the velocity change around BSRs cannot found unlike in other regions [*Yuan et al.*, 1999; *Crutchley et al.*, 2015].

Methane concentrations sampled from overlying seawater columns and subsurface pore water of both active and inactive mud volcanoes in the Nankai margin have been reported to be generally less than 200 ppm [*Miyazaki et al.*, 2009; *Tsunogai et al.*, 2012; *Toki et al.*, 2013; *Pape et al.*, 2014]. The observed seismic velocities in the mud conduits of the KK#3 mud volcano are distinctly lower than those in the sedimentary sequences outside the mud conduits (Figure 4.7c). A similar difference in seismic velocities was found in a diapir-like structure at the deep depth in the Nankai margin [*Tsuji et al.*, 2015]. Comparing our modeled velocity profiles with observed values taking into account the uncertainty in the velocity profiles, the total mass fraction of methane ($m_{\mathrm{CH_4}}^{\mathrm{tot}}$) inside the KK#3 mud volcano of the Nankai margin could be around 2000–3000 ppm (Figure 4.7c). Differences in downward trends between modeled and observed velocities in the mud conduits would arise from our major assumptions, including a constant total mass fraction of methane and/or disregarding the presence and growth of bubbles, as we investigated stationary gas-charged fluidized mud conduits in this study. Despite these issues and the large uncertainty in velocity estimation, our estimation using seismic velocities undoubtedly reveals that methane concentration in an active mud volcano may be an order of magnitude higher than previously thought from geochemical measurements. This will be not surprising, given that our result displays the methane amount within the bulk of the outlet while all previous estimates glimpse single methane streams. While other hydrocarbons and CO_2 are found in submarine mud volcanoes [e.g., *Milkov et al.*, 2003], they are minor components and unlikely to influence our estimated velocity.

Methane released from the seafloor is thought to make little influence on methane budgets in atmosphere [e.g., *Lelieveld et al.*, 1998; *Wuebbles and Hayhoe*, 2002], because methane is dissolved and oxidized in seawater columns within a couple of years [e.g., *Reeburgh et al.*, 1991; *Valentine et al.*, 2001]. However, our calculation showed higher methane concentrations than previously reported from overlying seawater columns and subsurface pore water of the mud volcanoes in the Mediterranean Ridge and the Nankai accretionary margins. We thus expect that only a very small fraction of the total methane inside the active KK#3 mud volcano might be oxidized beneath the seafloor [*Niemann et al.*, 2006; *Sauter et al.*, 2006], with the vast majority of the methane escaping into the overlying water column [*Niemann et al.*, 2006; *Feseker et al.*, 2014]. The total methane released from submarine mud volcanoes into the water column is reported to be 27 Tg/yr [*Milkov et al.*, 2003]. However, this value is highly uncertain, because the total number of submarine mud volcanoes and the temporal variability in methane emissions are unknown. Given that the diameter of a single feeder of a mud volcano is 10 m and the dynamic viscosity is of an order of around 10^4–10^6 Pa·s [*Kopf and Behrmann*, 2000; *Manga et al.*, 2009; *Rudolph et al.*, 2011], methane expelled from the KK#3 mud volcano associated with the ascent of fluidized mud is estimated to be no lower than of an order of magnitude of 10^{-1}–10^0 Tg/yr, assuming that the stationary discharge is driven by a background diapiric flow. If this value is representative of submarine mud volcanoes in general, while the studied mud volcano is rather active, then the total methane released from the mud volcanoes could be at least twice the previously estimated amount. These results can help guide the reestimation of the previously reported global methane flux from the seafloor [*Kvenvolden et al.*, 2001]. Although additional information, including the ascent speed of ejecta from the mud volcano, is required to constrain the effective methane efflux from a deep-water mud volcano, our method for submarine mud volcanoes using seismics enables a first-order estimate of global methane flux from mud volcanoes. Since a long-term observation on top of a mud volcano [*Feseker et al.*, 2014] and our seismic estimation inside the mud volcano provide methane concentration that are an order of magnitude higher than previously thought at each active mud volcano, we would expect a much larger total methane flux from submarine mud volcanoes worldwide than the previous calculation. This new estimation combined with our seismic method, long-term observations, and deep-drillings will provide an opportunity to reexamine the role of mud volcanism on subseafloor carbon cycling and dynamics of mud eruptions.

4.7 Conclusion

The methane concentration inside the mud conduits of a deep-water mud volcano was studied using seismic velocity profiles. Application of our scheme to submarine mud volcanoes in the Mediterranean Ridge and the Nankai accretionary margins showed that the methane concentrations in the mud volcanoes are higher than expected from seawater measurements from above the crest of the mud volcano and pore waters from a shallow subsurface of the mud volcano, and are compatible with those from deep-drilling. Our estimation inside the mud volcano using seismics and long-term observation studies of the top of a mud volcano, and downhole logging and *in situ* measurements from deep-drillings shed light upon that the total methane released from submarine mud volcanoes worldwide would much higher than previously thought. Although further studies are required, the scheme using seismic data reported in this study is universally applicable and provides a robust estimation of the amount of methane in the conduits of offshore mud volcanoes. These estimate approaches can constrain the global methane efflux from deep-water mud volcanoes when additional information is made available.

4.8 Connection to other chapters

This chapter will be summarized as: (1) methane concentration inside a submarine mud volcano is studied using seismics, (2) an estimate for an active submarine mud volcano showed a higher CH_4 amount than expected, and (3) our scheme helps assess a global stationary methane flux from offshore mud volcanoes. The result presented in this chapter provides a potential amount of methane gas inside a submarine mud volcano. This issue can be forwarded to discuss the role of mud eruptions from submarine mud volcanoes on subseafloor methane cycle or carbon cycle. This chapter is connected to Chapters 2 and 3 in which magnitude of eruptions and ascent of ejecta from submarine mud volcanoes are strongly related to amount of gas in the mud conduits studied in this chapter. There is also hope that using the scheme presented in this chapter will help improve our knowledge of seismic velocity structure inside submarine mud volcanoes, although tomographic inversion of marine seismic refraction data may be preferable. This will help better constrain the properties and sedimentary structure in the mud conduits of submarine mud volcanoes as addressed in Chapter 1.

Chapter 5

Discussion

My interests in this thesis lie mainly in understanding roles of submarine mud volcanism on subseafloor material cycling as noted in Chapter 1, although there is likely no specifically encompassing theme to the results obtained in this thesis. This chapter thus delivers discussions issuing how submarine mud volcanism makes a contribution to subseafloor sediment transfer, fluid migration, and carbon cycle, examined through all results presented in the previous chapters of this thesis.

5.1 Sediment recycling and submarine mud volcanism

The result presented in Chapter 2 provides important findings including (1) the frequent occurrence of pie-type (i.e., gentle slopes) submarine mud volcanoes in the accretionary wedges characterized by low-taper angles and high rates of incoming sediments and (2) the pie-type mud volcanoes act as efficient players to transfer large quantities of sediments to the seafloor. A unique mass balance of extruded muds and incoming sediments within a wedge in each subduction margin is thus presumable. Chapter 3 and previous studies reviewed in Chapter 1 manifest that source depths and ejecta paths vary in different submarine mud volcanoes. These results suggest each submarine mud volcano has a unique contribution to the subseafloor material cycling. The ascent mechanism discussed in Chapter 3 can be thus utilized as primary constraints on subseafloor sediment transfer through submarine mud volcanism. In particular, the submarine mud volcano, rooting in the mud source at deep depths or yielding a high speed ascent of its ejecta as shown in

Chapter 3, makes a big contribution to transfer sediment efficiently between deep depths and the seafloor. Specifically, the presented result provides depths and thermal information into the source of large amounts of sediment, which delineates dynamic sediment cycling between the seafloor and deep depths. Moreover, the result in Chapter 3 suggests that submarine mud volcanism accommodates or links to subseafloor tectonic setting and and its influence on the dynamic tectonics. Chapter 4 also sheds light on larger amounts of methane than expected are present inside submarine mud volcanoes from a long-term observation and my seismic method. This implies that gases play a more important role as an efficient driver of sediment transfer to the seafloor than previous thought.

The role of submarine mud volcanism on the subseafloor sediment cycle has profound effects on deformations, seismicity, and thermal regimes within the wedge through its influence on effective stresses. Furthermore, as presented in Chapter 2, nearly all of submarine mud volcanoes are polygenetic, suggesting that they reuse their main conduits dozens of times and thus serve efficiently to transfer sediments from deep depths to the seafloor. Despite the fact, sediment budget extruded by submarine mud volcanoes has been little debated. Given the number of submarine mud volcanoes (> 1000? [*Milkov*, 2000; *Dimitrov*, 2002]), diapiric ascent (Stokes' flow), and their properties including width of mud conduits [*Kopf and Behrmann*, 2000; *Kopf*, 2002] and dynamic viscosity [*Kopf and Behrmann*, 2000; *Manga et al.*, 2009; *Rudolph and Manga*, 2010], global fluidized mud flux from submarine mud volcanoes will be calculated to be an order of magnitude of 10^2–10^7 Tg/yr. These values are minimum estimates, because the estimates assume the slow upward flow while a high speed ascent is favorable in some submarine mud volcanoes as discussed in Chapter 3. Thus, submarine mud volcanism may make a most tremendous service to subseafloor sediment cycle between deep depths and the seafloor among sediment extrusion/mobilization phenomena.

While no studies have examined the source size of submarine mud volcanoes, distribution of submarine mud volcanoes presented in Chapters 1 and 2 helps assess the spatial source size. Spatial size of mud chambers rooted in submarine mud volcanoes, though the issue whether mud chambers exist or not remains controversial, holds promise in further understanding of submarine mud volcanism and its contribution to subseafloor material cycling. Thickness in the mud chamber can be approximated by the Rayleigh-Taylor (RT) instability [e.g., *Chandrasekhar*, 1961], which arises when a denser layer overlies a less dense layer. Herein I estimate the thickness using the analytical solution of the simple three-layer geometry for the RT instability [*Wilcock and Whitehead*, 1991], comprising the issued central layer of thickness h, interleaved between two equal half-spaces of considerably higher viscosity ($\eta_1 = \eta_3 \gg \eta_2$), where η_1, η_2, and η_3 are viscosities at upper half-space, central layer, and lower half-space, respectively. At large values of the viscosity ratio $\epsilon = \eta_1/\eta_2$, a characteristic wavelength λ at the fastest growing equilibrium is given by [*Wilcock and Whitehead*, 1991]:

$$\frac{\lambda}{h} = \pi(2\epsilon)^{1/3}. \tag{5.1}$$

In the problem investigated here, the observed spacing of submarine mud volcanoes L can correspond to the fastest growing wavelength λ. The thickness in the mud chamber is thus obtained as $h = L/(2\pi^3\epsilon)^{1/3}$ from equation (5.1). Here, the spacing L, constrained by distribution of submarine mud volcanoes overviewed in Chapters 1 and 2, is served as the distance between a given submarine mud volcano and neighboring mud volcanoes within the same mud field (see Figures 1.11–1.16 for example). The spacing may be around or less than $L = 10$ km. If I assume the viscosities of upper layer of a representative value $\eta_1 \sim 10^{16}$ Pa·s [*Shimizu*, 1995] in the overlying sedimentary wedge and mud chamber of a low value $\eta_2 \sim 10^4$ Pa·s [*Rudolph and Manga*, 2010], the thickness of mud chamber is calculated to be an order of magnitude of 10^{-1} m. All the same, assuming a lower value of $\eta_1 \sim 10^{14}$ Pa·s at the upper layer and a high value of $\eta_2 \sim 10^6$ Pa·s in the mud chamber [*Kopf and Behrmann*, 2000], the thickness of mud chamber will be an order of magnitude of 10^0 m. This estimate suggests that thickness of mud chamber (mud source) rooted from submarine mud volcanoes may be less than 10 m, and such thin sources of fluidized muds at deep depths might drive submarine mud volcanism that plays a profound role in subseafloor sediment cycle.

5.2 Fluid discharge and submarine mud volcanism

Subsurface water, or groundwater, is important for the Earth system through the broader hydrologic cycle, climate, oceans, and global biogeochemical cycles [*Moore*, 1996; *Taylor et al.*, 2013; *Maher and Chamberlain*, 2014]. For example, the total global volume of groundwater in the upper couple of kilometers of continental crust is estimated to be 1.6–3.0×10^7 km^3, while modern groundwater less than 50 years old holds a small percentage of the total budget [*Gleeson et al.*, 2015]. The global rate of groundwater recharge is thought to be an order of magnitude of 10^4 km^3/yr [*Döll and Fiedler*, 2008; *Gleeson et al.*, 2015]. Submarine hydrothermal system is a drastic player for fluid release, yielding the total fluid flux from hydrothermal ridge flank of 2.5–7.3×10^{12} m^3/yr [*Mottl and Wheat*, 1994; *Elderfield and Schultz*, 1996; *Johnson and Pruis*, 2003], while global fluid flux from the seafloor through general marine sediments has been estimated to be a minor fraction having $\sim 7.5 \times 10^{10}$ m^3/yr [*Anderson et al.*, 2014].

Major fluid discharge from submarine mud volcanoes is transferred by ejecta ascent, while the ascent has a variety of its mechanism as presented in Chapter 3. Given the number of submarine mud volcanoes (> 1000? [*Milkov*, 2000; *Dimitrov*, 2002]), diapiric ascent, and their properties including width of mud conduits [*Kopf and Behrmann*, 2000; *Kopf*, 2002] and dynamic viscosity [*Kopf and Behrmann*, 2000; *Manga et al.*, 2009; *Rudolph and Manga*, 2010], global fluid flux from submarine mud volcanoes will be calculated to be an order of magnitude of $> 10^7$–10^{13} m^3/yr. This estimate is consistent with individual results from a fluid supply of 1.5×10^5 m^3/yr estimated from Atlante mud volcano in the Barbados accretionary prism [*Henry et al.*, 1996] and a flux of 9.4×10^4 m^3/yr from Dvurechenskii mud volcano in Black Sea [*Aloisi et al.*, 2004], while these results are minimum estimates. Mud discharge measured at Lusi mud volcano, onshore East Java, offers $\sim 10^5$ m^3/day from its main crater during the first year of the massive discharge [*Mazzini et al.*, 2007], which brackets the above estimate. While total areas of submarine mud volcanoes hold percentages of $< 0.005\%$ of the global seafloor and even the minimum estimate obtained here, the total fluid flux from submarine mud volcanoes is similar to or greater than that from the regular seafloor and the hydrothermal system. The result presented in Chapter 2 suggests that the pie-type mud volcanoes, mainly developed in accretionary margins characterized by high sediment influx, act as efficient players to migrate large amounts of fluids to the seafloor. Moreover, as also shown in Chapter 2, submarine mud volcanoes reuse their main conduits multiple times over a very long time and serve efficiently to transfer fluids to the seafloor as they are polygenetic. These results suggest that submarine mud volcanism makes a major contribution to long-term global fluid fluxes from the seafloor.

5.3 Carbon cycling and submarine mud volcanism

Marine environment stores a vast reservoir of methane of $> 10^{19}$ g carbon [e.g., *Zhang et al.*, 2011]. Since methane is dissolved and oxidized within a couple of years in seawater columns [e.g., *Reeburgh et al.*, 1991; *Valentine et al.*, 2001], methane released from the seafloor is thought to make little influence on methane budgets in atmosphere [*Lelieveld et al.*, 1998; *Houweling et al.*, 2000; *Wuebbles and Hayhoe*, 2002]. The total methane oxidized in seawater columns and shallow sediments is estimated to be 75–304 Tg/yr [*Reeburgh*, 2007]. The gas released by mud volcanoes is composed predominantly of methane [*Dimitrov*, 2002; *Milkov et al.*, 2003]. A Gas flux ranges the order of $\sim 10^3$ m^3/day at submarine mud volcanoes in the Barbados accretionary margin [*Henry et al.*, 1996]. The total methane released from submarine mud volcanoes into the overlying seawater column was reported to be 27 Tg/yr [*Milkov et al.*, 2003]. In addition, because gas hydrates outcroped by subsurface disintegration can ascend upwards from the subseafloor to the seasurface due to their buoyancy as observed in Hydrate Ridge [*Paull et al.*, 2002], submarine mud volcanoes could be players to release methane directly into the atmosphere through massive mud eruptions capturing hydrates as examined in Chapters 2 and 3. The assessment of the methane flux in the seawater column thus holds promise on evaluating the influence on biogeochemical processes near the seabed and reestimate of the methane flux into the atmosphere which may contribute to solve the “Missing methane” problem.

Chapter 4 aimed at understanding potential methane concentrations inside submarine mud volcanoes using seismics in order to reestimate a long-term methane flux. Velocity estimates presented in Chapter 4 picks larger values due to the surrounding sequences that yield higher velocities. But this indicates that the velocity determination displays its maximum estimate, suggesting that our final results on the methane amount are minimum estimates as a larger gas amount draws a lower velocity. Although Chapter 4 shows case studies, this chapter thus provides a very important result especially for estimates of total global methane fluxes from submarine mud volcanoes. From several data including seawater samples above the mud volcano and pore waters at both shallow and deep depths, I found that the model represented in Chapter 4 produces methane concentrations inside the mud volcano which is compatible with or at least within the same order of magnitude of those from deep-drilling measurements. Despite uncertainties in total number, physical properties, and temporal variability of submarine mud volcanoes, the total methane released from submarine mud volcanoes could be at least an order of magnitude of 10^2 Tg/yr assuming the slow discharge mechanism as noted in Chapter 4. My work in this chapter using seismic schemes, a recent long-term observation [*Feseker et al.*, 2014], and measurements from deep-drilling [*Emeis et al.*, 1996] suggests that the global methane effluxes had been largely underestimated. Moreover, because the total methane flux estimated here is produced from slow ejecta ascent while high-speed ascent is often favorable for some submarine mud volcanoes presented in Chapter 3, the total flux might be much larger. Even small amounts of methane ($\sim$ 1 vol%) will cause expansion at depths < 1 km leading buoyancy [e.g., *Brown*, 1990], which may have profound effects of eruptional dynamics of submarine mud volcanoes discussed in Chapters 2 and 3. Since high methane flux is considered in many submarine mud volcanoes as presented in Chapter 4, the amount of methane investigated in this thesis plays an important issue into the dynamics of mud volcanism as well as subsurface carbon cycle.

Chapter 6

Conclusions

The research presented in this thesis explores the three topics related to submarine mud volcanism and subseafloor material cycling that span the fields of geology, sedimentology, geophysics, and geochemistry, as well as the intersection between them. This work can be summarized as having addressed the following main questions:

1. How does submarine mud volcanism make a contribution to subseafloor sediment transfer? (Chapters 2 and 3)

2. How does submarine mud volcanism make a contribution to subseafloor fluid migration? (Chapters 2 and 3)

3. How does submarine mud volcanism make a contribution to subseafloor carbon cycle? (Chapter 4)

The answers to these questions have been answered in the previous chapters of this thesis, and the main points can be briefly summarized as belows:

1. Submarine mud volcanoes play unique roles in efficiency of sediment transfer from depths in different tectonic settings. A rapid extrusion of muds as well as clasts is often favorable in some submarine mud volcanoes, possibly implying larger total mass effluxes from submarine mud volcanoes than previously expected.

2. Fluid migration driven by mud eruptions is also dependent on tectonic settings. Fluid discharge from submarine mud volcanoes plays an significant role in global

fluid flux. A rapid fluid transfer is often occurred in some submarine marine mud volcanoes, suggesting that the dynamic fluid exchange between deep depths and the seafloor is likely taken place.

3. A submarine mud volcano plays an unexpectedly important role in subseafloor methane cycle. Since methane amount affects biosphere around the mud volcano, the more significant contribution to subseafloor carbon cycle is expected than previously thought.

All the results provided in this thesis represent an increase in our understanding of submarine mud volcanism and its relation to subseafloor material cycling.

References

Abidin, H. Z., R. J. Davies, M. A. Kusuma, H. Andreas, and T. Deguchi (2009), Subsidence and uplift of Sidoarjo (East Java) due to the eruption of the Lusi mud volcano (2006–present), *Envir. Geol.*, *57*(4), 833–844, doi:10.1007/s00254-008-1363-4.

Akhmetzhanov, A. M., et al. (2008), Deep-water depositional systems and cold seeps of the Western Mediterranean, Gulf of Cadiz and Norwegian continental margins, In: A. M. Akhmetzhanov, N. H. Kenyon, M. K. Ivanov, G. Westbrook, A. Mazzini (Eds.), Preliminary Results of Investigations during the TTR-16 Cruise of RV Professor Logachev May-July, 2006, Intergovernmental Oceanographic Commission technical series, 76, UNESCO, Paris, 91 pp.

Akoumianaki, I., H. Nomaki, M. Pachiadaki, K. A. Kormas, H. Kitazato, and H. Tokuyama (2012), Low bacterial diversity and high labile organic matter concentrations in the sediments of the Medee deep-sea hypersaline anoxic basin, *Microbes Environ.*, *27*(4), 504–508, doi:10.1264/jsme2.ME12045.

Aldrich, L. T., and A. O. Nier (1946), The Abundance of He^3 in Atmospheric and Well Helium, *Phys. Rev.*, *70*, 983, doi:10.1103/PhysRev.70.983.2.

Algar, C. K., and B. P. Boudreau (2010), Stability of bubbles in a linear elastic medium: Implications for bubble growth in marine sediments, *J. Geophys. Res.*, *115*, F03012, doi:10.1029/2009JF001312.

Aloisi, G., M. Drews, K. Wallmann, and G. Bohrmann (2004), Fluid expulsion from the Dvurechenskii mud volcano (Black Sea): Part I. Fluid sources and relevance to Li, B, Sr, I and dissolved inorganic nitrogen cycles, *Earth Planet. Sci. Lett.*, *225*(3–4), 347–363, doi:10.1016/j.epsl.2004.07.006.

Amante, C. and B. W. Eakins (2009), ETOPO1 1 Arc-Minute Global Relief Model: Procedures, Data Sources and Analysis, NOAA Technical Memorandum NESDIS NGDC-24, National Geophysical Data Center, NOAA, doi:10.7289/V5C8276M.

Amorèse, D. (2007), Applying a change-point detection method on frequency-magnitude distributions, *Bull. Seismol. Soc. Am.*, *97*(5), 1742–1749, doi:10.1785/0120060181.

Anderson, B. W., L. A. Coogan, and K. M. Gillis (2014), Fluid seepage velocities through marine sediments constrained by a global compilation of interstitial water ${SO_4}^{2\,-}$, Mg^{2+}, and Ca^{2+} profiles, *J. Geophys. Res. Solid Earth*, *119*, 6823–6840, doi: 10.1002/2014JB011022.

Anderson, D. L. (1981), Rise of deep diapirs, *Geology*, *9*(1), 7–9, doi:10.1130/0091-7613(1981)9<7:RODD>2.0.CO;2.

Aoki, Y., and T. P. Sidiq (2014), Ground deformation associated with the eruption of Lumpur Sidoarjo mud volcano, east Java, Indonesia, *J. Volcanol. Geotherm. Res.*, *278–279*, 96–102, doi:10.1016/j.jvolgeores.2014.04.012.

Aringhieri, R. (2004), Nanoporosity Characteristics of Some Natural Clay Minerals and Soils, *Clays Clay Miner.*, *52*(6), 700–704, doi:10.1346/CCMN.2004.0520604.

Ashi, J. and A. Taira (1992), Structure of the Nankai accretionary prism as revealed from

IZANAGI sidescan imagery and multichannel seismic reflection profiling, *Isl. Arc*, *1*, 104–115, doi:10.1111/j.1440-1738.1992.tb00063.x.

Ashi, J., S. Lallemant, H. Masago, and the Expedition 315 Scientists (2009), Expedition 315 summary, *Proc. Integrated Ocean Drill. Program*, *314/315/316*, 1–57, doi: 10.2204/iodp.proc.314315316.121.2009.

Ashi, J., H. Tokuyama, and A. Taira (2002), Distribution of methane hydrate BSRs and its implication for the prism growth in the Nankai Trough, *Mar. Geol.*, *187*(1–2), 177–191, doi:10.1016/S0025-3227(02)00265-7.

Ashi, J., et al. (2006), Onboard Report of YK06-03 Cruise, SHINKAI 6500/YOKOSUKA, Japan Agency for Marine-Earth Science and Technology (JAMSTEC), Yokosuka, Japan.

Ashi, J., K. Ikehara, M. Kinoshita, and KY04-11 and KH-10-03 shipboard scientists (2012), Settling of Earthquake-Induced Turbidity on the Accretionary Prism Slope of the Central Nankai Subduction Zone, In Yamada, Y. et al. (Eds.), *Submarine Mass Movements and Their Consequences, Advances in Natural and Technological Hazards Research*, Springer Netherlands, 561–571, doi:10.1007/978-94-007-2162-3_50.

Ashi, J., R. Sawada, A. Omura, and K. Ikehara (2014), Accumulation of an earthquake-induced extremely turbid layer in a terminal basin of the Nankai accretionary prism, *Earth Planets Space*, *66*(1), 51, doi:10.1186/1880-5981-66-51.

Athy, L. F. (1930), Density, porosity, and compaction of sedimentary rocks, *AAPG Bull.*, *14*, 1–24.

Baba, K., and Y. Yamada (2004), BSRs and Associated Reflections as an Indicator of Gas Hydrate and Free Gas Accumulation: An Example of Accretionary Prism and Forearc Basin System along the Nankai Trough, off Central Japan, *Resour. Geol.*, *54*(1), 11–24, doi:10.1111/j.1751-3928.2004.tb00183.x.

Bagnold, R. A. (1954), Experiments on a Gravity-Free Dispersion of Large Solid Spheres in a Newtonian Fluid under Shear, *Proc. R. Soc. A Math. Phys. Eng. Sci.*, *225*(1160), 49–63, doi:10.1098/rspa.1954.0186.

Barber, A. J., S. Tjokrosapoetro, and T. R. Charlton (1986), Mud volcanoes, shale diapirs, wrench faults, and melanges in accretionary complexes, Eastern Indonesia, *AAPG Bull.*, *70*, 1729–1741.

Barker, C. (1996), *Thermal Modeling of Petroleum Generation: Theory and Applications*, Elsevier, Amsterdam.

Barker, C. E., and R. H. Goldstein (1990), Fluid-inclusion technique for determining maximum temperature in calcite and its comparison to the vitrinite reflectance geothermometer, *Geology*, *18*(10), 1003–1006, doi:10.1130/0091-7613(1990)018<1003:FITFDM>2.3.CO;2.

Barker, Ch. E., and M. J. Pawlewicz (1986), The correlation of vitrinite reflectance with maximum temperature in humic organic matter, In: Buntebarth, G., and L. Stegena (Eds.), *Paleogeothermics*, Springer, Berlin, 79–93.

Båth, M. (1966), Earthquake energy and magnitude, *Phys. Chem. Earth*, *7*, 115–165, doi:10.1016/0079-1946(66)90003-6.

Batzle, M., and Z. Wang (1992), Seismic properties of pore fluids, *Geophysics*, *57*(11), 1396–1408, doi:10.1190/1.1443207.

Beardsmore, G. R., and J. P. Cull (2001), *Crustal Heat Flow—A Guide to Measurement and Modeling*, Cambridge University Press, Edinburgh.

Bekins, B. A., A. M. McCaffrey, and S. J. Dreiss (1994), The influence of kinetics on the smectite to illite transition in the Barbados accretionary prism, *J. Geophys. Res.*, *99*(B9), 18147–18158, doi:10.1029/94JB01187.

Ben-Avraham, Z., G. Smith, M. Reshef, and E. Jungslager (2002), Gas hydrate and mud volcanoes on the southwest African continental margin off South Africa, *Geology*, *30*(10), 927–930, doi:10.1130/0091-7613(2002)030<0927:GHAMVO>2.0.CO;2.

Berkowitz, R. (2015), Active mud volcano field discovered off southeast Alaska, *Eos*, *96*, doi:10.1029/2015EO040447.

Bethke, C. M. (1986), Inverse hydrogeologic analysis of the distribution and origin of Gulf Coast-type geopressured zones, *J. Geophys. Res.*, *91*(B6), 6535–6545, doi:10.1029/JB091iB06p06535.

Biot, M. A. (1941), General Theory of Three-Dimensional Consolidation, *J. Appl. Phys.*, *12*(2), 155–164, doi:10.1063/1.1712886.

Blackwell, D. D., J. L. Steele, and C. A. Brott (1980), The terrain effect on terrestrial heat flow, *J. Geophys. Res.*, *85*(B9), 4757–4772, doi:10.1029/JB085iB09p04757.

Blinova, V. N., M. C. Comas, M. K. Ivanov, E. N. Poludetkina, and T. V. Matveeva (2011), Active mud volcanism in the West Alboran Basin: Geochemical evidence of hydrocarbon seepage, *Mar. Pet. Geol.*, *28*(8), 1483–1504, doi:10.1016/j.marpetgeo.2011.06.001.

Boetius, A., and F. Wenzhöfer (2013), Seafloor oxygen consumption fuelled by methane from cold seeps, *Nat. Geosci.*, *6*, 725–734, doi:10.1038/ngeo1926.

Bohrmann, G., et al. (2003), Mud volcanoes and gas hydrates in the Black Sea: New data from Dvurechenskii and Odessa mud volcanoes, *Geo-Mar. Lett.*, *23*(3-4), 239–249, doi:10.1007/s00367-003-0157-7.

Bohrmann, G., et al. (2011), Report and preliminary results of RV MARIA S. MERIAN Cruise MSM 15/2, Istanbul (Turkey) — Piraeus (Greece), 10 May - 2 June 2010. Origin and structure of methane, gas hydrates and fluid flows in the Black Sea, Berichte, Fachbereich Geowissenschaften, Universität Bremen, No. 278, Bremen, 130 p.

Bonini, M. (2008), Elliptical mud volcano caldera as stress indicator in an active compressional setting (Nirano, Pede-Apennine margin, northern Italy), *Geology*, *36*(2), 131–134, doi:10.1130/G24158A.1.

Bonini, M. (2009), Mud volcano eruptions and earthquakes in the Northern Apennines and Sicily, Italy, *Tectonophys.*, *474*(3-4), 723–735, doi:10.1016/j.tecto.2009.05.018.

Bonini, M. (2012), Mud volcanoes: Indicators of stress orientation and tectonic controls, *Earth-Sci. Rev.*, *115*, 121–152, doi:10.1016/j.earscirev.2012.09.002.

Boudreau, B. P., B. S. Gardiner, and B. D. Johnson (2001), Rate of growth of isolated bubbles in sediments with a diagenetic source of methane, *Limnol. Oceanogr.*, *46*(3), 616–622, doi:10.4319/lo.2001.46.3.0616.

Brown, K. M. (1990), The nature and hydrogeologic significance of mud diapirs and diatremes for accretionary systems, *J. Geophys. Res.*, *95*(B6), 8969–8982, doi: 10.1029/JB095iB06p08969.

Brown, K., and G. K. Westbrook (1988), Mud diapirism and subcretion in the Barbados Ridge Accretionary Complex: The role of fluids in accretionary processes, *Tectonics*, *7*(3), 613–640, doi:10.1029/TC007i003p00613.

Brown, K. M., D. M. Saffer, and B. A. Bekins (2001), Smectite diagenesis, pore-water freshening, and fluid flow at the toe of the Nankai wedge, *Earth Planet. Sci. Lett.*, *194*(1–2), 97–109, doi:10.1016/S0012-821X(01)00546-5.

Buerk, D., I. Klaucke, H. Sahling, and W. Weinrebe (2010), Morpho-acoustic variability of cold seeps on the continental slope offshore Nicaragua: Result of fluid flow interaction with sedimentary processes, *Mar. Geol.*, *275*, 53–65, doi:10.1016/j.margeo.2010.04.007.

Bürk, D. (2007), Geoacoustic investigations of cold vents and sedimentary processes at the active continental margin offshore Nicaragua, dissertation thesis, 163 pp., Christian-Albrechts-Universität, Kiel, Germany.

Bustin, R. M. (1983), Heating during thrust faulting in the Rocky Mountains: friction or fiction?, *Tectonophys.*, *95*(3–4), 309–328, doi:10.1016/0040-1951(83)90075-6.

Byerlee, J. D. (1978), Friction of rocks, *Pure Appl. Geophys.*, *116*(4–5), 615–626, doi: 10.1007/BF00876528.

Calais, E., C. DeMets, and J. M. Nocquet (2003), Evidence for a post-3.16-Ma change in Nubia—Eurasia—North America plate motions?, *Earth Planet. Sci. Lett.*, *216*(1–2), 81–92, doi:10.1016/S0012-821X(03)00482-5.

Camerlenghi, A., and F. McCoy (1990), Physiography and structure of Bacino Bannock (Eastern Mediterranean), *Geo-Mar. Lett.*, *10*(1), 23–30, doi:10.1007/BF02431018.

Camerlenghi, A., and G. A. Pini (2009), Mud volcanoes, olistostromes and Argille scagliose in the Mediterranean region, *Sedimentology*, *56*(1), 319–365, doi:10.1111/j.1365-3091.2008.01016.x.

Camerlenghi, A., M. B. Cita, B. Della Vedova, N. Fusi, L. Mirabile, and G. Pellis (1995), Geophysical evidence of mud diapirism on the Mediterranean Ridge accretionary complex, *Mar. Geophys. Res.*, *17*(2), 115–141, doi:10.1007/BF01203423.

Caprais, J.-C., N. Lanteri, P. Crassous, P. Noel, L. Bignon, P. Rousseaux, P. Pignet, and A. Khripounoff (2010), A new CALMAR benthic chamber operating by submersible: First application in the cold-seep environment of Napoli mud volcano (Mediterranean Sea), *Limnol. Oceanogr. Methods*, *8*(6), 304–312, doi:10.4319/lom.2010.8.304.

Cartwright, J., M. Huuse, and A. Aplin (2007), Seal bypass systems, *AAPG Bull.*, *91*(8), 1141–1166, doi:10.1306/04090705181.

Ceramicola, S., D. Praeg, A. Cova, D. Accettella, and M. Zecchin (2014), Seafloor distribution and last glacial to postglacial activity of mud volcanoes on the Calabrian accretionary prism, Ionian Sea, *Geo-Mar. Lett.*, *34*(2-3), 111–129, doi:10.1007/s00367-013-0354-y.

Chamot-Rooke, N., A. Rabaute, and C. Kreemer (2005a), Western Mediterranean Ridge mud belt correlates with active shear strain at the prism-backstop geological contact, *Geology*, *33*(11), 861–864, doi:10.1130/G21469.1.

Chamot-Rooke, N., et al. (2005b), DOTMED, Deep Offshore Tectonics of the Mediterranean, A synthesis of deep marine data in the Eastern Mediterranean, Mérmoire de la Société Géologique de France & American Association of Petroleum Geologists, numéro spécial, 177, pp.64.

Chandrasekhar, S. (1961), *Hydrodynamic and Hydromagnetic Stability*, 652 pp., Oxford Univ., Oxford, U. K.

Charlou, J. L., J. P. Donval, T. Zitter, N. Roy, P. Jean-Baptiste, J. P. Foucher, and J. Woodside (2003), Evidence of methane venting and geochemistry of brines on mud volcanoes of the eastern Mediterranean Sea, *Deep Sea Res. Part I Oceanogr. Res. Pap.*, *50*(8), 941–958, doi:10.1016/S0967-0637(03)00093-1.

Chaumillon, E., and J. Mascle (1997), From foreland to forearc domains: New multichannel seismic reflection survey of the Mediterranean ridge accretionary complex (Eastern Mediterranean), *Mar. Geol.*, *138*(3–4), 237–259, doi:10.1016/S0025-3227(97)00002-9.

Chaumillon, E., J. Mascle, and J. Hoffmann (1996), Deformation of the western Mediterranean Ridge: importance of Messinian evaporitic formations, *Tectonophys.*, *263*(1–4), 163–190, doi:10.1016/S0040-1951(96)00035-2.

Chen, S.-C., S.-K. Hsu, Y. Wang, S.-H. Chung, P.-C. Chen, C.-H. Tsai, C.-S. Liu, H.-S. Lin, and Y.-W. Lee (2014), Distribution and characters of the mud diapirs and mud volcanoes off southwest Taiwan, *J. Asian Earth Sci.*, *92*, 201–214, doi:10.1016/j.jseaes.2013.10.009.

Chen, Y., T. Liu, and X. Chen (2015), Velocity analysis using similarity-weighted semblance, *Geophysics*, *80*(4), A75–A82, doi:10.1190/GEO2014-0618.1.

Cheng, A.-L., and W.-L. Huang (2004), Selective adsorption of hydrocarbon gases on clays and organic matter, *Org. Geochem.*, *35*(4), 413–423, doi:10.1016/j.orggeochem.2004.01.007.

Chigira, M., and K. Tanaka (1997), Structural features and the history of mud volcanoes in Southern Hokkaido, Northern Japan, *J. Geol. Soc. Japan*, *103*, 781–791, doi:10.5575/geosoc.103.781.

Chiodini, G., W. D'Alessandro, and F. Parello (1996), Geochemistry of gases and waters discharged by the mud volcanoes at Paterno, Mt. Etna (Italy), *Bull. Volcanol.*, *58*, 51–58, doi:10.1007/s004450050125.

Chiu, J.-K., W.-H. Tseng, and C.-S. Liu (2006), Distribution of gassy sediments and mud volcanoes offshore southwestern Taiwan, *Terr. Atmos. Ocean. Sci.*, *17*, 709–722.

Claerbout, J. F., and J. L. Black (2005), *Basic earth imaging (Version 2.4)*, Stanford Exploration Project, http://sepwww.stanford.edu/sep/prof/, accessed 14 December 2015.

Clauser, C., and E. Huenges (1995), Thermal Conductivity of Rocks and Minerals, In: T. J. Ahrens (ed.), Rock Physics and Phase Relations—a Handbook of Physical Constants, *AGU Reference Shelf*, *3*, 105–126.

Clift, P., and P. Vannucchi (2004), Controls on tectonic accretion versus erosion in subduction zones: Implications for the origin and recycling of the continental crust, *Rev. Geophys.*, *42*, RG2001, doi:10.1029/2003RG000127.

Cohen, A. (1993), Halite-clay interplay in the Israeli Messinian, *Sediment. Geol.*, *86*(3–4), 211–228, doi:10.1016/0037-0738(93)90023-X.

Colten-Bradley, V. A. (1987), Role of pressure in smectite dehydration—Effects on geopressure and smectite-to-illite transformation, *AAPG Bull.*, *71*(11), 1414–1427.

Corey, A. T. (1949), *Influence of shape on the fall velocity of sand grains*, MS thesis, Colo. A & M College, Fort Collins, Colo.

Corselli, C., and F. S. Aghib (1987), Brine formation and gypsum precipitation in the Bannock Basin, eastern Mediterranean, *Mar. Geol.*, *75*(1–4), 185–199, doi:10.1016/0025-3227(87)90103-4.

Corselli, C., and D. Basso (1996), First evidence of benthic communities based on chemosynthesis on the Napoli mud volcano (Eastern Mediterranean) *Mar. Geol.*, *132*(1–4), 227–239, doi:10.1016/0025-3227(95)00163-8.

Coussot, P., and J. M. Piau (1994), On the behavior of fine mud suspensions, *Rheol. Acta*, *33*, 175–184, doi:10.1007/BF00437302.

Craig, H. (1961), Isotopic variations in meteoric waters, *Science*, *133*, 1702–1708, doi:10.1126/science.133.3465.1702.

Craig, H., J. E. Lupton, J. A. Welhan, and R. Poreda (1978), Helium isotope ratios in Yellowstone and Lassen Park volcanic gases, *Geophys. Res. Lett.*, *5*, 897–900, doi:10.1029/GL005i011p00897.

Crosdale, P. J., B. B. Beamish, and M. Valix (1998), Coalbed methane sorption related to coal composition, *Int. J. Coal Geol.*, *35*(1–4), 147–158, doi:10.1016/S0166-5162(97)00015-3.

Crutchley, G. J., D. R. A. Fraser, I. A. Pecher, A. R. Gorman, G. Maslen, and S. A. Henrys (2015), Gas migration into gas hydrate-bearing sediments on the southern Hikurangi margin of New Zealand, *J. Geophys. Res. Solid Earth*, *120*, 725–743, doi:10.1002/2014JB011503.

da Cruz, F., S. Emam, M. Prochnow, J.-N. Roux, and F. Chevoir (2005), Rheophysics of dense granular materials: Discrete simulation of plane shear flows, *Phys. Rev. E*, *72*(2), 021309, doi:10.1103/PhysRevE.72.021309.

Dade, W. B., and H. E. Huppert (1998), Long-runout rockfalls, *Geology*, *26*, 803–806, doi:10.1130/0091-7613(1998)026<0803:LRR>2.3.CO;2.

Dählmann, A., and G. J. de Lange (2003), Fluid-sediment interactions at Eastern Mediterranean mud volcanoes: a stable isotope study from ODP Leg 160, *Earth Planet. Sci. Lett.*, *212*(3–4), 377–391, doi:10.1016/S0012-821X(03)00227-9.

Daigle, H., and B. Dugan (2014), Pore size controls on the base of the methane hydrate stability zone in the Kumano Basin, offshore Japan, *Geophys. Res. Lett.*, *41*, doi:10.1002/2014GL062135.

Damm, E., and G. Budéus (2003), Fate of vent-derived methane in seawater above the Håkon Mosby mud volcano (Norwegian Sea), *Mar. Chem.*, *82*, 1–11, doi:10.1016/S0304-4203(03)00031-8.

Davies, R. J., and S. A. Stewart (2005), Emplacement of giant mud volcanoes in the South Caspian Basin: 3D seismic reflection imaging of their root zones, *J. Geol. Soc.*, *162*, 1–4, doi:10.1144/0016-764904-082.

Davies, R. J., M. Brumm, M. Manga, R. Rubiandini, R. Swarbrick, and M. Tingay (2008), The East Java mud volcano (2006 to present): An earthquake or drilling trigger?, *Earth Planet. Sci. Lett.*, *272*(3), 627–638, doi:10.1016/j.epsl.2008.05.029.

Davis, D. M., and T. Engelder (1985), The role of salt in fold-and-thrust belts, *Tectonophys.*, *119*(1–4), 67–88, doi:10.1016/0040-1951(85)90033-2.

Davis, D., J. Suppe, and F. A. Dahlen (1983), Mechanics of fold-and-thrust belts and accretionary wedges, *J. Geophys. Res.*, *88*(B2), 1153–1172, doi:10.1029/JB088iB02p01153.

De Lange, G. J., and H.-J. Brumsack (1998), Pore-water indications for the occurrence of gas hydrates in eastern Mediterranean mud dome structures, In: Robertson, A. H. F., et al. (eds.), *Proc. Ocean Drill. Program Sci. Res.*, *160*, 569–574, doi: 10.2973/odp.proc.sr.160.042.1998.

Della Vedova, B., G. Pellis, A. Camerlenghi, J. P. Foucher, and F. Harmegnies (2003), Thermal history of deep-sea sediments as a record of recent changes in the deep circulation of the eastern Mediterranean, *J. Geophys. Res.*, *108*(C9), 8110, doi: 10.1029/2002JC001402.

DeMets, C., R. G. Gordon, D. F. Argus, and S. Stein (1994), Effect of recent revisions to the geomagnetic reversal time scale on estimates of current plate motions, *Geophys. Res. Lett.*, *21*, 2191–2194. doi:10.1029/94GL02118.

de Voogd, B., C. Truffert, N. Chamot-Rooke, P. Huchon, S. Lallemant, and X. Le Pichon (1992), Two-ship deep seismic soundings in the basins of the Eastern Mediterranean Sea (Pasiphae cruise), *Geophys. J. Int.*, *109*(3), 536–552, doi:10.1111/j.1365-246X.1992.tb00116.x.

Dewey, J. F., M. L. Helman, E. Turco, D. H. W. Hutton, and S. D. Knott (1989), Kinematics of the western Mediterranean, in *Alpine Tectonics*, edited by M. P. Coward, D. Dietrich, and R. G. Park, *Geol. Soc. Spec. Publ.*, *45*, 265–283.

Dietrich, W. E. (1982), Settling Velocity of Natural Particles, *Water Resour. Res.*, *18*(6), 1615–1626, doi:10.1029/WR018i006p01615.

Dimitrov, L. I. (2002), Mud volcanoes—the most important pathway for degassing deeply buried sediments, *Earth Sci. Rev.*, *59*(1-4), 49–76, doi:10.1016/S0012-8252(02)00069-7.

Döll, P., and K. Fiedler (2008), Global-scale modeling of groundwater recharge, *Hydrol. Earth Syst. Sci.*, *12*, 863–885, doi:10.5194/hess-12-863-2008.

Domenico, S. N. (1977), Elastic properties of unconsolidated porous sand reservoirs, *Geophysics*, *42*(7), 1339–1368, doi:10.1190/1.1440797.

Driesner, T., and C. A. Heinrich (2007), The system H_2O-NaCl. Part I: Correlation formulae for phase relations in temperature-pressure-composition space from 0 to 1000°C, 0 to 5000 bar, and 0 to 1 X_{NaCl}, *Geochim. Cosmochim. Acta*, *71*(20), 4880–4901, doi:10.1016/j.gca.2006.01.033.

Drury, M. J. (1986), *Thermal Conductivity, Thermal Diffusivity, Density and Porosity of Crystalline Rocks*, Earth Physics Branch Open File Report no.86–5, Earth Physics Branch, Ottawa.

Duan, M., and S. Mao (2006), A thermodynamic model for calculating methane solubility, density and gas phase composition of methane-bearing aqueous fluids from 273 to 523 K and 1 to 2000 bar, *Geochim. Cosmochim. Acta*, *70*(13), 3369–3386, doi:10.1016/j.gca.2006.03.018.

Dupré, S., et al. (2007), Seafloor geological studies above active gas chimneys off Egypt (Central Nile Deep Sea Fan), *Deep Sea Res. Part I Oceanogr. Res. Pap.*, *54*(7), 1146–1172, doi:10.1016/j.dsr.2007.03.007.

Ekström, G., and C. P. Stark (2013), Simple Scaling of Catastrophic Landslide Dynamics, *Science*, *339*(6126), 1416–1419, doi:10.1126/science.1232887.

Elderfield, H., and A. Schultz (1996), Mid-ocean ridge hydrothermal fluxes and the chemical composition of the ocean, *Annu. Rev. Earth Planet. Sci.*, *24*, 191–224, doi:10.1146/annurev.earth.24.1.191.

Emeis, K.-C., Robertson, A. H. F., Richter, C., et al. (1996), *Proc. Ocean Drill. Program, Init. Repts.*, *160*, doi:10.2973/odp.proc.ir.160.1996.

Emerman, S. H., and D. L. Turcotte (1983), A fluid model for the shape of accretionary wedges, *Earth Planet. Sci. Lett.*, *63*(3), 379–384, doi:10.1016/0012-821X(83)90111-5.

Emery, K. O., B. C. Heezen, and T. D. Allan (1966), Bathymetry of the eastern Mediterranean Sea, *Deep Sea Res. Oceanogr. Abstr.*, *13*(2), 173–192, doi:10.1016/0011-7471(66)91098-9.

Erickson, A. J. (1970), The measurement and interpretation of heat flow in the Mediterranean and Black Seas, Ph.D. thesis, 272 pp., Mass. Inst. of Technol., Cambridge, Mass.

Erickson, S. N., and R. D. Jarrard (1998), Velocity-porosity relationships for water-saturated siliciclastic sediments, *J. Geophys. Res.*, *103*(B12), 30385–30406, doi:10.1029/98JB02128.

Etiope, G., and A. V. Milkov (2004), A new estimate of global methane flux from onshore and shallow submarine mud volcanoes to the atmosphere, *Envir. Geol.*, *46*, 997–1002, doi:10.1007/s00254-004-1085-1.

Expedition 315 Scientists (2009), Expedition 315 Site C0002, *Proc. Integr. Ocean Drill. Program*, *314/315/316*, 76 pp., doi:10.2204/iodp.proc.314315316.124.2009.

Faugéres, J. C., É. Gonthier, C. Bobier, and R. Griboulard (1997), Tectonic control on sedimentary processes in the southern termination of the Barbados Prism, *Mar. Geol.*, *140*(1–2), 117–140, doi:10.1016/S0025-3227(96)00102-8.

Feistel, R. (2008), A Gibbs function for seawater thermodynamics for −6 to 80°C and salinity up to 120 g kg^{-1}, *Deep Sea Res. Part I*, *55*(12), 1639–1671, doi:10.1016/j.dsr.2008.07.004.

Fernandes, R. M. S., B. A. C. Ambrosius, R. Noomen, L. Bastos, M. J. R. Wortel, W. Spakman, and R. Govers (2003), The relative motion between Africa and Eurasia as derived from ITRF2000 and GPS data, *Geophys. Res. Lett.*, *30*, 1828, doi:10.1029/2003GL017089.

Fernandes, R. M. S., J. M. Miranda, R. M. L. Meijininger, M. S. Bos, R. Noomen, L. Bastros, B. A. C. Ambrousius, and R. E. M. Riva (2007), Surface velocity field of the Ibero-Magh-rebian segment of the Eurasia-Nubia plate boundary, *Geophys. J. Int.*, *169*, 315–324, doi:10.1111/j.1365-246X.2006.03252.x.

Fernández-Ibáñez, F., J. I. Soto, M. D. Zoback, and J. Morales (2007), Present-day stress field in the Gibraltar Arc (western Mediterranean), *J. Geophys. Res.*, *112*, B08404, doi:10.1029/2006JB004683.

Feseker, T., A. Dählmann, J.-P. Foucher, and F. Harmegnies (2009), *In-situ* sediment temperature measurements and geochemical porewater data suggest highly dynamic fluid flow at Isis mud volcano, eastern Mediterranean Sea, *Mar. Geol.*, *261*(1–4), 128–137, doi:10.1016/j.margeo.2008.09.003.

Feseker, T., K. Brown, C. Blanchet, F. Scholz, M. Nuzzo, A. Reitz, M. Schmidt, and C. Hensen (2010), Active mud volcanoes on the upper slope of the western Nile deep-sea fan—first results from the P362/2 cruise of R/V Poseidon, *Geo-Mar. Lett.*, *30*(3–4), 169–186, doi:10.1007/s00367-010-0192-0.

Feseker, T., A. Boetius, F. Wenzhöfer, J. Blandin, K. Olu, D. R. Yoerger, R. Camilli, C. R. German, and D. de Beer (2014), Eruption of a deep-sea mud volcano triggers rapid sediment movement, *Nat Commun.*, *5*, 5385, doi:10.1038/ncomms6385.

Fink, H. G., M. Strasser, M. Römer, M. Kölling, K. Ikehara, T. Kanamatsu, D. Dinten, A. Kioka, T. Fujiwara, K. Kawamura, S. Kodaira, and G. Wefer (2014), Evidence for Mass Transport Deposits at the IODP JFAST-Site in the Japan Trench, in *Submarine Mass Movements and Their Consequences*, *Advances in Natural and Technological Hazards Research*, *37*, edited by S. Krastel et al., pp. 33–43, Springer International Publishing, doi:10.1007/978-3-319-00972-8_4.

Fomel, S. (2007a), Shaping regularization in geophysical-estimation problems, *Geophysics*, *72*(2), R29–R36, doi:10.1190/1.2433716.

Fomel, S. (2007b), Local seismic attributes, *Geophysics*, *72*(3), A29–A33, doi:10.1190/1.2437573.

Fomel, S. (2009), Velocity analysis using *AB* semblance, *Geophys. Prospect.*, *57*, 311–321, doi:10.1111/j.1365-2478.2008.00741.x.

Foster, D. J., and C. C. Mosher (1992), Suppression of multiple reflections using the Radon transform, *Geophysics*, *57*(3), 386–395, doi:10.1190/1.1443253.

Fruehn, J., T. Reston, R. von Huene, and J. Bialas (2002), Structure of the Mediterranean Ridge accretionary complex from seismic velocity information, *Mar. Geol.*, *186*(1-2), 43–58, doi:10.1016/S0025-3227(02)00172-X.

Fryer, P. (2012), Serpentinite Mud Volcanism: Observations, Processes, and Implications, *Ann. Rev. Mar. Sci.*, *4*(1), 345–373, doi:10.1146/annurev-marine-120710-100922.

Fryer, P., C. G. Wheat, and M. J. Mottl (1999), Mariana blueschist mud volcanism: Implications for conditions within the subduction zone, *Geology*, *27*(2), 103–106, doi:10.1130/0091-7613(1999)?027<0103:MBMVIF>?2.3.CO;2.

Fryer, P., J. Gharib, K. Ross, I. Savov, and M. J. Mottl (2006), Variability in serpentinite mudflow mechanisms and sources: ODP drilling results on Mariana forearc seamounts, *Geochem. Geophys. Geosyst.*, *7*, Q08014, doi:10.1029/2005GC001201.

Fujioka, K. (2012), Serpentine seamounts in the Izu-Bonin-Mariana Trenches and serpentine bodies in the Outer zone of the Southwest Japan, *Res. Rep. Kanagawa prefect. Mus. Nat. Hist.*, *14*, 181–192. [in Japanese]

Fujioka, K., T. Tanaka, and K. Aoike (1995), Serpentine Seamount in Izu-Bonin and Mariana Forearcs –Observation by a submersible and its relation to onland serpentine belt–, *J. Geograph. (Chigaku Zasshi)*, *104*(3), 473–494, doi:10.5026/jgeography.104.3_473. [in Japanese with English Abstr.]

Fukushima, Y., J. Mori, M. Hashimoto, and Y. Kano (2009), Subsidence associated with the LUSI mud eruption, East Java, investigated by SAR interferometry, *Mar. Pet. Geol.*, *26*(9), 1740–1750, doi:10.1016/j.marpetgeo.2009.02.001.

Fusi, N., and N. H. Kenyon (1996), Distribution of mud diapirism and other geological structures from long-range sidescan sonar (GLORIA) data, in the Eastern Mediterranean Sea, *Mar. Geol.*, *132*(1-4), 21–38, doi:10.1016/0025-3227(95)00151-4.

Gamberi, F., and M. Rovere (2010), Mud diapirs, mud volcanoes and fluid flow in the rear of the Calabrian Arc Orogenic Wedge (southeastern Tyrrhenian sea), *Basin Res.*, *22*(4), 452–464, doi:10.1111/j.1365-2117.2010.00473.x.

Gardiner, B. S., B. P. Boudreau, and B. D. Johnson (2003), Growth of disk-shaped bubbles in sediments, *Geochim. Cosmochim. Acta*, *67*, 1485–1494, doi:10.1016/S0016-7037(02)01072-4.

Gardner, J. M. (2001), Mud Volcanoes revealed and sampled on the Western Moroccan Continental Margin, *Geophys. Res. Lett.*, *28*(2), 339–342, doi:10.1029/2000GL012141.

Gardner, J. M., and P. Shashkin (2000), Gulf of Cadiz/Moroccan margin (leg 2). Mud diapirism and mud volcanism study. Side scan sonar. In: Kenyon, N. H., M. K. Ivanov, M.K., A. M. Akhmetzhanov, and G. G. Akhmanov (Eds.), Multidisciplinary Study of Geological Processes on the North East Atlantic and Western Mediterranean Margins, IOC Technical Series, vol. 56.

GDR MiDi (2004), On dense granular flows, *Eur. Phys. J. E*, *14*(4), 341–365, doi:10.1140/epje/i2003-10153-0.

Gennari, G., S. Spezzaferri, M. C. Comas, A. Rüggeberg, C. Lopez-Rodriguez, and L. M.

Pinheiro (2013), Sedimentary sources of the mud-breccia and mud volcanic activity in the Western Alboran Basin, *Mar. Geol.*, *339*, 83–95, doi:10.1016/j.margeo.2013.04.002.

Gieskes, J., et al. (1989), Hydrogeochemistry in the Barbados Accretionary Complex: ODP leg 110, *Palaeogeogr. Palaeoclimatol. Palaeoecol.*, *71*, 83–96, doi:10.1016/0031-0182(89)90031-X.

Ginsburg, G. D., A. V. Milkov, V. A. Soloviev, A. V. Egorov, G. A. Cherkashev, P. R. Vogt, K. Crane, T. D. Lorenson, and M. D. Khutorskoy (1999), Gas hydrate accumulation at the Håkon Mosby Mud Volcano, *Geo-Mar. Lett.*, *19*, 57–67, doi:10.1007/s003670050093.

Giordano, D., J. K. Russell, and D. B. Dingwell (2008), Viscosity of magmatic liquids: A model, *Earth Planet. Sci. Lett.*, *271*, 123–134, doi:10.1016/j.epsl.2008.03.038.

Gleeson, T., K. M. Befus, S. Jasechko, E. Luijendijk, and M. B. Cardenas (2015), The global volume and distribution of modern groundwater, *Nat. Geosci.*, doi: 10.1038/ngeo2590.

Godon, A., N. Jendrzejewski, M. Castrec-Rouelle, A. Dia, F. Pineau, J. Boulègue, and M. Javoy (2004), Origin and evolution of fluids from mud volcanoes in the Barbados accretionary complex, *Geochim. Cosmochim. Acta*, *68*(9), 2153–2165, doi: 10.1016/j.gca.2003.08.021.

Goldfinger, C. (2011), Submarine Paleoseismology Based on Turbidite Records, *Annu. Rev. Mar. Sci.*, *3*, 35–66, doi:10.1146/annurev-marine-120709-142852.

Goto, S., M. Yamano, M. Kinoshita, and O. Matsubayashi (2007), Heat flow distribution at a mud volcano in Kumano Basin, east of Kii Peninsula, central Japan, *Eos Trans. AGU*, *88*(52), Fall Meet. Suppl., Abstract V13B-1342.

Grevemeyer, I., et al. (2004), Fluid flow through active mud dome Mound Culebra offshore Nicoya Peninsula, Costa Rica: evidence from heat flow surveying, *Mar. Geol.*, *207*(1-4), 145–157, doi:10.1016/j.margeo.2004.04.002.

Gutenberg, B., and C. F. Richter (1944), Frequency of earthquakes in California, *Bull. Seismol. Soc. Am.*, *34*(4), 185–188.

Gutscher, M.-A., N. Kukowski, J. Malavieille, and S. Lallemand (1996), Cyclical behavior of thrust wedges: Insights from high basal friction sandbox experiments, *Geology*, *24*(2), 135–138, doi:10.1130/0091-7613(1996)024<0135:CBOTWI>2.3.CO;2.

Gutscher, M.-A., N. Kukowski, J. Malavieille, and S. Lallemand (1998), Material transfer in accretionary wedges from analysis of a systematic series of analog experiments, *J. Struct. Geol.*, *20*(4), 407–416, doi:10.1016/S0191-8141(97)00096-5.

Gutscher, M.-A., S. Dominguez, G. K. Westbrook, P. Gente, N. Babonneau, T. Mulder, E. Gonthier, R. Bartolome, J. Luis, F. Rosas, and Delila and DelSis Scientific Teams (2009a), Tectonic shortening and gravitational spreading in the Gulf of Cadiz accretionary wedge: observations from multi-beam bathymetry and seismic profiling, *Mar. Petrol. Geol.*, *26*, 647–659, doi:10.1016/j.marpetgeo.2007.11.008.

Gutscher, M.-A., S. Dominguez, G. K. Westbrook, and P. Leroy (2009b), Deep structure, recent deformation and analog modeling of the Gulf of Cadiz accretionary wedge: Implications for the 1755 Lisbon earthquake, *Tectonophys.*, *475*, 85–97, doi:10.1016/j.tecto.2008.11.031.

Haese, R. R., C. Hensen, and G. J. de Lange (2006), Pore water geochemistry of eastern Mediterranean mud volcanoes: Implications for fluid transport and fluid origin, *Mar. Geol.*, *225*(1–4), 191–208, doi:10.1016/j.margeo.2005.09.001.

Hale, D. (2009), Structure-oriented smoothing and semblance, Technical Report CWP-635, Center for Wave Phenomena, Colorado School of Mines, Golden, CO.

Hamamoto, H., M. Yamano, and S. Goto (2005), Heat flow measurement in shallow seas through long-term temperature monitoring, *Geophys. Res. Lett.*, *32*, L21311, doi:10.1029/2005GL024138.

Hamamoto, H., M. Yamano, S. Goto, M. Kinoshita, K. Fujino, and K. Wang (2011), Heat flow distribution and thermal structure of the Nankai subduction zone off the Kii Peninsula, *Geochem. Geophys. Geosyst.*, *12*, Q0AD20, doi:10.1029/2011GC003623.

Harris, R. N., F. Schmidt-Schierhorn, and G. Spinelli (2011), Heat flow along the NanTroSEIZE transect: Results from IODP Expeditions 315 and 316 offshore the Kii Peninsula, Japan, *Geochem. Geophys. Geosyst.*, *12*, Q0AD16, doi:10.1029/2011GC003593.

Heasler, H. P., and R. C. Surdam (1985), Thermal evolution of coastal California with application to hydrocarbon maturation, *AAPG Bull.*, *69*, 1386–1400.

Helgerud, M. B., W. F. Waite, S. H. Kirby, and A. Nur (2009), Elastic wave speeds and moduli in polycrystalline ice Ih, sI methane hydrate, and sII methane-ethane hydrate, *J. Geophys. Res.*, *114*, B02212, doi:10.1029/2008JB006132.

Henry, P., X. Le Pichon, S. Lallemant, J.-P. Foucher, G. Westbrook, and M. Hobart (1990), Mud volcano field seaward of the Barbados Accretionary Complex: A deep-towed side scan sonar survey, *J. Geophys. Res.*, *95*(B6), 8917–8929, doi:10.1029/JB095iB06p08917.

Henry, P., et al. (1996), Fluid flow in and around a mud volcano field seaward of the Barbados accretionary wedge: Results from Manon cruise, *J. Geophys. Res.*, *101*(B9), 20297–20323, doi:10.1029/96JB00953.

Hensen, C., K. Wallmann, M. Schmidt, C. R. Ranero, and E. Suess (2004), Fluid expulsion related to mud extrusion off Costa Rica—A window to the subducting slab, *Geology*, *32*, 201–204, doi:10.1130/G20119.1.

Hensen, C., M. Nuzzo, E. Hornibrook, L. M. Pinheiro, B. Bock, V. H. Magalhães, and W. Brückmann (2007), Sources of mud volcano fluids in the Gulf of Cadiz—indications for hydrothermal imprint, *Geochim. Cosmochim. Acta*, *71*(5), 1232–1248, doi:10.1016/j.gca.2006.11.022.

Herschel, W. H., and R. Bulkley (1926), Konsistenzmessungen von Gummi-Benzollösungen, *Kolloid-Zeitschrift*, *39*(4), 291–300, doi:10.1007/BF01432034.

Hess, K. U., and D. B. Dingwell (1996), Viscosities of hydrous leucogranitic melts: A non-Arrhenian model, *Am. Mineral.*, *81*, 1297–1300.

Heuret, A., C. P. Conrad, F. Funiciello, S. Lallemand, and L. Sandri (2012), Relation between subduction megathrust earthquekes, trench sediment thickness and upper plate strain, *Geophys. Res. Lett.*, *39*, L05304, doi:10.1029/2011GL050712.

Hieke, W., F. Werner, and H.-W. Schenke (1996), Geomorphological study of an area with mud diapirs south of Crete (Mediterranean Ridge), *Mar. Geol.*, *132*(1-4), 63–93, doi:10.1016/0025-3227(95)00154-9.

Higgins, G. E., and J. B. Saunders (1974), Mud volcanoes—Their nature and origin, in *Contributions to the Geology and Paleobiology of the Caribbean and Adjacent Areas. Dedicated to the 80th Birthday of Hans G. Kugler*, *Verhandlungen Naturforschenden Gesellschaft von Basel*, vol. *84*, edited by P. Jung et al., pp. 1–520, Naturforsch. Ges., Basel, Switzerland.

Hill, R. (1952), The Elastic Behaviour of a Crystalline Aggregate, *Proc. Phys. Soc. Sect. A*, *65*(5), 349–354, doi:10.1088/0370-1298/65/5/307.

Hinrichs, K.-U., J. M. Hayes, S. P. Sylva, P. G. Brewer, and E. F. DeLong (1999), Methane-consuming archaebacteria in marine sediments, *Nature*, *398*, 802–805, doi: 10.1038/19751.

Horai, K. (1971), Thermal conductivity of Rock-Forming Minerals, *J. Geophys. Res.*, *76*(5), 1278–1308, doi:10.1029/JB076i005p01278.

Houweling, S., F. Dentener, and J. Lelieveld (2000), Simulation of preindustrial atmospheric methane to constrain the global source of natural wetlands, *J. Geophys. Res.*, *105*, 17,243–17,255, doi:10.1029/2000JD900193.

Huang, X., and M. H. García (1998), A Herschel-Bulkley model for mud flow down a slope, *J. Fluid Mech.*, *374*, 305–333, doi:10.1017/S0022112098002845.

Huguen, C., J. Mascle, E. Chaumillon, A. Kopf, J. Woodside, and T. Zitter (2004), Structural setting and tectonic control of mud volcanoes from the Central Mediterranean Ridge (Eastern Mediterranean), *Mar. Geol.*, *209*(1-4), 245–263, doi: 10.1016/j.margeo.2004.05.002.

Huguen, C., et al. (2009), Menes caldera, a highly active site of brine seepage in the Eastern Mediterranean sea: "In situ" observations from the NAUTINIL expedition (2003), *Mar. Geol.*, *261*(1–4), 138–152, doi:10.1016/j.margeo.2009.02.005.

Hyndman, R. D., K. Wang, and M. Yamano (1995), Thermal constraints on the seismogenic portion of the southwestern Japan subduction thrust, *J. Geophys. Res.*, *100*(B8), 15373–15392, doi:10.1029/95JB00153.

Ijiri, A. (2009), Origin of Fluid in Submarine Mud Volcanoes, *J. Geograph. (Chigaku Zasshi)*, *118*(3), 435–454, doi:10.5026/jgeography.118.435. [in Japanese with English Abstr.]

Inagaki, F. et al. (2009), Kumano Mud-Volcano Drilling: A Window to the Deep-Biosphere, *Cruise Report: CK09-01 Chikyu training cruise Leg. 1*, Japan Agency for Marine-Earth Science and Technology, Yokosuka, Japan.

Inagaki, F., Y. Kubo, and Expedition 906 Shipboard Scientists (2012), *JAMSTEC Chikyu Expedition 906: The Kumano Mud-Volcano Drilling II*, *Preliminary Expedition Report*, Japan Agency for Marine-Earth Science and Technology, Yokosuka, Japan.

Istadi, B. P., G. H. Pramono, P. Sumintadireja, and S. Alam (2009), Modeling study of growth and potential geohazard for LUSI mud volcano: East Java, Indonesia, *Mar. Pet. Geol.*, *26*, 1724–1739, doi:10.1016/j.marpetgeo.2009.03.006.

Ivanov, M. K., A. F. Limonov, and T. C. E. van Weering (1996), Comparative characteristics of the Black Sea and Mediterranean Ridge mud volcanoes, *Mar. Geol.*, *132*(1–4), 253–271, doi:10.1016/0025-3227(96)00165-X.

Ivanov, M. K., N. H. Kenyon, J.-S. Laberg, and V. N. Blinova (2010), Cold seeps, coral mounds and deep-water depositional systems of the Alboran Sea, Gulf of Cadiz and Norwegian Continental Margin. Preliminary results of investigations during the TTR-17 cruise of RV Professor Logachev, June–July, 2008: IOC Technical Series, 94, 144 pp.

Iversen, N., and B. B. Jørgensen (1993), Diffusion coefficients of sulfate and methane in marine sediments: Influence of porosity, *Geochim. Cosmochim. Acta*, *57*(3), 571–578, doi:10.1016/0016-7037(93)90368-7.

Iverson, R. M. (1997), The physics of debris flows, *Rev. Geophys.*, *35*(3), 245–296, doi: 10.1029/97RG00426.

Izumitani, N., T. Sagawa, M. Murayama, H. Asahi, H. Kitazato, Y. Nakamura, M. Shirai, J. Ashi, and H. Tokuyama (2009), Chronology and sedimentation of hyper salinity lake (Medee lake) in the eastern Mediterranean, in *Abstract L135-012 presented at Japan Geoscience Union Meeting 2009, Makuhari, Chiba, Japan, May 2009.*

Jamialahmadi, M., C. Branch, and J. Müller-Steinhagen (1994), Terminal bubble rise velocity in liquids, *Trans. Inst. Chem. Eng.*, *72*, 119–122.

Jerosch, K., M. Schlüter, J.-P. Foucher, A.-G. Allais, M. Klages, and C. Edy (2007), Spatial distribution of mud flows, chemoautotrophic communities, and biogeochemical habitats at Håkon Mosby Mud Volcano, *Mar. Geol.*, *243*, 1–17, doi:10.1016/j.margeo.2007.03.010.

Jiménez, J. A., and O. S. Madsen (2003), A Simple Formula to Estimate Settling Velocity of Natural Sediments, *J. Waterw. Port, Coastal, Ocean Eng.*, *129*(2), 70–78, doi:10.1061/(ASCE)0733-950X(2003)129:2(70).

Johnson, H. P., and M. J. Pruis (2003), Fluxes of fluid and heat from the oceanic crustal reservoir, *Earth Planet. Sci. Lett.*, *216*(4), 565–574, doi:10.1016/S0012-821X(03)00545-4.

Judd, A. G., and M. Hovland (2007), *Seabed Fluid Flow: The Impact on Geology, Biology, and the Marine Environment*, 475 pp., Cambridge Univ. Press, Cambridge.

Judd, A. G., M. Hovland, L. I. Dimitrov, S. García Gil, and V. Jukes (2002), The geological methane budget at continental margins and its influence on climate change, *Geofluids*, *2*, 109–126, doi:10.1046/j.1468-8123.2002.00027.x.

Jurado-Rodríguez, M. J., and F. Martínez (1998), Some clues about the Napoli and Milano mud volcanoes from an integrated log-core approach, In: Robertson, A. H. F., et al. (eds.), *Proc. Ocean Drill. Program Sci. Res.*, *160*, 607–624, doi: 10.2973/odp.proc.sr.160.043.1998.

Kastens, K. A. (1991), Rate of outward growth of the Mediterranean ridge accretionary complex, *Tectonophys.*, *199*(1), 25–50, doi:10.1016/0040-1951(91)90117-B.

Kastner, M., H. Elderfield, and J. B. Martin (1991), Fluids in convergent margins: what do we know about their composition, origin, role in diagenesis and importance for oceanic chemical fluxes?, *Philos. Trans. R. Soc. Lond. Ser. A*, *355*, 243–259, doi:10.1098/rsta.1991.0045.

Kawamura, K., T. Sasaki, T. Kanamatsu, A. Sakaguchi, and Y. Ogawa (2012), Large submarine landslides in the Japan Trench: A new scenario for additional tsunami generation, *Geophys. Res. Lett.*, *39*, L05308, doi:10.1029/2011GL050661.

Kenyon, N. H., M. K. Ivanov, A. M. Akhmetzhanov, and G. G. Akhmanov (2002), Geological processes in the Mediterranean and Black seas and North East Atlantic. Preliminary results of investigations during the TTR-11 cruise of RV Professor Logachev, Tech. Ser., 62, 89 pp., Intergovt. Oceanogr. Comm., Paris.

Kikvadze, O., V. Lavrushin, B. Pokrovskii, and B. Polyak (2010), Gases from mud volcanoes of western and central Caucasus, *Geofluids*, *10*, 486–496, doi:10.1111/j.1468-8123.2010.00309.x.

Kim, S.-S., and P. Wessel (2011), New global seamount census from altimetry-derived gravity data, *Geophys. J. Int.*, *186*(2), 615–631, doi:10.1111/j.1365-246X.2011.05076.x.

Kioka, A., and J. Ashi (2015), Episodic massive mud eruptions from submarine mud volcanoes examined through topographical signatures, *Geophys. Res. Lett.*, *42*(20), 8406–8414, doi:10.1002/2015GL065713.

Kioka, A., J. Ashi, A. Sakaguchi, T. Sato, S. Muraoka, A. Yamaguchi, H. Hamamoto, K. Wang, and H. Tokuyama (2015), Possible mechanism of mud volcanism at the prism-backstop contact in the western Mediterranean Ridge Accretionary Complex, *Mar. Geol.*, *363*, 52–64, doi:10.1016/j.margeo.2015.01.014.

Kitamura, M., H. Mukoyoshi, P. M. Fulton, and T. Hirose (2012), Coal maturation by frictional heat during rapid fault slip, *Geophys. Res. Lett.*, *39*, L16302, doi:10.1029/2012GL052316.

Klaucke, I., D. G. Masson, C. J. Petersen, W. Weinrebe, and C. R. Ranero (2008), Multifrequency geoacoustic imaging of fluid escape structures offshore Costa Rica: Implications for the quantification of seep processes, *Geochem. Geophys. Geosyst.*, *9*(4), Q04010, doi:10.1029/2007GC001708.

Knittel, K., and A. Boetius (2009), Anaerobic oxidation of methane: progress with an unknown process, *Annu. Rev. Microbiol.*, *63*, 311–334, doi:10.1146/annurev.micro.61.080706.093130.

Kodaira, S., T. No, Y. Nakamura, T. Fujiwara, Y. Kaiho, S. Miura, N. Takahashi, Y. Kaneda, and A. Taira (2012), Coseismic fault rupture at the trench axis during the 2011 Tohoku-oki earthquake, *Nat. Geosci.*, *5*(9), 646–650, doi:10.1038/ngeo1547.

Kopf, A. J. (1999), Fate of sediment during plate convergence at the Mediterranean Ridge accretionary complex: Volume balance of mud extrusion versus subduction and/or accretion, *Geology*, *27*, 87–90.

Kopf, A. J. (2002), Significance of mud volcanism, *Rev. Geophys.*, *40*(2), 1005, doi: 10.1029/2000RG000093.

Kopf, A. J. (2003), Global methane emission through mud volcanoes and its past and present impact on the Earth's climate, *Int. J. Earth Sci.*, *92*(5), 806–816, doi: 10.1007/s00531-003-0341-z.

Kopf, A., J. H. Behrmann (2000), Extrusion dynamics of mud volcanoes on the Mediterranean Ridge accretionary complex, *Geol. Soc. London Spec. Publ.*, *174*, 169-204, doi: 10.1144/GSL.SP.1999.174.01.10.

Kopf, A., and A. Deyhle (2002), Back to the roots: boron geochemistry of mud volcanoes and its implications for mobilization depth and global B cycling, *Chem. Geol.*, *192*(3–4), 195–210, doi:10.1016/S0009-2541(02)00221-8.

Kopf, A., A. H. F. Robertson, and N. Volkmann (2000), Origin of mud breccia from the Mediterranean Ridge accretionary complex based on evidence of the maturity of organic matter and related petrographic and regional tectonic evidence, *Mar. Geol.*, *166*(1-4), 65–82, doi:10.1016/S0025-3227(00)00009-8.

Kopf, A., D. Klaeschen, and J. Mascle (2001), Extreme efficiency of mud volcanism in dewatering accretionary prisms, *Earth Planet. Sci. Lett.*, *189*(3-4), 295–313, doi: 10.1016/S0012-821X(01)00278-3.

Kopf, A., J. Mascle, and D. Klaeschen (2003), The Mediterranean Ridge: A mass balance across the fastest growing accretionary complex on Earth, *J. Geophys. Res.*, *108*(B8), 2372, doi:10.1029/2001JB000473.

Kopf, A. J., et al. (2004), Report and preliminary results of SONNE cruise SO175, Miami - Bremerhaven, 12.11. - 30.12.2003, Berichte aus dem Fachbereich Geowissenschaften der Universität Bremen, 228, Department of Geosciences, Bremen University.

Kopf, A. J., et al. (2012), Report and preliminary results of RV Poseidon Cruise P410: MUDFLOW (Mud volcanism, Faulting and Fluid Flow on the Mediterranean Ridge Accretionary Complex), Heraklion / Greece, 12.03.2011 — Taranto / Italy, 01.04.2011. Berichte aus dem Fachbereich Geowissenschaften der Universität Bremen, 284. Department of Geosciences, Bremen University.

Kopf, A., et al. (2013), Report and preliminary results of RV Sonne cruise SO222: MEMO—MeBo drilling and in situ long-term monitoring in the Nankai Trough accretionary complex, Japan. Berichte, MARUM—Zentrum für Marine Umweltwissenschaften, Fachbereich Geowissenschaften, Universität Bremen, 297, 121 pp.

Kopp, C., J. Fruehn, E. R. Flueh, C. Reichert, N. Kukowski, J. Bialas, and D. Klaeschen (2000), Structure of the Makran subduction zone from wide-angle and reflection seismic data, *Tectonophys.*, *329*(1-4), 171–191, doi:10.1016/S0040-1951(00)00195-5.

Kossel, E., N. Bigalke, E. Piñero, and M. Haeckel (2013), The SUGAR Toolbox — A library of numerical algorithms and data for modelling of gas hydrate systems and marine environments, *GEOMAR Report (N. Ser.)*, *8*, 160, doi:10.3289/geomar_rep_ns_8_2013.

Krail, P. M. (1994), Vertical cable as a subsalt imaging tool, *Lead. Edge*, *13*(8), 885–887, doi:10.1190/1.1437049.

Kreemer, C., and N. Chamot-Rooke (2004), Contemporary kinematics of the southern Aegean and the Mediterranean Ridge, *Geophys. J. Int.*, *157*(3), 1377–1392, doi:10.1111/j.1365-246X.2004.02270.x.

Kukowski, N., T. Schillhorn, K. Huhn, U. von Rad, S. Husen, and E. Flueh (2001), Morphotectonics and mechanics of the central Makran accretionary wedge off Pakistan, *Mar. Geol.*, *173*, 1–19, doi:10.1016/S0025-3227(00)00167-5.

Kukowski, N., S. E. Lallemand, J. Malavieille, M.-A. Gutscher, and T. J. Reston (2002), Mechanical decoupling and basal duplex formation observed in sandbox experiments with application to the Western Mediterranean Ridge accretionary complex, *Mar. Geol.*, *186*(1-2), 29–42, doi:10.1016/S0025-3227(02)00171-8.

Kuramoto, S. et al. (2001), Surface observations of subduction related mud volcanoes and large thrust sheets in the Nankai subduction margin; Report on YK00-10 and YK01-04 cruises, *JAMSTEC Deep Sea Res.*, *19*, 131–139.

Kuribayashi, E., and F. Tatsuoka (1975), Brief review of liquefactions during earthquakes in Japan, *Soil Found.*, *15*, 81–92, doi:10.3208/sandf1972.15.4_81.

Kvenvolden, K. A. (1988), Methane hydrate — A major reservoir of carbon in the shallow geosphere?, *Chem. Geol.*, *71*(1-3), 41–51, doi:10.1016/0009-2541(88)90104-0.

Kvenvolden, K. A., T. D. Lorenson, and W. Reeburgh (2001), Attention turns to naturally occurring methane seepage, *Eos Trans. AGU*, *82*(40), 457–457, doi:10.1029/01EO00275.

Lagrée, P.-Y., L. Staron, and S. Popinet (2011), The granular column collapse as a continuum: validity of a two-dimensional Navier-Stokes model with a $\mu(I)$-rheology, *J. Fluid Mech.*, *686*, 378–408, doi:10.1017/jfm.2011.335.

Lajeunesse, E., A. Mangeney-Castelnau, and J. P. Vilotte (2004), Spreading of a granular mass on a horizontal plane, *Phys. Fluids*, *16*(7), 2371–2381, doi:10.1063/1.1736611.

Lajeunesse, E., J. B. Monnier, and G. M. Homsy (2005), Granular slumping on a horizontal surface, *Phys. Fluids*, *17*, 103302, doi:10.1063/1.2087687.

Lallemant, S., C. Truffert, L. Jolivet, P. Henry, N. Chamot-Rooke, and B. de Voogd (1994), Spatial transition from compression to extension in the Western Mediterranean Ridge accretionary complex, *Tectonophys.*, *234*(1-2), 33–52, doi:10.1016/0040-1951(94)90203-8.

Lance, S., P. Henry, X. Le Pichon, S. Lallemant, H. Chamley, F. Rostek, J.-C. Faugères, E. Gonthier, and K. Olu (1998), Submersible study of mud volcanoes seaward of the Barbados accretionary wedge: sedimentology, structure and rheology, *Mar. Geol.*, *145*(3–4), 255–292, doi:10.1016/S0025-3227(97)00117-5.

Langseth, M. G., G. K. Westbrook, and M. A. Hobart (1988), Geophysical survey of a mud volcano seaward of the Barbados Ridge Accretionary Complex, *J. Geophys. Res.*, *93*(B2), 1049, doi:10.1029/JB093iB02p01049.

Lazar, C. S., R. J. Parkes, B. A. Cragg, S. L'Haridon, and L. Toffin (2011), Methanogenic diversity and activity in hypersaline sediments of the centre of the Napoli mud volcano, Eastern Mediterranean Sea, *Envir. Microbiol.*, *13*(8), 2078–2091, doi:10.1111/j.1462-2920.2011.02425.x.

Lee, M. W. (2002), Biot-Gassmann theory for velocities of gas hydrate-bearing sediments, *Geophysics*, *67*(6), 1711–1719, doi:10.1190/1.1527072.

Legros, F. (2002), The mobility of long-runout landslides, *Eng. Geol.*, *63*(3–4), 301–331, doi:10.1016/S0013-7952(01)00090-4.

Lein, A., P. Vogt, K. Crane, A. Egorov, and M. Ivanov (1999), Chemical and isotopic evidence for the nature of the fluid in CH_4-containing sediments of the Haakon Mosby Mud Volcano, *Geo-Mar. Lett.*, *19*, 76–83, doi:10.1007/s003670050095.

Lelieveld, J., P. Crutzen, and F. Dentener (1998), Changing concentration, lifetime and climate forcing of atmospheric methane, *Tellus, Ser. B*, *50*(2), 128–150, doi:10.1034/j.1600-0889.1998.t01-1-00002.x.

Lemarchand, D., J. Gaillardet, E. Lewin, and C. J. Allègre (2002), Boron isotope systematics in large rivers: Implications for the marine boron budget and paleo-pH reconstruction over the Cenozoic, *Chem. Geol.*, *190*, 123–140, doi:10.1016/S0009-2541(02)00114-6.

León, R., et al. (2012), New discoveries of mud volcanoes on the Moroccan Atlantic continental margin (Gulf of Cádiz): morpho-structural characterization, *Geo-Mar. Lett.*, 32(5-6), 473–488, doi:10.1007/s00367-012-0275-1.

Le Pichon, X., N. Lybéris, J. Angelier, and V. Renard (1982), Strain distribution over the east Mediterranean ridge: A synthesis incorporating new Sea-Beam data, *Tectonophys.*, *86*(1-3), 243–274, doi:10.1016/0040-1951(82)90069-5.

Le Pichon, X., N. Chamot-Rooke, S. Lallemant, R. Noomen, and G. Veis (1995), Geodetic determination of the kinematics of central Greece with respect to Europe: Implications for Eastern Mediterranean Tectonics, *J. Geophys. Res.*, *100*(B7), 12675–12690, doi:10.1029/95JB00317.

Le Pichon, X., S. J. Lallemant, N. Chamot-Rooke, D. Lemeur, and G. Pascal (2002), The Mediterranean Ridge backstop and the Hellenic nappes, *Mar. Geol.*, *186*(1-2), 111–125, doi:10.1016/S0025-3227(02)00175-5.

Li, L., A. D. Switzer, Y. Wang, R. Weiss, Q. Qiu, C.-H. Chan, and P. Tapponnier (2015), What caused the mysterious eighteenth century tsunami that struck the southwest Taiwan coast?, *Geophys. Res. Lett.*, *42*, 8498–8506, doi:10.1002/2015GL065567.

Limonov, A. F., J. M. Woodside, M. B. Cita, and M. K. Ivanov (1996), The Mediterranean Ridge and related mud diapirism: a background, *Mar. Geol.*, *132*(1-4), 7–19, doi:10.1016/0025-3227(96)00150-8.

Limonov, A. F., M. K. Ivanov, and J.-P. Foucher (1998), Deep-towed side-scan survey of the United Nations Rise, eastern Mediterranean, *Geo-Mar. Lett.*, *18*(2), 115–126, doi:10.1007/s003670050059.

Liu, C.-S., I. L. Huang, and L. S. Teng (1997), Structural features off southwestern Taiwan, *Mar. Geol.*, *137*(3–4), 305–319, doi:10.1016/S0025-3227(96)00093-X.

Løseth, H., L. Wensaas, B. Arntsen, and M. Hovland (2003), Gas and fluid injection triggering shallow mud mobilization in the Hordaland Group, North Sea, *Geol. Soc. Spec. Publ.*, *216*, 159–172, doi:10.1144/GSL.SP.2003.216.01.10.

Lube, G., H. E. Huppert, R. S. J. Sparks, and M. A. Hallworth (2004), Axisymmetric collapses of granular columns, *J. Fluid Mech.*, *508*, 175–199, doi:10.1017/S0022112004009036.

Luo, S., and D. Hale (2012), Velocity analysis using weighted semblance, *Geophysics*, *77*(2), U15–U22, doi:10.1190/GEO2011-0034.1.

Lupi, M., E. H. Saenger, F. Fuchs, and S. A. Miller (2013), Lusi mud eruption triggered by geometric focusing of seismic waves, *Nat. Geosci.*, *6*(8), 642–646, doi:10.1038/ngeo1884.

Lüschen, E., C. Müller, H. Kopp, M. Engels, R. Lutz, L. Planert, A. Shulgin, and Y. S. Djajadihardja (2011), Structure, evolution and tectonic activity of the eastern Sunda forearc, Indonesia, from marine seismic investigations, *Tectonophys.*, *508*, 6–21, doi:10.1016/j.tecto.2010.06.008.

Lykousis, V., et al. (2004), New evidence of extensive active mud volcanism in the Anaximander mountains (Eastern Mediterranean): The “ATHINA” mud volcano, *Environ. Geol.*, *46*(8), 1030–1037, doi:10.1007/s00254-004-1090-4.

Lykousis, V., et al. (2009), Mud volcanoes and gas hydrates in the Anaximander mountains (Eastern Mediterranean Sea), *Mar. Pet. Geol.*, *26*(6), 854–872, doi:10.1016/j.marpetgeo.2008.05.002.

Machiyama, H., et al. (2012), YOKOSUKA Cruise Report YK12-17: Survey for detailed mapping for topography and geological structure of mud volcanoes off Tanegashima, Japan Agency for Marine-Earth Science and Technology (JAMSTEC), Yokosuka, Japan.

Maekawa, H., et al. (2006), KR06-15 Cruise Report: Geological expedition of the serpentine seamounts in the Mariana forearc, Japan Agency for Marine-Earth Science and Technology, Yokosuka, Japan.

Magalhães, V. H. (2007), Authigenic carbonates and fluid escape structures in the Gulf of Cadiz, Ph.D. Thesis, University of Aveiro, Aveiro, 421 pp.

Maher, K., and C. P. Chamberlain (2014), Hydrologic regulation of chemical weathering and the geologic carbon cycle, *Science*, *343*, 1502–1504, doi:10.1126/science.1250770.

Manga, M. (2007), Did an earthquake trigger the May 2006 eruption of the Lusi Mud volcano?, *Eos Trans. AGU*, *88*(18), 201, doi:10.1029/2007EO180009.

Manga, M., and E. Brodsky (2006), Seismic triggering of eruptions in the far field: Volcanoes and geysers, *Annu. Rev. Earth Planet. Sci.*, *34*, 263–291, doi:10.1146/annurev.earth.34.031405.125125.

Manga, M., and M. Bonini (2012), Large historical eruptions at subaerial mud volcanoes, Italy, *Nat. Hazards Earth Syst. Sci.*, *12*(11), 3377–3386, doi:10.5194/nhess-12-3377-2012.

Manga, M., M. Brumm, and M. L. Rudolph (2009), Earthquake triggering of mud volcanoes, *Mar. Petrol. Geol.*, *26*(9), 1785–1798, doi:10.1016/j.marpetgeo.2009.01.019.

Manga, M., I. Beresnev, E. E. Brodsky, J. E. Elkhoury, D. Elsworth, S. E. Ingebritsen, D. C. Mays, and C. Wang (2012), Changes in permeability caused by transient stresses: Field observations, experiments, and mechanisms, *Rev. Geophys.*, *50*(2), RG2004, doi:10.1029/2011RG000382.

Marschall, H. R., P. A. E. Pogge von Strandmann, H. M. Seitz, T. Elliott, and Y. Niu (2007), The lithium isotopic composition of orogenic eclogites and deep subducted slabs, *Earth Planet. Sci. Lett.*, *262*, 563–580, doi:10.1016/j.epsl.2007.08.005.

Martin, J. B., M. Kastner, P. Henry, X. Le Pichon, and S. Lallement (1996), Chemical and isotopic evidence for sources of fluids in a mud volcano field seaward of the Barbados accretionary wedge, *J. Geophys. Res.*, *101*(B9), 20325–20345, doi:10.1029/96JB00140.

Mau, S., H. Sahling, G. Rehder, E. Suess, P. Linke, and E. Soeding (2006), Estimates of methane output from mud extrusions at the erosive convergent margin off Costa Rica, *Mar. Geol.*, *225*(1-4), 129–144, doi:10.1016/j.margeo.2005.09.007.

Mavko, G., T. Mukerji, and J. Dvorkin (2009), *The Rock Physics Handbook: Tools for Seismic Analysis in Porous Media, Second Edition*, Cambridge Univ. Press, Cambridge, U.K., 511 pp.

Mazzini, A., H. Svensen, G. G. Akhmanov, G. Aloisi, S. Planke, A. Malthe-Sørenssen, and B. Istadi (2007), Triggering and dynamic evolution of the LUSI mud volcano, Indonesia, *Earth Planet. Sci. Lett.*, *261*(3-4), 375–388, doi:10.1016/j.epsl.2007.07.001.

McClusky, S., et al. (2000), Global Positioning System constraints on plate kinematics and dynamics in the eastern Mediterranean and Caucasus, *J. Geophys. Res.*, *105*(B3), 5695–5719, doi:10.1029/1999JB900351.

McGinnis, D. F., J. Greinert, Y. Artemov, S. E. Beaubien, and A. Wüest (2006), Fate of rising methane bubbles in stratified waters: How much methane reaches the atmosphere?, *J. Geophys. Res.*, *111*, C09007, doi:10.1029/2005JC003183.

McKenzie, D. (1972), Active Tectonics of the Mediterranean Region, *Geophys. J. R. Astron. Soc.*, *30*(2), 109–185, doi:10.1111/j.1365-246X.1972.tb02351.x.

McKenzie, D. (1978), Active tectonics of the Alpine-Himalayan belt: the Aegean Sea and surrounding regions, *Geophys. J. R. Astron. Soc.*, *55*(1), 217–254, doi:10.1111/j.1365-246X.1978.tb04759.x.

Medialdea, T., L. Somoza, L. M. Pinheiro, M. C. Fernández-Puga, J. T. Vázquez, R. León, M. K. Ivanov, V. Magalhaes, V. Díaz-del-Río, and R. Vegas (2009), Tectonics and mud volcano development in the Gulf of Cádiz, *Mar. Geol.*, *261*(1–4), 48–63, doi:10.1016/j.margeo.2008.10.007.

MEDINAUT/MEDINETH Shipboard Scientific Parties (2000), Linking Mediterranean brine pools and mud volcanism, *Eos Trans. AGU*, *81*(51), 625–632, doi:10.1029/EO081i051p00625-02.

Mellors, R., D. Kilb, A. Aliyev, A. Gasanov, and G. Yetirmishli (2007), Correlations between earthquakes and large mud volcano eruptions, *J. Geophys. Res.*, *112*, B04304, doi:10.1029/2006JB004489.

Milkov, A. V (2000), Worldwide distribution of submarine mud volcanoes and associated gas hydrates, *Mar. Geol.*, *167*(1-2), 29–42, doi:10.1016/S0025-3227(00)00022-0.

Milkov, A. V., R. Sassen, T. V. Apanasovich, and F. G. Dadashev (2003), Global gas flux from mud volcanoes: A significant source of fossil methane in the atmosphere and the ocean, *Geophys. Res. Lett.*, *30*(2), 1037, doi:10.1029/2002GL016358.

Milkov, A. V., P. R. Vogt, K. Crane, A. Y. Lein, R. Sassen, and G. A. Cherkashev (2004), Geological, geochemical, and microbial processes at the hydrate-bearing Håkon Mosby mud volcano: a review, *Chem. Geol.*, *205*, 347–366, doi:10.1016/j.chemgeo.2003.12.030.

Millot, R., C. Guerrot, C. Innocent, Ph. Négrel, and B. Sanjuan (2011), Chemical, multi-isotopic (Li–B–Sr–U–H–O) and thermal characterization of Triassic formation waters from the Paris Basin, *Chem. Geol.*, *283*(3–4), 226–241, doi: 10.1016/j.chemgeo.2011.01.020.

Misra, S., and P. N. Froelich (2012), Lithium Isotope History of Cenozoic Seawater: Changes in Silicate Weathering and Reverse Weathering, *Science*, *335*(6070), 818–823, doi:10.1126/science.1214697.

Miyake, Y., Y. Sugimura, and Y. Hirao (1975), Uranium, thorium, and potassium contents in granitic and basaltic rocks in Japan, in *The Natural Radiation Environment II*, pp. 535–558, Rice University, Houston, Tex.

Miyazaki, J., R. Higa, T. Toki, J. Ashi, U. Tsunogai, T. Nunoura, H. Imachi, and K. Takai (2009), Molecular characterization of potential nitrogen fixation by anaerobic methane-oxidizing archaea in the methane seep sediments at the number 8 Kumano Knoll in the Kumano Basin, offshore of Japan, *Appl. Environ. Microbiol.*, *75*(22), 7153–7162, doi:10.1128/AEM.01184-09.

Montgomery, D. R., and M. Manga (2003), Streamflow and Water Well Responses to Earthquakes, *Science*, *300*(5628), 2047–2049, doi:10.1126/science.1082980.

Moore, J. C., and P. Vrolijk (1992), Fluids in accretionary prisms, *Rev. Geophys.*, *30*(2), 113–135, doi:10.1029/92RG00201.

Moore, W. S. (1996), Large groundwater inputs to coastal waters revealed by ^{226}Ra enrichments, *Nature*, *380*, 612–614, doi:10.1038/380612a0.

Morita, S., J. Ashi, K. Aoike, and S. Kuramoto (2004), Evolution of Kumano basin and sources of clastic ejecta and pore fluid in Kumano mud volcanoes, Eastern Nanaki Trough, In: Proceedings of the International Symposium on Methane Hydrates and Fluid Flow in Upper Accretionary Prisms, Engineering Geology Laboratory, Department of Civil & Earth Resources Engineering, Kyoto University, Kyoto, Japan, pp. 92–99.

Morita, S., C.-S. Liu, C.-Y. Ku, H. Machiyama, S. Lin, W. Soh, and S. Shimizu (2009), Fluid Circulation in a Region of Submarine Mounds off Southwest Taiwan: High-resolution Seismic Records from the Continental Slope Ridge, *J. Geograph. (Chigaku Zasshi)*, *118*(3), 424–434, doi:10.5026/jgeography.118.424. [in Japanese with English Abstr.]

Morse, P. M., and K. U. Ingard (1986), *Theoretical acoustics*, Princeton University Press, Princeton, N. J.

Mörz, T., et al. (2005), Styles and productivity of mud diapirism along the Middle American Margins: Part II. Mound Culebra and Mounds 11 and 12, in *Mud Volcanoes, Geodynamics and Seismicity, NATO Sci. Ser. IV, vol. 51*, edited by Martinelli, G., and B. Panahi, pp. 49–76, Springer, Dordrecht, Netherlands.

Mottl, M. J., and C. G. Wheat (1994), Hydrothermal circulation through mid-ocean ridge flanks: Fluxes of heat and magnesium, *Geochim. Cosmochim. Acta*, *58*(10), 2225–2237, doi:10.1016/0016-7037(94)90007-8.

Müller, R. D., M. Sdrolias, C. Gaina, and W. R. Roest (2008), Age, spreading rates, and spreading asymmetry of the world's ocean crust, *Geochem. Geophys. Geosyst.*, 9(4), Q04006, doi:10.1029/2007GC001743.

Muramatsu, Y., U. Fehn, and S. Yoshida (2001), Recycling of iodine in fore-arc areas: Evidence from the iodine brines in Chiba, Japan, *Earth Planet. Sci. Lett.*, *192*, 583–593, doi:10.1016/S0012-821X(01)00483-6.

Muraoka, S., J. Ashi, T. Kanamatsu, A. Sakaguchi, and K. Aoike (2011), Geological study of deposits and rocks in the deep underground used by samples of mud volcanoes developed in Kumano Trough, SW Japan, in *Abstract T21B-2353 presented at 2011 Fall Meeting*, *AGU*, *San Francisco*, *Calif.*, *5-9 Dec.*

Murton, B. J., and J. Biggs (2003), Numerical modelling of mud volcanoes and their flows using constraints from the Gulf of Cadiz, *Mar. Geol.*, *195*(1–4), 223–236, doi: 10.1016/S0025-3227(02)00690-4.

Nakamura, K. (1977), Volcanoes as possible indicators of tectonic stress orientation — principle and proposal, *J. Volcanol. Geotherm. Res.*, *2*, 1–16, doi:10.1016/0377-0273(77)90012-9.

Neurauter, T. W., and H. H. Roberts (1994), Three generations of mud volcanoes on the Louisiana continental slope, *Geo-Mar. Lett.*, *14*(2–3), 120–125, doi: 10.1007/BF01203723.

Nguyen, Q. D., and D. V Boger (1992), Measuring the Flow Properties of Yield Stress Fluids, *Annu. Rev. Fluid Mech.*, *24*(1), 47–88, doi:10.1146/annurev.fl.24.010192.000403.

Niemann, H., et al. (2006), Novel microbial communities of the Haakon Mosby mud volcano and their role as a methane sink, *Nature*, *443*, 854–858, doi:10.1038/nature05227.

Nishio, Y., A. Ijiri, T. Toki, Y. Morono, M. Tanimizu, K. Nagaishi, and F. Inagaki (2015), Origins of lithium in submarine mud volcano fluid in the Nankai accretionary wedge, *Earth Planet. Sci. Lett.*, *414*, 144–155, doi:10.1016/j.epsl.2015.01.018.

Normark, W. R., and D. J. W. Piper (1998), Preliminary evaluation of recent movement on structures within the Santa Monica Basin, offshore southern California, U.S. Geological Survey Open-File Report, 98-518, 60 p.

Oehler, D. Z., and C. C. Allen (2010), Evidence for pervasive mud volcanism in Acidalia Planitia, Mars, *Icarus*, *208*(2), 636–657, doi:10.1016/j.icarus.2010.03.031.

O'Hara, K. (2004), Paleo-stress estimates on ancient seismogenic faults based on frictional heating of coal, *Geophys. Res. Lett.*, *31*, L03601, doi:10.1029/2003GL018890.

O'Hara, K., K. Mizoguchi, T. Shimamoto, J. C. Hower (2006), Experimental frictional heating of coal gouge at seismic slip rates: Evidence for devolatilization and thermal pressurization of gouge fluids, *Tectonophys.*, *424*(1-2), 109–118, doi:10.1016/j.tecto.2006.07.007.

Ohmori, K., A. Taira, H. Tokuyama, A. Sakaguchi, M. Okamura, A. Aihara (1997), Paleothermal structure of the Shimanto accretionary prism, Shikoku, Japan: Role of an out-of-sequence thrust, *Geology*, *25*, 327–330, doi:10.1130/0091-7613(1997)025<0327:PSOTSA>2.3.CO;2.

Olu, K., S. Lance, M. Sibuet, P. Henry, A. Fiala-Médioni, and A. Dinet (1997), Cold seep communities as indicators of fluid expulsion patterns through mud volcanoes seaward of the Barbados accretionary prism, *Deep Sea Res. Part I*, *44*(5), 811–841, doi:10.1016/S0967-0637(96)00123-9.

Olu-Le Roy, K., M. Sibuet, A. Fiala-Médioni, S. Gofas, C. Salas, A. Mariotti, J.-P. Foucher, and J. Woodside (2004), Cold seep communities in the deep eastern Mediterranean Sea: composition, symbiosis and spatial distribution on mud volcanoes, *Deep Sea Res. Part I*, *51*(12), 1915–1936, doi:10.1016/j.dsr.2004.07.004.

Orphan, V. J., C. H. House, K.-U. Hinrichs, K. D. McKeegan, and E. F. DeLong (2001), Methane-consuming archaea revealed by directly coupled isotopic and phylogenetic analysis, *Science*, *293*, 484–487, doi:10.1126/science.1061338.

Otsuka, H., S. Morita, M. Tanahashi, and J. Ashi (2015), Foldback reflectors near methane hydrate bottom-simulating reflectors: Indicators of gas distribution from 3D seismic images in the eastern Nankai Trough, *Isl. Arc*, *24*(2), 145–158, doi:10.1111/iar.12099.

Papadopoulos, G. A., and G. Lefkopoulos (1993), Magnitude-distance relations for liquefaction in soil from earthquakes, *Bull. Seismol. Soc. Am.*, *83*, 925–938.

Papadopoulos, G. A., E. Daskalaki, A. Fokaefs, and N. Giraleas (2007), Tsunami hazards in the Eastern Mediterranean: strong earthquakes and tsunamis in the East Hellenic Arc and Trench system, *Nat. Hazards Earth Syst. Sci.*, *7*, 57–64, doi:10.5194/nhess-7-57-2007.

Pape, T., P. Geprägs, S. Hammerschmidt, P. Wintersteller, J. Wei, T. Fleischmann, G. Bohrmann, and A. J. Kopf (2014), Hydrocarbon seepage and its sources at mud volcanoes of the Kumano forearc basin, Nankai Trough subduction zone, *Geochem. Geophys. Geosyst.*, *15*, doi:10.1002/2013GC005057.

Pasquale, V., M. Verdoya, and P. Chiozzi (2001), Radioactive heat generation and its thermal effects in the Alps-Apennines boundary zone, *Tectonophys.*, *331*, 269–283, doi:10.1016/S0040-1951(00)00294-8.

Patacca, E., R. Sartori, and P. Scandone (1993), Tyrrhenian basin and Apennines. Kinematic evolution and related dynamic constraints, in Recent Evolution and Seismicity of the Mediterranean Region, pp. 161–171, Springer, Netherlands.

Paull, C. K., P. G. Brewer, W. Ussler, E. T. Peltzer, G. Rehder, and D. Clague (2002), An experiment demonstrating that marine slumping is a mechanism to transfer methane from seafloor gas-hydrate deposits into the upper ocean and atmosphere, *Geo-Mar. Lett.*, *22*(4), 198–203, doi:10.1007/s00367-002-0113-y.

Paull, C. K., W. R. Normark, W. Ussler III, D. W. Caress, and R. Keaten (2008), Association among active seafloor deformation, mound formation, and gas hydrate growth and accumulation within the seafloor of the Santa Monica Basin, offshore California, *Mar. Geol.*, *250*(3–4), 258–275, doi:10.1016/j.margeo.2008.01.011.

Paull, C. K., et al. (2015), Active mud volcanoes on the continental slope of the Canadian Beaufort Sea, *Geochem. Geophys. Geosyst.*, *16*(9), 3160–3181, doi: 10.1002/2015GC005928.

Pearce, F. D., S. Rondenay, M. Sachpazi, M. Charalampakis, and L. H. Royden (2012), Seismic investigation of the transition from continental to oceanic subduction along the western Hellenic Subduction Zone, *J. Geophys. Res.*, *117*, B07306, doi: 10.1029/2011JB009023.

Peckmann, J., A. Reimer, U. Luth, C. Luth, B. T. Hansen, C. Heinicke, J. Hoefs, and J. Reitner (2001), Methane-derived carbonates and authigenic pyrite from the northwestern Black Sea, *Mar. Geol.*, *177*, 129–150, doi:10.1016/S0025-3227(01)00128-1.

Perez-Garcia, C., T. Feseker, J. Mienert, and C. Berndt (2009), The Håkon Mosby mud volcano: 330000 years of focused fluid flow activity at the SW Barents Sea slope, *Mar. Geol.*, *262*(1-4), 105–115, doi:10.1016/j.margeo.2009.03.022.

Perissoratis, C., Chr. Ioakim, S. Alexandri, J. Woodside, P. Nomikou, A. Dählmann, D. Casas, K. Heeschen, H. Amman, G. Rousakis, V. Lykousis (2011), Thessaloniki Mud Volcano, the Shallowest Gas Hydrate-Bearing Mud Volcano in the Anaximander Mountains, Eastern Mediterranean, *J. Geol. Res.*, *2011*, 247983, doi:10.1155/2011/247983.

Petersen, C. J., I. Klaucke, W. Weinrebe, and C. R. Ranero (2009), Fluid seepage and mound formation offshore Costa Rica revealed by deep-towed sidescan sonar and sub-bottom profiler data, *Mar. Geol.*, *266*(1-4), 172–181, doi:10.1016/j.margeo.2009.08.004.

Pierre, C., G. Bayon, M.-M. Blanc-Valleron, J. Mascle, and S. Dupré (2014), Authigenic carbonates related to active seepage of methane-rich hot brines at the Cheops mud volcano, Menes caldera (Nile deep-sea fan, eastern Mediterranean Sea), *Geo-Mar. Lett.*, *34*(2–3), 253–267, doi:10.1007/s00367-014-0362-6.

Pinheiro, L. M., et al. (2003), Mud volcanism in the Gulf of Cadiz: results from the TTR-10 cruise, *Mar. Geol.*, *195*(1–4), 131–151, doi:10.1016/S0025-3227(02)00685-0.

Platt, J. P. (2000), Calibrating the bulk rheology of active obliquely convergent thrust belts and forearc wedges from surface profiles and velocity distributions, *Tectonics*, *19*(3), 529–548, doi:10.1029/1999TC001121.

Polonia, A., A. Camerlenghi, F. Davey, and F. Storti (2002), Accretion, structual style and syn-contractional sedimentation in the Eastern Mediterranean Sea, *Mar. Geol.*, *186*(1–2), 127–144, doi:10.1016/S0025-3227(02)00176-7.

Pondrelli, M., A. P. Rossi, G. G. Ori, S. van Gasselt, D. Praeg, and S. Ceramicola (2011), Mud volcanoes in the geologic record of Mars: The case of Firsoff crater, *Earth Planet. Sci. Lett.*, *304* (3–4), 511–519, doi:10.1016/j.epsl.2011.02.027.

Praeg, D., S. Ceramicola, R. Barbieri, V. Unnithan, and N. Wardell (2009), Tectonically-driven mud volcanism since the late Pliocene on the Calabrian accretionary prism, central Mediterranean Sea, *Mar. Pet. Geol.*, *26* (9), 1849–1865, doi: 10.1016/j.marpetgeo.2009.03.008.

Premoli Silva, I., E. Erba, S. Spezzaferri, and M. B. Cita (1996), Age variation in the source of the diapiric mud breccia along and across the axis of the Mediterranean Ridge Accretionary Complex, *Mar. Geol.*, *132* (1–4), 175–202, doi:10.1016/0025-3227(95)00160-3.

Quigley, T. M., and A. S. Mackenzie (1988), The temperatures of oil and gas formation in the sub-surface, *Nature*, *333*, 549–552, doi:10.1038/333549a0.

Rabaute, A., and N. Chamot-Rooke (2007), Quantitative mapping of active mud volcanism at the western Mediterranean Ridge-backstop contact, *Mar. Geophys. Res.*, *28* (3), 271–295, doi:10.1007/s11001-007-9031-8.

Rabaute, A., N. Chamot-Rooke, and Deep Offshore Tectonics of the Mediterranean (DOTMED) Team (2003), Tectonics and mud volcanism at the western Mediterranean Ridge-backstop contact, *Geophys. Res. Abstr.*, *5*, 12007.

Ranero, C. R., and R. von Huene (2000), Subduction erosion along the Middle America convergent margin, *Nature*, *404*, 748–752, doi:10.1038/35008046.

Ransom, B., A. J. Spivack, and M. Kastner (1995), Stable Cl isotopes in subduction-zone pore waters: Implications for fluid-rock reactions and the cycling of chlorine, *Geology*, *23*, 715–718, doi:10.1130/0091-7613(1995)023<0715:SCIISZ>2.3.CO;2.

Reeburgh, W. S. (2007), Oceanic methane biogeochemistry, *Chem. Rev.*, *107* (2), 486–513, doi:10.1021/cr050362v.

Reeburgh, W. S., B. B. Ward, S. C. Whalen, K. A. Sandbeck, K. A. Kilpatrick, and L. J. Kerkhof (1991), Black-sea methane geochemistry, *Deep Sea Res., Part A*, *38*, S1189–S1210, doi:10.1016/s0198-0149(10)80030-5.

Reilinger, R. et al. (2006), GPS constraints on continental deformation in the Africa-Arabia-Eurasia continental collision zone and implications for the dynamics of plate interactions, *J. Geophys. Res.*, *111* (B5), B05411, doi:10.1029/2005JB004051.

Reston, T. J., J. Fruehn, R. von Huene, and IMERSE Working Group (2002a), The structure and evolution of the western Mediterranean Ridge, *Mar. Geol.*, *186* (1-2), 83–110, doi:10.1016/S0025-3227(02)00174-3.

Reston, T. J., R. von Huene, T. Dickmann, D. Klaeschen, and H. Kopp (2002b), Frontal accretion along the western Mediterranean Ridge: the effect of Messinian evaporites on wedge mechanics and structural style, *Mar. Geol.*, *186* (1-2), 59–82, doi:10.1016/S0025-3227(02)00173-1.

Reusch, A., J. Moernaut, F. S. Anselmetti, and M. Strasser (2016), Sediment mobilization deposits from episodic subsurface fluid flow—A new tool to reveal long-term earthquake records?, *Geology*, *44*(4), doi:10.1130/G37410.1.

Reuss, A. (1929), Berechnung der Fließgrenze von Mischkristallen auf Grund der Plastizitätsbedingung für Einkristalle, *Z. angew. Math. Mech.*, *9*, 49–58, doi: 10.1002/zamm.19290090104.

Richards, J. R. (2011), Report into the Past, Present, and Future Social Impacts of Lumpur Sidoarjo, Tech. rep., Humanitus Sidoarjo Fund.

Ridd, M. F. (1970), Mud volcanoes in New Zealand, *AAPG Bull.*, *54*, 601–616.

Roberts, H. H. (2001), Improved geohazards and benthic habitat evaluations: digital acoustic data with ground truth calibrations, OCS Study MMS 2001-050, U.S. Dept. of the Interior, Minerals Mgmt. Service, Gulf of Mexico OCS Region, New Orleans, La. 116 pp + appendices.

Robertson, A., and Ocean Drilling Program Leg 160 Scientific Party (1996), Mud volcanism on the Mediterranean Ridge: Initial results of Ocean Drilling Program Leg 160, *Geology*, *24*(3), 239–242, doi:10.1130/0091-7613(1996)024<0239:MVOTMR>2.3.CO;2.

Rovere, M., F. Gamberi, A. Mercorella, H. Rashed, A. Gallerani, E. Leidi, M. Marani, V. Funari, and G. A. Pini (2014), Venting and seepage systems associated with mud volcanoes and mud diapirs in the southern Tyrrhenian Sea, *Mar. Geol.*, *347*, 153–171, doi:10.1016/j.margeo.2013.11.013.

Roy, R., A. Beck, and Y. Touloukian (1981), Thermophysical properties of rocks, in *Physical Properties of Rocks and Minerals*, edited by Y. Touloukian, W. Judd, and R. Roy, pp. 409–502, Hemisphere Publishing Corp., New York.

Rubey, W. W., and M. K. Hubbert (1959), Role of fluid pressure in mechanics of overthrust faulting. II. Overthrust belt in geosynclinal area of western Wyoming in light of fluid pressure hypothesis, *Geol. Soc. Am. Bull.*, *70*, 167–206.

Rudolph, M. L., and M. Manga (2010), Mud volcano response to the 4 April 2010 El Mayor-Cucapah earthquake, *J. Geophys. Res.*, *115*, B12211, doi:10.1029/2010JB007737.

Rudolph, M. L., and M. Manga (2012), Frequency dependence of mud volcano response to earthquakes, *Geophys. Res. Lett.*, *39*, L14303, doi:10.1029/2012GL052383.

Rudolph, M. L., L. Karlstrom, and M. Manga (2011), A prediction of the longevity of the Lusi mud eruption, Indonesia, *Earth Planet. Sci. Lett.*, *308*(1-2), 124–130, doi: 10.1016/j.epsl.2011.05.037.

Rudolph, M. L., M. Shirzaei, M. Manga, and Y. Fukushima (2013), Evolution and future of the Lusi mud eruption inferred from ground deformation, *Geophys. Res. Lett.*, *40*, 1089–1092, doi:10.1002/grl.50189.

Rudolph, M. L., M. Manga, M. Tingay, and R. J. Davies (2015), Influence of seismicity on the Lusi mud eruption, *Geophys. Res. Lett.*, *42*, 7436–7443, doi:10.1002/2015GL065310.

Ryan, T. A. (1960), Significance tests for multiple comparison of proportions, variances, and other statistics, *Psychol. Bull.*, *57*(4), 318–328, doi:10.1037/h0044320.

Ryan, W. B. F., K. A. Kastens, and M. B. Cita (1982), Geological evidence concerning compressional tectonics in the Eastern Mediterranean, *Tectonophys.*, *86*(1-3), 213–219, doi:10.1016/0040-1951(82)90068-3.

Saffer, D. M., and B. A. Bekins (2006), An evaluation of factors influencing pore pressure in accretionary complexes: Implications for taper angle and wedge mechanics, *J. Geophys. Res.*, *111*(B4), B04101, doi:10.1029/2005JB003990.

Saffer, D. M., and H. J. Tobin (2011), Hydrogeology and Mechanics of Subduction Zone Forearcs: Fluid Flow and Pore Pressure, *Annu. Rev. Earth Planet. Sci.*, *39*(1), 157–186, doi:10.1146/annurev-earth-040610-133408.

Saffer, D., L. McNeill, T. Byrne, E. Araki, S. Toczko, N. Eguchi, K. Takahashi, and the Expedition 319 Scientists (2010), NanTroSEIZE Stage 2: NanTroSEIZE riser/riserless observatory, *Proc. Integrated Ocean Drill. Program*, *319*, doi:10.2204/iodp.proc.319.2010.

Sahling, H., D. G. Masson, C. R. Ranero, V. Hühnerbach, W. Weinrebe, I. Klaucke, D. Bürk, W. Brückmann, and E. Suess (2008), Fluid seepage at the continental margin offshore Costa Rica and southern Nicaragua, *Geochem. Geophys. Geosyst.*, *9*(5), Q05S05, doi:10.1029/2008GC001978.

Sakaguchi, A., and H. Mukoyoshi (2012), How to make a geothermometer for high-resolution measurements of the reflectance of small vitrinite particles, *J. Geol. Soc. Japan*, *118*(4), 240–244, doi:10.5575/geosoc.2012.0002.

Sakaguchi, A., A. Yanagihara, K. Ujiie, H. Tanaka, and M. Kameyama (2007), Thermal maturity of a fold-thrust belt based on vitrinite reflectance analysis in the Western Foothills complex, western Taiwan, *Tectonophys.*, *443*(3–4), 220–232, doi: 10.1016/j.tecto.2007.01.017.

Sakaguchi, A., G. Kimura, M. Strasser, E. Screaton, D. Curewitz, and M. Murayama (2011), Episodic seafloor mud brecciation due to great subduction zone earthquakes, *Geology*, *39*, 919–922, doi:10.1130/G32043.1.

Sano, Y., T. Hara, N. Takahata, S. Kawagucci, M. Honda, Y. Nishio, W. Tanikawa, A. Hasegawa, and K. Hattori (2014), Helium anomalies suggest a fluid pathway from mantle to trench during the 2011 Tohoku-Oki earthquake, *Nat. Commun.*, *5*, 3084, doi:10.1038/ncomms4084.

Sauter, E. J., S. I. Muyakshin, J.-L. Charlou, M. Schlüter, A. Boetius, K. Jerosch, E. Damm, J.-P. Foucher, and M. Klages (2006), Methane discharge from a deep-sea submarine mud volcano into the upper water column by gas hydrate-coated methane bubbles, *Earth Planet. Sci. Lett.*, *243*(3-4), 354–365, doi:10.1016/j.epsl.2006.01.041.

Sawolo, N., E. Sutriono, B. P. Istadi, and A. B. Darmoyo (2009), The LUSI mud volcano triggering controversy: Was it caused by drilling?, *Mar. Pet. Geol.*, *26*(9), 1766–1784, doi:10.1016/j.marpetgeo.2009.04.002.

Scholl, D. W., T. Plank, J. Morris, R. von Huene, M. J. Mottl (1994), Science opportunities in Ocean Drilling to investigate recycling processes and material fluxes at subduction zones, *Proceedings of a JOI/USSAC workshop, Avalon, Calif., 12-17 June*, 84 pp.

Scholz, F., C. Hensen, A. Reitz, R. L. Romer, V. Liebetrau, A. Meixner, S. M. Weise, and M. Haeckel (2009), Isotopic evidence (^{87}Sr/^{86}Sr, δ^7Li) for alteration of the oceanic crust at deep-rooted mud volcanoes in the Gulf of Cadiz, NE Atlantic Ocean, *Geochim. Cosmochim. Acta*, *73*, 5444–5459, doi:10.1016/j.gca.2009.06.004.

Schulz, H.-M., K.-C. Emeis, and N. Volkmann (1997), Organic carbon provenance and maturity in the mud breccia from the Napoli mud volcano: Indicators of origin and burial depth, *Earth Planet. Sci. Lett.*, *147*(1-4), 141–151, doi:10.1016/S0012-821X(97)00013-7.

Screaton, E., D. Saffer, P. Henry, and S. Hunze (2002), Porosity loss within the underthrust sediments of the Nankai accretionary complex: Implications for overpressures, *Geology*, *30*(1), 19–22, doi:10.1130/0091-7613(2002)030<0019:PLWTUS>2.0.CO;2.

Seewald, J. S. (2003), Organic—inorganic interactions in petroleum-producing sedimentary basins, *Nature*, *426*, 327–333, doi:10.1038/nature02132.

Seewald, J. S., B. C. Benitez-Nelson, and J. K. Whelan (1998), Laboratory and theoretical constraints on the generation and composition of natural gas, *Geochim. Cosmochim. Acta*, *62*, 1599–1617, doi:10.1016/S0016-7037(98)00000-3.

Setzmann, U., and W. Wagner (1991), A New Equation of State and Tables of Thermodynamic Properties for Methane Covering the Range from the Melting Line to 625 K at Pressures up to 100 MPa, *J. Phys. Chem. Ref. Data*, *20*(6), 1061–1155, doi:10.1063/1.555898.

Shakirov, R., A. Obzhirov, E. Suess, A. Salyuk, and N. Biebow (2004), Mud volcanoes and gas vents in the Okhotsk Sea area, *Geo-Mar. Lett.*, *24*(3), 140–149, doi:10.1007/s00367-004-0177-y.

Shaw, B., N. N. Ambraseys, P. C. England, M. A. Floyd, G. J. Gorman, T. F. G. Higham, J. A. Jackson, J.-M. Nocquet, C. C. Pain, and M. D. Piggott (2008), Eastern Mediterranean tectonics and tsunami hazard inferred from the AD 365 earthquake, *Nat. Geosci.*, *1*(4), 268–276, doi:10.1038/ngeo151.

Shimizu, I. (1995), Kinetics of pressure solution creep in quartz: theoretical considerations, *Tectonophys.*, *245*(3–4), 121–134, doi:10.1016/0040-1951(94)00230-7.

Shipley, T. H., P. L. Stoffa, and D. F. Dean (1990), Underthrust sediments, fluid migration paths, and mud volcanoes associated with the accretionary wedge off Costa Rica: Middle America Trench, *J. Geophys. Res.*, *95*(B6), 8743–8752, doi:10.1029/JB095iB06p08743.

Shirzaei, M., M. L. Rudolph, and M. Manga (2015), Deep and shallow sources for the Lusi mud eruption revealed by surface deformation, *Geophys. Res. Lett.*, *42*, 5274–5281, doi:10.1002/2015GL064576.

Sibson, R. H. (1985), A note on fault reactivation, *J. Struct. Geol.*, *7*(6), 751–754, doi:10.1016/0191-8141(85)90150-6.

Sissingh, W. (1977), Biostratigraphy of Cretaceous calcareous nanno-plankton, *Geological Mijnbouw*, *56*, 37–65.

Söding, E., K. Wallmann, E. Suess, and E. Flüh (2002), RV Meteor cruise report M54/2 + M54/3, Fluids and subduction Costa Rica 2002 : M54/2 Caldera - Caldera, 13.8.-7.9.2002 ; M54/3A Caldera - Caldera, 10.9.-28.9.2002 ; M54/3B Caldera - Curacao, 01.10.-11.10.2002, Forschungszentrum für Marine Geowissenschaften: GEOMAR-

Report, 111, Kiel, Germany, doi:10.3289/GEOMAR_REP_111_2003.

Somoza, L., et al. (2003), Seabed morphology and hydrocarbon seepage in the Gulf of Cádiz mud volcano area: Acoustic imagery, multibeam and ultra-high resolution seismic data, *Mar. Geol.*, *195*(1–4), 153–176, doi:10.1016/S0025-3227(02)00686-2.

Somoza, L., T. Medialdea, R. León, G. Ercilla, J. T. Vázquez, M. Farran, J. Hernández-Molina, J. González, C. Juan, and M. C. Fernández-Puga (2012), Structure of mud volcano systems and pockmarks in the region of the Ceuta Contourite Depositional System (Western Alborán Sea), *Mar. Geol.*, *332–334*, 4–26, doi:10.1016/j.margeo.2012.06.002.

Speranza, F., L. Minelli, A. Pignatelli, and M. Chiappini (2012), The Ionian Sea: The oldest in situ ocean fragment of the world?, *J. Geophys. Res.*, *117*, B12101, doi: 10.1029/2012JB009475.

Stamatakis, M. G., E. G. Baltatzis, and S. B. Skounakis (1987), Sulfate minerals from a mud volcano in the Katakolo area, western Peloponnesus, Greece, *Am. Mineral.*, *72*, 839–841.

Staron, L., and E. J. Hinch (2005), Study of the collapse of granular columns using two-dimensional discrete-grain simulation, *J. Fluid Mech.*, *545*, 1–27, doi: 10.1017/S0022112005006415.

Stein, C. A., and S. Stein (1992), A model for the global variation in oceanic depth and heat flow with lithospheric age, *Nature*, *359*, 123–129.

Stewart, S. A., and R. J. Davies (2006), Structure and emplacement of mud volcano systems in the South Caspian Basin, *AAPG Bull.*, *90*, 771–786, doi:10.1306/11220505045.

Stoessell, R. K., and P. Byrne (1982), Methane solubilities in clay slurries, *Clays and Clay Minerals*, *30*(1), 67–72.

Stoffyn-Egli, P., F. T. MacKenzie (1984), Mass balance of dessolved lithium in the ocean, *Geochim. Cosmochim. Acta*, *48*, 859–872, doi:10.1016/0016-7037(84)90107-8.

Stolper, D. A., et al. (2014), Formation temperatures of thermogenic and biogenic methane, *Science*, *344*(6191), 1500–1503, doi:10.1126/science.1254509.

Strasser, M., M. Kölling, C. dos Santos Ferreira, H. G. Fink, T. Fujiwara, S. Henkel, K. Ikehara, T. Kanamatsu, K. Kawamura, S. Kodaira, M. Römer, G. Wefer, and R/V Sonne Cruise SO219A (incl. A. Kioka) and JAMSTEC Cruise MR12-E01 scientists (2013), A slump in the trench: Tracking the impact of the 2011 Tohoku-Oki earthquake, *Geology*, *41*(8), 935–938, doi:10.1130/G34477.1.

Sugihara, T., M. Kinoshita, E. Araki, T. Kimura, M. Kyo, Y. Namba, Y. Kido, Y. Sanada, and M. Thu (2014), Re-evaluation of temperature at the updip limit of locked portion of Nankai megasplay inferred from IODP Site C0002 temperature observatory, *Earth Planets Space*, *66*, 107, doi:10.1186/1880-5981-66-107.

Sullivan, S., L. J. Wood, and P. Mann (2004), Distribution, nature and origin of Mobile mud features offshore Trinidad, In: Post, P. J., et al. (eds), Salt-sediment interactions and hydrocarbon prospectivity: Concepts, applications, and case studies for the 21st century: Gulf Coast Section SEPM 24th Annual Research Conference, pp. 840–867.

Sumner, R. H., and G. K. Westbrook (2001), Mud diapirism in front of the Barbados accretionary wedge: the influence of fracture zones and North America–South America plate motions, *Mar. Petrol. Geol.*, *18*(5), 591–613, doi:10.1016/S0264-8172(01)00010-1.

Sun, Q., S. Wu, J. Cartwright, T. Lüdmann, and G. Yao (2013), Focused fluid flow systems of the Zhongjiannan Basin and Guangle Uplift, South China Sea, *Basin Res.*, *25*(1), 97–111, doi:10.1111/j.1365-2117.2012.00551.x.

Sweeney, J. J., and A. K. Burnham (1990), Evaluation of a simple model of vitrinite reflectance based on chemical kinetics, *Am. Assoc. Petrol. Geol. Bull.*, 74, 1559–1570.

Taira, A., I. Hill, J. Firth, et al. (1991), *Proceedings of the Ocean Drilling Program*, *Initial Reports*, *131*, 301 pp., Ocean Drill. Program, College Station, Tex.

Talukder, A. R., M. C. Comas. and J. I. Soto (2003), Pliocene to Recent mud diapirism and related mud volcanoes in the Alboran Sea (Western Mediterranean), *Geol. Soc. Spec. Publ.*, *216*, 443–459, doi:10.1144/GSL.SP.2003.216.01.29.

Talukder, A. R., J. Bialas, D. Klaeschen, D. Buerk, W. Brueckmann, T. Reston, and M. Breitzke (2007), High-resolution, deep tow, multichannel seismic and sidescan sonar survey of the submarine mounds and associated BSR off Nicaragua pacific margin, *Mar. Geol.*, *241*(1-4), 33–43, doi:10.1016/j.margeo.2007.03.002.

Tanaka, K. L. (1997), Sedimentary history and mass flow structures of Chryse and Acidalia Planitiae, Mars, *J. Geophys. Res.*, *102*(E2), 4131, doi:10.1029/96JE02862.

Taylor, R. G., et al. (2013), Ground water and climate change, *Nature Clim. Change*, *3*, 322–329, doi:10.1038/nclimate1744.

Terakawa, T., C. Hashimoto, and M. Matsu'ura (2013), Changes in seismic activity following the 2011 Tohoku-oki earthquake: Effects of pore fluid pressure, *Earth Planet. Sci. Lett.*, *365*, 17–24, doi:10.1016/j.epsl.2013.01.017.

Tingay, M., M. L. Rudolph, M. Manga, R. J. Davies, and C.-Y. Wang (2015), Initiation of the Lusi mudflow disaster, *Nat. Geosci.*, *8*, 493–494, doi:10.1038/ngeo2472.

Tinivella, U., F. Accaino, and B. Della Vedova (2008), Gas hydrates and active mud volcanism on the South Shetland continental margin, Antarctic Peninsula, *Geo-Mar. Lett.*, *28*(2), 97–106, doi:10.1007/s00367-007-0093-z.

Todd, T., and G. Simmons (1972), Effect of pore pressure on the velocity of compressional waves in low-porosity rocks, *J. Geophys. Res.*, *77*(20), 3731–3743, doi:10.1029/JB077i020p03731.

Toki, T., R. Higa, A. Tanahara, K. Ijiri, U. Tsunogai, and J. Ashi (2013), Origin of pore water in Kumano mud volcanoes, *Chikyukagaku (Geochemistry)*, *47*(4), 221–236. [in Japanese with English Abstr.]

Toki, T., R. Higa, A. Ijiri, U. Tsunogai, and J. Ashi (2014), Origin and transport of pore fluids in the Nankai accretionary prism inferred from chemical and isotopic compositions of pore water at cold seep sites off Kumano, *Earth Planets Space*, *66*(1), 137, doi:10.1186/s40623-014-0137-3.

Tokuyama, H., J. Ashi, Y. Nakamura, M. Shirai, K. Kameo, M. Watanabe, H. Asahi, T.

Kanahara, and onboard scientists of KH-06-4 Leg6 (2007), Brine Lake in the eastern Mediterranean Sea, in *Abstract presented at the 114th Annual meeting of The Geological Society of Japan, Hokkaido, Japan.*

Topin, V., Y. Monerie, F. Perales, and F. Radjaï (2012), Collapse Dynamics and Runout of Dense Granular Materials in a Fluid, *Phys. Rev. Lett.*, *109*(18), 188001, doi: 10.1103/PhysRevLett.109.188001.

Tran, A., M. L. Rudolph, and M. Manga (2015), Bubble mobility in mud and magmatic volcanoes, *J. Volcanol. Geotherm. Res.*, *294*, 11–24, doi: 10.1016/j.jvolgeores.2015.02.004.

Tréhu, A. M., M. E. Torres, G. F. Moore, E. Suess, and G. Bohrmann (1999), Temporal and spatial evolution of a gas hydrate—bearing accretionary ridge on the Oregon continental margin, *Geology*, *27*(10), 939–942, doi:10.1130/0091-7613(1999)027<0939:TASEOA>2.3.CO;2.

Treude, T., A. Boetius, K. Knittel, K. Wallmann, and B. Jørgensen (2003), Anaerobic oxidation of methane above gas hydrates at Hydrate Ridge, NE Pacific Ocean, *Mar. Ecol. Prog. Ser.*, *264*, 1–14, doi:10.3354/meps264001.

Truffert, C., N. Chamot-Rooke, S. Lallemant, B. De Voogd, P. Huchon, and X. Le Pichon (1993), The Crust of the Western Mediterranean Ridge From Deep Seismic Data and Gravity Modelling, *Geophys. J. Int.*, *114*(2), 360–372, doi:10.1111/j.1365-246X.1993.tb03924.x.

Tryon, M. D., K. M. Brown, M. E. Torres, A. M. Trehu, J. McManus, and R. W. Collier (1999), Measurements of transience and downward fluid flow near episodic methane gas vents, Hydrate Ridge, Cascadia, *Geology*, *27*(12), 1075–1078, doi:10.1130/0091-7613(1999)027<1075:MOTADF>2.3.CO;2.

Tsuji, T., J. Ashi, M. Strasser, and G. Kimura (2015), Identification of the static backstop and its influence on the evolution of the accretionary prism in the Nankai Trough, *Earth Planet. Sci. Lett.*, *431*, 15–25, doi:10.1016/j.epsl.2015.09.011.

Tsunogai, U., K. Maegawa, S. Sato, D. D. Komatsu, F. Nakagawa, T. Toki, and J. Ashi (2012), Coseimic massive methane release from a submarine mud volcano, *Earth Planet. Sci. Lett.*, *341-344*, 79–85, doi:10.1016/j.epsl.2012.06.004.

Turcotte, D. L., D. C. Mcadoo, and J. G. Caldwell (1978), An elastic-perfectly plastic analysis of the bending of the lithosphere at a trench, *Tectonophys.*, *47*(3–4), 193–205, doi:10.1016/0040-1951(78)90030-6.

Ujiié, Y. (2000), Mud diapirs observed in two piston cores from the landward slope of the northern Ryukyu Trench, northwestern Pacific Ocean, *Mar. Geol.*, *163*, 149–167, doi:10.1016/S0025-3227(99)00113-9.

Valentine, D. L. (2011), Emerging Topics in Marine Methane Biogeochemistry, *Annu. Rev. Mar. Sci.*, *3*, 147–171, doi:10.1146/annurev-marine-120709-142734.

Valentine, D. L., D. C. Blanton, W. S. Reeburgh, and M. Kastner (2001), Water column methane oxidation adjacent to an area of active hydrate dissociation, Eel River Basin, *Geochim. Cosmochim. Acta*, *65*, 2633–2640, doi:10.1016/S0016-7037(01)00625-1.

Van den Beukel, J., and R. Wortel (1988), Thermo-mechanical modelling of arc-trench regions, *Tectonophys.*, *154*, 177–193, doi:10.1016/0040-1951(88)90101-1.

van Loon, A. J. (2010), Sedimentary volcanoes: Overview and implications for the definition of a volcano on Earth, In: Cañón-Tapia, E., and A. Szakács (eds.), *What Is a Volcano?*, *Geol. Soc. Am. Spec. Pap.*, *470*, 31–41, doi:10.1130/2010.2470(03).

Van Rensbergen, P., M. De Batist, J. Klerkx, R. Hus, J. Poort, M. Vanneste, N. Granin, O. Khlystov, and P. Krinitsky (2002), Sublacustrine mud volcanoes and methane seeps caused by dissociation of gas hydrates in Lake Baikal, *Geology*, *30*, 631–634, doi: 10.1130/0091-7613(2002)030<0631:SMVAMS>2.0.CO;2.

Van Rensbergen, P., D. Depreiter, B. Pannemans, and J.-P. Henriet (2005), Seafloor expression of sediment extrusion and intrusion at the El Arraiche mud volcano field, Gulf of Cadiz, *J. Geophys. Res.*, *110*, F02010, doi:10.1029/2004JF000165.

Vigier, N., and Y. Goddéris (2015), A new approach for modeling Cenozoic oceanic lithium isotope paleo-variations: the key role of climate, *Clim. Past*, *11*, 635–645, doi: :10.5194/cp-11-635-2015.

Viola, G., M. Andreoli, Z. Ben-Avraham, I. Stengel, and M. Reshef (2005), Offshore mud volcanoes and onland faulting in southwestern Africa: neotectonic implications and constraints on the regional stress field, *Earth Planet. Sci. Lett.*, *231*(1–2), 147–160, doi:10.1016/j.epsl.2004.12.001.

Vogt, P. R., K. Crane, E. Sundvor, M. D. Max, and S. L. Pfirman (1994), Methane-generated(?) pockmarks on young, thickly sedimented oceanic crust in the Arctic: Vestnesa ridge, Fram strait, *Geology*, *22*(3), 255–258, doi:10.1130/0091-7613(1994)022<0255:MGPOYT>2.3.CO;2.

Vogt, P. R., G. Cherkashev, G. Ginsburg, G. Ivanov, A. Milkov, K. Crane, A. Sundvor, N. Pimenov, and A. Egorov (1997), Haakon Mosby Mud Volcano provides unusual example of venting, *Eos, Trans. Am. Geophys. Union*, *78*(48), 549–557, doi:10.1029/97EO00326.

Volgin, A. V, and J. M. Woodside (1996), Sidescan sonar images of mud volcanoes from the Mediterranean Ridge: possible causes of variations in backscatter intensity, *Mar. Geol.*, *132*(1–4), 39–53, doi:10.1016/0025-3227(95)00152-2.

Vona, A., G. Giordano, A. A. De Benedetti, R. D'Ambrosio, C. Romano, and M. Manga (2015), Ascent velocity and dynamics of the Fiumicino mud eruption, Rome, Italy, *Geophys. Res. Lett.*, *42*, 6244–6252, doi:10.1002/2015GL064571.

von Huene, R., and D. W. Scholl (1991), Observations at convergent margins concerning sediment subduction, subduction erosion, and the growth of continental crust, *Rev. Geophys.*, *29*(3), 279–316, doi:10.1029/91RG00969.

von Rad, U., H. Rösch, U. Berner, M. Geyh, V. Marchig, and H. Schulz (1996), Authigenic carbonates derived from oxidized methane vented from the Makran accretionary prism off Pakistan, *Mar. Geol.*, *136*(1–2), 55–77, doi:10.1016/S0025-3227(96)00017-5.

Wagner, W., and A. Pruß (2002), The IAPWS formulation 1995 for the thermodynamic properties of ordinary water substance for general and scientific use, *J. Phys. Chem. Ref. Data*, *31*(2), 387–535, doi:10.1063/1.1461829.

Wallmann, K., P. Linke, E. Suess, G. Bohrmann, H. Sahling, M. Schlüter, A. Dählmann, S. Lammers, J. Greinert, and N. von Mirbach (1997), Quantifying fluid flow, solute mixing, and biogeochemical turnover at cold vents of the eastern Aleutian subduction zone, *Geochim. Cosmochim. Acta*, *61*(24), 5209–5219, doi:10.1016/S0016-7037(97)00306-2.

Wang, C.-Y. (2007), Liquefaction beyond the near field, *Seismol. Res. Lett.*, *78*(5), 512–517, doi:10.1785/gssrl.78.5.512.

Wang, C.-Y., and M. Manga (2010), Hydrologic responses to earthquakes and a general metric, *Geofluids*, *10*(1–2), 206–216, doi:10.1111/j.1468-8123.2009.00270.x.

Wang, K., and E. E. Davis (1992), Thermal effects of marine sedimentation in hydrothermally active areas, *Geophys. J. Int.*, *110*(1), 70–78, doi:10.1111/j.1365-246X.1992.tb00714.x.

Wang, K., and Y. Hu (2006), Accretionary prisms in subduction earthquake cycles: The theory of dynamic Coulomb wedge, *J. Geophys. Res.*, *111*, B06410, doi:10.1029/2005JB004094.

Wang, K., R. D. Hyndman, and M. Yamano (1995), Thermal regime of the southwest Japan subduction zone: Effects of age history of the subducting plate, *Tectonophys.*, *248*(1-2), 53–69, doi:10.1016/0040-1951(95)00028-L.

Watkins, J. S., L. A. Walters, and R. H. Godson (1972), Dependence of in-situ compressional-wave velocity on porosity in unsaturated rocks, *Geophysics*, *37*(1), 29–35, doi:10.1190/1.1440249.

Wessel, P., and W. H. F. Smith (1998), New, improved version of generic mapping tools released, *Eos Trans. AGU*, *79*(47), 579–579, doi:10.1029/98EO00426.

Westbrook, G. K., and T. J. Reston (2002), The accretionary complex of the Mediterranean Ridge: tectonics, fluid flow and the formation of brine lakes—an introduction to the special issue of Marine Geology, *Mar. Geol.*, *186*(1-2), 1–8, doi:10.1016/S0025-3227(02)00169-X.

Wheildon, J., T. R. Evans, and R. W. Girdler (1974), Thermal conductivity, density, and sonic velocity measurements of samples of anhydrate and halite from sites 224 and 227, *Init. Rep. Deep Sea Drill. Proj.*, *23*, 909–911, doi:10.2973/dsdp.proc.23.127.1974.

White, D. E. (1955), Violent mud-volcano eruption of Lake City hot springs, northeastern California, *Bull. Geol. Soc. Am.*, *66*, 1109–1130, doi:10.1130/0016-7606(1955)66[1109:VMEOLC]2.0.CO;2.

Whiticar, M. J. (1990), A geochemical perspective of natural gas and atmospheric methane, *Org. Geochem.*, *16*(1-3), 531–547, doi:10.1016/0146-6380(90)90068-B.

Wiedicke, M., S. Neben, and V. Spiess (2001), Mud volcanoes at the front of the Makran accretionary complex, Pakistan, *Mar. Geol.*, *172*(1-2), 57–73, doi:10.1016/S0025-3227(00)00127-4.

Wilcock, W. S. D., and J. A. Whitehead (1991), The Rayleigh-Taylor instability of an embedded layer of low-viscosity fluid, *J. Geophys. Res. Solid Earth*, **96**(B7), 12193–12200, doi:10.1029/91JB00339.

Wilhelms, A., S. R. Larter, I. Head, P. Farrimond, R. di-Primio, and C. Zwach (2001), Biodegradation of oil in uplifted basins prevented by deep-burial sterilization, *Nature*, *411*, 1034–1037, doi:10.1038/35082535.

Winkler, K., and A. Nur (1982), Seismic attenuation: effects of pore fluids and frictional-sliding, *Geophysics*, *47*(1), 1–15, doi:10.1190/1.1441276.

Woodside, J. M., and A. V. Volgin (1996), Brine pools associated with Mediterranean Ridge mud diapirs: an interpretation of echo-free patches in deep tow sidescan sonar data, *Mar. Geol.*, *132*(1–4), 55–61, doi:10.1016/0025-3227(95)00153-0.

Woodside, J. M., J. Mascle, T. A. C. Zitter, A. F. Limonov, M. Ergün, A. Volkonskaia, shipboard scientists of the PRISMED II Expedition (2002), The Florence Rise, the Western Bend of the Cyprus Arc, *Mar. Geol.*, *185*(3–4), 177–194, doi:10.1016/S0025-3227(02)00194-9.

Wuebbles, D. J., and K. Hayhoe (2002), Atmospheric methane and global change, *Earth Sci. Rev.*, *57*, 177–210, doi:10.1016/s0012-8252(01)00062-9.

Wunder, B., A. Meixner, R. L. Romer, and W. Heinrich (2006), Temperature-dependent isotopic fractionation of lithium between clinopyroxene and high-pressure hydrous fluids, *Contrib. Mineral. Petrol.*, *151*(1), 112–120, doi:10.1007/s00410-005-0049-0.

Wyllie, M. R. J., A. R. Gregory, and L. W. Gardner (1956), Elastic wave velocities in heterogeneous and porous media, *Geophysics*, 21(1), 41–70, doi:10.1190/1.1438217.

Wyllie, M. R. J., A. R. Gregory, and G. H. F. Gardner (1958), An experimental investigation of factors affecting elastic wave velocities in porous media, *Geophysics*, *23*(3), 459–493, doi:10.1190/1.1438493.

Yakimov, M. M., et al. (2013), Microbial life in the Lake Medee, the largest deep-sea salt-saturated formation, *Sci. Rep.*, *3*, 3554, doi:10.1038/srep03554.

Yamaguchi, T. I., M. Yamano, T. Nagao, and S. Goto (2001), Distribution of radioactive heat production around an active fault and in accretionary prisms of southwest Japan, *Phys. Earth Planet. Inter.*, *126*(3–4), 269–277, doi:10.1016/S0031-9201(01)00260-6.

Yamano, M., S. Uyeda, Y. Aoki, and T. H. Shipley (1982), Estimates of heat flow derived from gas hydrates, *Geology*, *10*(7), 339–343, doi:10.1130/0091-7613(1982)10<339:EOHFDF>2.0.CO;2.

Ye, S., J. Bialas, E. R. Flueh, A. Stavenhagen, R. von Huene, G. Leandro, and K. Hinz (1996), Crustal structure of the Middle American Trench off Costa Rica from wide-angle seismic data, *Tectonics*, *15*(5), 1006–1021, doi:10.1029/96TC00827.

Yilmaz, Ö. (2001), *Seismic Data Analysis: Processing, Inversion and Interpretation of Seismic Data*, Society of Exploration Geophysicists, Tulsa, USA, doi: 10.1190/1.9781560801580.

You, C. F., and J. Gieskes (2001), Hydrothermal alteration of hemi-pelagic sediments: Experimental evaluation of geochemical processes in shallow subduction zones, *Appl.*

Geochem., *16*, 1055–1066, doi:10.1016/S0883-2927(01)00024-5.

You, C. F., A. J. Spivack, J. H. Smith, and J. M. Gieskes (1993), Mobilization of boron in convergent margins: Implications for the boron geochemical cycle, *Geology*, *21*(3), 207–210, doi:10.1130/0091-7613(1993)021<0207:MOBICM>2.3.CO;2.

You, C. F., P. R. Castillo, J. M. Gieskes, L. H. Chan, and A. J. Spivack (1996), Trace element behavior in hydrothermal experiments: Implications for fluid processes at shallow depths in subduction zones, *Earth Planet. Sci. Lett.*, *140*, 41–52, doi:10.1016/0012-821X(96)00049-0.

Yuan, T., G. D. Spence, R. D. Hyndman, T. A. Minshull, and S. C. Singh (1999), Seismic velocity studies of a gas hydrate bottom-simulating reflector on the northern Cascadia continental argin: Amplitude modeling and full waveform inversion, *J. Geophys. Res.*, *104*(B1), 1179–1191, doi:10.1029/1998JB900020.

Zhang, L., L.-H. Chan, J. M. Gieskes (1998), Lithium isotope geochemistry of pore waters from Ocean Drilling Program Sites 918 and 919, Irminger Basin, *Geochim. Cosmochim. Acta*, *62*(14), 2437–2450, doi:10.1016/S0016-7037(98)00178-1.

Zhang, X., K. C. Hester, W. Ussler, P. M. Walz, E. T. Peltzer, and P. G. Brewer (2011), In situ Raman-based measurements of high dissolved methane concentrations in hydrate-rich ocean sediments, *Geophys. Res. Lett.*, *38*, L08605, doi:10.1029/2011GL04714.

Zitellini, N., et al. (2009), The quest for the Africa—Eurasia plate boundary west of the Strait of Gibraltar, *Earth Planet. Sci. Lett.*, *280*(1–4), 13–50, doi: 10.1016/j.epsl.2008.12.005.

Zitter, T. A. C., C. Huguen, and J. M. Woodside (2005), Geology of mud volcanoes in the eastern Mediterranean from combined sidescan sonar and submersible surveys, *Deep Sea Res. Part I Oceanogr. Res. Pap.*, *52*(3), 457–475, doi:10.1016/j.dsr.2004.10.005.

Zühlsdorff, L., and V. Spieß (2004), Three-dimensional seismic characterization of a venting site reveals compelling indications of natural hydraulic fracturing, *Geology*, *32*(2), 101–104, doi:10.1130/G19993.1.

Appendix A

Additional Materials for Chapters 1 and 2

This supplementary material contains a supplemental table (Table A.1) for Chapters 1 and 2. The dataset provides a catalog that includes heights and radii of submarine mud volcanoes compiled from bathymetric data and literature, which produces the results presented in Chapters 1 and 2. The data in the table are summarized in Figures 1.9, 1.10, and 2.1. All data in the table are properly cited and referred in the reference list of main text.

Table A.1: Topographical properties of submarine mud volcanoes compiled in this study (modified from *Kioka and Ashi* [2015]). Note that the diameter D_{mean} here denotes the mean diameter $D_{\mathrm{mean}} = (D_{\mathrm{min}} + D_{\mathrm{max}})/2$, if both the maximum diameter D_{max} and minimum diameter D_{min} are available for the given mud volcano, and otherwise denotes a representative diameter. S_{min}, S_{max}, and S_{mean} represent minimum, maximum, and mean surface slopes of the given mud volcano that are calculated from heights H and diameters D_{max}, D_{min}, and D_{mean}, respectively. Data in this table are partially summarized and illustrated in Figures 1.9, 1.10, and 2.1. An updated version of this catalog is planned to be posted on the author's website: http://ofgs.aori.u-tokyo.ac.jp/kioka/kioka-res-e.html.

Long. (+E)	Lat. (+N)	D_{max} (km)	D_{min} (km)	D_{mean} (km)	H (m)	S_{min} (deg)	S_{max} (deg)	S_{mean} (deg)	Name	Mud volcano field	Region	Refs
24.425	33.812	4.52	0.84	2.68	110	2.8	14.7	4.7	Alberto da Ottaviano	Prometheus-2	E. Mediterranean	[1]
30.271	35.332	NaN	NaN	2.5	35	NaN	NaN	1.6	Amsterdam	Anaximander Mts	E. Mediterranean	[2]
22.714	33.767	NaN	NaN	5	222	NaN	NaN	5.1	Antaeus	Pan di Zucchero	E. Mediterranean	[3]
24.717	33.797	1.6	0.68	1.14	80	5.7	13.2	8	Areda/Ardea	Olimpi	E. Mediterranean	[1]
20.857	36.021	NaN	NaN	2	80	NaN	NaN	4.6	Aros	Cobblestone	E. Mediterranean	[3]
30.213	35.392	NaN	NaN	2	120	NaN	NaN	6.8	Athina	Anaximander Mts	E. Mediterranean	[4]
24.75	33.738	2.32	1.8	2.06	130	6.4	8.2	7.2	Bergamo	Olimpi	E. Mediterranean	[5]
25.483	33.508	NaN	NaN	2.5	80	NaN	NaN	3.7	Dublin	United Nations	E. Mediterranean	[6]
24.645	33.855	NaN	NaN	1.9	160	NaN	NaN	9.6	Fuerstenfeldbruck	Olimpi	E. Mediterranean	[7]
24.713	33.75	1.64	1.32	1.48	90	6.3	7.8	6.9	Hilo	Olimpi	E. Mediterranean	[5]
22.823	33.803	2.2	1	1.6	70	3.6	8	5	Jessica	Pan di Zucchero	E. Mediterranean	[1]
30.562	35.432	0.9	0.6	0.75	50	6.3	9.5	7.6	Kazan	Anaximander Mts	E. Mediterranean	[2]
30.458	35.728	NaN	NaN	1.2	135	NaN	NaN	12.7	Kula	Anaximander Mts	E. Mediterranean	[2]
24.588	33.782	NaN	NaN	1.5	60	NaN	NaN	4.6	Landshut	Olimpi	E. Mediterranean	[7]
24.65	33.783	NaN	NaN	1.7	70	NaN	NaN	4.7	Leipzig	Olimpi	E. Mediterranean	[8]
24.568	33.855	NaN	NaN	0.2	50	NaN	NaN	26.6	Lich	Olimpi	E. Mediterranean	[9]
24.417	33.817	1.32	0.68	1	70	6.1	11.6	8	Luigi	Prometheus-2	E. Mediterranean	[1]
24.677	33.618	NaN	NaN	3	100	NaN	NaN	3.8	Maidstone	Olimpi	E. Mediterranean	[8]
24.453	33.825	1.16	0.88	1.02	160	15.4	20	17.4	Maier	Prometheus-2	E. Mediterranean	[1]
22.183	34.398	6.7	4.9	5.8	129	2.2	3	2.5	Medee-Hakuho	Medee	E. Mediterranean	[10]
24.778	33.733	2.6	2.12	2.36	110	4.8	5.9	5.3	Milano	Olimpi	E. Mediterranean	[5]
24.605	33.78	NaN	NaN	1	40	NaN	NaN	4.6	Milford Haven	Olimpi	E. Mediterranean	[8]
24.725	33.732	1.2	0.96	1.08	110	10.4	12.9	11.5	Monza	Olimpi	E. Mediterranean	[5]
24.557	33.665	5	3	4	180	4.1	6.8	5.1	Moscow	Olimpi	E. Mediterranean	[11]
24.683	33.725	3.52	2.96	3.24	130	4.2	5	4.6	Napoli	Olimpi	E. Mediterranean	[5]

Table A.1: *Continued.*

Long. (+E)	Lat. (+N)	$D_{\max}$ (km)	$D_{\min}$ (km)	D_{mean} (km)	H (m)	$S_{\min}$ (deg)	$S_{\max}$ (deg)	S_{mean} (deg)	Name	Mud volcano field	Region	Refs
20.88	35.926	2.5	2	2.25	35	1.6	2	1.8	Novorossiysk	Cobblestone	E. Mediterranean	[12]
22.847	33.754	1.8	1.04	1.42	80	5.1	8.7	6.4	Oriana	Pan di Zucchero	E. Mediterranean	[1]
22.798	33.792	7.28	2.6	4.94	160	2.5	7	3.7	Pan di Zucchero	Pan di Zucchero	E. Mediterranean	[1]
22.775	33.768	6.6	2.8	4.7	160	2.8	6.5	3.9	Pan di Zucchero-2	Pan di Zucchero	E. Mediterranean	[1]
24.73	33.753	1.36	0.6	0.98	60	5	11.3	7	Procida	Olimpi	E. Mediterranean	[1]
20.801	35.853	NaN	NaN	1.8	70	NaN	NaN	4.4	Prometheus	Cobblestone	E. Mediterranean	[13]
24.433	33.837	2.56	1.76	2.16	120	5.4	7.8	6.3	Prometheus-2	Prometheus-2	E. Mediterranean	[5]
30.892	35.38	NaN	NaN	1	50	NaN	NaN	5.7	Saint Ouen l'Aumone	Anaximander Mts	E. Mediterranean	[14]
30.483	35.752	NaN	NaN	1	50	NaN	NaN	5.7	San Remo	Anaximander Mts	E. Mediterranean	[2]
24.683	33.767	1.88	0.96	1.42	120	7.3	14	9.6	Sorrento	Olimpi	E. Mediterranean	[5]
25.583	33.475	2	1	1.5	35	2	4	2.7	Stoke-on-Trent	United Nations	E. Mediterranean	[15]
24.607	33.677	NaN	NaN	1	40	NaN	NaN	4.6	Stvor	Olimpi	E. Mediterranean	[7]
31.7	34.8	1.7	1.2	1.45	85	5.7	8.1	6.7	Texel	Florence Rise	E. Mediterranean	[16]
30.251	35.479	1.9	1.3	1.6	60	3.6	5.3	4.3	Thessaloniki	Anaximander Mts	E. Mediterranean	[17]
30.78	35.378	NaN	NaN	0.9	80	NaN	NaN	10.1	Tuzlukush	Anaximander Mts	E. Mediterranean	[14]
24.712	33.765	0.88	0.76	0.82	80	10.3	11.9	11	Warnsdorf	Olimpi	E. Mediterranean	[5]
24.667	33.777	NaN	NaN	1.1	60	NaN	NaN	6.2	Weilheim	Olimpi	E. Mediterranean	[7]
28.159	32.135	NaN	NaN	1.5	25	NaN	NaN	1.9	Cheops	Nile fan W. Province	E. Mediterranean	[18]
28.178	32.108	NaN	NaN	1	40	NaN	NaN	4.6	Chephren	Nile fan W. Province	E. Mediterranean	[19]
29.75	31.675	2.5	2.2	2.35	40	1.8	2.1	1.9	Giza	Nile fan C. Province	E. Mediterranean	[20]
30.135	31.969	2	1.5	1.75	50	2.9	3.8	3.3	North Alex	Nile fan C. Province	E. Mediterranean	[21]
31.39	32.362	3.7	3.2	3.45	50	1.5	1.8	1.7	Isis	Nile fan E. Province	E. Mediterranean	[21]
31.592	32.328	4.6	3	3.8	90	2.2	3.4	2.7	Osiris	Nile fan E. Province	E. Mediterranean	[21]
31.71	32.37	2.8	2.6	2.7	90	3.7	4	3.8	Amon	Nile fan E. Province	E. Mediterranean	[21]
63.005	24.247	2.2	1.4	1.8	65	3.4	5.3	4.1	Mound A	Oman abyssal plain	Makran	[22]
63.062	24.257	1.7	1.2	1.45	36	2.4	3.4	2.8	Mound B	Oman abyssal plain	Makran	[22]
63.006	24.254	NaN	NaN	0.38	7.3	NaN	NaN	2.2	Mound 3	Oman abyssal plain	Makran	[22]
15.648	39.179	NaN	NaN	2	35	NaN	NaN	2	Richthofen (RMV)	Paola Ridge	S. Tyrrhenian Sea	[23]
15.629	39.143	NaN	NaN	4.2	55	NaN	NaN	1.5	Mojsisovics (MMV)	Paola Ridge	S. Tyrrhenian Sea	[23]
16.917	38.193	NaN	NaN	1.5	100	NaN	NaN	7.6	Madonna dello Ionio (NW)	Spartivento basin	C. Mediterranean	[24]
16.933	38.187	NaN	NaN	2	140	NaN	NaN	8	Madonna dello Ionio (SE)	Spartivento basin	C. Mediterranean	[24]

Table A.1: *Continued.*

Long. (+E)	Lat. (+N)	D_{max} (km)	D_{min} (km)	D_{mean} (km)	H (m)	S_{min} (deg)	S_{max} (deg)	S_{mean} (deg)	Name	Mud volcano field	Region	Refs
17.083	38.267	NaN	NaN	0.5	30	NaN	NaN	6.8	Cerere	Spartivento basin	C. Mediterranean	[25]
16.733	38.717	NaN	NaN	0.2	25	NaN	NaN	14	Catanzaro	Spartivento basin	C. Mediterranean	[25]
17.183	38.617	NaN	NaN	2	70	NaN	NaN	4	Venere 1	Crotone basin	C. Mediterranean	[25]
17.2	38.617	NaN	NaN	2	50	NaN	NaN	2.9	Venere 2	Crotone basin	C. Mediterranean	[25]
17.683	38.85	NaN	NaN	2.5	50	NaN	NaN	2.3	Minerva	Crotone basin	C. Mediterranean	[25]
16.8	37.467	NaN	NaN	2	150	NaN	NaN	8.5	Athena	Inner Calabrian prism	C. Mediterranean	[25]
17.467	38.117	NaN	NaN	2.5	200	NaN	NaN	9.1	Giunone	Inner Calabrian prism	C. Mediterranean	[25]
17.273	37.803	9	7	8	350	4.4	5.7	5	Pythagoras	Inner Calabrian prism	C. Mediterranean	[24]
17.617	38.217	NaN	NaN	1.2	40	NaN	NaN	3.8	Sartori	Inner Calabrian prism	C. Mediterranean	[25]
-87.291	11.291	1.29	1.14	1.22	80	7.1	8	7.5	Mound Tucan	Momotombo	Nicaragua	[26]
-87.267	11.28	1.09	0.81	0.95	100	10.4	13.9	11.9	Mound Congo	Momotombo	Nicaragua	[26]
-87.255	11.274	1.06	0.92	0.99	70	7.5	8.7	8.1	Mound Carablanca	Momotombo	Nicaragua	[26]
-87.166	11.254	2.15	1.63	1.89	180	9.5	12.5	10.8	Mound Baula I	Baula Massive	Nicaragua	[27]
-87.14	11.24	0.75	0.7	0.73	70	10.6	11.3	10.9	Mound Baula II	Baula Massive	Nicaragua	[26]
-87.132	11.238	0.9	0.63	0.77	110	13.7	19.2	16	Mound Baula III	Baula Massive	Nicaragua	[26]
-87.124	11.226	0.71	0.5	0.61	70	11.2	15.6	13	Mound Baula IV	Baula Massive	Nicaragua	[26]
-87.109	11.223	1.26	0.84	1.05	120	10.8	15.9	12.9	Mound Baula V	Baula Massive	Nicaragua	[26]
-87.155	11.205	0.48	0.38	0.43	25	5.9	7.5	6.6	Mound Iguana	Central	Nicaragua	[28]
-87.182	11.205	0.92	0.87	0.89	60	7.4	7.9	7.7	Mound Quetzal	Central	Nicaragua	[28]
-87.151	11.186	0.89	0.69	0.79	40	5.1	6.6	5.8	Mound Buho	Central	Nicaragua	[26]
-87.2	11.184	0.52	0.49	0.51	50	10.9	11.5	11.2	Mound Pargo	Central	Nicaragua	[26]
-87.14	11.178	1.10	0.85	0.97	60	6.3	8	7	Mound Hormiga	Central	Nicaragua	[28]
-87.115	11.176	0.74	0.59	0.66	50	7.7	9.6	8.6	Mound Bocaraca	Central	Nicaragua	[26]
-87.129	11.166	0.69	0.44	0.56	50	8.3	12.9	10.1	Mound Oropel	Central	Nicaragua	[26]
-86.912	11.038	0.94	0.78	0.86	130	15.5	18.4	16.8	Mound Perezoso	Perezoso	Nicaragua	[26]
-86.904	11.019	0.62	0.58	0.6	30	5.5	5.9	5.7	Mound Colibri	Perezoso	Nicaragua	[26]
-87.085	11.031	1.48	0.54	1.01	70	5.4	14.5	7.9	R1.1	Mound Ridge I	Nicaragua	[26]
-87.096	11.022	1.05	0.65	0.85	70	7.6	12.2	9.4	R1.2	Mound Ridge I	Nicaragua	[26]
-87.035	11.036	0.86	0.41	0.64	60	7.9	16.3	10.7	R2.2	Mound Ridge II	Nicaragua	[26]
-87.051	11.02	1.02	0.65	0.84	90	10	15.5	12.2	R2.4	Mound Ridge II	Nicaragua	[26]
-87.066	11.011	1.46	1.15	1.31	110	8.6	10.8	9.6	R2.5	Mound Ridge II	Nicaragua	[26]

Table A.1: *Continued.*

Long. (+E)	Lat. (+N)	D_{max} (km)	D_{min} (km)	D_{mean} (km)	H (m)	S_{min} (deg)	S_{max} (deg)	S_{mean} (deg)	Name	Mud volcano field	Region	Refs
-87.078	11.006	1.2	0.68	0.94	110	10.4	17.9	13.2	R2.6	Mound Ridge II	Nicaragua	[26]
-87.093	11.01	0.88	0.71	0.80	80	10.3	12.7	11.4	R2.7	Mound Ridge II	Nicaragua	[26]
-86.957	11.036	0.5	0.44	0.47	40	9.1	10.3	9.7	R3.1	Mound Ridge III	Nicaragua	[26]
-87.011	11	1.36	0.73	1.05	70	5.9	10.9	7.6	Morpho	Mound Ridge III	Nicaragua	[26]
-87.02	10.996	1.02	0.92	0.97	60	6.7	7.4	7.1	R3.4	Mound Ridge III	Nicaragua	[26]
-87.029	10.989	0.53	0.47	0.5	40	8.6	9.7	9.1	R3.5	Mound Ridge III	Nicaragua	[26]
-86.305	10.297	1.5	0.7	1.1	115	8.7	18.2	11.8	Mound Culebra	Nicoya	Costa Rica	[29]
-86.19	10.008	1.8	0.7	1.25	140	8.8	21.8	12.6	Mound 10	Nicoya	Costa Rica	[30]
-85.908	9.669	1.6	0.75	1.18	80	5.7	12	7.8	unnamed	Hongo (Nicoya)	Costa Rica	[31]
-85.884	9.657	1.2	1.2	1.2	75	7.1	7.1	7.1	Mound Jaguar	Hongo (Nicoya)	Costa Rica	[32]
-85.833	9.603	1.3	0.75	1.03	80	7	12	8.9	Mound 6	Hongo (Nicoya)	Costa Rica	[32]
-85.822	9.606	1	0.8	0.9	60	6.8	8.5	7.6	Mound 5	Hongo (Nicoya)	Costa Rica	[32]
-85.81	9.614	0.5	0.5	0.5	70	15.6	15.6	15.6	Mound 4	Hongo (Nicoya)	Costa Rica	[32]
-85.797	9.606	0.8	0.5	0.65	70	9.9	15.6	12.2	Mound 3	Hongo (Nicoya)	Costa Rica	[32]
-84.621	9.033	NaN	NaN	0.2	40	NaN	NaN	21.8	Mound Quepos	Osa	Costa Rica	[33]
-84.303	8.92	NaN	NaN	0.15	15	NaN	NaN	11.3	Mound 11a	Osa	Costa Rica	[34]
-84.304	8.923	NaN	NaN	0.3	25	NaN	NaN	9.5	Mound 11b	Osa	Costa Rica	[34]
-84.31	8.932	0.8	0.6	0.7	38	5.4	7.2	6.2	Mound 12	Osa	Costa Rica	[35]
-84.315	8.938	NaN	NaN	0.5	5	NaN	NaN	1.1	Grillo	Osa	Costa Rica	[34]
-57.6	14.333	NaN	NaN	2.5	33	NaN	NaN	1.5	unnamed	unknown	Barbados	[36]
-57.763	13.863	NaN	NaN	0.4	35	NaN	NaN	9.9	Volcano A	Manon	Barbados	[37]
-57.733	13.85	0.82	0.48	0.65	25	3.5	5.9	4.4	Volcano C	Manon	Barbados	[37]
-57.647	13.828	1	0.6	0.8	5	0.6	1	0.7	Atlante	Manon	Barbados	[38]
-57.712	13.842	0.63	0.63	0.63	5	0.9	0.9	0.9	Cyclops	Manon	Barbados	[38]
-57.543	13.778	NaN	NaN	1	180	NaN	NaN	19.8	Mount Manon	Manon	Barbados	[39]
-59.584	10.39	NaN	NaN	1.2	75	NaN	NaN	7.1	unnamed	Basin-fill area	Trinidad	[40]
-59.679	10.373	NaN	NaN	3	130	NaN	NaN	5	unnamed	Basin-fill area	Trinidad	[40]
-59.607	10.331	NaN	NaN	2.8	138	NaN	NaN	5.6	unnamed	Basin-fill area	Trinidad	[40]
-6.603	35.235	5.4	4.3	4.85	255	5.4	6.8	6	Al Idrissi	El Arraiche	Gulf of Cádiz	[41]
-6.733	35.427	NaN	NaN	4	160	NaN	NaN	4.6	Kidd	El Arraiche	Gulf of Cádiz	[42]
-6.763	35.366	NaN	NaN	2	160	NaN	NaN	9.1	Adamastor	El Arraiche	Gulf of Cádiz	[42]

Table A.1: *Continued.*

Long. (+E)	Lat. (+N)	D_{max} (km)	D_{min} (km)	D_{mean} (km)	H (m)	S_{min} (deg)	S_{max} (deg)	S_{mean} (deg)	Name	Mud volcano field	Region	Refs
-6.775	35.317	NaN	NaN	0.5	25	NaN	NaN	5.7	Lazarillo de Tormes	El Arraiche	Gulf of Cádiz	[41]
-6.758	35.282	4.1	2.3	3.2	252	7	12.4	9	Gemini W	El Arraiche	Gulf of Cádiz	[41]
-6.758	35.282	4.1	2.3	3.2	169	4.7	8.4	6	Gemini E	El Arraiche	Gulf of Cádiz	[41]
-6.71	35.285	NaN	NaN	1.2	80	NaN	NaN	7.6	Don Quichote	El Arraiche	Gulf of Cádiz	[41]
-6.645	35.3	2.45	1.82	2.14	141	6.6	8.8	7.5	Mercator	El Arraiche	Gulf of Cádiz	[41]
-6.7	35.255	2.9	2.1	2.5	143	5.6	7.8	6.5	Fiuza	El Arraiche	Gulf of Cádiz	[41]
-8.006	36.156	5.7	5	5.35	316	6.3	7.2	6.7	Lolita	Guadalquivir ridge	Gulf of Cádiz	[43]
-9.001	35.46	NaN	NaN	2	150	NaN	NaN	8.5	Bonjardim	Deep south Portuguese	Gulf of Cádiz	[44]
-8.632	35.583	NaN	NaN	1.2	30	NaN	NaN	2.9	Olenin	Deep south Portuguese	Gulf of Cádiz	[45]
-8.422	35.787	1.5	1.5	1.5	80	6.1	6.1	6.1	Carlos Ribeiro	Deep south Portuguese	Gulf of Cádiz	[45]
-7.333	35.662	NaN	NaN	1.5	85	NaN	NaN	6.5	Captain Arutyunov	Spanish Morrocan margin	Gulf of Cádiz	[46]
-7.086	35.372	NaN	NaN	3.8	266	NaN	NaN	8	Ginsburg	Middle Moroccan	Gulf of Cádiz	[47]
-7.394	36.092	2.6	1.8	2.2	190	8.3	11.9	9.8	Faro	TASYO	Gulf of Cádiz	[48]
-7.322	36.186	1	0.85	0.93	105	11.9	13.9	12.8	H1 (Hesperides MVs)	TASYO	Gulf of Cádiz	[48]
-7.317	36.183	1.1	0.9	1	150	15.3	18.4	16.7	H2 (Hesperides MVs)	TASYO	Gulf of Cádiz	[48]
-7.307	36.183	1.1	0.7	0.9	130	13.3	20.4	16.1	H3 (Hesperides MVs)	TASYO	Gulf of Cádiz	[48]
-7.533	36.183	2	1	1.5	233	13.1	25	17.3	Coruna	TASYO	Gulf of Cádiz	[49]
-7.608	36.115	NaN	NaN	1.8	255	NaN	NaN	15.8	Cornide	TASYO	Gulf of Cádiz	[49]
-7.433	36.075	1.2	0.9	1.05	150	14	18.4	15.9	Cibeles	TASYO	Gulf of Cádiz	[48]
-7.333	36.058	1.5	1.2	1.35	75	5.7	7.1	6.3	Almazan	TASYO	Gulf of Cádiz	[48]
-7.439	35.872	0.9	0.85	0.88	110	13.7	14.5	14.1	Aveiro	TASYO	Gulf of Cádiz	[48]
-7.111	35.766	NaN	NaN	1.8	110	NaN	NaN	7	Tasyo	TASYO	Gulf of Cádiz	[45]
-7.15	36.517	1.5	1.1	1.3	80	6.1	8.3	7	Anastasya	Gualdalquivir Diapiric Ridge	Gulf of Cádiz	[48]
-7.25	36.483	0.9	0.8	0.85	60	7.6	8.5	8	Tarsis	Gualdalquivir Diapiric Ridge	Gulf of Cádiz	[48]
-7.217	36.442	2.1	1.5	1.8	97	5.3	7.4	6.2	Pipoca	Gualdalquivir Diapiric Ridge	Gulf of Cádiz	[48]
-7.617	36.233	0.9	0.9	0.9	52	6.6	6.6	6.6	Gades	Gualdalquivir Diapiric Ridge	Gulf of Cádiz	[48]
-7.685	36.125	1.7	1.2	1.45	165	11	15.4	12.8	Iberico	Gualdalquivir Diapiric Ridge	Gulf of Cádiz	[49]
-7.857	35.394	0.89	NaN	NaN	68	8.7	NaN	NaN	MVSEIS	western Moroccan	Gulf of Cádiz	[50]
-7.861	35.305	0.64	NaN	NaN	51	9	NaN	NaN	Moundforce	western Moroccan	Gulf of Cádiz	[50]
-7.845	35.337	0.58	NaN	NaN	81	15.7	NaN	NaN	Pixie	western Moroccan	Gulf of Cádiz	[50]
-7.816	35.345	0.53	NaN	NaN	92	19.2	NaN	NaN	Dixie	western Moroccan	Gulf of Cádiz	[50]

Table A.1: *Continued.*

Long. (+E)	Lat. (+N)	$D_{\max}$ (km)	$D_{\min}$ (km)	D_{mean} (km)	H (m)	$S_{\min}$ (deg)	$S_{\max}$ (deg)	S_{mean} (deg)	Name	Mud volcano field	Region	Refs
-7.666	35.479	0.91	NaN	NaN	98	12.2	NaN	NaN	Las Negras	western Moroccan	Gulf of Cádiz	[50]
-7.601	35.382	1.93	NaN	NaN	205	12	NaN	NaN	Madrid	western Moroccan	Gulf of Cádiz	[50]
-7.548	35.519	1.68	NaN	NaN	184	12.4	NaN	NaN	Guadix	western Moroccan	Gulf of Cádiz	[50]
-7.506	35.383	1.98	NaN	NaN	175	10	NaN	NaN	Almanzor	western Moroccan	Gulf of Cádiz	[50]
-7.44	35.408	2.85	NaN	NaN	337	13.3	NaN	NaN	El Cid	western Moroccan	Gulf of Cádiz	[50]
-7.179	35.43	1.39	NaN	NaN	88	7.2	NaN	NaN	Boabdil	Middle Moroccan	Gulf of Cádiz	[50]
-6.973	35.394	0.94	NaN	NaN	107	12.8	NaN	NaN	Al Gacel	Middle Moroccan	Gulf of Cádiz	[50]
-7.201	35.591	NaN	NaN	2	110	NaN	NaN	6.3	Jesus Baraza	Middle Moroccan	Gulf of Cádiz	[45]
-7.146	35.514	NaN	NaN	1	100	NaN	NaN	11.3	Student	Middle Moroccan	Gulf of Cádiz	[45]
-7.258	35.474	NaN	NaN	1.1	150	NaN	NaN	15.3	Shouen	Middle Moroccan	Gulf of Cádiz	[51]
-7.1	35.425	4.4	3.7	4.05	250	6.5	7.7	7	Yuma	Middle Moroccan	Gulf of Cádiz	[47]
-7.191	35.392	NaN	NaN	0.75	40	NaN	NaN	6.1	Darwin	Middle Moroccan	Gulf of Cádiz	[51]
-8.781	35.519	NaN	NaN	1	130	NaN	NaN	14.6	Bomboca	Deep Portuguese margin	Gulf of Cádiz	[51]
-9.108	35.213	NaN	NaN	0.8	50	NaN	NaN	7.1	Soloviev	Deep Portuguese margin	Gulf of Cádiz	[52]
-4.885	36.1	1.45	NaN	1.2	82	6.5	NaN	7.8	Perejil	W. Alboran Basin (N)	W. Mediterranean	[53]
-4.933	36.047	0.82	NaN	NaN	36	5	NaN	NaN	Kalinin	W. Alboran Basin (N)	W. Mediterranean	[53]
-4.623	35.562	1.63	NaN	NaN	183	12.7	NaN	NaN	Granada	W. Alboran Basin (S)	W. Mediterranean	[53]
-4.5	35.628	0.65	NaN	NaN	40	7	NaN	NaN	Marrakech	W. Alboran Basin (S)	W. Mediterranean	[53]
-4.53	35.423	1.63	NaN	NaN	84	5.9	NaN	NaN	Dhaka	W. Alboran Basin (S)	W. Mediterranean	[53]
-4.557	35.398	0.62	NaN	NaN	39	7.2	NaN	NaN	Mulhacen M1	W. Alboran Basin (S)	W. Mediterranean	[53]
-4.57	35.407	0.43	NaN	NaN	27	7.2	NaN	NaN	Mulhacen M2a	W. Alboran Basin (S)	W. Mediterranean	[53]
-4.565	35.41	0.38	NaN	NaN	26	7.8	NaN	NaN	Mulhacen M2b	W. Alboran Basin (S)	W. Mediterranean	[53]
-4.573	35.408	0.28	NaN	NaN	23	9.2	NaN	NaN	Mulhacen M2c	W. Alboran Basin (S)	W. Mediterranean	[53]
-4.575	35.403	0.45	NaN	NaN	26	6.6	NaN	NaN	Mulhacen M2d	W. Alboran Basin (S)	W. Mediterranean	[53]
-4.733	35.722	1.13	NaN	NaN	89	9	NaN	NaN	Carmen	W. Alboran Basin (S)	W. Mediterranean	[53]
-4.618	35.452	0.55	NaN	NaN	28	5.8	NaN	NaN	Maya	W. Alboran Basin (S)	W. Mediterranean	[53]
-4.713	35.577	0.63	0.54	0.59	37	6.7	7.8	7.2	Ceuta	W. Alboran Basin (S)	W. Mediterranean	[53]
-4.692	35.592	1.05	NaN	NaN	41	4.5	NaN	NaN	Tarifa	W. Alboran Basin (S)	W. Mediterranean	[53]
137.087	33.714	1.9	1.2	1.55	143	8.6	13.4	10.5	Kumano Knoll 1	Kumano	Nankai	[54]
136.921	33.675	1.2	NaN	NaN	16	1.5	NaN	NaN	Kumano Knoll 2	Kumano	Nankai	[54]
136.671	33.633	2.3	1.9	2.1	110	5.5	6.6	6	Kumano Knoll 3	Kumano	Nankai	[54]

Table A.1: *Continued.*

Long. (+E)	Lat. (+N)	D_{max} (km)	D_{min} (km)	D_{mean} (km)	H (m)	S_{min} (deg)	S_{max} (deg)	S_{mean} (deg)	Name	Mud volcano field	Region	Refs
136.633	33.656	1.1	0.9	1	72	7.5	9.1	8.2	Kumano Knoll 4	Kumano	Nankai	[54]
136.568	33.677	1.7	1.2	1.45	155	10.4	14.5	12.1	Kumano Knoll 5	Kumano	Nankai	[55]
136.562	33.687	2.2	NaN	NaN	143	7.4	NaN	NaN	Kumano Knoll 6	Kumano	Nankai	[54]
136.569	33.734	2.3	1.4	1.85	85	4.2	6.9	5.2	Kumano Knoll 7	Kumano	Nankai	[54]
136.557	33.604	1.1	0.8	0.95	34	3.5	4.8	4.1	Kumano Knoll 8	Kumano	Nankai	[56]
136.559	33.633	1.2	1	1.1	10	0.9	1.1	1	Kumano Knoll 9	Kumano	Nankai	[57]
136.282	33.548	1.4	1.2	1.3	123	10	11.6	10.7	Kumano Knoll 10	Kumano	Nankai	[57]
136.707	33.388	0.6	0.5	0.55	28	5.3	6.4	5.8	Kumano Knoll 11	Kumano	Nankai	[57]
136.666	33.523	0.8	0.6	0.7	24	3.4	4.5	3.9	Kumano Knoll 12	Kumano	Nankai	[57]
136.915	33.768	1.4	0.6	1	47	3.9	9	5.4	Kumano Knoll 13	Kumano	Nankai	[57]
131.508	30.322	NaN	NaN	4	270	NaN	NaN	7.7	unknown	Tanagashima	Ryukyu	[58]
131.842	30.917	5	4	4.5	100	2.3	2.9	2.5	MV2	Tanagashima	Ryukyu	[58]
131.78	30.985	2.52	2.01	2.27	175	7.9	9.9	8.8	MV5	Tanagashima	Ryukyu	[59]
-125.078	44.627	1.8	0.7	1.25	63	4	10.2	5.7	unnamed	Hydrate Ridge	Cascadia	[60]
-125.056	44.667	0.65	0.3	0.48	18	3.2	7	4.4	unnamed	Hydrate Ridge	Cascadia	[60]
118.873	22.148	NaN	NaN	0.35	20	NaN	NaN	6.6	unnamed	S. China sea Continetal Slope	Taiwan	[61]
120.413	22.184	NaN	NaN	0.2	15	NaN	NaN	8.5	unnamed	Kaoping Shelf	Taiwan	[62]
120.408	22.381	NaN	NaN	0.22	34	NaN	NaN	17.2	unnamed	Kaoping Submarine Canyon	Taiwan	[62]
119.813	22.229	NaN	NaN	0.2	3	NaN	NaN	1.7	unnamed	Yung-An Linearment	Taiwan	[62]
120.163	22.615	NaN	NaN	0.14	1.8	NaN	NaN	1.5	unnamed	Kaohsiung	Taiwan	[62]
120.388	22.158	NaN	NaN	1.25	95	NaN	NaN	8.6	MV1	Kaoping Slope	Taiwan	[63]
120.372	22.159	NaN	NaN	0.6	85	NaN	NaN	15.8	MV2	Kaoping Slope	Taiwan	[63]
120.338	22.159	NaN	NaN	2	145	NaN	NaN	8.3	MV3	Kaoping Slope	Taiwan	[63]
120.323	22.143	NaN	NaN	1.9	140	NaN	NaN	8.4	MV4	Kaoping Slope	Taiwan	[63]
120.31	22.137	NaN	NaN	2.2	175	NaN	NaN	9	MV5	Kaoping Slope	Taiwan	[63]
120.29	22.122	NaN	NaN	1.3	135	NaN	NaN	11.7	MV6	Kaoping Slope	Taiwan	[63]
120.316	22.179	NaN	NaN	1.1	65	NaN	NaN	6.7	MV7	Kaoping Slope	Taiwan	[63]
120.299	22.163	NaN	NaN	0.68	75	NaN	NaN	12.4	MV8	Kaoping Slope	Taiwan	[63]
120.24	22.081	NaN	NaN	2.8	240	NaN	NaN	9.7	MV9	Kaoping Slope	Taiwan	[63]
120.256	22.059	NaN	NaN	3.3	345	NaN	NaN	11.8	MV10	Kaoping Slope	Taiwan	[63]
120.34	21.998	NaN	NaN	3	240	NaN	NaN	9.1	MV11	Kaoping Slope	Taiwan	[63]

Table A.1: *Continued.*

Long. (+E)	Lat. (+N)	D_{max} (km)	D_{min} (km)	D_{mean} (km)	H (m)	S_{min} (deg)	S_{max} (deg)	S_{mean} (deg)	Name	Mud volcano field	Region	Refs
120.556	21.828	NaN	NaN	4.1	280	NaN	NaN	7.8	MV12	Kaoping Slope	Taiwan	[63]
120.406	21.782	NaN	NaN	2.5	115	NaN	NaN	5.3	MV13	Kaoping Slope	Taiwan	[63]
110.792	15.183	NaN	NaN	2.05	160	NaN	NaN	8.9	MV1	Zhongjiannan Basin	South China Sea	[64]
110.783	15.167	NaN	NaN	2.29	214	NaN	NaN	10.6	MV2	Zhongjiannan Basin	South China Sea	[64]
111	15.1	NaN	NaN	2.03	198	NaN	NaN	11	MV3	Zhongjiannan Basin	South China Sea	[64]
110.967	15.45	NaN	NaN	1.4	145	NaN	NaN	11.7	MV4	Zhongjiannan Basin	South China Sea	[64]
NaN	NaN	NaN	NaN	3	40	NaN	NaN	1.5	unnamed	Lombok	Lesser Sunda Isl.	[65]
-56.313	-60.875	NaN	NaN	2.9	210	NaN	NaN	8.2	Chiavalz	Shetland	Antarctic Penins.	[66]
-56.753	-61.028	NaN	NaN	0.8	115	NaN	NaN	16	Flop	Shetland	Antarctic Penins.	[66]
-56.472	-60.865	NaN	NaN	2	185	NaN	NaN	10.5	Sernio	Shetland	Antarctic Penins.	[66]
-56.717	-61.075	NaN	NaN	5.8	255	NaN	NaN	5	Vualt	Shetland	Antarctic Penins.	[66]
15.094	-30.246	NaN	NaN	0.35	40	NaN	NaN	12.9	unnamed	Orange Basin	SW Africa	[67]
15.057	-30.328	NaN	NaN	0.6	10	NaN	NaN	1.9	unnamed	Orange Basin	SW Africa	[68]
15.075	-30.385	NaN	NaN	0.15	10	NaN	NaN	7.6	unnamed	Orange Basin	SW Africa	[69]
-118.647	33.799	NaN	NaN	0.37	30	NaN	NaN	9.2	NE Mound	Santa Monica Basin	California	[70]
-118.668	33.789	NaN	NaN	0.26	35	NaN	NaN	15.1	SW Mound	Santa Monica Basin	California	[71]
-91.478	27.918	NaN	NaN	0.6	30	NaN	NaN	5.7	unknown	Block 53 (Green Canyon)	Gulf of Mexico	[72]
-91.488	27.867	NaN	NaN	0.61	15	NaN	NaN	2.8	unknown	Block 97 (Green Canyon)	Gulf of Mexico	[73]
-91.361	27.838	0.5	0.45	0.48	35	8	8.8	8.4	unknown	Block 143 (Green Canyon)	Gulf of Mexico	[73]
14.728	72.005	1.38	1.365	1.37	16	1.3	1.3	1.3	Haakon Mosby	SW Barents Sea Slope	Barents Sea	[74]
33.446	43.339	NaN	NaN	1.2	60	NaN	NaN	5.7	Vassoevich	central Black Sea	Black Sea	[75]
34.983	44.283	1.2	0.8	1	25	2.4	3.6	2.9	Dvurechenskii	Sorokin Trough	Black Sea	[76]
35.077	44.313	1	0.6	0.8	75	8.5	14	10.6	NIOZ	Sorokin Trough	Black Sea	[75]
35.177	44.293	2.8	2.25	2.53	140	5.7	7.1	6.3	Kazakov	Sorokin Trough	Black Sea	[77]
35.267	44.422	NaN	NaN	0.5	50	NaN	NaN	11.3	Tbilisi	Sorokin Trough	Black Sea	[75]
35.397	44.392			0.7	50	NaN	NaN	8.1	Istanbul	Sorokin Trough	Black Sea	[75]
33.103	43.248	NaN	NaN	1.5	60	NaN	NaN	4.6	TREDMAR	central Black Sea	Black Sea	[75]
33.705	43.234	NaN	NaN	0.9	40	NaN	NaN	5.1	Kovalevskii	central Black Sea	Black Sea	[75]
146.644	19.551	NaN	NaN	22.3	1693	NaN	NaN	8.6	Conical	Mariana Trench	Mariana	[78]
146.902	19.267	NaN	NaN	22.4	1461	NaN	NaN	7.4	Pacman	Mariana Trench	Mariana	[78]
147.035	19.021	18.9	17.5	18.2	999	6	6.5	6.3	South Pacman	Mariana Trench	Mariana	[79]

Table A.1: *Continued.*

Long. (+E)	Lat. (+N)	D_{max} (km)	D_{min} (km)	D_{mean} (km)	H (m)	S_{min} (deg)	S_{max} (deg)	S_{mean} (deg)	Name	Mud volcano field	Region	Refs
146.991	18.754	NaN	NaN	26.1	1188	NaN	NaN	5.2	Quaker	Mariana Trench	Mariana	[80]
146.95	18.619	17.4	11.7	14.6	799	5.2	7.8	6.3	South Quaker	Mariana Trench	Mariana	[81]
147.342	18.641	NaN	NaN	19.3	1028	NaN	NaN	6.1	Northeast Blue (NE)	Mariana Trench	Mariana	[79]
147.102	18.111	NaN	NaN	42	2365	NaN	NaN	6.4	Big Blue	Mariana Trench	Mariana	[78]
147.175	16.981	27.4	23	25.2	1269	5.3	6.3	5.8	Turquoise	Mariana Trench	Mariana	[78]
147.209	16.527	NaN	NaN	26.3	1824	NaN	NaN	7.9	Celestial	Mariana Trench	Mariana	[78]
147.117	16.049	14.9	13.6	14.3	764	5.9	6.4	6.1	Peacock	Mariana Trench	Mariana	[82]
147.201	15.763	25.8	18.2	22	828	3.7	5.2	4.3	Blue Moon	Mariana Trench	Mariana	[82]
146.22	13.948	17.4	16.9	17.2	1040	6.8	7	6.9	North Chamorro	Mariana Trench	Mariana	[78]
146.004	13.783	20.6	15.5	18.1	1200	6.6	8.8	7.6	South Chamorro	Mariana Trench	Mariana	[82]
146.049	13.227	NaN	NaN	15.1	1165	NaN	NaN	8.8	Deep Blue	Mariana Trench	Mariana	[83]
142.96	24.02	NaN	NaN	20	1645	NaN	NaN	9.3	Fujin	Izu-Ogasawara Trench	Izu-Ogasawara	[84]
141.8	23.71	25	15	20	1911	8.7	14.3	10.8	Raijin	Izu-Ogasawara Trench	Izu-Ogasawara	[84]
142.957	24.015	40	25	32.5	2040	5.8	9.3	7.2	Honza	Izu-Ogasawara Trench	Izu-Ogasawara	[84]
141.917	31.542	NaN	NaN	11	500	NaN	NaN	5.2	Sumisu	Izu-Ogasawara Trench	Izu-Ogasawara	[85]
141.833	30.917	NaN	NaN	12	720	NaN	NaN	6.8	Torishima	Izu-Ogasawara Trench	Izu-Ogasawara	[85]

(1) *Camerlenghi et al.* [1995]; (2) *Lykousis et al.* [2009]; (3) *Rabaute and Chamot-Rooke* [2007]; (4) *Lykousis et al.* [2004]; (5) *Camerlenghi et al.* [1995]; *Hieke et al.* [1996]; (6) *Limonov et al.* [1998]; (7) *Hieke et al.* [1996]; (8) *Hieke et al.* [1996]; *Huguen et al.* [2004]; (9) *Kopf et al.* [2001, 2012]; (10) *Kioka et al.* [2015]; (11) *Hieke et al.* [1996]; *Volgin and Woodside* [1996]; *Huguen et al.* [2004]; (12) *Ivanov et al.* [1996]; *Rabaute and Chamot-Rooke* [2007]; (13) *Camerlenghi et al.* [1995]; *Rabaute and Chamot-Rooke* [2007]; (14) *Zitter et al.* [2005]; (15) *Limonov et al.* [1998]; *Huguen et al.* [2004]; (16) *Woodside et al.* [2002]; (17) *Lykousis et al.* [2009]; *Perissoratis et al.* [2011]; (18) *Pierre et al.* [2014]; (19) *Huguen et al.* [2009]; (20) *Feseker et al.* [2010]; (21) *Dupré et al.* [2007]; (22) *Wiedicke et al.* [2001]; (23) *Gamberi and Rovere* [2010]; *Rovere et al.* [2014]; (24) *Praeg et al.* [2009]; (25) *Ceramicola et al.* [2014]; (26) *Bürk* [2007]; (27) *Buerk et al.* [2010]; (28) *Talukder et al.* [2007]; (29) *Grevemeyer et al.* [2004]; (30) *Mau et al.* [2006]; (31) *Sahling et al.* [2008]; *Petersen et al.* [2009]; (32) *Petersen et al.* [2009]; (33) *Söding et al.* [2002]; (34) *Klaucke et al.* [2008]; (35) *Mörz et al.* [2005]; *Klaucke et al.* [2008]; (36) *Sumner and Westbrook* [2001]; (37) *Lance et al.* [1998]; (38) *Henry et al.* [1996]; *Lance et al.* [1998]; (39) *Godon et al.* [2004]; (40) *Sullivan et al.* [2004]; (41) *Van Rensbergen et al.* [2005]; (42) *Gardner and Shashkin* [2000]; *Van Rensbergen et al.* [2005]; (43) *Somoza et al.* [2003]; *Kopf et al.* [2004]; *Van Rensbergen et al.* [2005]; (44) *Pinheiro et al.* [2003]; *Akhmetzhanov et al.* [2008]; (45) *Pinheiro et al.* [2003]; (46) *Kopf et al.* [2004]; (47) *Gardner* [2001]; *Kopf et al.* [2004]; (48) *Somoza et al.* [2003]; (49) *Somoza et al.* [2003]; *Magalhães* [2007]; (50) *León et al.* [2012]; (51) *Akhmetzhanov et al.* [2008]; (52) *Akhmetzhanov et al.* [2008]; *Ivanov et al.* [2010]; (53) *Somoza et al.* [2012]; (54) *Morita et al.* [2004]; (55) *Morita et al.* [2004]; *Nishio et al.* [2015]; (56) *Ashi et al.* [2006]; (57) *Kopf et al.* [2013]; (58) *Ujiié* [2000]; (59) *Machiyama et al.* [2012]; (60) *Tréhu et al.* [1999]; (61) *Chiu et al.* [2006]; *Morita et al.* [2009]; (62) *Chiu et al.* [2006]; (63) *Chen et al.* [2014]; (64) *Sun et al.* [2013]; (65) *Lüschen et al.* [2011]; (66) *Tinivella et al.* [2008]; (67) *Ben-Avraham et al.* [2002]; *Viola et al.* [2005]; (68) *Ben-Avraham et al.* [2002]; (69) *Viola et al.* [2005]; (70) *Normark and Piper* [1998]; *Paull et al.* [2008]; (71) *Paull et al.* [2008]; (72) *Roberts* [2001]; (73) *Neurauter and Roberts* [1994]; (74) *Vogt et al.* [1997]; *Jerosch et al.* [2007]; (75) *Kenyon et al.* [2002]; (76) *Bohrmann et al.* [2003]; *Feseker et al.* [2009]; (77) *Bohrmann et al.* [2011]; (78) *Fryer et al.* [1999]; *Maekawa et al.* [2006]; (79) *Maekawa et al.* [2006]; *Fryer* [2012]; (80) *Fryer et al.* [2006]; *Maekawa et al.* [2006]; (81) *Maekawa et al.* [2006]; (82) *Fryer et al.* [1999]; (83) *Fryer* [2012]; (84) *Fujioka* [2012]; (85) *Fujioka et al.* [1995].

Appendix B

Additional Materials for Chapter 3

This chapter presents additional information in order to document the results presented in Chapter 3. Section B.1 provides a brief description of the thermal parameters used to model 2-D thermal structure. The used parameters are summarized in Table 3.2. Each layer addressed here is guided in Figure 3.4. Section B.2 shows time-temperature simulations on the resulted values of vitrinite reflectance to estimate the experienced peak temperatures of clasts. Other additional figures and tables include: photos of studied samples (Figures B.3 and B.4), nannofossil data (Tables B.1 and B.2), and vitrinite reflectance data (Tables B.3 and B.4).

B.1 Thermal parameters in 2-D thermal model

Thermal conductivity of uppermost layer 1 is assumed to be 1.0 W/m/K based on in-situ measurement in the MEDRIFF corridor [*Della Vedova et al.*, 2003]. As for layers 2–5, this study adopts representative values at overriding plate part and underthrusting sediment layer [e.g., *Beardsmore and Cull*, 2001; *Clauser and Huenges*, 1995; *Turcotte et al.*, 1978] as the downward increase due to decreasing porosity. The RHP rate of layers 1–4 is assumed to be 1.5 μW/m^3. This value seems to be an adequate value, because previous studies in the Nankai accretionary prism whose source is mostly terrigenous have been reported to be 1.5–2.2 μW/m^3 [e.g., *Hyndman et al.*, 1995; *Yamaguchi et al.*, 2001]. For the highly compacted or dewatered subducting sediments, as the highest sediment thermal conductivity values of 3.0 ± 0.5 W/m/K have been found [*Roy et al.*, 1981; *Drury*, 1986; *Barker*, 1996], this study hence adopts 3.0 W/m/K in the subducting sediment layer 5. Shales with the density of 2700 kg/m^3 shows RHP rate of 2.5 μW/m^3 [*Pasquale et al.*, 2001]. *Hyndman et al.* [1995] also reports relatively higher value of RHP rate of shales, 1.8 μW/m^3. Hence this study also adopts that of 2.0 μW/m^3 at subducting Aptian shale and older Mesozoic sediments (layer 5). As for layer 6, this study employs a representative value of thermal parameters in oceanic lithosphere [e.g., *Heasler and Surdam*, 1985; *Van den Beukel and Wortel*, 1988; *Hyndman et al.*, 1995]. The most representative values of marine evaporites are as follows: calcite (4.0–5.0 W/m/K), gypsum (2.0–3.0 W/m/K), anhydrite ($\sim$5.0 W/m/K) and halite (>6.5 W/m/K) [e.g., *Horai*, 1971]. Thermal conductivity of evaporites layer at the depth of 200–300 mbsf at DSDP (Deep Sea Drilling Project) Leg 23 Site 225 and 227 in the Red Sea represented 4.4–5.6 W/m/K [*Wheildon et al.*, 1974]. The basinal evaporites presumably consist mainly of halite [e.g., *Cohen*, 1993], and additionally *Polonia et al.* [2002] interpreted the lower unit of evaporite succession is composed of almost halite though the upper unit is composed of marls and gypsum. Hence this study adopts thermal conductivity of 5.0 W/m/K in layer 7. Thermal capacity of evaporite would be close to the one in other layers based on the density and heat capacity ($\sim$0.8–1.1 kJ/kg/K). Evaporites essentially contain little radioactive elements and hence RHP is extremely small or null, thus this study assumed it to be 0.01 μW/m^3 at layer 7. At backstop segment (layer 8), a representative value of thermal conductivity and RHP within continental crust likely agrees with seismic velocity characteristics is used.

B.2 Time-temperature paths on vitrinite reflectance

We herein simulated $T_{\max}$ values from time-temperature paths based on the kinetic formulation of *Sweeney and Burnham* [1990]. For the Aptian shale and other E. Cretaceous mudstone samples, our time-temperature simulations were based on the assumption of subduction under steady-state plate motion of 40 mm/yr, because the Nubian-Aegean convergence rate is estimated to have been 30–40 mm/yr since 13 Ma [e.g., *Le Pichon et al.*, 1995]. The initial sedimentation age and the final eruption age were assumed as 120 Ma and 0 Ma, respectively, and the initial and final temperatures were taken as 5°C and 14°C, respectively. Figure B.1 is a schematic illustration of this model. We assumed

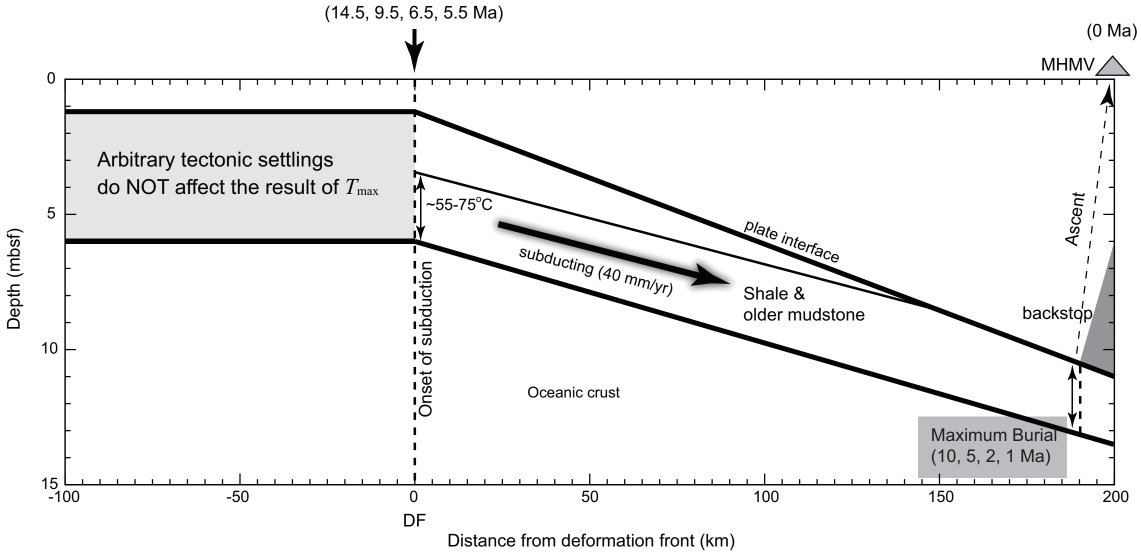

Figure B.1: Schematic illustration of time-burial path used in this study (see text).

that shales and other mudstones started subducting at the deformation front at 14.5–5.5 Ma and reached its maximum burial depth at 10–1 Ma, then ascended through the wedge and erupted at 0 Ma, a reasonable age given that MHMV has signs of recent eruptions. In the deformation front below the plate interface, the temperature was assumed to be 55–75°C based on the thermal structure presented in Figure 3.6. Note that arbitrary tectonic events before the onset of subducting, such as downdropping or burial, do not affect $T_{\max}$ values at the maximum burial depth, because we assumed that shale did not experience temperatures before subduction that would have affected kinetic results. Thus, in our model, the cooling rate between maximum depth and eruption also affects $T_{\max}$. The resulting $T_{\max}$ values were similar at the same vitrinite reflectance values even though the maximum burial depth was variable (Figure B.2). Ro values of 0.44%, 0.59%, and 0.74% from shale and values of 0.89%, 1.04%, and 1.19% from other mudstones resulted in $T_{\max}$ values of about 82 ± 4°C, 108 ± 3°C, 134 ± 3°C, 153 ± 3°C, 164 ± 3°C, and 173 ± 3°C, respectively, in our model.

The convergence rate is considered to be changed within the investigated period [e.g., *Le Pichon et al.*, 1995]. But this is not an important issue in our study, because the kinetic calculation within the heating rate that we consider does not affect the resultant maximum

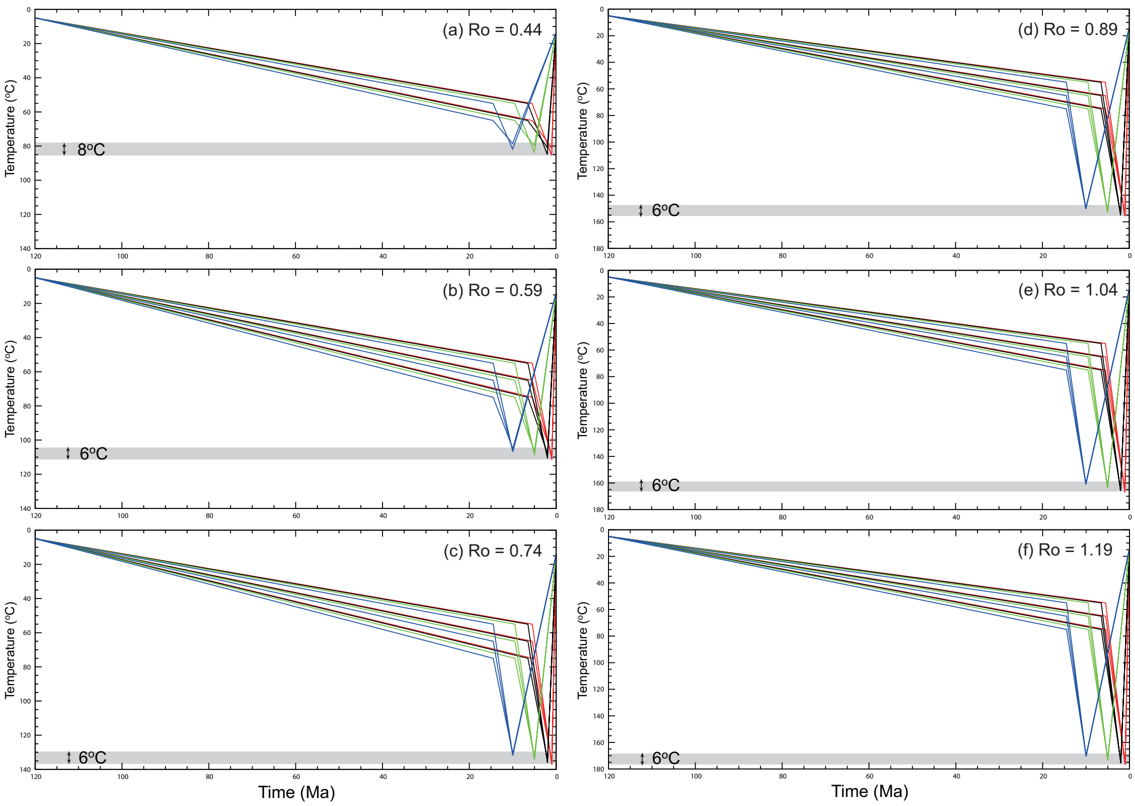

Figure B.2: Examples of the possible time-temperature paths that result in the same vitrinite reflectance values of shale samples (a) Ro = 0.44%; (b) Ro = 0.59%; (c) Ro = 0.74%, and other mudstone samples (d) Ro = 0.89%; (e) Ro = 1.04%; (f) Ro = 1.19%. Time-temperature paths are defined by four time points: initial deposition age (120 Ma in all cases), onset of subduction, maximum burial, and erupted age (0 Ma in all cases). Simulations assumed constant subduction of 40 mm/yr. Times of subduction onset and maximum burial vary for curves in red (5.5 and 1 Ma), black (6.5 and 2 Ma), green (9.5 and 5 Ma), and blue (14.5 and 10 Ma). Each of these four scenarios is shown for temperatures at the onset of subduction of 55°C, 65°C and 75°C.

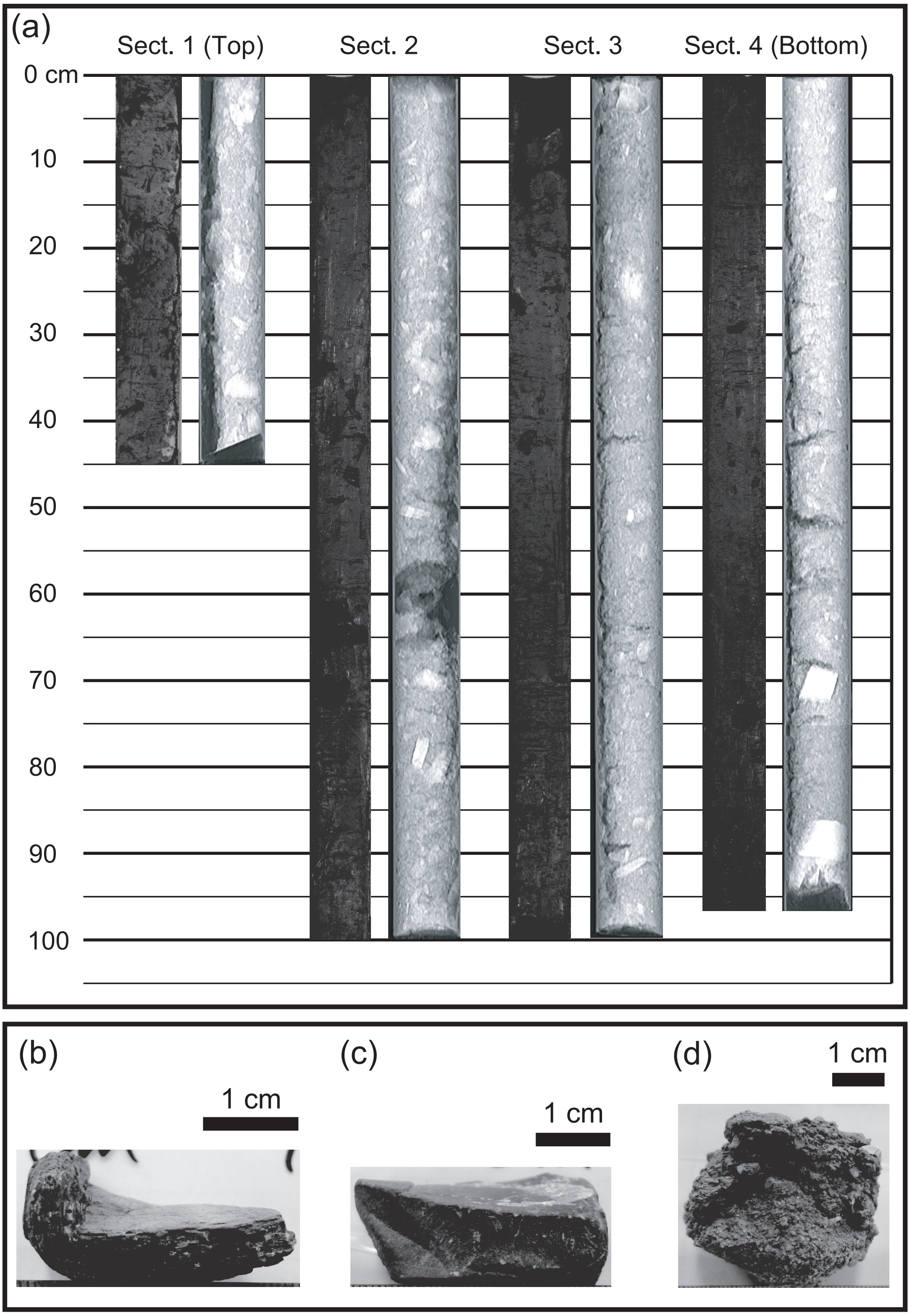

Figure B.3: (a) Photos and X-ray CT scan images of NSS-PC03 core. The CT scan images show that the core captures many clasts. Examples of clasts from MHMV cores; (b) shale from section 1 of NSS-PC03 core (#C023); (c) siltstone from section 1 of NSS-PC02 core (#C036); (d) conglomerate from section 2 of NSS-PC02 core (#C057).

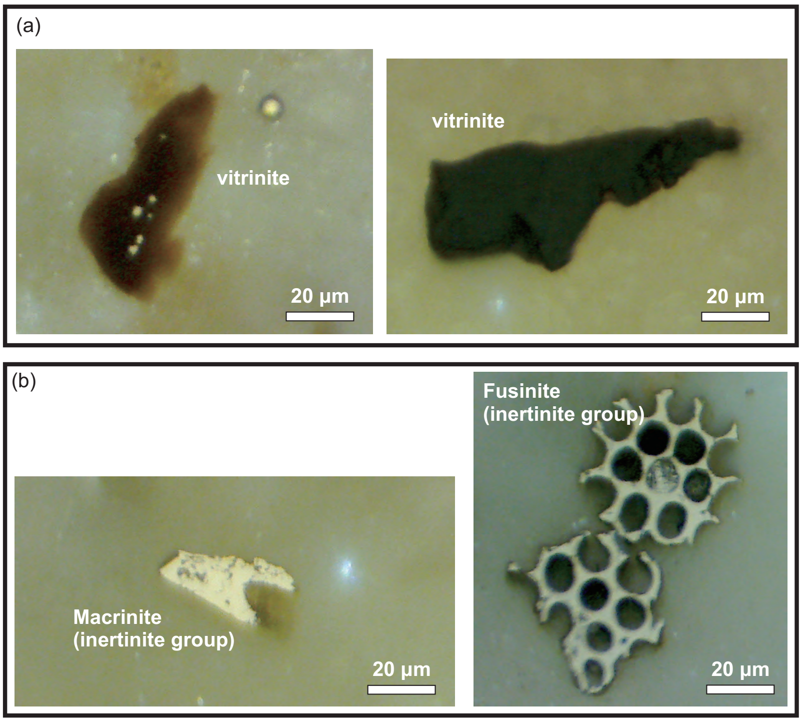

Figure B.4: Examples of maceral fragment within slab samples: (a) partial bitumen (vitrinite) within shale (left: sample #C118, 0.62% reflectance) and mudstone (right: sample #C097, 1.18% reflectance); (b) inertinite macerals with charcoal-like structure and high reflectance.

temperature $T_{\max}$ considerably. A net mean rate is considered to be 30–40 mm/yr since the onset of Aegean spreading of 13 Ma [e.g., *Le Pichon et al.*, 1995]. The paper claims that the convergence rate has slowed down since 6–3 Ma. Thus, the following different thermal scenario with the shale of Ro = 0.74 can be considered: (1) onset of subducting of the shale sample at 8 Ma, (2) continuing subduction with a higher convergence rate of 60 mm/yr from 8 to 6 Ma, (3) the slower rates since 6 Ma and maximum burial of shale at 1 Ma, and (4) shale sample brought up to seafloor at 0 Ma. The resultant maximum temperature $T_{\max}$ should be 128°C, and this value is close to the ones estimated from steady subducting rate of 40 mm/yr ($T_{\max} = 134 \pm 3$°C). Thus, the kinetic calculation that we consider does not change resulting thermal paths of at maximum a couple of kelvins in maximum temperature $T_{\max}$.

We do not estimate the thermal path that mudstones from backstop may track using kinetic simulations, because we cannot infer their reasonable thermal history. However,

Table B.1: Estimated ages of clast samples based on nannofossil analysis (A, abundant; C, common; R, rare; +, present but not counted).

age				Ber.–Cen.	Aptian	Ber.–Bar.		Ber.–Bar.		Ber.–Bar.		Bar.–Alb.
Zone (Sissingh, 1977)				CC1–CC10	CC7	CC1–CC6		CC1–CC6		CC2–CC6		CC6–CC8
sample ID	Tethys: *	range	C011	C015	C032	C045	C075	C093	C097	C098	C110	C117
Abundancy			R	C	C	A	R	A	R	R	R	R
Biscutum spp.			+									
Cretarhabdus conicus					1	+						
Helenea chiastia	*	Jura–CC10						1				
Manivitella pemmatoidea				1	2							
Markalius inversus				1	1							
Micrantholithus hoschulzii		CC1–CC7			1	1		4		+		+
Nannoconus bermudezii		CC2–CC6								+		
Nannoconus colomii		CC1–CC6								+		
Nannoconus steinmannii	*	CC1–CC6				2		2		+		+
Nannoconus spp. (narrow canal)		CC1–CC6				8		1		+		+
Rhagodiscus angustus		CC7b–CC26			1							
Rhagodiscus asper	*	Berr.–Cen.		1		+		4				
Rucinolithus cf. *irregularis*		CC7–CC8			1							
Watznaueria barnesae			+	93	93	89	+	84	+	+	+	+
Watznaueria biporta				3								
Watznaueria communis		Jur.–Tur.				+						
Zeugrhabdotus embergeri	*	l. Jur.–e. Cret.	+	1		+		4				+
Total No. (%)				100	100			100				

*Tethys: Tethyan type flora

if we use empirical relationship of equation (3.2), maximum temperatures are obtained as $T_{\max}(\text{Ro} = 0.89) = 139°\text{C}$, $T_{\max}(\text{Ro} = 1.04) = 159°\text{C}$, and $T_{\max}(\text{Ro} = 1.19) = 176°\text{C}$. This means the minor differences of maximum temperatures between empirical and kinetic equations, with no more than 10°C in the investigated mudstones.

Table B.2: Estimated ages of matrix samples from Section 4 of Core NSS-PC02 based on nannofossil analysis (+, present but not counted).

Age			Apt.-Alb., mid. Mioc.	Berr.-Haut., l. Oligocene., e. Miocene	Berr.-Haut., Alb.-Cen., mid. Mio.(?)	Berr.-Haut., Apt.-Cenm., e. Mio.	e.-m. Cret., Paleogene-mid. Mio.	Berr.-Haut., l. Olig.-Mio.	Berr.-Hau., Alb.-Maast., mid. Eoc.-	Alb-Cenom., ~m.Mio.
Zone			CC7-CC8, NN6	CC1-CC4, NP23-24, NN3	CC1-4, CC9-10, NN6?	CC1-4, CC7-9, NN3-4	CC1-CC10, ~NN6	CC1-4, Olig.-Mio. Zone	CC1-4, CC8-26, NP16-25,	CC8-CC10, ~NN6
	sample	**range**	10 cm	20 cm	30 cm	40 cm	50 cm	60 cm	70 cm	80 cm
Cenozoic species	*Coccolithus miopelagicus*	l. Olig.-Miocene						+	+	
	Coccolithus pelagicus	Paleogene-recent	+	+	+	+	+	+	+	+
	Cyclicargolithus abisectus	NP24-NN4				+				
	Cyclicargolithus floridanus	Paleog.-NN6	+	+	+	+	+		+	+
	Dictyococcites bisectus	NP16-NP25							+	
	Discoaster deflandrei	Paleog.-Miocene		+	+			+		
	Discoaster spp.									
	Helicosphaera carteri	Miocene-recent	+	+	+	+			+	
	Helicosphaera euphratis	Paleog.-mid. Miocene							+	
	Reticulofenestra pseudoumbilicus	mid. Miocene-e.Plio.	+							
	Reticulofenestra spp.		+	+	+		+			;
	Sphenolithus abies	Mio.-e.Plio.		+	+					
	Sphenolithus belemnos	NN3		+						
	Sphenolithus distentus	NP23-NP24		+						
	Sphenolithus heteromorphus	NN3-NN5				+				
	Sphenolithus moriformis	Paleog.-Miocene								
Mesozoic species	*Broinsonia matalosa*	Apt.-Campan.								
	Cruciellipsis cuvilleri	CC1-CC4		+	+	+		+	+	
	Eiffelithus turriseffelii	CC9-CC26			+					
	Hayesites albiensis	CC7-CC9				+				
	Hayesites irregularis	CC7-CC8	+							
	Hayesites radiatus								+	
	Helenea chiastia	Jura-CC10	+	+	+	+	+		+	
	Lithraphidites carniolensis	Cretaceous			+	+	+			
	Manivitella pemmatoidea			+	+	+		+	+	+
	Micrantholites hoschulzii								+	
	Nannoconus steinmannii	Jura-CC6		+	+					
	Nannoconus spp.								+	
	Retecapsa angustiforata	CC2-CC26								
	Rhagodiscus asper	Berr.-Cenomanian	+					+	+	+
	Staurolithites crux		+						+	
	Watznaueria barnesae		+	+	+	+	+	+	+	+
	Watznaueria biporta		+		+					+
	Watznaueria britannica	Jura-CC9				+	+			
	Zeugrhabdotus embergeri	Alb-CC26			+	+			+	+

Table B.3: Random mean vitrinite reflectance data from clasts.

Sample#	Ro (%)	SD	N	lithology	Age
C001	1.29	0.32	27	conglomerate	
C002	0.98	0.27	17	siltstone	
C004	0.45	0.12	100	shale	
C005	0.87	0.19	19	shale	
C008	0.84	0.15	23	siltstone	
C009	0.46	0.15	18	shale	
C010	0.58	0.21	45	shale	
C011	0.52	0.17	97	shale	
C012	0.47	0.18	15	shale	
C013	0.49	0.10	31	shale	
C014	0.54	0.09	17	shale	
C015	0.62	0.18	81	shale	Berr.–Cenom.
C023	0.48	0.17	80	shale	
C025	0.54	0.11	37	shale	
C028	1.19	0.31	23	siltstone	
C029	0.55	0.06	75	shale	
C030	1.08	0.11	38	siltstone	
C032	1.02	0.09	86	siltstone	Apt.
C036	0.99	0.16	36	siltstone	
C040	0.48	0.10	43	shale	
C045	0.97	0.35	81	siltstone	Berr.–Barr.
C046	1.00	0.18	14	claystone	
C047	0.35	0.17	65	sandstone	
C048	0.76	0.42	24	sandstone	
C053	0.50	0.32	60	shale	

Sample#	Ro (%)	SD	N	lithology	Age
C056	0.55	0.12	51	shale	
C057	0.49	0.21	43	conglomerate	
C061	0.62	0.23	25	siltstone	
C062	0.52	0.09	25	shale	
C064	1.06	0.40	21	shale	
C070	1.23	0.22	11	limestone	
C071	1.06	0.10	20	siltstone	
C072	0.68	0.19	42	shale	
C073	1.08	0.31	46	siltstone	
C075	0.50	0.12	75	shale	
C076	0.46	0.11	93	shale	
C091	0.62	0.07	71	shale	
C092	0.88	0.34	56	shale	
C093	1.21	0.22	55	siltstone	Berr.–Cenom.
C094	0.51	0.30	86	shale	
C095	1.22	0.20	61	siltstone	
C096	1.01	0.26	73	siltstone	
C097	1.22	0.17	101	siltstone	
C098	1.17	0.28	87	siltstone	Berr.–Cenom.
C104	0.52	0.17	42	shale	
C108	0.74	0.12	50	shale	
C110	1.03	0.09	51	conglomerate	
C117	0.90	0.11	42	limestone	Berr.–Alb.
C118	0.62	0.21	90	shale	

Table B.4: Random mean vitrinite reflectance data from matrix.

Sample#	Ro (%)	SD (%)	N	Comments
M003	0.50	0.19	76	Few reworked vitrinites
M006	0.46	0.14	46	Few reworked vitrinites
M011	0.64	0.18	70	Some inertinites
M013	0.55	0.20	60	Some inertinites
M016	0.64	0.29	50	Many vitrinites with high reflectance
M019	0.63	0.21	90	Many vitrinites with high reflectance
M021	0.62	0.20	75	Some inertinites
M023	0.69	0.21	35	Few reworked vitrinites
M025	0.68	0.21	70	Few reworked vitrinites
M026	0.56	0.22	100	Some inertinites, brown coals ($N > 20$)
M027	0.51	0.22	69	Many vitrinites with $> 2.0\%$; brown coals ($N > 20$)
M030	0.50	0.18	100	Some fusinites, brown coals ($N > 20$)

Appendix C

Additional Materials for Chapter 4

This supplementary material contains 4 additional sections (Sections C.1–C.4), and 14 supplemental figures (Figures C.1–C.14) for Chapter 4. Section C.1 notes geochemical and sedimentary evidence for the studied Kumano Knoll No. 3 (KK#3) mud volcano in the Nankai accretionary margin that shows that this mud volcano is currently active. Section C.2 provides calculation of a elastic-wave velocity over the seawater column above the studied KK#3 mud volcano. Section C.3 conveys porosity functions employed in the mud conduits of the KK#3 mud volcano. Section C.4 addresses geothermal information of the KK#3 mud volcano that constrains a downward profile of temperature in the mud conduits of the mud volcano. All the mud volcanoes and IODP sites found in Sections C.1, C.3, and C.4 are navigated in Figure 4.7a. Figures C.1–C.5 represent super-gathers of neighboring 5 CMPs within the mud conduit, in order to show common high-amplitudes found among the CMPs are candidates for seismic reflectors. Another example is demonstrated in Figure 4.5. Figures C.6–C.9 provide normal moveout (NMO) corrections of selected CMPs within the mud conduit of the studied submarine mud volcano, from the weighted semblance-based velocity analysis. Figures C.10 and C.11 demonstrate trace similarity among the given CMP and neighboring CMPs within the mud conduit. The similar examples are found in Figure 4.6. Figure C.12 shows deviation in velocity profiles among neighboring CMPs in order to evaluate uncertainty in our velocity analysis. Figure C.13 represents porosity functions that constrain porosity profiles in the mud conduits of the mud volcano in order to produce modeled velocities in Figure 4.7c. Figure C.14 shows

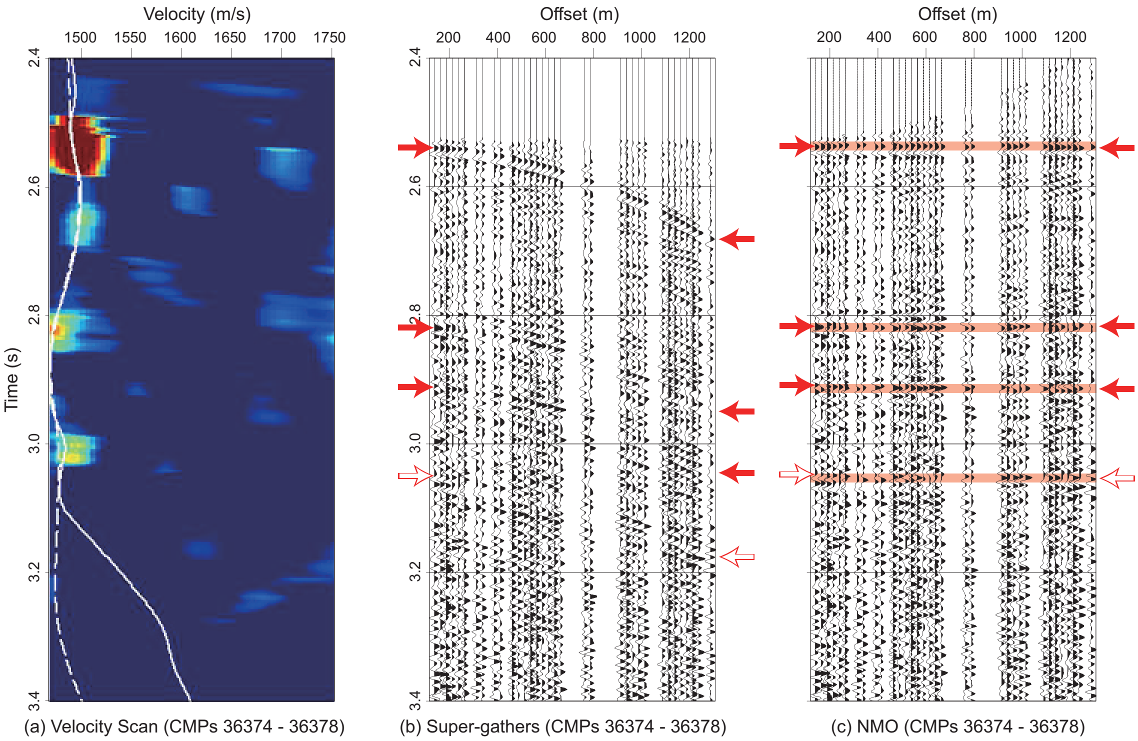

Figure C.1: Super-gathers among neighboring 5 CMPs in the western part of the mud conduit of the KK#3 mud volcano. (a) Velocity spectra of the super-gathers. The white solid line draws automatic picking velocities, while the white dash line shows optimum velocities. (b) Super-gathers in the western part of the mud conduit. (c) Moveout-operated super-gathers applying the optimum velocities.

profiles of modeled velocities when the porosity inside an active mud volcano is assumed to be unchanged downward for comparison of Figure 4.7c in Section 4.6.

C.1 Sedimentary evidence from the KK#3 mud volcano

At the KK#3 mud volcano in the Kumano basin of the Nankai margin (Figure 3a in the main text), a high methane flux and randomly distributed clam shells have been found [*Kuramoto et al.*, 2001; *Pape et al.*, 2014]. A short core, sampled at the KK#3 mud volcano during *R/V Hakuho-maru* (JAMSTEC, Japan) KH-11-9 Cruise, documents poorly sorted sandy silt matrix of debris flow merely with a thin hemipelagic layer at the surface. A large clast is also present at 20 cmbsf in the core, suggesting that the last massive eruption is young enough not to having sunk back into the conduits against their

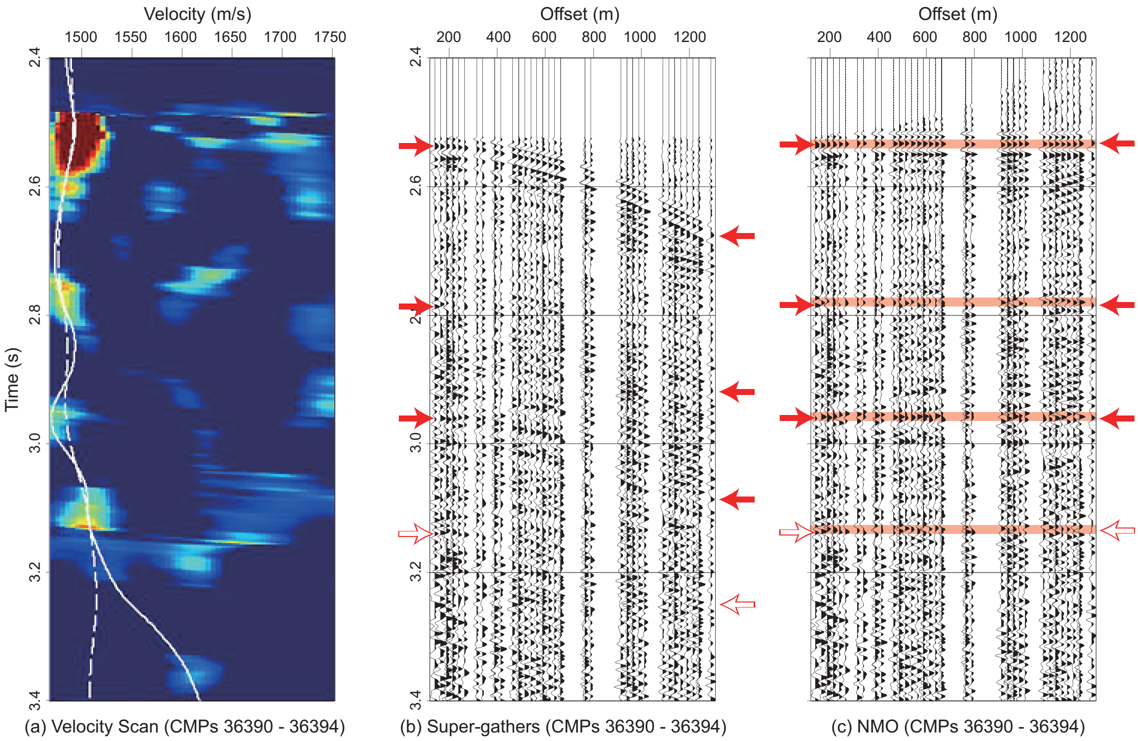

Figure C.2: Super-gathers among neighboring 5 CMPs in the central part of the mud conduit of the KK#3 mud volcano. (a) Velocity spectra of the super-gathers. The white solid line draws automatic picking velocities, while the white dash line shows optimum velocities. (b) Super-gathers in the central part of the mud conduit. (c) Moveout-operated super-gathers applying the optimum velocities.

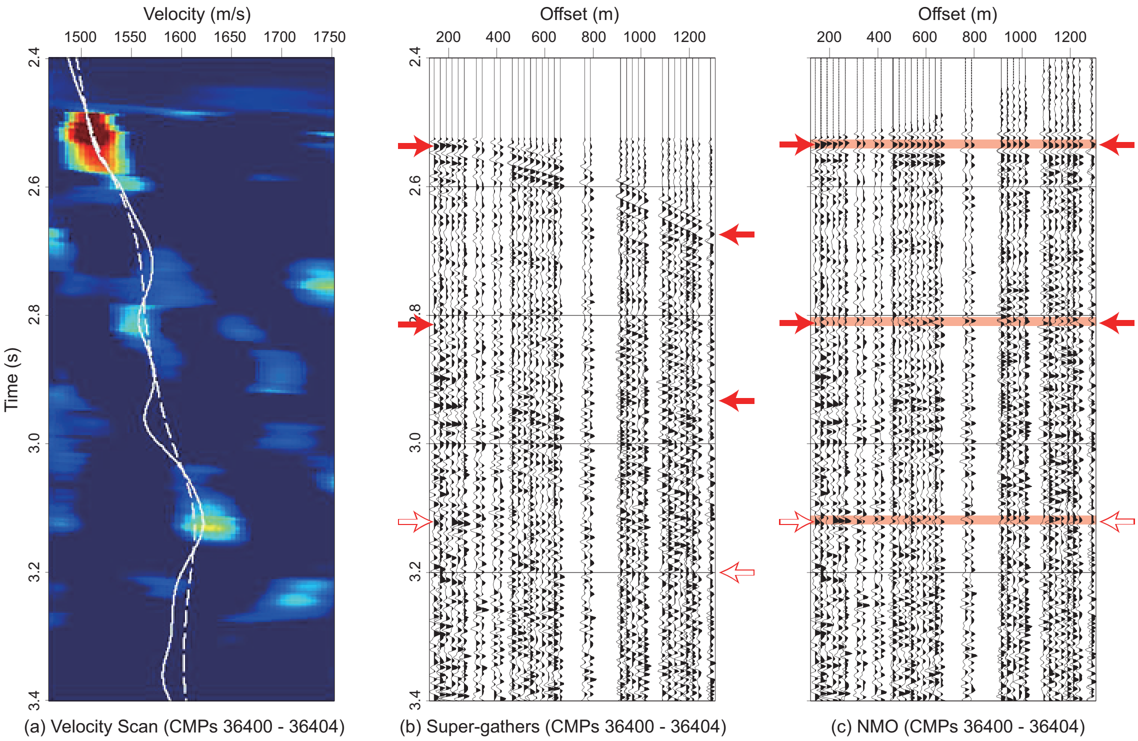

Figure C.3: Super-gathers among neighboring 5 CMPs in the central part of the mud conduit of the KK#3 mud volcano. (a) Velocity spectra of the super-gathers. The white solid line draws automatic picking velocities, while the white dash line shows optimum velocities. (b) Super-gathers in the central part of the mud conduit. (c) Moveout-operated super-gathers applying the optimum velocities.

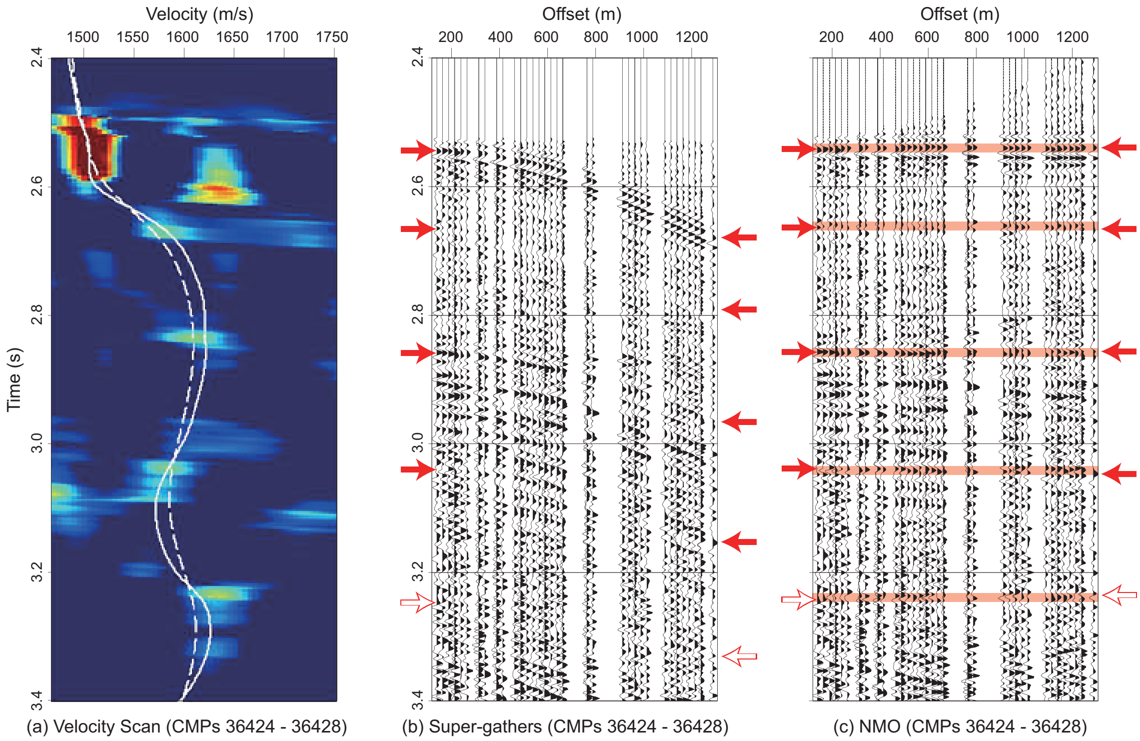

Figure C.4: Super-gathers among neighboring 5 CMPs in the eastern part of the mud conduit of the KK#3 mud volcano. (a) Velocity spectra of the super-gathers. The white solid line draws automatic picking velocities, while the white dash line shows optimum velocities. (b) Super-gathers in the central part of the mud conduit. (c) Moveout-operated super-gathers applying the optimum velocities.

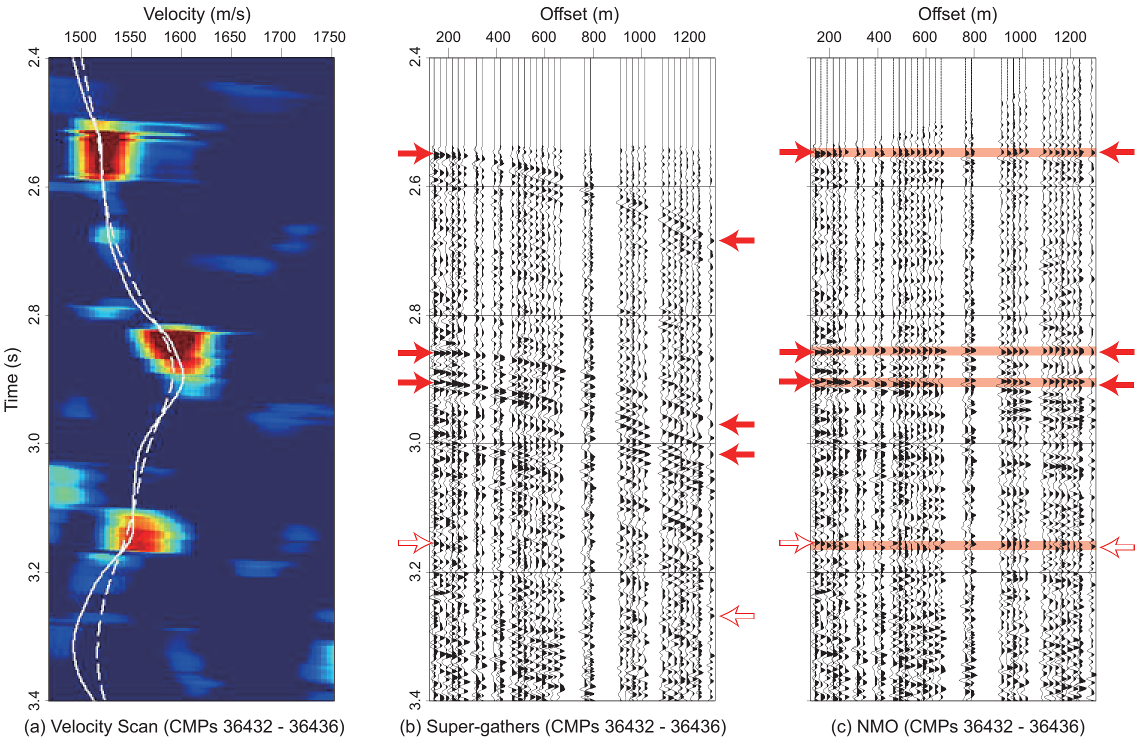

Figure C.5: Super-gathers among neighboring 5 CMPs in the eastern part of the mud conduit of the KK#3 mud volcano. (a) Velocity spectra of the super-gathers. The white solid line draws automatic picking velocities, while the white dash line shows optimum velocities. (b) Super-gathers in the central part of the mud conduit. (c) Moveout-operated super-gathers applying the optimum velocities.

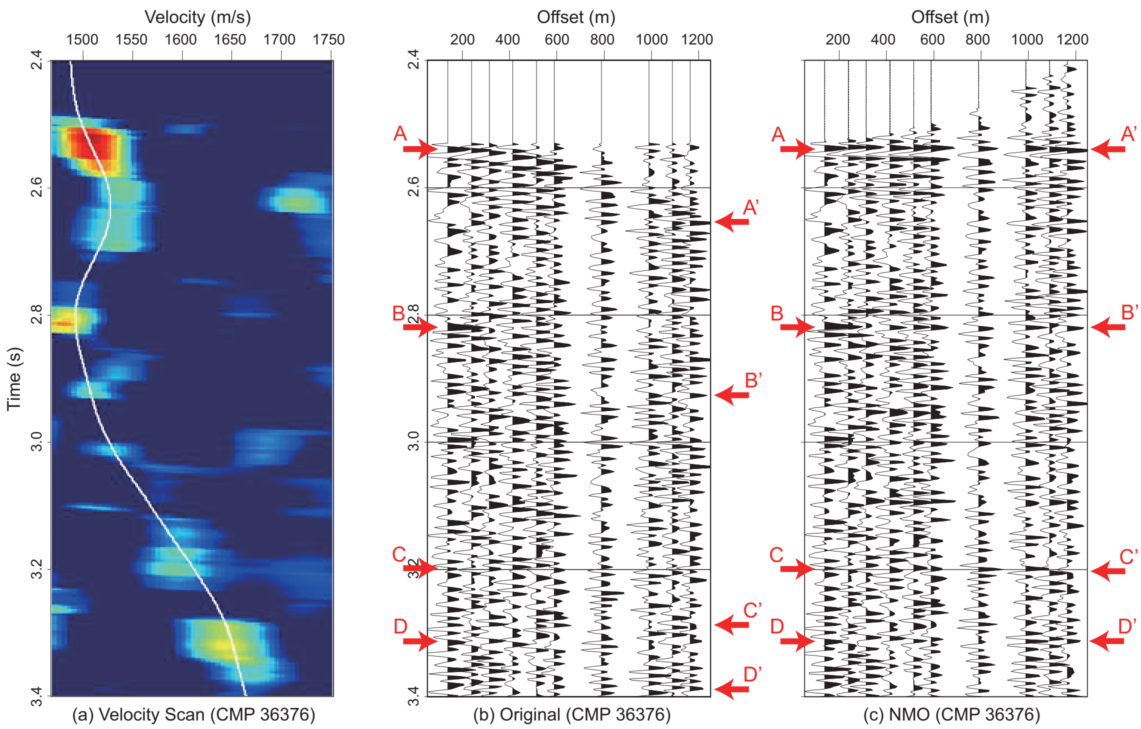

Figure C.6: The NMO correction in CMP 36376, situated in the western part of the mud conduit of the studied mud volcano. (a) A velocity scan map and optimum NMO velocities produced from the weighted semblance-based velocity analysis. (b) The traces without the NMO correction. (c) NMO corrected traces. Some of seismic event points are guided in red arrows to pilot the NMO correction.

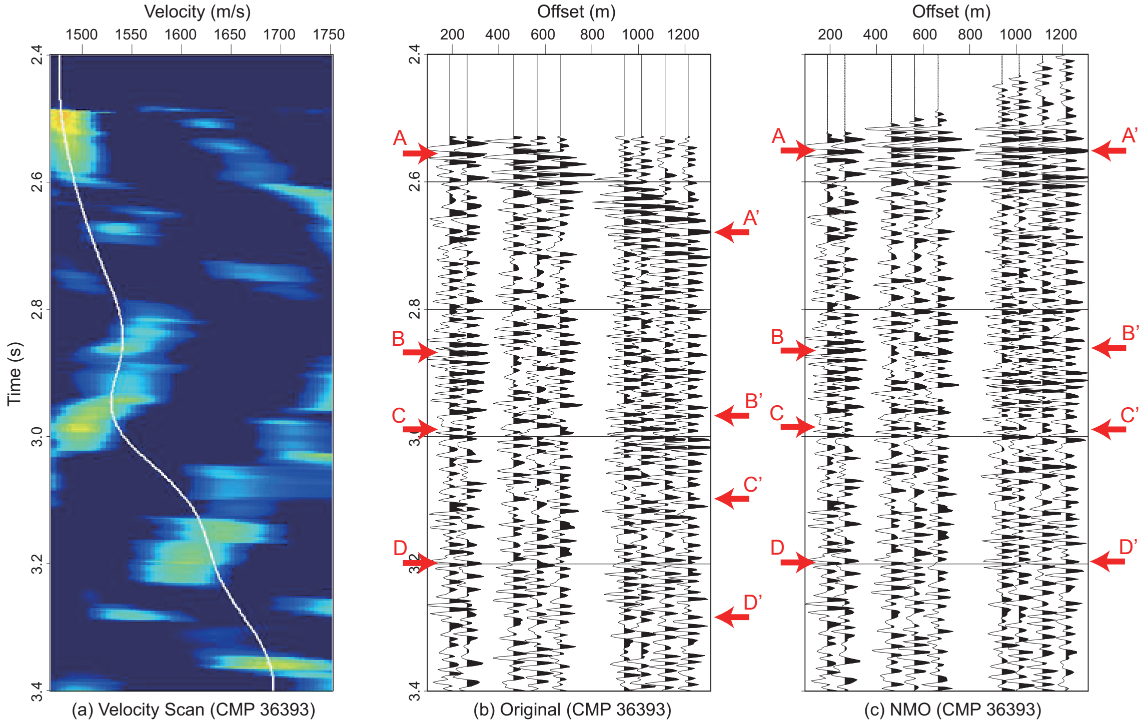

Figure C.7: The NMO correction in CMP 36393, situated in the central part of the mud conduit of the studied mud volcano. (a) A velocity scan map and optimum NMO velocities produced from the weighted semblance-based velocity analysis. (b) The traces without the NMO correction. (c) NMO corrected traces. Some of seismic event points are guided in red arrows to pilot the NMO correction.

background viscosity. Several core samplings from other cruises report the same picture [e.g., *Kopf et al.*, 2013], as well as many rock fragments are observed on the crest [e.g., *Kuramoto et al.*, 2001]. Thus, the KK#3 mud volcano is an active mud volcano with that figures the last massive eruption no earlier than several hundred years ago, as estimated from the sedimentation rate at the neighboring IODP Site C0002 [*Ashi et al.*, 2009; *Harris et al.*, 2011].

C.2 Elastic-wave velocity in the seawater column

To convert the weighted semblance-based RMS velocity to the interval velocity at a certain depth produced in Section 4.5.2, the elastic-wave velocity in the overlying seawater column is required to calculate because the optimum velocities cannot be detected from the semblance map in the water column. The seismic velocity at a certain wa-

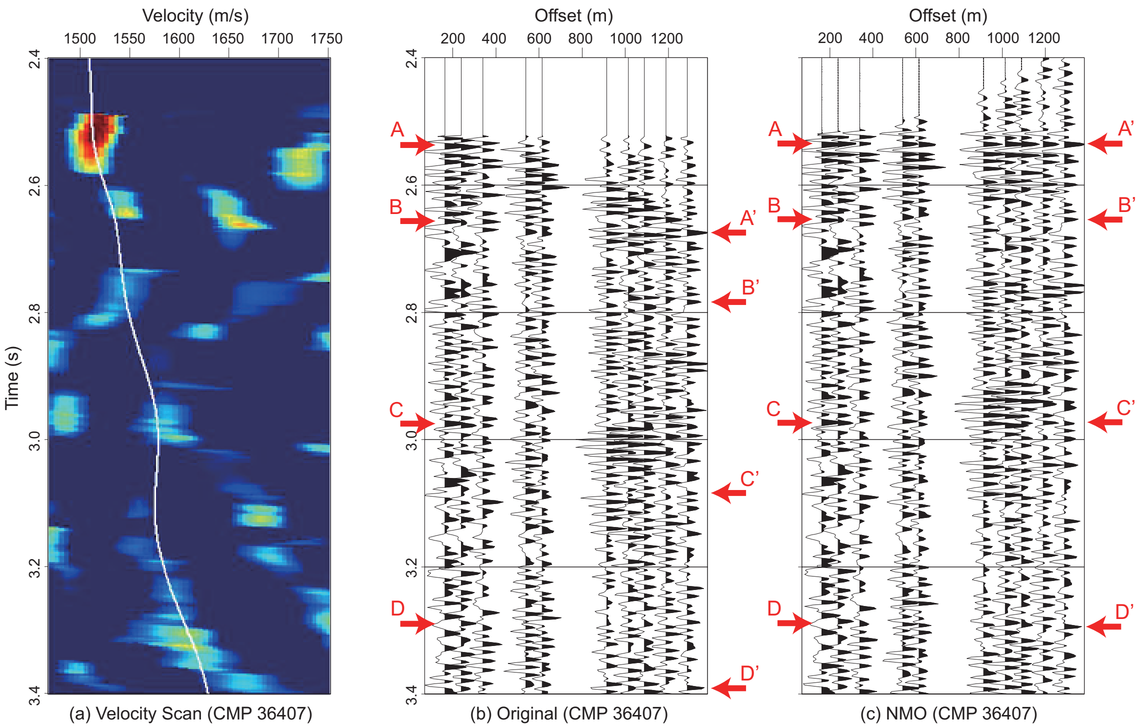

Figure C.8: The NMO correction in CMP 36407, situated in the central part of the mud conduit of the studied mud volcano. (a) A velocity scan map and optimum NMO velocities produced from the weighted semblance-based velocity analysis. (b) The traces without the NMO correction. (c) NMO corrected traces. Some of seismic event points are guided in red arrows to pilot the NMO correction.

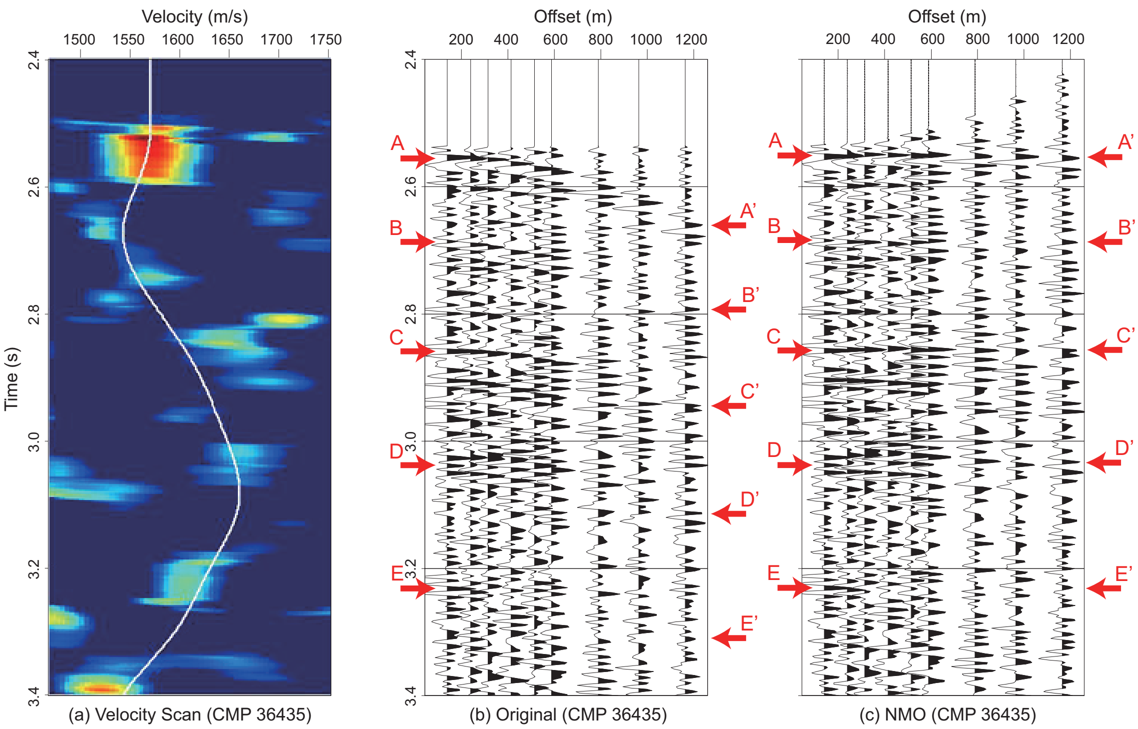

Figure C.9: The NMO correction in CMP 36435, situated in the eastern part of the mud conduit of the studied mud volcano. (a) A velocity scan map and optimum NMO velocities produced from the weighted semblance-based velocity analysis. (b) The traces without the NMO correction. (c) NMO corrected traces. Some of seismic event points are guided in red arrows to pilot the NMO correction.

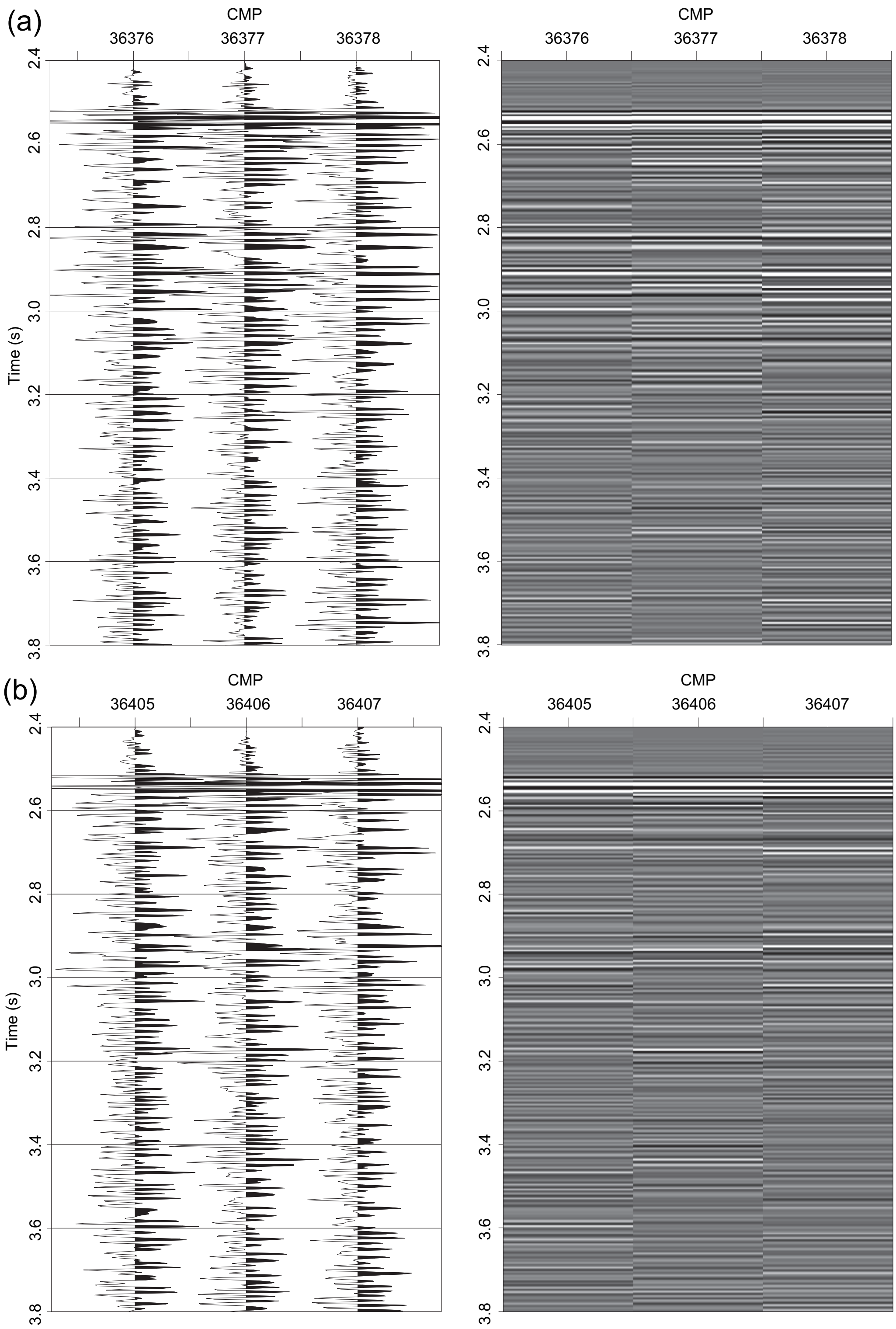

Figure C.10: Wiggle and raster plots of waveforms recorded in neighboring three CMPs located in mud conduits of the studied submarine mud volcano, in order to see similarity in traces between the given CMP and neighboring 2 CMPs: (a) Western part of the mud conduits and (b) Central part of the mud conduits. Other examples are demonstrated in Figure 4.6.

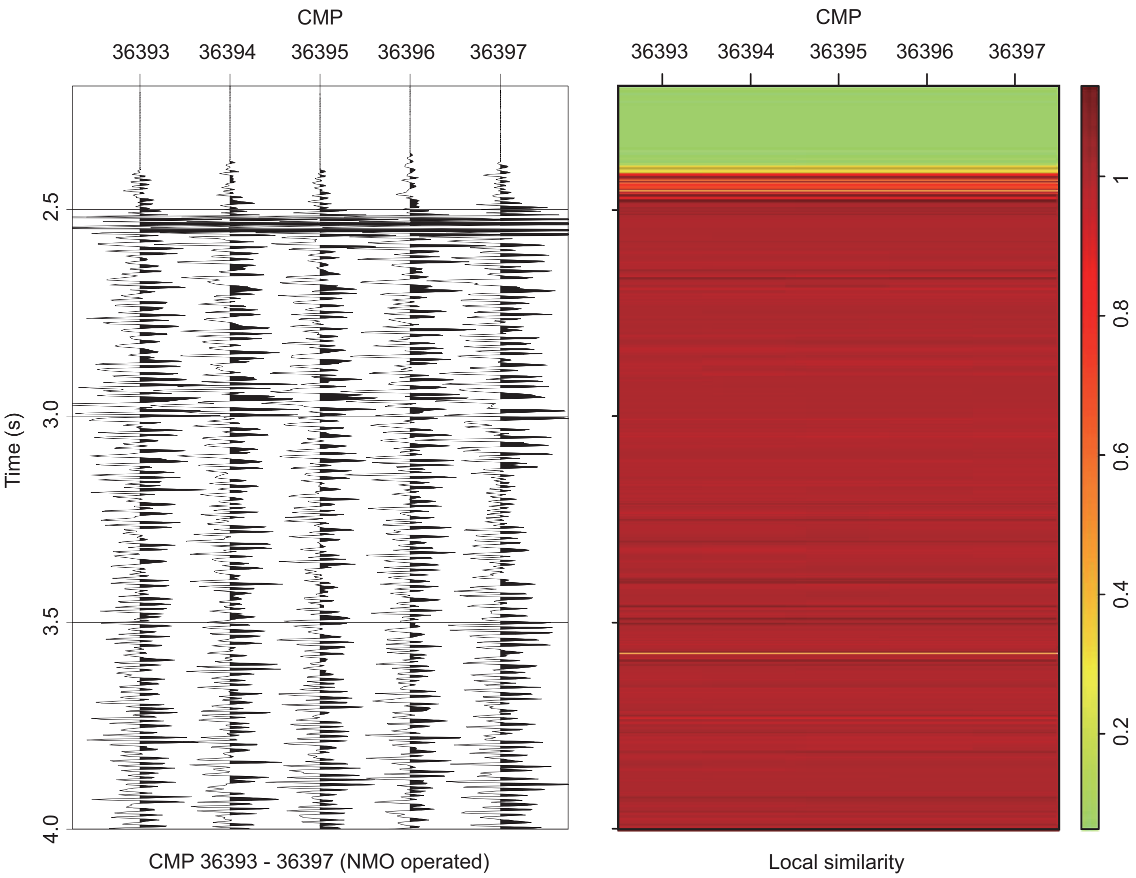

Figure C.11: Local similarity in traces between the given CMP and neighboring 4 CMPs within the mud conduit of the studied mud volcano. Local similarity is calculated with the help of shaping regularization [*Fomel*, 2007b].

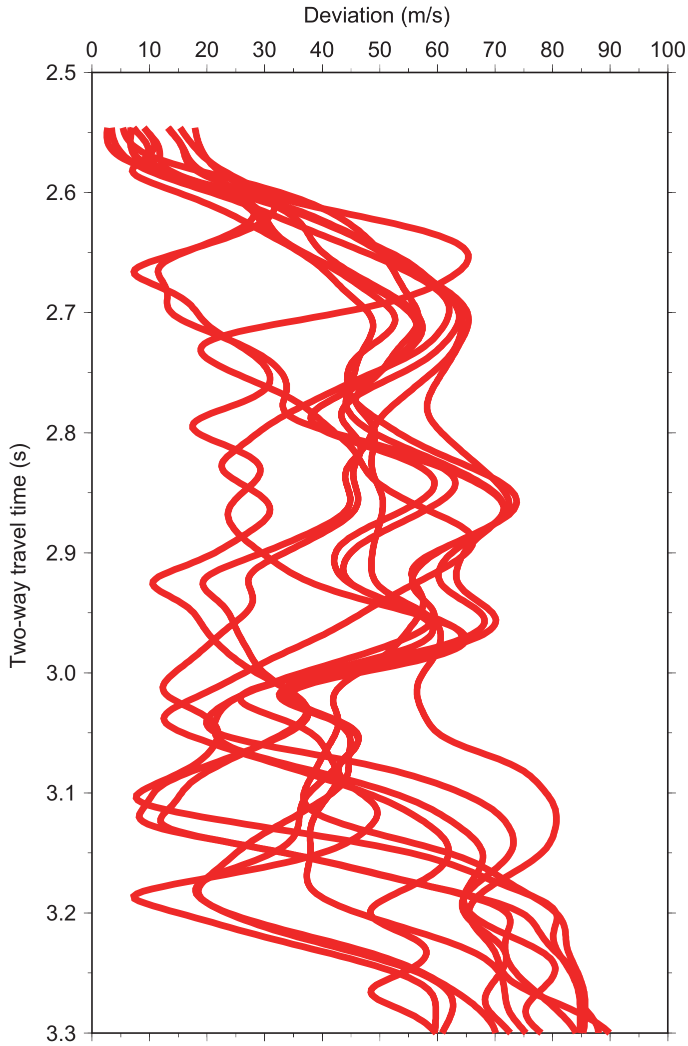

Figure C.12: Deviation in RMS velocity profiles among neighboring 5 CMPs within the mud conduit of studied mud volcano. The produced velocities have uncertainties of up to ±5% at deep depths within this time domain. Velocity profiles found in Figure 4.7c are produced from the TWT over ∼ 2.5–3.3 TWT s.

ter depth in the seawater column is theoretically given by the isentropic sound of speed in this study, using the thermodynamic properties to the Gibbs function and its temperature and pressure derivatives [*Wagner and Pruß*, 2002; *Feistel*, 2008]. Data of the expendable conductivity-temperature-depth system (XCTD) measured at the neighboring site (136°31.28'E, 33°31.50'N), about 20 km southwestward from the studied mud volcano, during the MR10-04 Leg 1 cruise in August 2010 are used to produce the downward profiles of temperature, hydrostatic pressure, and salinity, with that are partially extrapolated over the deeper depths. The pressure calculated here is also taken into account in derivation of model velocities. The XCTD data are available from the website http://www.godac.jamstec.go.jp/darwin/cruise/mirai/MR10-04_leg1/e.

C.3 Porosity profile in the mud conduits of the KK#3 mud volcano

A porosity over the upper several tens of meters of an active submarine mud volcano in the Nankai margin shows little fluctuation downward, as known from a recent deep-drilling expedition into the body of a mud volcano. Porosity values inside the KK#5 and KK#6 mud volcanoes in the Nankai margin display relatively narrow variations downward within $\phi \simeq 0.52 \pm 0.05$ [*Inagaki et al.*, 2009; *Muraoka et al.*, 2011], suggesting that they may suffer from little gravitational compaction resulting from their recent mud eruptions. In practice, however, the porosity would be increased or decreased by expanding methane or overburden over deeper depths of our interest. We thus take into account these effects by incorporating porosity data obtained from other submarine mud volcanoes where previous studies have reported porosity profiles at deep depths. The relationship between porosity and depth in the mud conduits of a submarine mud volcano is given by a commonly used equation:

$$\phi(z) = \phi_\infty + (\phi_0 - \phi_\infty) \exp(-kz), \tag{C.1}$$

where ϕ_0 is the initial porosity at the depth of $z = 0$, ϕ_∞ is the minimum porosity at an infinite depth, and k is the compaction coefficient (m^{-1}) [e.g., *Athy*, 1930; *Rubey and Hubbert*, 1959]. These parameters are determined by the nonlinear least-squares estimates

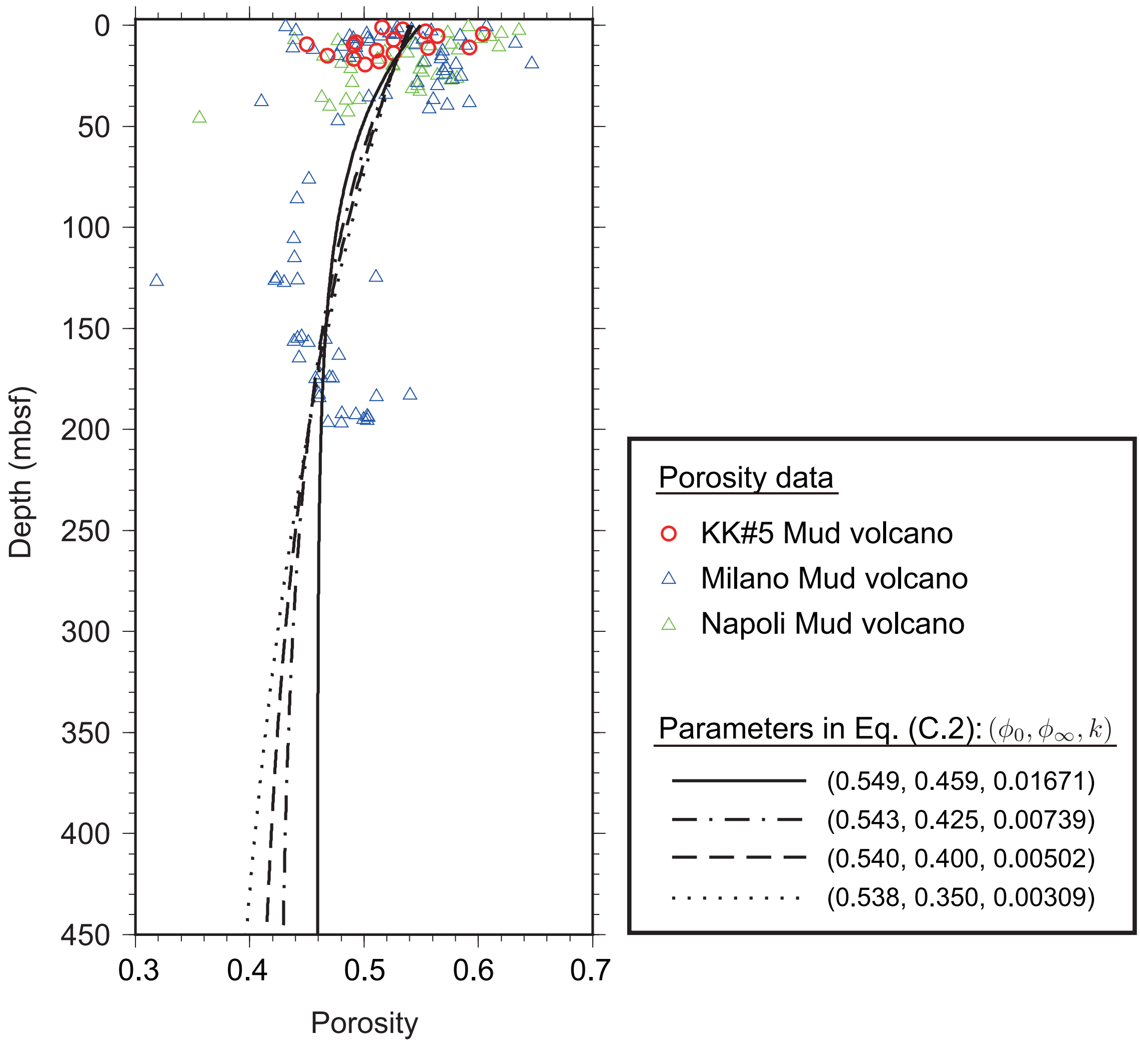

Figure C.13: Porosity profiles inside a submarine mud volcano. Red solid triangles, blue and green open circles represent porosities of mud volcano deposits obtained from the Site C9004 of the CK09-01 Leg 1 located at the center of the KK#5 mud volcano [*Inagaki et al.*, 2009], the ODP 160 Site 970A/970C/970D at Milano mud volcano, and the ODP 160 Site 971D/971E at Napoli mud volcano [*Emeis et al.*, 1996], respectively (outliers removed). Porosity functions are built using equation (C.1) with incorporating these measurement data (see Section C.3). A best-fit curve between porosity and depth is illustrated in a black solid plot. Possible values of the minimum porosity ϕ_∞ examined here are constrained by the porosity profiles at the IODP Sites C0002 [*Expedition 315 Scientists*, 2009] and C0009 [*Saffer et al.*, 2010].

of the model using measured porosity profiles from KK#5 mud volcano in the Nankai [*Inagaki et al.*, 2009], Milano and Napoli mud volcanoes in the eastern Mediterranean Sea [*Emeis et al.*, 1996] (Figure C.13). Since these submarine mud volcanoes are developed at similar water depths, a difference in effective vertical stress among them is not major concern. Porosity functions formulated here with being extrapolated over deep depths are used to produce modeled velocities illustrated in Figure 4.7.

C.4 Thermal information inside the KK#3 mud volcano

We assume the stationary temperature profile of the active KK#3 mud volcano, while the temperature profile is fluctuated through the heat flow associated with the mud volcano's activity [e.g, *Feseker et al.*, 2014; *Pape et al.*, 2014]. Downhole temperature measurements at the neighboring sites show thermal gradients over the deep-depths yield 42–43 K/km at the IODP Site C0002 [*Ashi et al.*, 2009; *Sugihara et al.*, 2014] and 26 K/km at the IODP Site C0009 [*Saffer et al.*, 2010]. The thermal gradient of the neighboring active KK#5 mud volcano that are obtained by sediment temperature measurements from deep-drilling has 29 K/km [*Inagaki et al.*, 2012]. The surface heat flow from an active mud volcano often has a higher value than a background heat flow observed from surrounding sedimentary sequences [e.g., *Goto et al.*, 2007; *Kopf et al.*, 2013]. The surface heat flow in the basin sedimentary sequences near the KK#3 mud volcano shows 44 mW/m^2 [*Hamamoto et al.*, 2011], but unfortunately no reliable surface heat flow from the KK#3 mud volcano has been observed so far. The thermal gradient at the KK#3 mud volcano is thus assumed to be $\Delta T = 0.042$ K/m, as determined by an observed heat flow from its neighbor KK#4 Mud volcano (60 mW/m^2) and a measurement of a thermal conductivity from matrix of the mud volcano (1.44 W/m/K) using a needle probe from a piston core obtained at the KK#3 mud volcano [*Goto et al.*, 2007; *Hamamoto et al.*, 2011]. Bottom water temperature T_{sf} is employed as a uniform value of 2°C, though the temperature variations are large with up to ±0.2°C in the studied area [*Hamamoto et al.*, 2005, 2011; *Pape et al.*, 2014].

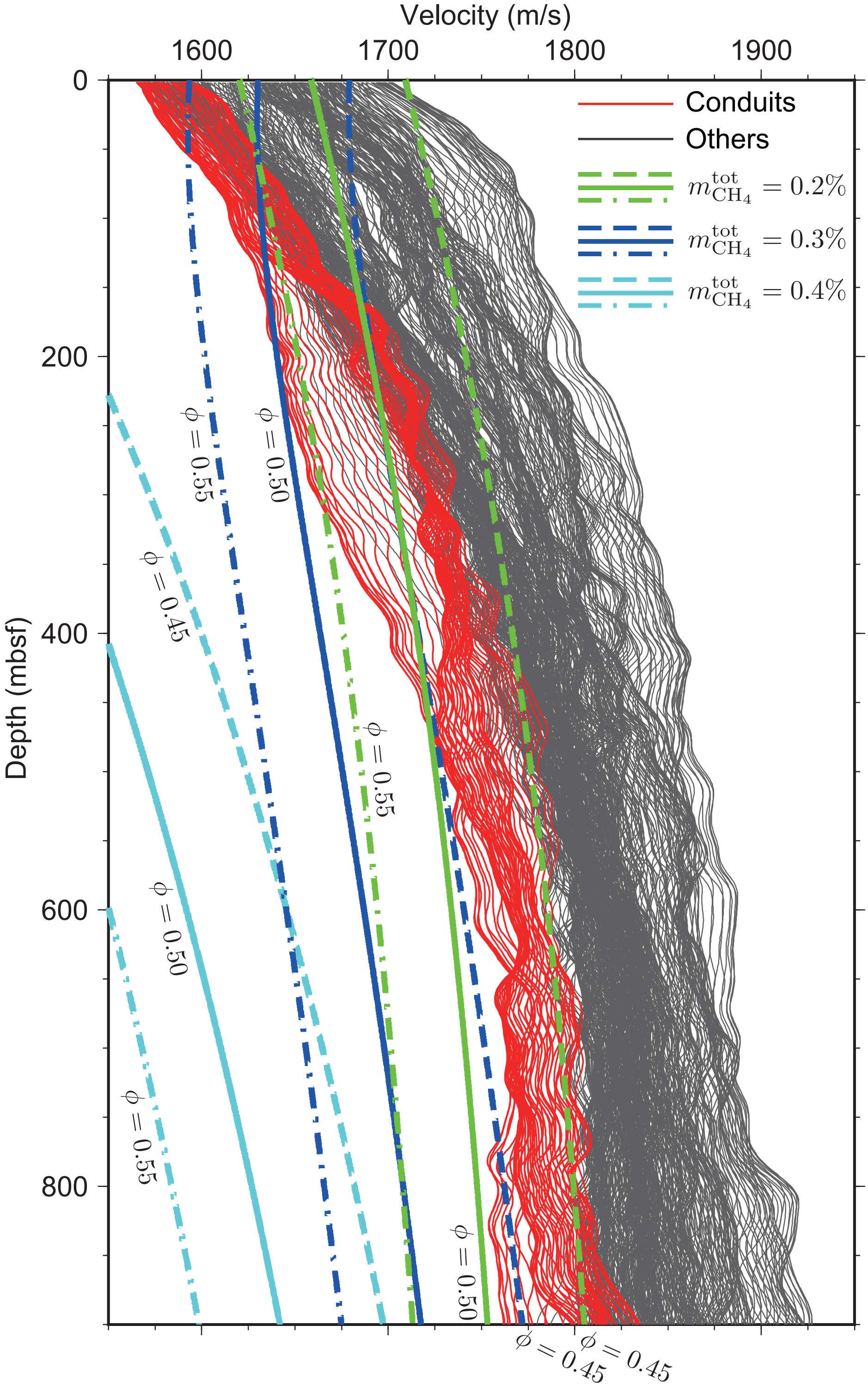

Figure C.14: Velocity profiles from the mud conduits of the KK#3 mud volcano (red lines), sedimentary sequences outside the mud conduits (dark gray lines), and modeled velocities below the top of the mud volcano with varying total methane mass fractions $m^{tot}_{CH_4} = 0.2$, 0.3, and 0.4% (green, blue, and cyan lines, respectively), and constant porosity profiles $\phi(z) = 0.45$, 0.50, and 0.55 (dash, solid, and dash-dot lines, respectively) for comparison. Please see Figure 4.7c that demonstrates modeled velocities implemented the porosity functions addressed in Section C.3.